

City Research Online

City St George's, University of London

Citation: Lazareva, A. (2017). An automated image processing system for the detection of photoreceptor cells in adaptive optics retinal images. (Unpublished Doctoral thesis, City, University of London)

This is the accepted version of the paper.

This version of the publication may differ from the final published version. To cite this item please consult the publisher's version.

Permanent repository link: https://openaccess.city.ac.uk/id/eprint/19164/

Copyright and Reuse: Copyright and Moral Rights remain with the author(s) and/or copyright holders. Copies of full items can be used for personal research or study, educational, or not-for-profit purposes without prior permission or charge, unless otherwise indicated, provided that the authors, title and full bibliographic details are credited, a hyperlink and/or URL is given for the original metadata page and the content is not changed in any way. For full details of reuse please refer to City Research Online policy.

City Research Online: http://openaccess.city.ac.uk/ publications@citystgeorges.ac.uk

CITY, UNIVERSITY OF LONDON

SCHOOL OF MATHEMATICS, COMPUTER SCIENCE, AND ENGINEERING

PhD in Information Engineering



An Automated Image Processing System for the Detection of Photoreceptor Cells in Adaptive Optics Retinal Images

Anfisa Lazareva

Thesis is submitted in partial fulfilment of the requirements for the degree of Doctor of Philosophy

September 2017

I hereby declare that the presented work in this thesis is my own or was developed in a joint effort with other members of research groups as it is stated and referenced in the text accordingly.

London, _____

_____

(Anfisa Lazareva)

Abstract

The rapid progress in Adaptive Optics (AO) imaging, in the last decades, has had a transformative impact on the entire approach underpinning the investigations of retinal tissues. Capable of imaging the retina in vivo at the cellular level, AO systems have revealed new insights into retinal structures, function, and the origins of various retinal pathologies. This has expanded the field of clinical research and opened a wide range of applications for AO imaging. The advances in image processing techniques contribute to a better observation of retinal microstructures and therefore more accurate detection of pathological conditions. The development of automated tools for processing images obtained with AO allows for objective examination of a larger number of images with time and cost savings and thus facilitates the use of AO imaging as a practical and efficient tool, by making it widely accessible to the clinical ophthalmic community.

In this work, an image processing framework is developed that allows for enhancement of AO high-resolution retinal images and accurate detection of photoreceptor cells. The proposed framework consists of several stages: image quality assessment, illumination compensation, noise suppression, image registration, image restoration, enhancement and detection of photoreceptor cells. The visibility of retinal features is improved by tackling specific components of the AO imaging system, affecting the quality of acquired retinal data. Therefore, we attempt to fully recover AO retinal images, free from any induced degradation effects. A comparative study of different methods and evaluation of their efficiency on retinal datasets is performed by assessing image quality. In order to verify the achieved results, the cone packing density distribution was calculated and correlated with statistical histological data. From the performed experiments, it can be concluded that the proposed image processing framework can effectively improve photoreceptor cell image quality and thus can serve as a platform for further investigation of retinal tissues. Quantitative analysis of the retinal images obtained with the proposed image processing framework can be used for comparison with data related to pathological retinas, as well as for understanding the effect of age and retinal pathology on cone packing density and other microstructures.

Acknowledgements

I would like to express my deepest appreciation to all those who provided me help and support throughout this research project. Firstly, I would like to thank Prof. Panos Liatsis, for inspiring guidance, constructive criticism and friendly advice. I would also like to express my gratitude to Dr Franziska Rauscher for her constant enthusiasm and time she took from her busy schedule to provide me with consultations on many aspects throughout these years. I sincerely thank my supervisor, Dr Gregory Slabaugh who has been actively supporting me in the last and most difficult year of my PhD.

My special thanks go to all my friends and family, who encouraged me in difficult moments and always believed in me. I am very grateful to all my colleagues from Computer Vision Group, who provided me with technical help when needed. On a personal basis, I would like to thank Dimitrios Papoulias, a bright and aspiring personality, for his valuable insights, moral support and all the effort that has pushed me in completing this project.

Table of Contents

Contents

Abstract 4

Acknowledgements 5

Table of Contents 6

List of Figures 10

List of Tables 17

Nomenclature 19

1. Introduction 23

1.1 Overview of the Problem Statement 23

1.2 The Optical System of the Human Eye 25

1.2.1 Anatomy of the Eye 25

1.2.2 Optical Aberrations 29

1.3 Adaptive Optics Imaging 34

1.3.1 History of AO Retinal Imaging 34

1.3.2 The rtx1 Adaptive Optics Retinal Camera 39

1.4 Applications of AO Retinal Imaging 41

1.5 Retinal Image Processing 45

1.6 Research Aim and Objectives 47

1.7 Contributions 48

1.8 Publications 49

1.9 Thesis Structure 50

2. Literature Review: Retinal Image Processing 52

2.1 Introduction 52
2.2 Image Acquisition in AO Systems 53
2.3 Image Registration 55
2.3.1 Classification 55
2.3.2 Image Registration in High-Resolution Retinal Imaging 57
2.4 Image Filtering 61
2.4.1 Noise Suppression 61
2.4.2 Illumination Compensation 63
2.5 Image Restoration 64
2.5.1 Deconvolution from Wavefront Sensing 64
2.5.2 Blind Deconvolution 65
2.5.3 Learning Methods 68
2.6 Automated Cone Detection 69
2.7 Literature Review Synopsis; Motivation for Research in Retinal Image Enhancement 71
3. Techniques and Analysis: Image Pre-processing 74
3.1 About This Chapter 74
3.2 Image Processing Framework 74
3.3 Image Quality Assessment 76
3.3.1 Blur Measure 78
3.3.2 Image Contrast 80
3.3.3 Image Variance 80
3.3.4 Evaluation of Image Quality Measures 80
3.4 Retrospective Illumination Correction 88
3.4.1 Image Model 88
3.4.2 Retrospective Illumination Correction using Low-pass Filtering and Division/Subtraction 89

3.4.3 Retrospective Correction using Homomorphic Filtering 90
3.4.4 Wavelet-based Filtering 91
3.4.5 Implementation of Retrospective Illumination Correction Methods 94
I. Illumination Correction using Low-pass Filtering and Division/Subtraction 95
II. Illumination Correction using Homomorphic Filtering 95
III. Wavelet-based Illumination Correction 96
IV. Wavelet-Fourier Filtering 107
3.4.6 Results of Uneven Illumination Correction 111
I. Visual Comparison of Uneven Illumination Correction Methods 111
II. Quantitative Assessment of Uneven Illumination Correction Methods 115
3.5 Noise Reduction 118
3.6 Image Registration 124
3.6.1 Introduction 124
3.6.2 Coarse Registration 126
3.6.3 Fine Registration 127
3.6.4 Lucky Averaging 128
3.6.5 Implementation and Results 129
I. Coarse Registration 129
II. Fine Registration 132
III. Lucky Averaging 135
3.7 Analysis and Discussion 141
4. Image Restoration 145
4.1 Introduction 145
4.2 Multi-variate Random Forest 149
4.3 Model of Point Spread Function in AO System 152
4.4 Implementation 156
4.4.1 Generation of Training Data 156
4.4.2 Training and Prediction 159
4.4.3 Image Restoration 163

4.5 Results and Evaluation 164
4.5.1 Experimental Validation using Synthetic Data 164
4.5.2 Experimental Validation using Real AO Retinal Images 168
4.6 Analysis and Discussion 175
5. Enhancement and Detection of Photoreceptor Cells 178
5.1 Hessian-LoG Filtering 178
5.2 Implementation and Results 181
5.2.1 Hessian-LoG filtering on Synthetic Image 181
5.2.2 Synthetic Data Generation 183
5.2.3 Cone Counting on Synthetic Data 187
5.2.4 Cone Counting on AO Retinal Images 193
5.2.5 Validation of Hessian-LoG Filtering on the Emmetropic Data Population 199
5.2.6 Image Deconvolution followed by Hessian-LoG Filter 208
5.3 Analysis and Discussion 217
6. Discussion and Conclusions 220
6.1 Summary of the Thesis Work 220
6.2 Contributions 232
6.3 Limitations of the Implemented Model 233
6.4 Proposal for Future Work 234
List of References 236

List of Figures

CHAPTER 1

FIGURE 1.1: The optical system of the human eye [22]. 25

FIGURE 1.2: Image formation within the human eye [25]. 26

FIGURE 1.3: Angular distribution of rods and cones in the retina [28]. 27

FIGURE 1.4: Light microscopic image depicting a retinal cross-section [29]. 27

FIGURE 1.5: *En face* sections of human retina acquired with differential interference contrast microscopy showing (a) cones at the fovea and (b) cones near the periphery (scale bar = 10 μm) [30]. 28

FIGURE 1.6: Schematic diagram of the retina for the right eye showing fovea, parafovea and perifovea in four retinal quadrants [31]. 28

FIGURE 1.7: Structural differences between rods and cones [22]. 29

FIGURE 1.8: Schematic drawing showing (a) a perfect lens with no chromatic aberration, (b) longitudinal chromatic aberration and (c) transverse chromatic aberration [37]. 31

FIGURE 1.9: Schematic drawing showing wavefront (WF) (a) in perfect and (b) aberrated (normal) eye [40]. 32

FIGURE 1.10: The first 21 Zernike polynomials [44]. 33

FIGURE 1.11: Retinal images for one subject (a) with and (b) without AO correction, acquired at 1.25 degree eccentricity on the temporal retina [69]. 37

FIGURE 1.12: AO retinal imaging system [4]. 37

FIGURE 1.13: Principle of measuring ocular aberrations with a wavefront sensor [70]. 39

FIGURE 1.14: Schematic diagram of the measurement principle of a Shack–Hartmann wavefront sensor. F is the focal length of the lenslet. Two Shack-Hartmann images for (a) perfect and (b) real eyes are also shown [57]. 39

FIGURE 1.15: Commercially available AO flood-illuminated instrument: rtx1, Imagine Eyes, Orsay, France [12]. 40

FIGURE 1.16: (A) Cone photoreceptor mosaic imaged with an AO fundus camera at 1 degree eccentricity on the temporal retina and (B) pseudocolor image of the same location with blue, green, and red representing the S, M, and L cones, respectively [73]. 42

FIGURE 1.17: Example of photoreceptor layer with drusen. The scale bar is 104 μm. 44

CHAPTER 2

FIGURE 2.1: A scheme of AO embedded in an imaging system, showing origins of the specific degradation processes. 54

FIGURE 2.2: Illustration of cone packing density and Voronoi tessellation calculation using the software program provided by Imaging Eyes (CK v0.1 and AO detect v0.1, Imaging Eyes, France) in a patient with rod-cone dystrophy [195]. 70

CHAPTER 3

FIGURE 3.1: The block-diagram of the proposed image processing framework. 76

FIGURE 3.2: Gradually blurred high-resolution retinal images. (a) Original high-resolution retinal image with corrected illumination; (b) image (a) blurred with the Gaussian low pass filter with k =4, σ = 1.2; (c) image (a) blurred with the Gaussian low pass filter with k =10, σ = 1.8. 82

FIGURE 3.3: Image quality variations for the gradually blurred retinal image sequence calculated with four different IQA models. 83

FIGURE 3.4: High-resolution retinal images selected from one dataset for image quality evaluation. The scale bar is 40 μm. 84

FIGURE 3.5: Scatter plots of different image quality measures versus human ratings for four retinal datasets acquired from different locations. Human ranking corresponds to the image quality sorted in descending order, from high (equal to one) to low (equal to seven). 86

FIGURE 3.6: Retinal dataset 4 evaluated using BM_1. 88

FIGURE 3.7: Wavelet decomposition of an image into sub-bands. (a) Original image; (b) 1-level wavelet decomposition; (c) 2-level wavelet decomposition. LL stands for the approximate image, the detailed information is represented by three components: horizontal (LH), vertical (HL), and diagonal (HH). 94

FIGURE 3.8: (a) Original high-resolution retinal image and (b) its surface plot. 95

FIGURE 3.9: Retinal image reconstructed using different types of wavelet transform. 97

FIGURE 3.10: High-resolution retinal images reconstructed using the approximation coefficients at decomposition levels 1-10. 98

FIGURE 3.11: High-resolution retinal images with corrected illumination using DB6 wavelet at decomposition levels 1-10. 100

FIGURE 3.12: Calculating the appropriate level of decomposition using (a) negative of local brightness variation, (b) homogeneity of approximated background and (c) their multiplication. 103

FIGURE 3.13: Flowchart showing the process of wavelet-based illumination correction with the automated selection of the decomposition level. 104

FIGURE 3.14: (a) Predefined illumination pattern; (b) high-resolution retinal image with no illumination background; (c) retinal image (b) multiplied with the illumination pattern (a) and (d) its surface plot. 105

FIGURE 3.15: Difference between the predefined illumination pattern and illumination estimated using approximation coefficients at level 6 obtained with different types of Daubechies wavelet transform. 106

FIGURE 3.16: Retinal image reconstructed using DB3 showing horizontal and vertical artefacts. 107

FIGURE 3.17: Gaussian filter used for eliminating the Fourier coefficients (a) at the abscissa for vertical stripes and (b) at the ordinate for horizontal stripes at the second level of decomposition. 108

FIGURE 3.18: Wavelet-Fourier filter applied to the illumination component of the retinal image. (a) Illumination component estimated using approximation coefficients; (b) 2-level wavelet decomposition of (a) showing that vertical and horizontal stripes concentrate in the vertical and horizontal sub-band components, respectively. 109

FIGURE 3.19: Result of wavelet-Fourier filter applied to the illumination component of the retinal image. (a) Illumination component with vertical stripes eliminated using the wavelet-Fourier filter; (b) vertical stripes that have been eliminated; (c) illumination component with horizontal stripes eliminated using the wavelet-Fourier filter; (d) horizontal stripes that have been eliminated. 110

FIGURE 3.20: High-resolution retinal image (a) before and (b) after applying the wavelet-Fourier filter. 111

FIGURE 3.21: Results of illumination correction showed on a section of high-resolution retinal image using four methods: wavelet-based filtering, low-pass filtering and division, homomorphic filtering, low-pass filtering and subtraction. 112

FIGURE 3.22: Surface plots and corresponding intensity profiles of retinal image processed by four different illumination correction methods. 114

FIGURE 3.23: Local brightness variation of the images obtained with different methods of illumination correction. 116

FIGURE 3.24: Sharpness measure of the images obtained with different methods of illumination correction. 116

FIGURE 3.25: Calculation of cut-off frequencies for the band pass filter. (a) High-resolution retinal image after illumination correction, (b) its power spectrum, and (c) radially averaged power spectrum with cut-off frequencies for Gaussian band pass filter shown with red markers. 119

FIGURE 3.26: Retinal image frames before (left) and after noise suppression (right) in four representative datasets. The scale bar is 40 μm. 122

FIGURE 3.27: The spectral power ratio between the images before and after image denoising. Black lines show the cut-off frequencies in the band-pass filter. 124

FIGURE 3.28: (a) Magnitude of cross power spectrum for the raw retinal images (c) and (b) for the images after illumination compensation and noise suppression (d). 130

FIGURE 3.29: Magnitude of the cross-power spectrum interpolated onto an array with finer sampling. 131

FIGURE 3.30: Sharpness measure for the sequence of images in the retinal dataset sorted in descending order. 132

FIGURE 3.31: Translation detected at the coarse stage of image registration in one of the retinal datasets: (a) horizontal and (b) vertical translation vectors. 132

FIGURE 3.32: Control points in the reference and test image, showing the difference in coordinates of the brightest pixel. 133

FIGURE 3.33: Control points for reference and test images. 134

FIGURE 3.34: Rotation angles calculated at the fine stage of image registration for one of the retinal datasets. 134

FIGURE 3.35: Sharpness measure map calculated in 20-by-20 pixel blocks for two retinal frames. 136

FIGURE 3.36: Image showing number of blocks used in the lucky averaging scheme for calculating one of the final images. 137

FIGURE 3.37: Average images after coarse registration (left) and fine registration (right) in four representative datasets. The scale bar is 40 μm 138

FIGURE 3.38: Sections of retinal images from each dataset showing the difference between normal averaging scheme (left) and lucky averaging (right). The scale bar is 60 μm. 140

FIGURE 3.39: Comparison of retinal images obtained at the pre-processing stages: (a) raw image, (b) image after illumination compensation, (c) image after noise suppression and (d) averaged registered image. The scale bar is 40 μm. 144

CHAPTER 4

FIGURE 4.1: Flowchart showing (a) the process of training, (b) prediction and image restoration in the proposed model for blind image deconvolution based on Random Forest. 148

FIGURE 4.2: Basic notation in the Random Decision Forest Model. 149

FIGURE 4.3: Prediction of target vector in the Random Forest Model. 151

FIGURE 4.4: Frequency histograms of Zernike coefficients in a normal population of human eyes compared with Gaussian probability distribution (solid line). Physical units of Zernike coefficients are in μm. Pupil diameters is 6 mm [247]. 155

FIGURE 4.5: Example of simulated blur kernels replicating PSFs of the imaging system after AO correction. 156

FIGURE 4.6: Step-by-step process of synthetic image generation. 157

FIGURE 4.7: Results of synthetic data generation and feature extraction, showing (a) ideal synthetic retinal image, (b) generated PSF, (c) the result of convolving image (a) with PSF (b), (d) HoG features extracted from windows centred at 50 brightest cones. 159

FIGURE 4.8: Mean error of predicted Zernike coefficients as a function of number of the trees in the Random Forest (left) and maximum depth of the trees (right). 160

FIGURE 4.9: The posterior probability distributions of 80 regression trees (shown with different colours). The thick green line is an ensemble posterior $p(\boldsymbol{a}|\boldsymbol{H}_i)$ obtained by averaging all tree posteriors with values showing the MAP (Y=41.1) and the corresponding predicted Zernike coefficient for defocus aberration (X=0.2019 μm). 162

FIGURE 4.10: The posterior probability distributions of 80 regression trees (shown with different colours). The thick green line is an ensemble posterior $p(\boldsymbol{a}|\boldsymbol{H}_i)$ obtained by performing KDE on the data from all the leaf nodes showing the MAP (Y=70.05) and the corresponding predicted Zernike coefficient for defocus aberration (X=0.1986 μm). 162

FIGURE 4.11: Results at the prediction stage showing the predicted PSFs, corresponding blurred images, images restored with the estimated PSFs and compared with the GT data in terms of RMSE. 167

FIGURE 4.12: Comparison between retinal images obtained after image registration (left) and image deconvolution (right) in four representative datasets in terms of sharpness measure (BM1) and PSNR, showing retinal images at different scales: 1.2mm, 154 μm and 40 μm. 172

FIGURE 4.13: Sections of AO retinal images restored with the proposed method (left) and the ALM method (right). The proposed method shows better separation of individual photoreceptor cells, while the ALM method seems to blur the photoreceptor cells with weak edges. The scale bar is 154 μm. 174

FIGURE 4.14: Power spectral ratios (a) between the images restored with the ALM and obtained after the registration stage and (b) between the images restored with the proposed deconvolution method and obtained after the registration stage. Black lines show the spatial frequencies of cone mosaic. 175

CHAPTER 5

FIGURE 5.1: Second-order partial derivatives of the Gaussian function: (a) f_{xx}, (b) f_{yy} and (c) f_{xy}. The scale of the Gaussian function, σ, is equal to 5. 180

FIGURE 5.2: The LoG filter. (a) 3D plot of the LoG; (b) cross-section of (a); (c) the LoG displayed as an image [264]. 181

FIGURE 5.3: Hessian-LoG filter applied to a synthetic image. (a) Original image; (b) image processed with the Hessian enhancement filter; (c) LoG filtered image of (b); (d) binary image of (c) with the threshold equal to 0.09. 182

FIGURE 5.4: A set of processed AO-corrected and synthetic images at different retinal locations. (a) AO retinal image at 0.59 mm eccentricity; (b) synthetic image imitating the retina at 0.59 mm eccentricity; (c) AO retinal image at 1.1 mm eccentricity; (d) synthetic image imitating the retina at 1.1 mm eccentricity. The scale bar is 31 μm. 184

FIGURE 5.5: Step-by-step results of Hessian-LoG filtering for cone detection on a synthetic retinal image. (a) Image with randomly distributed disks; (b) 186

synthetic retinal image; (c) image (b) processed with the blob enhancement filter; (d) image (c) convolved with the LoG operator; (e) image (d) with negative values set to 0; (f) binary mask with the boundary cones excluded; (g) result of cone detection overlaid on image (b) without the boundary cones; (h) result of cone detection overlaid on image (a) without the boundary cones.

FIGURE 5.6: Results of cone detection obtained by the proposed method and the algorithm of Li and Roorda; (a) and (b) cone coordinates overlaid on the image with disks from set A; (c) and (d) cone coordinates overlaid on the synthetic retinal image from set A; (e) and (f) cone coordinates overlaid on the image with disks from set B; (g) and (h) cone coordinates overlaid on the synthetic retinal image from set B. 189

FIGURE 5.7: Box-and-whisker plot showing the cone detection error expressed as percentage difference between the proposed method, the Li and Roorda algorithm, manual counting and GT. The size of each bar is defined by a minimum (Min) and a maximum (Max) cone detection error. Q2 represents the median error; Q1 and Q3 are the lower and upper quartiles, respectively. 191

FIGURE 5.8: Box-and-whisker plot showing the cone detection error between the proprietary software of Imagine Eyes, the proposed method, the Li and Roorda algorithm and manual counting. The size of each bar is defined by a minimum (Min) and a maximum (Max) cone detection error. Q2 represents the median error; Q1 and Q3 are the lower and upper quartiles, respectively. 195

FIGURE 5.9: Results of cone detection on the AO high-resolution retinal images with the proposed method and the Li and Roorda algorithm at different retinal locations: (a) and (b) at 0.89 mm Nasal, (c) and (d) at 0.89 mm Temporal eccentricity, (e) and (f) at 0.6 mm Nasal. White circles correspond to the cones missed by one of the examined cone counting methods but detected by another one. 198

FIGURE 5.10: Image enhancement with the Hessian-LoG filter. (a) Processed retinal image; (b) Hessian-LoG filtered image; (c) image (a) multiplied with image (b). The scale bar is 21 μm. 199

FIGURE 5.11: Example of retinal montage composed of six AO high-resolution retinal images. Sampling windows where cone packing density was assessed are shown with red and green rectangles. 200

FIGURE 5.12: Variation of cone packing densities with eccentricity in the nasal (N), temporal (T), superior (S) and inferior (I) quadrants obtained from the study of Curcio et al. [30] (black line), Chui et al. [84] (blue line) and data from the two age groups. 202

FIGURE 5.13: Bland-Altman plots showing differences between cone density measurements obtained from the study of Chui et al. and two age groups in respect to the histology data of Curcio et al. 206

FIGURE 5.14: Cone detection in two synthetic images, imitating the retina at 1.2 mm and 0.9 mm eccentricity before and after image restoration. Solid red circles and red dotted circles indicate FNs and FPs, respectively. 209

FIGURE 5.15: Cone coordinates detected in the retinal images before (left) and after image deconvolution (right) and overlaid on the AO retinal image 212

acquired at 0.9 mm. Red solid circles show the cones detected after image deconvolution but missed in the image after registration stage. Red dotted circles show the cones detected before image deconvolution but missed after the image was restored.

FIGURE 5.16: Comparison between retinal images obtained after image deconvolution (left) and enhancement with the Hessian-LoG filter (right) in four representative images in terms of sharpness measure (BM_1), showing retinal images at different scales: 1.2mm, 40 μm (upper row) and 154 μm (bottom row). 213

CHAPTER 6

FIGURE 6.1: Comparison of retinal images produced by the commercial software of Imagine Eyes (left) and the proposed image processing framework (right). 230

FIGURE 6.2: Sharpness measure map calculated for retinal images produced by the commercial software of Imagine Eyes (left) and the proposed image processing framework (right). 231

FIGURE 6.3: Resulting retinal image of the pathological retina obtained with the proposed image processing framework (left) and the software of Imagine Eyes (right). 232

List of Tables

CHAPTER 3

TABLE 3.1: Comparison of different image quality measures with human ratings in four retinal datasets acquired at different locations. 85

TABLE 3.2: Performance evaluation of four illumination correction methods in terms of local brightness variation and sharpness measure averaged for 10 retinal images. 117

TABLE 3.3: Results of parametric study, showing rotation angle tests, model approximations and absolute error. 135

CHAPTER 4

TABLE 4.1: Normalized Zernike polynomials in single (first column) and double-index notation (second column). 154

TABLE 4.2: Comparison between the GT and predicted vectors of Zernike coefficients. Each column represents a vector of 10 coefficients used for reconstructing the PSFs ($a_4, \sum_{m=7}^{15} a_m$) and the row gives a value of Zernike coefficient a_m for a corresponding type of aberration. 165

TABLE 4.3: Quality assessment of the AO retinal images obtained after image registration, image deconvolution performed with the proposed method and image restoration with the ALM averaged for 25 images. 173

CHAPTER 5

TABLE 5.1: Quality assessment of 10 processed AO-corrected and 10 synthetic retinal images. The values are shown as mean ±standard deviation (SD). 185

TABLE 5.2: Average TP, FP and FN ratios for sets A and B obtained by the proposed method, the algorithm of Li and Roorda and manual counting. 188

TABLE 5.3: Results of the reproducibility test showing (a) the concordance correlation coefficient ρ_c with p-values and confidence intervals (CI); (b) CoV; (c) results of the paired t-test showing associated t-test statistics and mean differences for the cone count estimates obtained by the proposed method, the algorithm of Li and Roorda and manual counting in respect to the GT. 192

TABLE 5.4: Cone density estimates obtained by the three automated methods and the average values of manual cone counts from four observers for 10 AO-corrected retinal images. 194

TABLE 5.5: Percentage differences between cone density estimates obtained by the three automated methods and average manual cone counts for 10 AO-corrected retinal images. 194

TABLE 5.6: Results of the reproducibility test showing (a) the concordance correlation coefficient ρ_c with p-values and CIs; (b) CoV; (c) results of the paired t-test showing associated t-statistics and mean differences for the cone density estimates obtained by the three automated methods and average manual counts. 196

TABLE 5.7: The range of cone densities for group 1 and group 2 at the retinal eccentricities of 0.30 mm to 1.40 mm along the nasal, superior and inferior meridians, respectively, and at the retinal eccentricities of 0.30 mm to 2.20 mm along the temporal meridian. The values are expressed as mean ± SD. 203

TABLE 5.8: Results of the reproducibility test showing the concordance correlation coefficient ρ_c with p-values and CIs, and CoV for the measurements acquired in the study of Chui et al. and two age groups in respect to the histology data of Curcio et al. at four retinal meridians. 204

TABLE 5.9: Results of the paired t-test showing associated t-statistics and mean differences for the cone density distribution obtained in the study of Chui et al. and two age groups in respect to the histology data of Curcio et al. across four retinal meridians. 205

TABLE 5.10: Average TP, FP and FN ratios for 1000 synthetic images obtained by the proposed cone counting method before and after image deconvolution stage. 208

TABLE 5.11: Comparison of cone density estimated in the images at different retinal eccentricities before and after image deconvolution with the histological data of Curcio et al. [30]. 211

Nomenclature

ABBREVIATIONS

AO	Adaptive Optics
AOSLO	Adaptive Optics Scanning Laser Ophthalmoscopy
AO-SDOCT	Adaptive Optics Spectral Domain Optical Coherence Tomography
LCA	Longitudinal Chromatic Aberration
TCA	Transverse Chromatic Aberration
LOA	Low-Order Aberrations
HOA	High-Order Aberrations
SLO	Scanning Laser Ophthalmoscope
OCT	Optical Coherence Tomography
WFS	Wavefront Sensing
CCD	Charge-Coupled Device
LED	Light-Emitting Diode
RPE	Retinal Pigment Epithelium
DR	Diabetic Retinopathy
AMD	Age-related Macular Degeneration
RNFL	Retinal Nerve Fibre Layer
ONH	Optic Nerve Head
SNR	Signal-to-Noise Ratio
FFT	Fast Fourier Transform
LPT	Log-Polar Transform
DWT	Discrete Wavelet Transform
CWT	Continuous Wavelet Transform
PSF	Point Spread Function
OTF	Optical Transfer Function
FR	Full-Reference
NR	No-Reference
BM	Blur Measure
RMS	Root Mean Square
FT	Fourier Transform
2D	Two-Dimensional
3D	Three-Dimensional

LL	Low-frequency approximation component
LH	Horizontal high-frequency detail component
HL	Vertical high-frequency detail component
HH	Diagonal high-frequency detail component
IDWT	Inverse Discrete Wavelet Transform
DB	Daubechies wavelet
POC	Phase-Only Correlation
IFFT	Inverse Fast Fourier Transform
SVD	Singular Value Decomposition
LoG	Laplacian of Gaussian
GLCM	Grey Level Co-occurrence Matrix
BD	Blind Deconvolution
MAP	Maximum A Posteriori
PSNR	Peak-Signal-to-Noise Ratio
GT	Ground Truth
HoG	Histograms of oriented Gradients
KDE	Kernel Density Estimation
RMSE	Root-Mean-Square Error
ALM	Augmented Lagrangian Method
TP	True Positives
FN	False Negatives
FP	False Positives
CoV	Coefficient of Variation
ICD	Inter-Cell Distance
ZP	Zernike Polynomial
SD	Standard Deviation
CI	Confidence Interval

ROMAN SYMBOLS

$I(x,y)$	2-D image matrix	-
$\bar{I}$	Mean intensity	-
E	Edge pixels detected with the Sobel filter	-
	Multi-variate differential entropy	-
BM	Blur Measure	-
$R(x,y)$	Reflectance	-
$L(x,y)$	Luminance	-
$H(x,y)$	Gaussian function	-
$O(x,y)$	Image with compensated illumination	-

t, T	Translation vector	-
s, S, C	Scale	-
D	Maximum Depth of Random Forest	-
	Homogeneity	-
H	Hessian matrix	-
	HoG feature vector	-
$g(\hat{x}, \hat{y})$	Gaussian function	-
f_c	Spatial frequency	cycles/degree or cycles/pixel
T	Transformation matrix	-
	Ensemble of trees in Random Forest Model	-
$F(u, v)$	Fourier Transform of an image	-
$C(u, v)$	Cross-Power Spectrum	-
e^2	Mean-squared error	-
R	Rotation matrix	degrees
I	Identity matrix	-
w	PSF	-
n	Noise	-
J	Smoothness prior for the signal	-
G	Smoothness prior for the PSF	-
a	Zernike coefficient	μm
f	Splitting function	-
U	Training dataset	-
Q	Information gain	-
p	Probability function	-
$P(u)$	Pupil function	-
l	Focal length of the optical system	μm
$Z(u)$	Zernike polynomial	

GREEK SYMBOLS

σ	Standard deviation	-
σ^2	Image variance	-
$\psi(t)$	Mother wavelet	-
μ	Mean image brightness	-
π	Mathematical constant ratio	-
δ	Dirac delta function	-

λ	Eigenvalue	-
	Wavelength of imaging beam	nm
$\varphi(u)$	Wavefront phase	-

SUBSCRIPTS

$W_{\varphi}[j_0, k]$	Approximation wavelet coefficients	-
$W_{\Psi}[j, k]$	Detailed wavelet coefficients	-
d_{cone}	Photoreceptor cell diameter	µm
F_{eye}	Focal length of human eye	mm
c_{RMS}	Root Mean Square contrast	-
I_T	Test image	-
I_R	Reference image	-
σ_i	Local brightness variation	-
B_{ver}	Image obtained by convolution with vertical strong low-pass filter	-
B_{hor}	Image obtained by convolution with horizontal strong low-pass-filter	-
f_w, f_a	Mapping functions	-
P_n	Frequency dependent power spectral densities of the noise	-
P_x	Frequency dependent power spectral densities of the signal	-
Q_2	Median error	-
Q_1	Lower quartile	-
Q_3	Upper quartile	-

1. Introduction

1.1 Overview of the Problem Statement

In ophthalmology, there are some diseases which do not present any immediate visual problems to the patient when they initially appear, but without treatment can cause permanent and irreversible damage to the visual system. According to the World Health Organization [1], the estimated number of visually impaired people in the world is 285 million, 39 million blind and 246 million having low vision. Cataract (51%) remains the leading cause of blindness globally, followed by glaucoma (8%), corneal opacities (4%), trachoma (3%) and retinal disorders such as age-related macular degeneration (5%) and diabetic retinopathy (1%) [1]. More than 82% of all blind persons are 50 years of age or older. With the decline in mortality and fertility rates, both contributing to a rapid aging of population in most countries, by 2020 the number of individuals with blindness might reach 76 million [2]. The data from global epidemiological studies indicated that up to 75% of all cases of blindness can be avoided through regular testing and careful treatment plan [3]. For this reason, it is of vital importance to develop powerful imaging techniques and tools, capable of detecting the signs of retinal degeneration and thereby assisting the diagnosis of eye pathologies during the early stages of their development.

Optical imaging is a common tool in ophthalmology that permits non-invasive, in vivo visualisation of the retina. However, due to inherent imperfections of the human eye, incoming light travelling through the optical components of the eye suffers from deviations, creating spatial and dynamic variations termed aberrations [4]. These ocular aberrations limit the acquisition of high quality retinal images and inevitably lead to poor resolution of the microscopic mosaic structure of the retina. In order to achieve more accurate visual reconstruction of the retina, it is imperative to correct the aforementioned aberrations.

AO is a technology aimed at minimising aberrations in optical systems and providing diffraction-limited imaging [4]. Initially developed to remove the effect of atmospheric turbulence for astronomical telescopes, it has been applied to ophthalmology and progressively developed over the past 20 years. The breakthrough in this area took place in

1997 [5], when images of the photoreceptor mosaic with optical compensation of aberrations were acquired in vivo by using a fundus camera equipped with AO. Since that time much effort has been applied to optical hardware improvement and new technologies. These innovations improved spatial resolution to the level necessary to distinguish individual retinal cells and retinal microstructures to assist eye professionals in recovering information required for studying normal and pathological living retinas. The development of AO systems has opened up new possibilities for visualizing the mosaic of the photoreceptor cells, capillaries and nerve fibre bundles with greater resolution. The benefits from AO technology have had an impact in a large range of different applications for clinical research [6-11]. Nowadays a number of imaging devices have an embedded AO system to enhance the quality and resolution of retinal images, including conventional fundus imaging [12, 13] scanning laser ophthalmoscopy (AOSLO) [9], [14], and spectral domain optical coherence tomography (AO-SDOCT) [15, 16]. AOSLO and AO flood-illuminated system offer a high lateral resolution which allows capturing individual photoreceptor cells of size down to ~2 μm [12], [17]. The lateral resolution of AO-SDOCT is at least twice as less, however this system has a greater axial resolution (3-6 μm) compared with >60 μm for AOSLO and AO flood-illumination systems, that allows assessment of retinal lamination [18]. High-resolution retinal imaging with a combination of existing visual tests enables correlation of function and spatial integrity at cellular level, which is essential in early detection of eye degeneration and disease. Further improvement of the quality of AO retinal images as well as development of automated diagnostic tools will ease visual interpretation of the images and promote AO imaging as a regular tool in clinical practice. Therefore, development of highly accurate and reliable image processing techniques is required in order to maximize the value of the acquired retinal data and to make the AO retinal imaging technology accessible to the clinical ophthalmic community.

The first chapter presents an overview of the concepts required for understanding this thesis. Firstly, an introduction to the human visual system is given, which focuses on the origins of wave aberrations obstructing high-resolution imaging and visualisation of the retina. A brief history of the development of ophthalmological instruments is also included, concentrating mostly on the invention of AO technology and its further progress. In the subsequent part, the most prominent applications and directions for AO imaging are presented. The benefits gained in clinical research as a result of the advances in image processing are also discussed along with the motivation which drives the research in the field of retinal image processing.

The final part of this chapter presents the aim and objectives of this project as well as the main contributions of the implemented work.

1.2 The Optical System of the Human Eye

1.2.1 Anatomy of the Eye

The human eye is a unique optical instrument. It represents a compound optical system that brings the outside world into focus on the retina, and thereby enables us to see [4]. The main optical components involved in the imaging process are illustrated in Figure 1.1. When the incoming light enters the eye, it firstly travels through the cornea, which together with the crystalline lens represents the refracting system of the eye. The amount of light is controlled by the iris, a coloured group of circular and radial muscles [19], which act as the aperture stop [20]. In bright light conditions, the circular muscles contract, whilst the radial muscles relax, so that the pupil shrinks to restrict light entering the eye. On the contrary, in dim light conditions the circular muscles relax and the radial muscles contract, resulting in dilation of the pupil, which allows more light to pass into the eye [21].

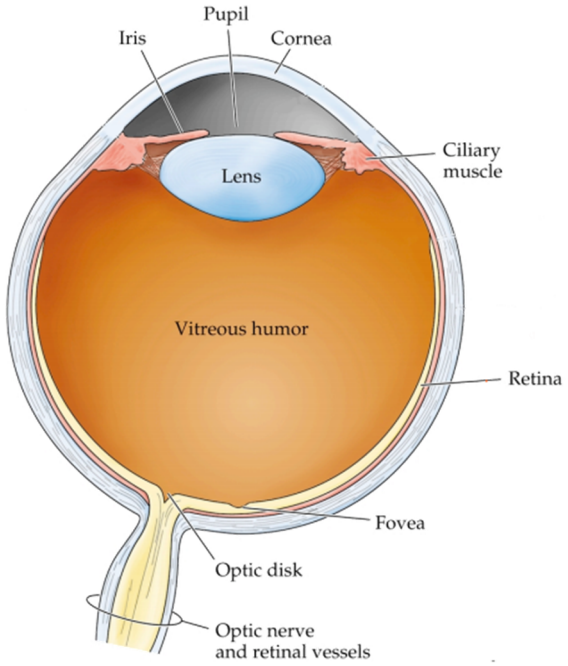


Figure 1.1: The optical system of the human eye [22].

The cornea has a greater index of refraction than surrounding air or covering tear film and is therefore responsible for the largest refractive change of incoming light rays. The crystalline lens has less optical power, but by contracting or relaxing the ciliary muscles surrounding the lens, it is able to change its shape and as a result its focal length [23]. This function of the lens is called accommodation. It allows the lens to adjust the refractive power of the eye, in order to project a focused image on the retina. The image produced on the retina is an inverted version of the real object. (For an aberration-free schematic drawing of the ideal image pathway within the eye, see Figure 1.2).

The retina is a light-sensitive layer at the back of the eye, an extension of the central nervous system connected to the brain via the optic nerve. When light focused by the lens reaches the retina, it is converted into neural signals which are then transferred to the brain via the optic nerve and perceived as images [24]. The processing of the incident light energy in the retina starts with the absorption of photons in the outer segments of photoreceptor cells.

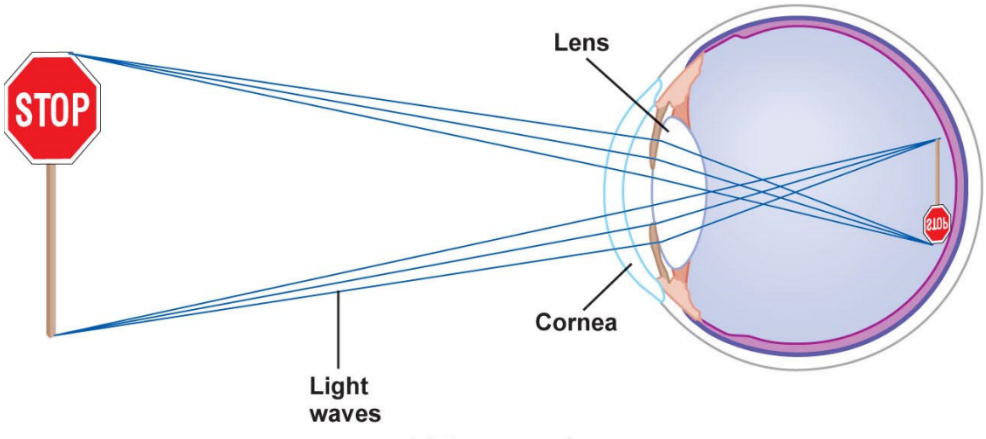


Figure 1.2: Image formation within the human eye [25].

The photoreceptors are essentially light-sensitive cells called rods and cones. Rods and cones can be distinguished by the shape of their outer segments, size, distribution across the retina, and functionality [26]. The distribution of photoreceptor cells is inhomogeneous across the retina. The concentration of cones is maximal at the fovea of the eye and decreases rapidly towards the peripheral areas (Figure 1.3 and Figure 1.5). The fovea and its centre, the foveola, are referred to as the centre point of image focus (0° eccentricity). The fovea is the small dimple in the inner retinal surface surrounded by the parafoveal belt and the perifoveal

outer region (Figure 1.3 and Figure 1.6). It is responsible for the sharpest vision due to the concentration of cones and no presence of scattering tissue above this specialised area (Figure 1.4). The fovea is devoid of rods and blood vessels. The population of rod receptors is concentrated in the periphery of the retina and it reaches its peak at about 20 degrees from the fovea. In total, there are approximately 5 million cones and about 120 million rods in the human retina [27].

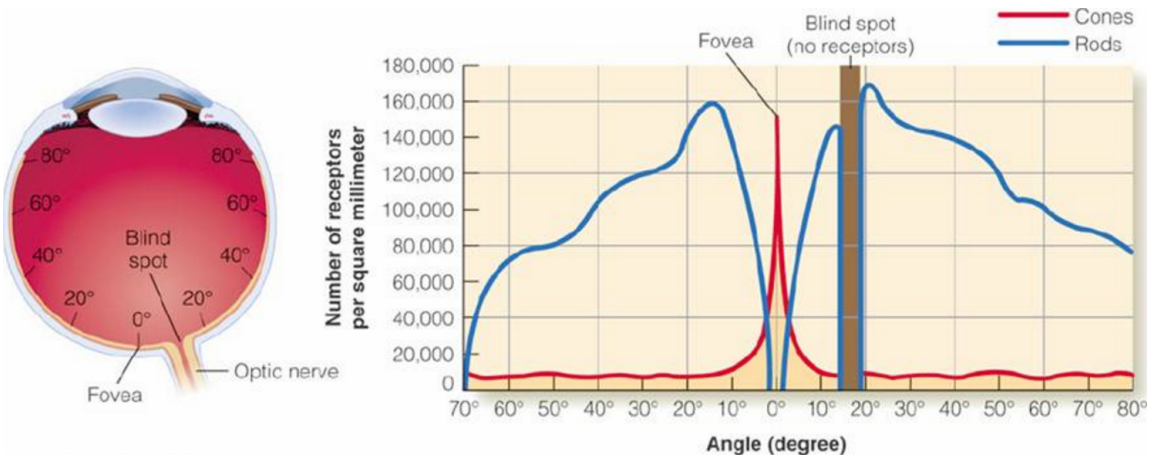


Figure 1.3: Angular distribution of rods and cones in the retina [28].

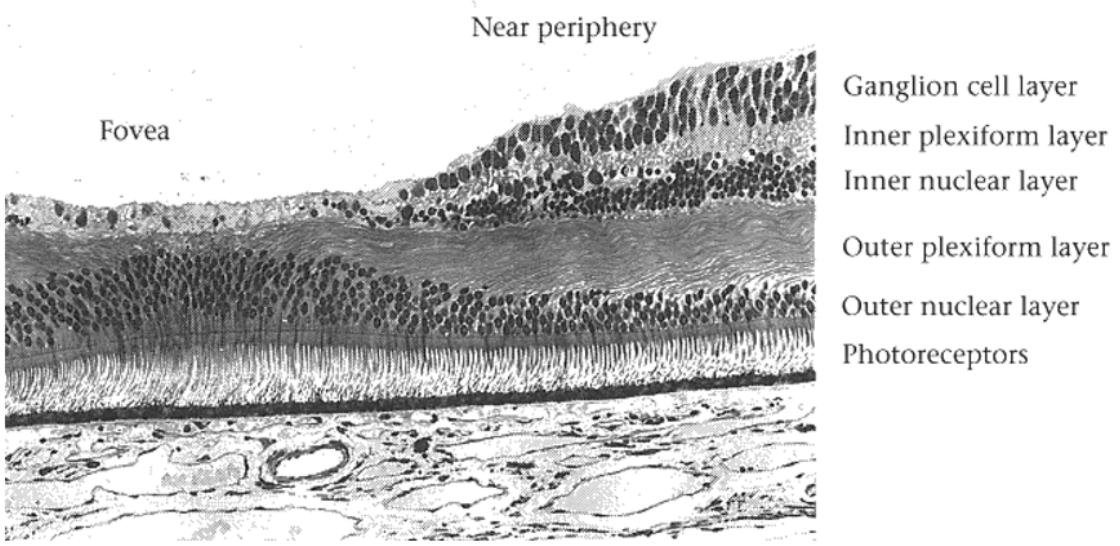


Figure 1.4: Light microscopic image depicting a retinal cross-section [29].

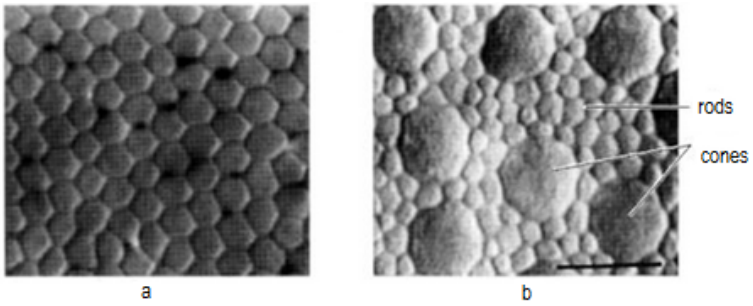


Figure 1.5: *En face* sections of human retina acquired with differential interference contrast microscopy showing (a) cones at the fovea and (b) cones near the periphery (scale bar = 10 µm) [30].

For descriptive purposes, the surface of the retina and its corresponding visual field are divided by vertical and horizontal lines into four quadrants (Figure 1.6). The vertical line divides the retina into nasal and temporal meridians and the horizontal line divides the retina into superior and inferior quadrants [26].

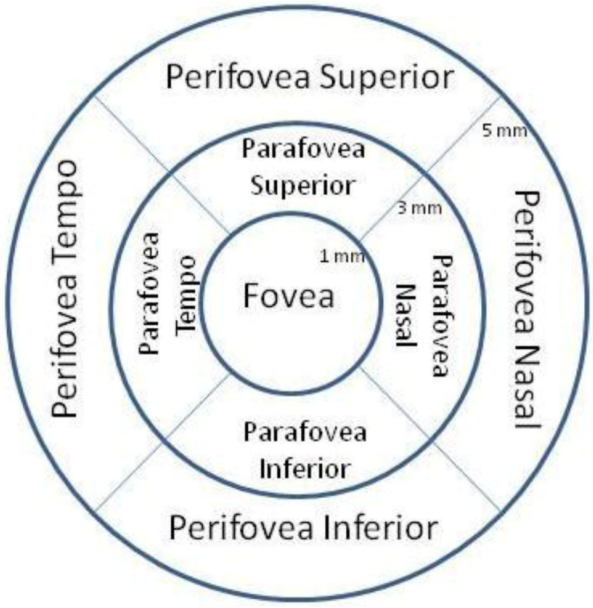


Figure 1.6: Schematic diagram of the retina for the right eye showing fovea, parafovea and perifovea in four retinal quadrants [31].

The rods are taller due to the longer outer segment, a structure filled with disks in which the light sensitive visual pigment (photopigment) is embedded (Figure 1.7). The photopigment of rods and cones is different. The rods' outer segment disks contain the photopigment rhodopsin. This absorbs a wide bandwidth of light which is then separated at light levels

lower than those required to breakdown cone photopigments. Hence, rods are highly sensitive to light and consequently, they are almost entirely responsible for night and peripheral vision [26].

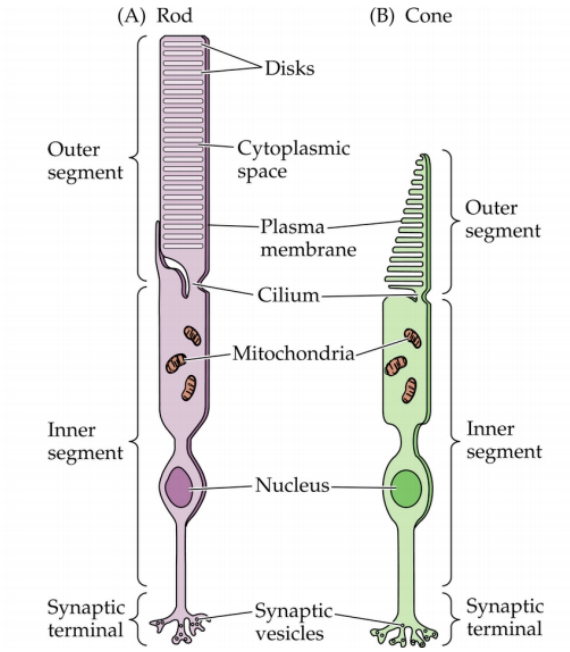


Figure 1.7: Structural differences between rods and cones [22].

Cones contain opsin as their photopigment, and based on the colour of light they absorb are separated in three types. One type of cones responds best to long wavelengths of light (L), another to medium wavelengths of light (M) and the last one to short wavelengths of light (S). The peak absorption of these cone cells is at 437, 533 and 564 nm, correspondingly [32]. Therefore, cones are responsible for colour vision and eye colour sensitivity. Also, cones have high spatial resolution and they are activated at the brighter light levels. On the other hand, rods respond best to white light, they do not mediate the colour, and have low spatial acuity.

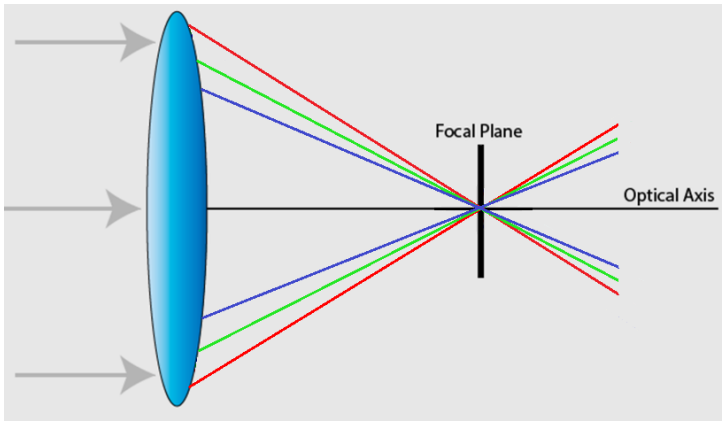
1.2.2 Optical Aberrations

In an ideal optical system, all rays of light from a point in the object plane converge to a single focal point in the image plane (Figure 1.8-a). However, such performance of an optical system is predicted only by paraxial approximation, simplified geometrical optics [33]. An aberration is a deviation of a ray from the behaviour predicted by the simplified rules of geometric optics. Aberrations can be caused by the lens shape, placement of optical elements

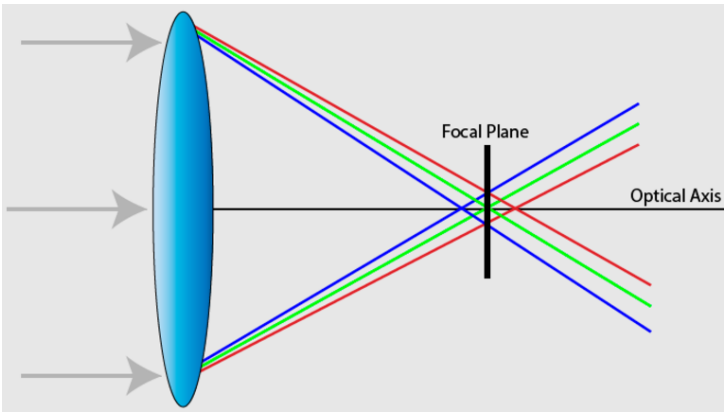
within a system, inhomogeneity of the optical media or due to the wave nature of light [34]. Optical systems are typically designed using paraxial optics which does not take aberrations into account; it treats light as a ray, and therefore omits the wave phenomena that cause aberrations. If not compensated for correctly, aberrations decrease the image quality of an optical system [35].

Aberrations are mainly divided into monochromatic (present with a single wavelength of light) and chromatic aberrations (present in multi-wavelength light). Chromatic aberrations result from dispersion of light, when different wavelengths of light pass through media at different speeds. Thus, a lens fails to focus all colours to the same convergence point [36]. Chromatic aberrations are further classified into two types: transverse and longitudinal. Longitudinal Chromatic Aberration (LCA) occurs when different wavelengths of colour do not converge at the same point after passing through a lens (Figure 1.8-b). Imaging with lenses that have LCA problems result in fringing around objects throughout the image [37]. Transverse Chromatic Aberration (TCA) occurs when a lens focus different wavelengths of light at different points along the focal plane (Figure 1.8-c). TCA are only visible towards the corners of the image in high-contrast areas [37]. Achromatic doublets and apochromatic lenses are usually employed in an optical setup in order to minimize the effects of chromatic aberrations [35].

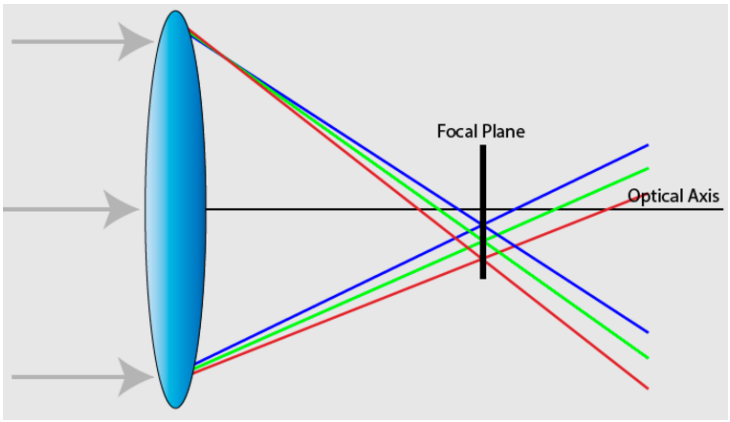
Monochromatic aberrations do not account for the effect that the frequency of light has on its propagation through a system. Therefore, they are not caused by dispersion but by the geometry/irregularity of the lens or mirror and occur both when light of narrow band is reflected and refracted. The optical systems are designed based on the paraxial approximation, which assumes that all rays entering the system are nearly parallel to each other and perpendicular to the lens. However, the actual path of a ray deviates from what the paraxial approximation predicts, giving a rise to monochromatic aberrations [38].



a



b

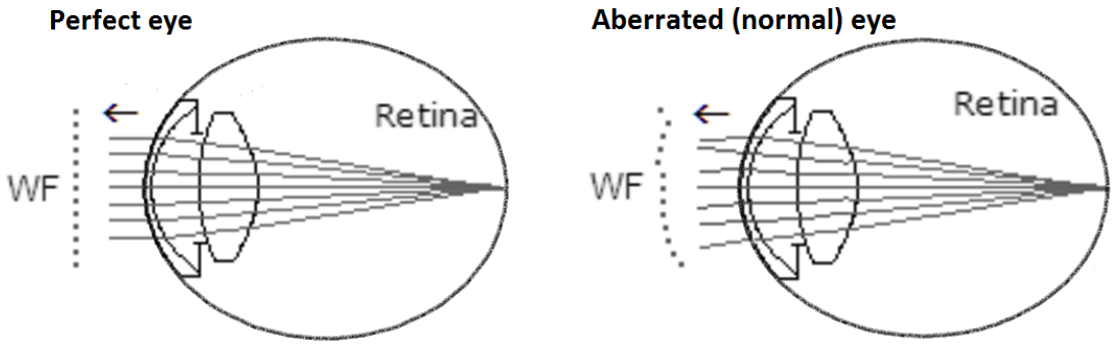


c

Figure 1.8: Schematic drawing showing (a) a perfect lens with no chromatic aberration, (b) longitudinal chromatic aberration and (c) transverse chromatic aberration [37].

Optic imperfections occur even in normal eyes. Wavefront aberrations define optical errors of the eye that prevent light from focusing perfectly on the retina, resulting in defects in the visual image (Figure 1.9) [39]. The cornea (the tear film–cornea interface, i.e. the surface between cornea and tear film, coating of the outer surface of the cornea) and the crystalline

lens, as the most powerful refractive components, are the main sources of aberrations in the human eye. The size of the pupil also influences the magnitude of wave aberrations in the eye. As the pupil enlarges, more peripheral rays enter the eye causing an increase in overall wave aberrations [27].



a b

Figure 1.9: Schematic drawing showing wavefront (WF) (a) in perfect and (b) aberrated (normal) eye [40].

In general, the magnitude of ocular aberrations is strongly dependent on individual factors such as age, state of accommodation, eye movements, tear film, and variations in the retinal shape, which can interact with the above factors [41].

Optic imperfections of the eye can be measured and expressed as wave aberration errors. Zernike polynomials can be used to quantify the aberrated wavefront of an optical system [42]. These polynomials represent a mathematical description of 3-dimensional (3D) wavefront deviation from the ideal planar wavefront located in the plane of the eye's pupil. Each polynomial characterises a specific form of surface deviation; while the sum of a set of weighted Zernike terms can produce a large number of more complex surface shapes, which can be fit to specific forms of wavefront aberrations. In principle, by including sufficient numbers of Zernike polynomials, any wavefront deformation can be described to a desired degree of accuracy [43]. Figure 1.10 presents the first 21 Zernike polynomials. Details on the mathematical description of aberrations using Zernike polynomials are given in Section 4.3.

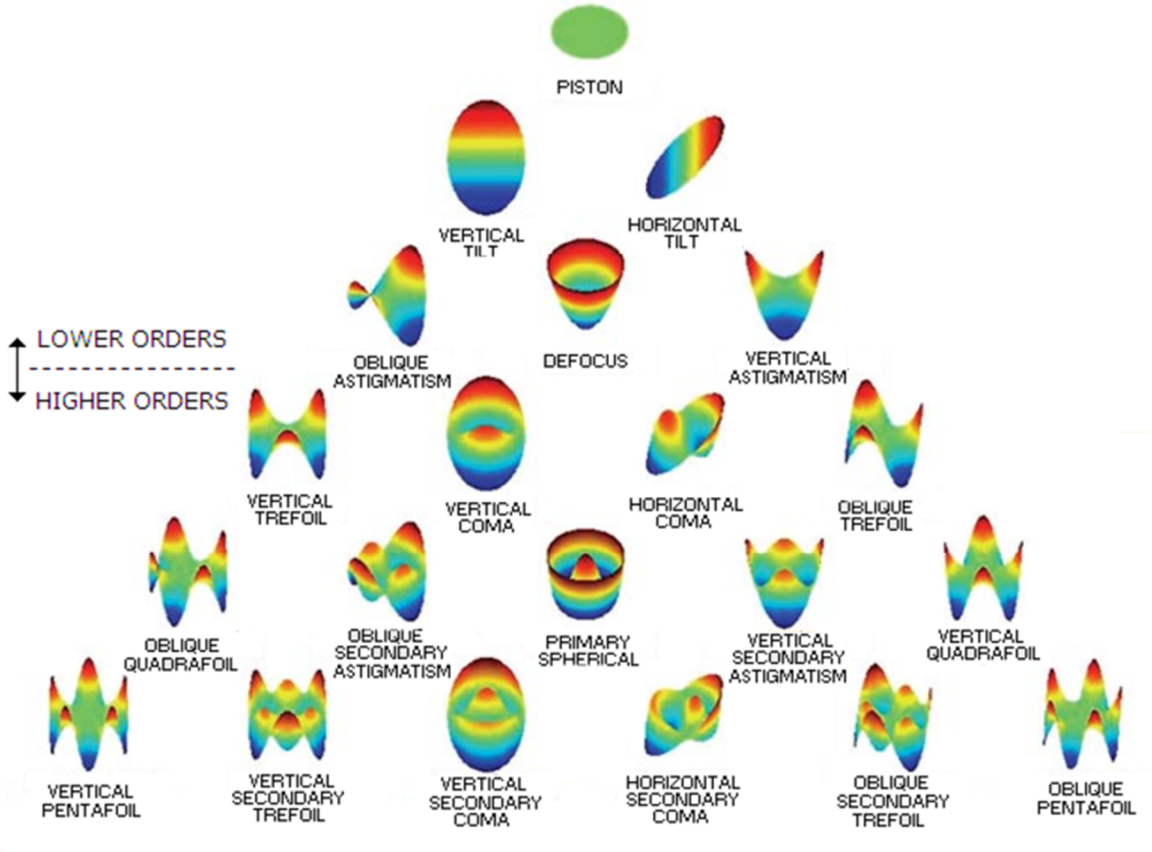


Figure 1.10: The first 21 Zernike polynomials [44].

Ocular aberrations can be classified into low-order (LOA) and high-order aberrations (HOA). LOA are defined as the first two orders of Zernike coefficients. Such LOA as defocus and astigmatism are the prevailing optical aberrations and they account for approximately 90% of the overall aberrations of the eye [45, 46]. Coma and spherical aberration of higher order are examples of terms describing the HOA commencing with third order Zernike coefficients. Even though HOA contribute just 10% of errors to the total variance of optical aberrations, their presence also results in the reduction of visual performance. LOA and HOA not only have an effect on vision, they in turn influence retinal imaging as well, as they distort the information present and reduce the maximum resolution obtainable by the imaging system [47].

In the last 20 years, advances in wavefront technology have allowed rapid and accurate measurements of wave aberrations of the eye with instruments termed aberrometers. On the other hand, an AO ophthalmic instrument is capable of measuring as well as correcting for

the imperfections of the eye, thus bringing the resolution of images down to the cellular level.

1.3 Adaptive Optics Imaging

1.3.1 History of AO Retinal Imaging

The development of adaptive optics originated from the astronomical and military communities. Astronomer Horace Babcock was the first to propose the idea of correction for the effects of atmospheric turbulence on images acquired with ground-based telescopes in 1953 [48]. By tracing individual rays of light through the optical system of a large telescope, he concluded that an adaptive optical element could remove the blur in stellar images from the time-varying aberrations produced by the turbulent atmosphere. However, Babcock was unable to realize his idea due to lack of advances in the technology of correction and measurement of wave aberrations [49]. The development of deformable mirrors for AO systems started in the early 1970s mainly driven by military contracts. The first practical system was introduced in 1973 at Itek, United States, and was described by Hardy et al. in 1974 [50]. In 1977, Hardy summarized in his review paper the advances made in the field of adaptive optics and analysed the performance of existing AO systems at that time [51]. Now adaptive optics is widely embedded in all advanced ground-based telescopes around the world.

Long before that, Smirnov was the first to start measuring the wave aberrations of the eye back in 1961 [49]. He used a subjective Vernier task to measure the retinal misalignment of rays entering through different parts of the pupil, providing a description of the third- and fourth-order aberrations [52]. These calculations were very time consuming and could not be applied in everyday practice, until advances in computing power made it possible to measure and compute the eye's wave aberrations in a few tens of milliseconds.

Advances in building wavefront measurement devices were accompanied by the development of ophthalmological equipment. In 1851, a breakthrough in the field of ophthalmology was made by Helmholtz, a German physician and physicist who invented the ophthalmoscope [53]. This design was further enhanced by Anagnostakis, who came up with the idea of making the instrument hand-held by adding a concave mirror [54]. In 1899,

Thorner further modified the ophthalmoscope which was later adapted as a camera objective. In 1910, Gullstrand developed the fundus camera, a device still used to image the retina today. After that, further improvements were made by Nordenson in 1925 [55]. The fundus camera model was commercialized by the Zeiss company in 1926 [56]. Since then it has been adopted by ophthalmologists in regular clinical practice. Advances in the initial design of the fundus camera comprised of blocking the redundant reflection from the corneal surface, increasing film sensitivity, and the electronic flash lamp, which allowed exposures brief enough to avoid eye movement blur [57].

The first in vivo images of human retina were acquired by Jackman and Webster in 1886. For this purpose, they used a system of an ophthalmoscopic mirror in conjunction with a two-inch microscope objective that was attached to the patient's head. Although filming required a 2.5 minutes exposure time, the resulting images were still very blurry [58]. The first useful photographic images of the retina, showing blood vessels, were obtained in 1891 by the German ophthalmologist Gerloff [59].

The invention of the scanning laser ophthalmoscope (SLO) by Robert Webb [60] advanced retinal imaging to the level of microscopic resolution. Having a higher degree of spatial sensitivity due to the use of such detectors, as the avalanche photodiode or the photomultiplier tube [61], this system was capable of imaging distinct layers of the living eye. This raster scanning instrument used confocal methods to reject extra light through a small pinhole, thus providing an optical sectioning capability. The application of optical coherence tomography (OCT) to the eye enabled even greater improvements in axial resolution, ranging as high as 1 to 3 μm in-vivo [57]. However, it was still not possible to resolve individual retinal cells due to optical aberrations in the eye.

The correction of optical aberrations of the eye was limited to only second order Zernike coefficients until the development of the Shack–Hartmann wavefront sensor. The Shack-Hartmann wavefront sensor is a technology evolved from the Hartmann Screen test invented by Johannes Hartmann (1865-1936), a German astrophysicist. To improve the quality of astronomical images, he constructed a screen with a series of holes in it, and placed the mask over the aperture of the 80 cm refracting telescope. A collimated beam shone through the mask effectively creates a discrete set of ray bundles that pass through the system. As a result, photographic plates exposed on either side of focus represent a "spot diagram" of the

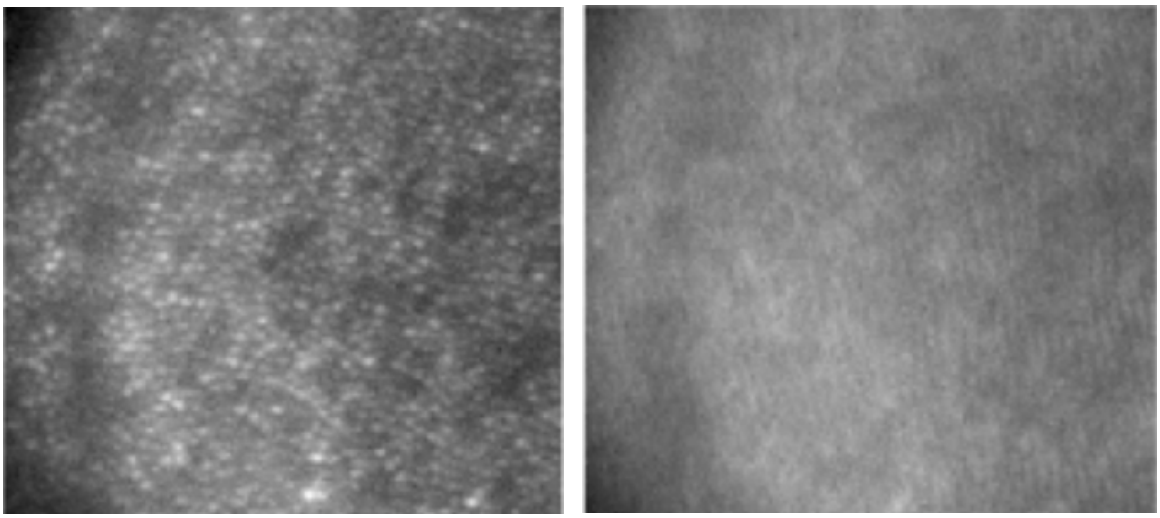
telescope. By shifting the location of the observation plane by fixed amounts and tracking the movements of the spots, the trajectory of each ray can be determined. In this way, Hartmann was able to refigure the lens of the refracting telescope and spectrographically identify calcium clouds with the system [62].

Further advances in adopting the Hartmann test to astronomical and military applications were made by Aden Meinel and Roland Shack. Meinel suggested measuring atmospheric aberrations while satellite images are captured using the Hartmann test. Roland Shack modified the technique by replacing the holes in the plate with lenses. In this way, it was possible to concentrate the light passing through the apertures to a focal spot. This resulted in a higher photon density and consequently allowed the spot pattern to be recorded. Given the sufficient diameter of the lenses, all the photons incident on the screen find their way to a focal spot. This design offered better photon efficiency than the Hartmann test. The next step in the implementation of the technique was to obtain a suitable array of lenses. In 1971, Roland Shack and Ben Platt modified the Hartmann sensor by replacing the array of hard apertures that Hartmann had used with an array of discrete micro-lenses [63].

In 1980s, Josef Bille and Roland Shack started using the lens array for measuring corneal topography [64]. This was the first noted application of the Shack-Hartmann technique in ophthalmology. Later, Bille and Liang showed that the Shack-Hartmann sensor can be adapted to measure aberrations of the eye [65]. These findings led to the development of closed-loop AO systems for the eye.

In 1989, Dreher et al. employed AO technology in ophthalmological imaging [66]. A deformable mirror was embedded in a scanning laser ophthalmoscope in order to correct the astigmatism in the subject's eye based on a prescription provided by conventional refraction. In 1993, at the University of Heidelberg, Liang developed a high resolution wavefront sensor which provided a more complete description of the eye's wave aberrations, measuring up to 10 radial Zernike orders [67]. The first AO closed-loop system built in 1997 [5] was not fully automated and required 15 min for each loop of wavefront calculation and correction. Since then, AO technology has advanced dramatically. The Shack–Hartmann wavefront sensor was automated, which led to its wide use in research and rapid commercialization. Nowadays, the AO system is integrated almost in all existing ophthalmic modalities, with

each offering different benefits [68]. Figure 1.11 shows a comparison of retinal images acquired with and without AO correction.



a b

Figure 1.11: Retinal images for one subject (a) with and (b) without AO correction, acquired at 1.25 degree eccentricity on the temporal retina [69].

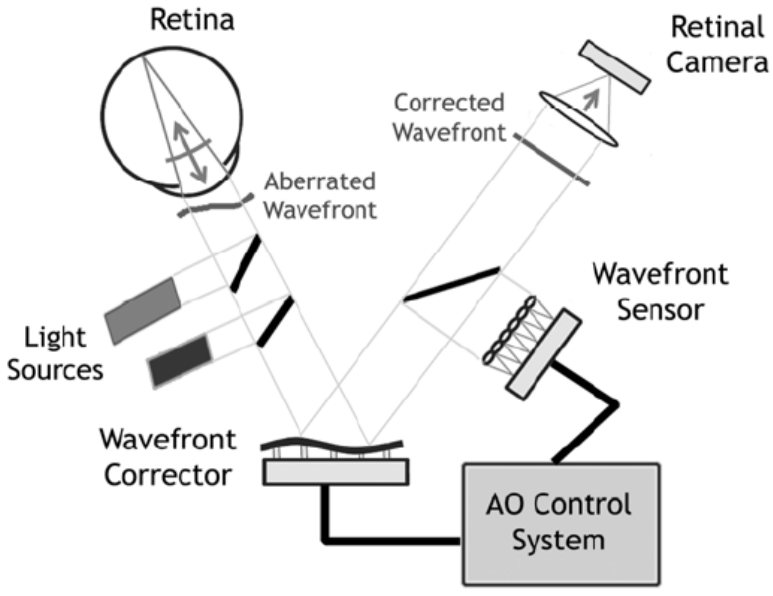


Figure 1.12: AO retinal imaging system [4].

The AO system consists of three key parts: the wavefront sensor, the wavefront corrector and the control computer. The wavefront sensor measures the eye's wave aberrations. The wavefront corrector − this can be a deformable mirror, a phase modulator, a spatial light

modulator, or liquid lenses − performs the correction of the eye's aberrations using actuators that deform/deflect its reflective surface. The AO controller, programmed with a computer, controls the interaction between the wavefront sensor and the wavefront corrector. The wavefront corrector interprets the measurements from the wavefront sensor and computes the appropriate commands that are sent to the wavefront corrector. In this way, the system operates in a feedback loop manner. This closed-loop mechanism is presented in Figure 1.12. At each iteration, the wavefront sensor measures the eye's aberrations and calculates the error between the current data and the target wavefront, which is transferred back to the controller. Based on this residual, the controller produces the signal for the wavefront corrector to further reduce aberrations in the next iteration, theoretically correcting retinal images up to the diffraction limit [4]. There are two sources of infrared non-coherent flood illumination in AO system. One is used for measuring and correcting the wavefront aberration of the eye, while the second source is used for retinal imaging. The AO-corrected retinal image is captured by a high-resolution imaging camera.

There are various wavefront sensing techniques available to measure the ocular aberrations of the human eye. The most common among them are the spatially resolved refractometer, the laser ray tracing technique, and the Shack–Hartmann wavefront sensor. The working principle of all wavefront sensors in the field of vision science and ophthalmology is the same, i.e. indirect measurement of local wavefront slopes and the reconstruction of the original wavefront by integrating these slopes [57].

The Shack–Hartmann wavefront sensor contains a lenslet array that consists of a two-dimensional (2D) array of a few hundred lenslets, all with the same diameter and focal length. The light directed from a laser beam is projected on the retinal field; when the light gets reflected from the retinal surface, it is deviated due to aberrations of the eye. In order to detect these deviations and calculate the wavefront, the reflected light is spatially sampled into many individual beams by the lenslet array forming multiple spots in the focal plane of the lenslets. A CCD camera placed in the focal plane of the lenslet array records the spot array pattern for the wavefront calculation. For a perfect eye (i.e., an aberration free or diffraction-limited eye), light reflected from the retina emerges from the pupil as a collimated beam, and produces a regularly spaced grid of spots in the focal plane of the lenslet array (Figure 1.13, Figure 1.14-a). On the contrary, for an aberrated eye, the light rays are deviating while passing through the eye's optics and therefore are displaced from

the optical axis of each lenslet (Figure 1.13, Figure 1.14-b). The displacement of each spot is proportional to the wavefront slope at the location of that lenslet in the pupil and is used to reconstruct the wave aberration of the eye.

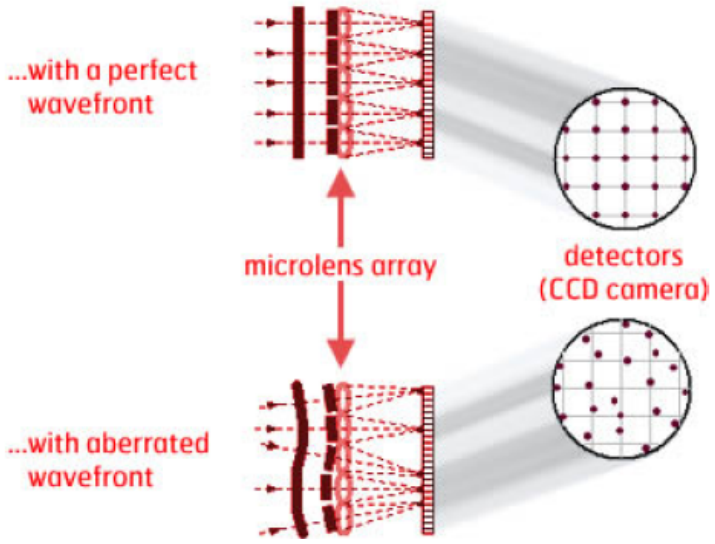


Figure 1.13: Principle of measuring ocular aberrations with a wavefront sensor [70].

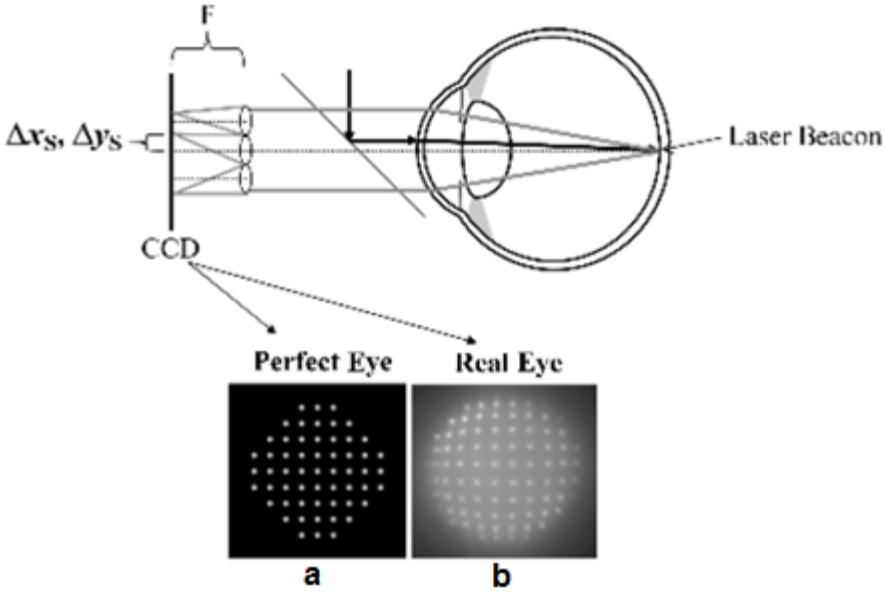


Figure 1.14: Schematic diagram of the measurement principle of a Shack–Hartmann wavefront sensor. F is the focal length of the lenslet. Two Shack–Hartmann images for (a) perfect and (b) real eyes are also shown [57].

1.3.2 The rtx1 Adaptive Optics Retinal Camera

Currently there are two types of AO imaging systems which provide *en face* images of retinal photoreceptor layer: the AOSLO [14] and flood-illuminated (flash) AO fundus camera [13]. In this thesis, a series of high-resolution retinal images have been acquired using a commercially available AO flood-illuminated instrument – rtx1, Imagine Eyes, Orsay, France (Figure 1.15). The core components of the system include a Shack-Hartmann wavefront sensor (HASO 32-eye, Imagine Optics, Orsay, France), a deformable mirror (MIRAO 53, Imagine Optics), and a low-noise high-resolution CCD camera (Roper Scientific, Tucson, AZ). The resolution of the CCD camera for a retinal image of 4˚x4˚ is 750x750 pixels, which corresponds to an area approximately 1.2 mm x 1.2 mm in the retina for an emmetropic eye. This yields a pixel to retina ratio for a raw single image frame of 1:1.6 μm. For measurement and correction of wavefront aberrations, a 750 nm super luminescent emitting diode (SLED) (A-IL) is used. An array of ten 950 nm light emitting diodes (LEDs) is employed to uniformly illuminate the iris. To provide an illumination field on the retina, the system is equipped with a 850 nm LED (R-IL). A LED miniature monitor is used as a fixation target in order to minimize eye movements during measurements. The rtx1 imaging system requires 9 ms of exposure time. The total acquisition time for the 40 frames is approximately 4 seconds with 105 ms time-intervals between the frames [71].



Figure 1.15: Commercially available AO flood-illuminated instrument: rtx1, Imagine Eyes, Orsay, France [12].

1.4 Applications of AO Retinal Imaging

For the last decades, the capabilities of AO systems have been continuously exploited, opening up new areas of clinical research and revealing new insights into retinal structures, function, and the origins of various retinal pathologies. In this section, we review the most prominent clinical findings, the leading applications of AO imaging which assisted this effort as well as possible future prospects.

Much of research and analysis of cellular-level retinal structures promoted by AO is captured in various papers [72-81]. As cones are easier to image due to their larger size and reflectivity, the major part of the research, especially in the early years, was devoted to the study of the cone mosaic (Figure 1.16), examination of cone features and its topological structure [5], [82]. Cone spacing, directionality and its reflectance were investigated in different regions of the retina [83-85]. This allowed researchers to establish the correlation between photoreceptor arrangement and retinal eccentricity; the findings showed a decrease in packing density of photoreceptor cells from the region of the fovea, towards the periphery [86]. Validation of the estimated density distribution of cone photoreceptors and associated spacing against histology measurements demonstrated good agreement [75], [87]. In some cases, additional statistical functions were derived in order to correlate the density and spatial distribution of the cone photoreceptors with the visual performance of the eye [73, 74]. Cone spacing and Nyquist limit were calculated across the retina in an attempt to understand the physical aspects of visual resolution of the human eye [65], [84], [86], [88]. A number of studies showed that the Nyquist sampling limit of the cone mosaic declines with the increase of eccentricity [65], [88, 89].

Further research in AO imaging focused on the optical properties of the cone mosaic [16], [47], [90-96]. By measuring the directional tuning of individual cones it was found that these cells are not randomly aligned, but tightly clustered pointing toward the pupil centre [97]. Moreover, it was demonstrated that the reflectance of individual cones is a dynamic property of the mosaic and independent from cone to cone. Factors which influence the intensity variation of the cone mosaic were studied in [97-100].

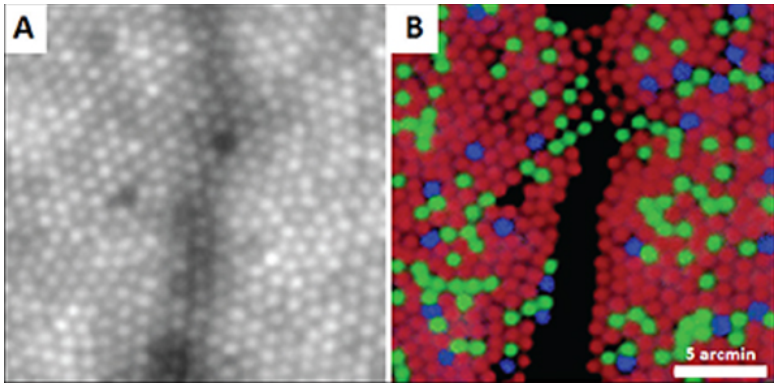


Figure 1.16: (A) Cone photoreceptor mosaic imaged with an AO fundus camera at 1 degree eccentricity on the temporal retina and (B) pseudocolor image of the same location with blue, green, and red representing the S, M, and L cones, respectively [73].

Apart from cone cells, other retinal microstructures were also imaged with the help of AO, including retinal pigment epithelium (RPE) cells [10], leukocyte blood cells [101], the smallest retinal blood vessels [11] and retinal ganglion cells (RGCs) [102, 103]. However, imaging of RGCs still remains a challenge due to the near transparent nature of these cells [104].

The aforementioned research studies provided a valuable collection of data on normal populations. This data represents a basis for characterizing the density, spacing distribution and brightness of healthy photoreceptor cells in vivo. The study of the retinas in healthy subjects assists medical professionals because normative data is the backbone for analysis and correlation with diseased eyes. The estimated normal ranges can be used for comparison with the data related to pathological photoreceptors, and can be employed for understanding the effect of age and retinal pathology on cone packing density and other microstructures. In this way, it is possible to characterise the microscopic structure of the diseased retina in vivo and as a result monitor and examine the progression of the eye disease and the efficacy of the proposed therapies over time in individual subjects.

The most common diseases that have been proved to cause vision loss are considered to be diabetic retinopathy (DR), age-related macular degeneration (AMD), cone-rod dystrophy and glaucoma [1]. DR is a chronic disease of the retinal microvasculature, which develops as a complication of diabetes [105]. In this case, AO retinal imaging has been used to detect pathological changes occurring in the early stages of DR. Several studies in DR patients

reported significant structural abnormalities across the retinal tissue, including the fovea [106-108]. Theoretically, the reconstruction of the entire retinal capillary network – including appearing abnormalities – can be accomplished by non-invasive imaging modalities, the key one being AO integrated into SDOCT. This could represent a valuable advantage of AO retinal imaging in comparison with current non-invasive imaging modalities [4].

Apart from vascular abnormalities, degenerative changes can also occur beyond the retina in DR. These changes are considered to be neurodegenerative and are linked to the functional loss in vision that patients undergo in the early stage of diabetes. Although it has not been yet proven, neuronal dysfunction is believed to be an early sign of DR [105], [109-111]. The application of AO in this field provides valuable information regarding the cellular changes as a function of mosaic geometry and reflectance in these retinal pathologies. Results on this subject were published by Parravano et al. [112]. In this study the authors demonstrated differences in intensity variation of healthy eyes and patients with DR. In particular, they found that the parafoveal cone photoreceptors appeared to have a higher variation in intensity, especially in the areas of intraretinal focal oedema. Similar findings are also reported in the work of Duncan et al. [113].

AO imaging is also used for prognosis of AMD. This disease manifests as a deterioration of retinal structure in the macula – a small area near the centre of the retina, the part of the eye which is responsible for sharp, central vision [4]. One of the first clinical signs in the progression of AMD is the appearance of soft drusen (Figure 1.17). Drusen are extracellular deposits that accumulate between the RPE and Bruch's membrane [114-116]. Their formation is thought to disrupt the overlying photoreceptors, leading to subsequent loss of vision.

Recently, AO imaging provided researchers with the capability to capture retinal nerve fibre layer (RNFL) and detailed images of the optic nerve head (ONH) [8, 9], [117]. Clinical evaluation of the structural changes at the ONH/RNFL level is valuable for the early diagnosis of glaucoma [118, 119]. The World Health Organization reports glaucoma as the second leading cause of blindness globally [120]. Glaucoma is a chronic disease causing progressive regional or diffuse thinning of the RNFL [121]. Axonal tissue loss in the RNFL

has been reported to be one of the earliest detectable glaucomatous changes, preceding morphologic changes of the optic nerve head.

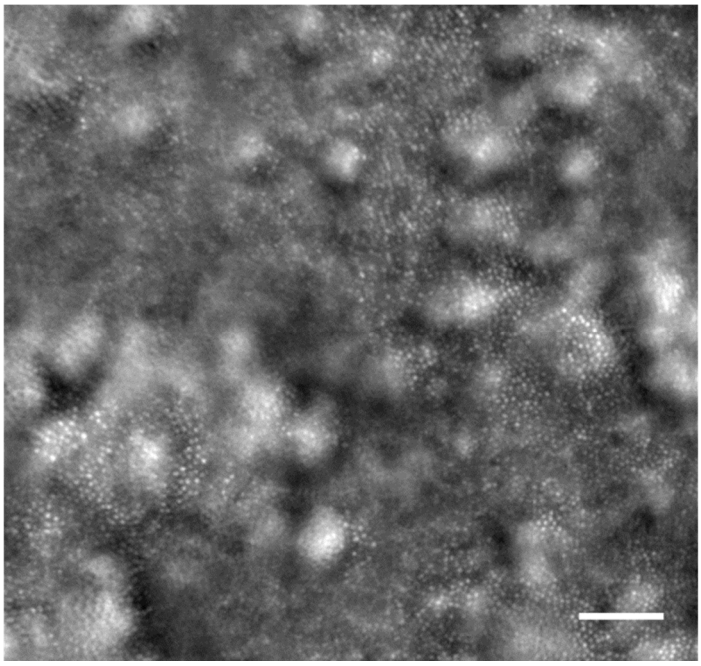


Figure 1.17: Example of photoreceptor layer with drusen. The scale bar is 104 μm.

AO imaging techniques are also applied for the examination of congenital diseases, such as dichromacy [77], [122], oligocone trichromacy [123], Stargardt disease [124] and Cone–Rod Dystrophy [125]. In most of those studies, retinal disorders were interpreted via quantitative correlations, based on the measurements of photoreceptor loss. For example, in the work of Carroll et al. [77] areas with defected cones have been linked with colour blindness. Despite a significant loss of foveal cones, the patient's visual acuity appeared to be normal. Similar findings were observed in the work of Talcott et al. [126], where patients with inherited retinitis pigmentosa had no changes in visual acuity or visual field, however significant differences in cone density and spacing were detected between control groups. The results in these studies showed that AO imaging has the capacity to detect retinal degeneration well before conventional clinical tests.

Likewise, AO imaging can be used to discriminate eye disorders which primarily affect rods, for example retinitis pigmentosa [127] and age-related macular degeneration [128]. Rod photoreceptors are characterised by their small diameter and broad angular tuning (the angle of the photoreceptor cell apertures with respect to the pupil), which restricts the amount of light necessary for imaging to be transferred back through the pupil [49]. For this reasons, it

is more difficult to image rod photoreceptor cells, even though similar studies concerned with in vivo imaging of the foveal cones, which are similar in size, have proved that this is possible [129]. However, a few studies have successfully managed to capture single rods in the living human eye and furthermore correlated the performed image analysis with existing histological data [72], [130]. As a separate problem, there is still a great degree of uncertainty regarding the distinction of cones and rods which occurs due to their difference in depth of focus [131]. Thus, the engagement of more sophisticated image processing procedures is required to get both, rods and cones, in focus.

To summarize, various studies have shown that AO can be successfully used in imaging the living human retina of healthy subjects as well as patients with progressive eye disorders. The quantitative analysis of high-resolution retinal images helps to understand the cellular basis of the phenotypic variability commonly observed in retinal disorders [123]. AO imaging combined with molecular genetic data can explain the aetiology of various retinal degenerations [68]. AO retinal imaging – if employed routinely in a clinical setting – could bring an important contribution to the process of treatment of eye diseases and the evaluation of prevention strategies. By observing the same retinal area over time with AO instruments, clinicians can now evaluate long-term effects that treatments have on individual photoreceptor cells [15], [83], [113]. Therefore, future applications of AO high-resolution imaging will include assisting clinicians in tracking retinal diseases and controlling the efficacy of specific therapy with great accuracy, helping to accelerate the search for new strategies to prevent serious visual loss.

1.5 Retinal Image Processing

Advances in image processing methods contribute to the progress of ophthalmic studies as well as any routine clinical medical application. Images obtained with AO instruments require post-processing before they can be of clinical use to aid prognosis or diagnosis. Post-processing procedures include enhancing the contrast [129], extracting the background of the image [71], image montaging [80], suppressing noise [72], registering a sequence of frames [129], [132], image deblurring [133], etc. Moreover, any quantitative image analysis requires automated models for an objective assessment. Some of the methods in high-resolution retinal imaging still imply manual interpretation of data, which may affect the

repeatability of the produced results. Other methods are based on the use of commercial graphics packages such as Adobe® Photoshop® (Adobe Systems, Mountain View, California) and ImageJ (National Institutes of Health, Bethesda, Maryland) [77], [125], [129], which are not specialized in processing high-resolution retinal images and therefore cannot provide high accuracy results.

AO retinal imaging technology integrated with automated post-processing techniques for high-resolution retinal images can provide an efficient diagnostic tool. Automated evaluation of retinal images using digital image analysis offers great potential benefits to both research and clinical environments. In a research setting, it allows to examine a large number of images time and cost-effectively, thereby offering more objective measurements than current observer driven techniques [134]. Advantages in a clinical context include the potential to perform larger number of automated tests enabling quantitative analysis of retinal tissue including identification of structural abnormalities. In particular, the wide field-of-view obtained by montaging images from different retinal locations assists clinicians to visually inspect a larger area of the patient's retina [80]. Accurate and reliable image processing techniques for automated tracking of photoreceptor cells and their counting provide means for quantitative assessment of retinal mosaic in healthy and pathological retinas [135]. Furthermore, detection of retinal features, extraction and quantitative measurements of retinal vascular topography allow analysis of morphological alterations in patients with diseases such as DR and glaucoma [134]. Combining these tools for processing high-resolution retinal images in a unified framework can significantly improve the accuracy of patient's diagnosis and efficiency of treatment process via monitoring the disease progression.

It is of utmost importance to develop highly efficient algorithms while providing the best image quality. Poor image quality can adversely affect the accuracy of automated detection algorithms as well as complicate visual interpretation of the images. As a result, evaluation of images with poor quality can lead to unreliable quantitative data, misdiagnosis, difficulty with treatment decisions, and inability to follow the disease progression due to limitations in reproducibility [136]. Improvements in contrast and resolution of retinal images allow for better observation of retinal microstructures and thus facilitate more accurate detection of desired retinal features. Methods for automated assessment of the image quality can provide a feedback to the operator during image acquisition and therefore improve the likelihood

that a good quality image will be employed in the interpretation of clinical studies. Development of retinal image processing techniques will eventually lead to regular use of automated diagnosis tools based on AO imaging, proving them to be a practical and efficient alternative to commonly used ophthalmic diagnostics.

A more detailed analysis of image processing techniques for AO high-resolution retinal images is presented in Chapter 2.

1.6 Research Aim and Objectives

The aim of this research project is to develop an automated computer vision system comprised of different image processing tools for enhancement of AO high-resolution retinal images and accurate detection of photoreceptor cells. The visibility of retinal features is improved by tackling specific components of the AO system, affecting the quality of acquired retinal data (Figure 2.1, Chapter 2). Enhancing the quality of retinal images maximizes the value of the retinal data and thus assists clinicians in the examination of the living retina and the diagnosis of different types of eye pathologies. Quantitative analysis of the final images obtained with the proposed image processing framework provides tools for characterization of the density and spacing distribution of photoreceptor cells in vivo. By collecting the associated retinal statistics, clinicians will be able to assess the effects of age and retinal pathologies on cone packing density. Moreover, by implementing the aforementioned image processing framework, a platform will be developed which can facilitate further post-processing and investigation of retinal microstructures (Chapter 6).

The main research objectives of the thesis are summarized below:

- To automatically measure the quality of high-resolution retinal images in order to ensure the appropriate selection and evaluation of image enhancement techniques in a way that correlates with human perception.
- To correct for uneven illumination in retinal images without corrupting the retinal features.
- To compensate for involuntary eye movements during image acquisition by implementing image registration.

- To suppress the noise present in the images, while preserving the integrity of retinal structures.
- To remove the residual optical aberrations by performing image deconvolution.
- To enhance the visibility of photoreceptor cells over other retinal microstructures, thus facilitating estimation of associated statistics.
- To implement detection and segmentation of photoreceptor cells for statistical correlation with histological data.

1.7 Contributions

A number of image processing frameworks have been designed for AO-corrected retinal images [71, 72], [80], [137, 138], however, still no significant progress has been made in order to compensate for the variety of possible degradation processes, interfering with the imaging system. In the current work, a novel image processing framework is implemented in an attempt to compensate for the identified degradation sources in AO system, at each step gradually improving the quality of AO retinal images and thereby recovering the true image. The main stages of the framework required the design and implementation of novel image processing techniques.

- In the illumination correction method, the selection of decomposition level is automated; this allows us to maintain the number of input variables in the system for each retinal image. To preserve the integrity of retinal features during illumination correction, we propose to apply a wavelet-Fourier filter to the restored images.
- The image registration stage is customized specifically for the compensation of eye saccadic movements in high-resolution retinal images. It allows for the detection of minor rotation and translation parameters. In order to take into account intra-frame variability, the transformed images are averaged using the so-called “lucky averaging” scheme.
- To address complex distortion of retinal images acquired with an AO instrument, a novel method for blind image deconvolution is proposed based on a multi-variate Random Forest regressor. A compact representation of the point spread function (PSF) significantly reduces the degree of uncertainty in image deconvolution as well as allows inference of a blur kernel without compromising its resolution. The feature

extraction technique is specially developed to allow for better generalization on a large set of retinal images, acquired at different retinal locations. To our knowledge, learning-based methods have not been previously used for AO retinal images.

- An automated algorithm based on the Hessian-Laplacian of Gaussian filter (LoG) is developed which allows for enhancement and detection of photoreceptor cells. In comparison with available state-of-the-art automated methods, the scale-based Hessian-LoG filter integrates both geometric and intensity image information in the process of cone detection. As a result, the proposed method provides highly accurate estimation of cone density.

Effectively, the implemented image processing framework will serve as a basis for further investigations of retinal tissue, thus contributing to the advance of image processing techniques in the field of ophthalmic clinical research.

1.8 Publications

The following is a list of peer-reviewed research papers published/prepared based on the work developed during this doctoral research.

JOURNAL PAPERS:

1. A. Lazareva, P. Liatsis, and F. G. Rauscher, "Hessian-LoG filtering for enhancement and detection of photoreceptor cells in adaptive optics retinal images," *J. Opt. Soc. Am. A*, vol. 33, no. 1, p. 84, Dec. 2015.

2. A. Lazareva, M. Francke, G. Slabaugh, L. L. Kernevez, W. Kiess, P. Liatsis, F. G. Rauscher, "Analysis of cone photoreceptor distribution in an emmetropic children and adolescent population," *Ophthalmology*, Manuscript in preparation.

CONFERENCE PROCEEDINGS:

1. A. Lazareva, P. Liatsis, and F. G. Rauscher, "An automated image processing system for the detection of photoreceptor cells in adaptive optics retinal images," in *2015 International Conference on Systems, Signals and Image Processing (IWSSIP)*, 2015, pp. 196–199.

2. A. Lazareva, M. Asad, G. Slabaugh, “Learning to Deblur Adaptive Optics Retinal Images,” in Karray F., Campilho A., Cheriet F. (eds) *Image Analysis and Recognition. ICIAR 2017*, Lecture Notes in Computer Science, vol. 10317, Springer, Cham.

1.9 Thesis Structure

This chapter provided a brief introduction into the field of AO retinal imaging and its current challenges. Chapter 2 presents a literature review on image processing techniques currently used for high-resolution retinal images, acquired with AO instruments. The survey covers different degradation sources which originate in the AO system and affect quality of high-resolution retinal images as well as image processing techniques employed to accurately compensate for the degradation effects. Chapter 3 gives a description of the chosen methodology for the image processing framework. A comparative analysis of different image pre-processing methods and evaluation of their efficiency on four representative retinal datasets is performed by assessing image quality. Following the stages of illumination compensation, noise suppression and image registration, the obtained final images are restored with the proposed image deconvolution method. Chapter 4 introduces a model for blind image deconvolution specifically designed for AO high-resolution retinal images. This model is validated on synthetically generated images as well as real AO high-resolution retinal images. The results are compared against the ground truth and state-of-the-art image deconvolution method.

Chapter 5 presents a fully automated method for enhancement and detection of photoreceptor cells. The performance of the proposed technique is evaluated on both synthetic and high-resolution retinal images, in terms of packing density. The results on the synthetic data are compared against the ground truth as well as cone counts obtained by the state-of-the-art algorithm. The packing density estimates calculated on the real retinal datasets are validated against manual counts collected by four independent observers and the results obtained by a commercial software and the state-of-the-art algorithm. In order to verify the resulting images with enhanced photoreceptor cells, the cone packing density distribution is also correlated with statistical histological data at the corresponding retinal locations.

Finally, chapter 6 summarizes the work presented in this thesis, discusses limitations of the framework, suggests refinements for optimisation of the implemented methods and proposes further steps for future research.

2. Literature Review: Retinal Image Processing

2.1 Introduction

Nowadays, digital image technologies for medical applications are developing at a fast pace due to the optimization of post-processing algorithms as well as the availability of powerful computers. The advancements made in ophthalmic imaging have offered new powerful tools enabling clinicians to investigate the structures and details of the eye previously unavailable to conventional clinical examination. The integration of AO in imaging systems compensates for wave aberrations, thus greatly improving retinal image resolution. The improvement in retinal image contrast and resolution allow better observation of retinal microstructures providing clinicians with the means to analyse their integrity and reveal pathological abnormalities. However, despite advances in optical system hardware, there has been modest development in software for post-processing and automatic analysis of retinal images. Advances in image processing methods are required to maximize the value of the acquired retinal data and to make the AO retinal imaging technology widely accessible to the clinical ophthalmic community. Accurate automated models are also mandatory, when the analysis requires post-processing of large quantities of data.

In this chapter, a literature review is undertaken with regards to the image processing techniques introduced so far for the acquired retina photography using AO imaging systems. In particular, image registration, image filtering, image restoration and automated methods for cone counting are discussed. For this purpose, different components of AO systems, which degrade the quality of retinal images are initially discussed and appropriate image processing algorithms for tackling the imposed distortions are suggested. The advantages, limitations and different aspects of existing AO imaging techniques are then discussed; moreover, refinements for the optimization of the imaging process are also suggested, which aim to compensate for the inherited resolution degradation effects, thus facilitating high fidelity results. In order to focus the scope of this overview, only image processing techniques applicable to high-resolution retinal images are presented. Details regarding

formulation of each image processing problem presented here are discussed in Chapters 3-5.

2.2 Image Acquisition in AO Systems

During acquisition, retinal images undergo a degradation process. This process can be separated into two types grouped by their origin: (a) distortions caused by eye movements or poor alignment of the eye with the system, i.e., due to human factors; and (b) degradation caused by the opto-electronic characteristics of the acquisition system such as illumination sources, lenses, the CCD array and the deformable mirror, i.e., caused by the optical system [139]. In order to minimize the effects of these degradation sources, a restoration process must be performed. To facilitate a better understanding of the origins of the specific degradation effects in terms of the components of an AO system, Figure 2.1 provides a functional block diagram of its main parts.

During the image acquisition, while the images are being captured, the human eye constantly performs saccadic movements [140] and as a result geometric transformations occur in the acquired image sequence. These motions include rapid jerks or saccades, slower drifts, and high frequency tremor, and are collectively referred to as “physiological nystagmus” or fixational eye movements. Fixational eye movements typically produce gaze instability of 10 or 15 arc minutes during sustained periods of attempted steady gaze [141]. These movements are too small to be registered with the naked eye, but they introduce significant distortion and artefacts to the image, especially when imaging at a high resolution. Therefore, we need to compensate for saccadic eye movements and calculate the performed geometric image transformations, in other words to register images, putting them into spatial alignment.

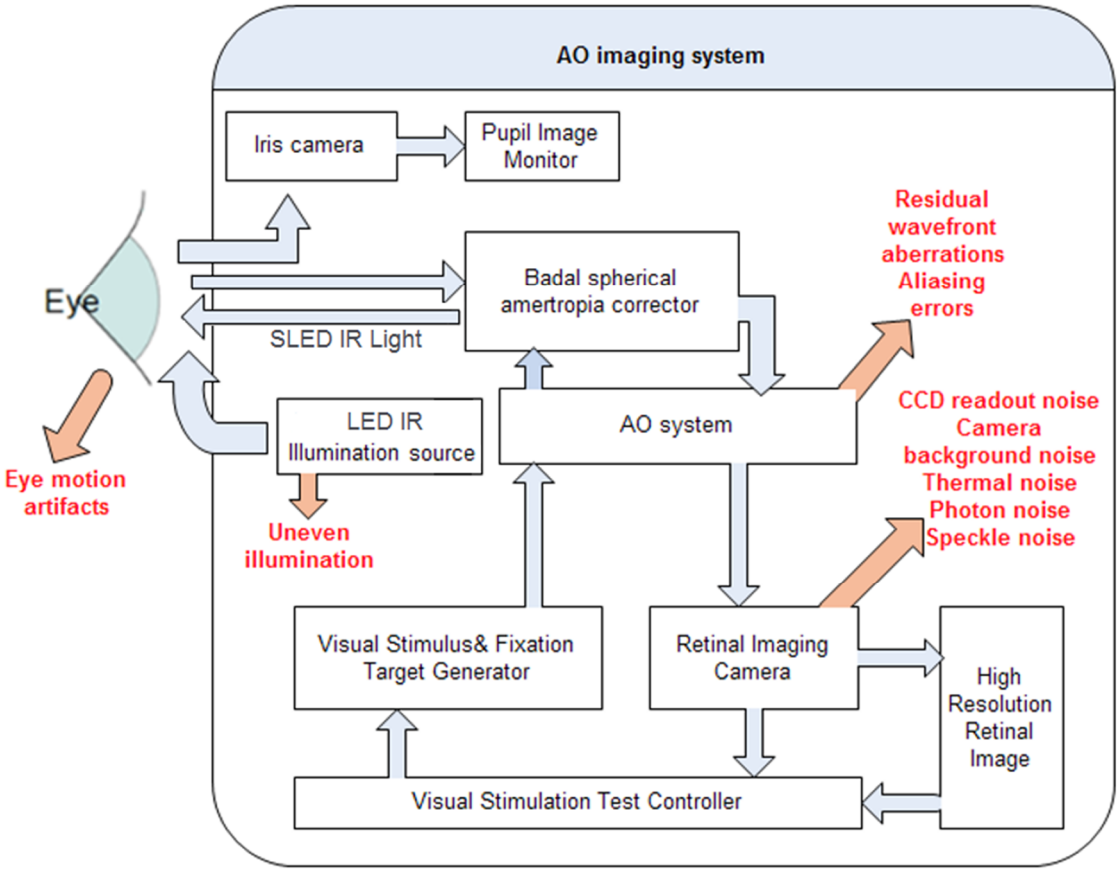


Figure 2.1: A scheme of AO embedded in an imaging system, showing origins of the specific degradation processes.

The AO imaging system is a complex system that suffers from various photoelectric noises, such as thermal noise, photon noise, dark current noise, CCD readout noise as well as camera background noise and so on [137]. Therefore, the resulting retinal images undergo a degradation process, which results in low signal-to-noise ratio (SNR) and low contrast. It is very important to choose suitable denoising methods according to the sources of noise, however, it is hard to decouple these in the AO system. Partially, noise can be tackled by image registration. By lining up multiple exposures of the same scene on top of each other and averaging pixel values, thermal and speckle noise can be significantly supressed and the signal-to-noise ratio increased [142]. For further improvements in image quality more sophisticated image enhancement and noise suppression algorithms are required.

Due to imperfections in the image formation process, high-resolution retinal images exhibit spurious intensity variations that do not exist in the original scene. This effect is commonly called shading or intensity inhomogeneity [143]. Identified experimental set-up limitations,

which possibly contribute to the aforementioned image corruption effects are non-uniform illumination, uneven spatial sensor sensitivity, camera imperfections, imperfections in the imaging optics, spatial inhomogeneity of the illuminating light source, light from nonuniformities in the human cornea or lens, natural vignetting, or artificial vignetting (due to misalignment of the subject's eye) [144]. Shading does not only alter the visual perception and analysis of the image, but more importantly, it may adversely affect automatic image processing procedures, such as segmentation, registration and feature extraction. For this reason, global intensity uniformity, i.e., the correction of shading over the entire image, is a necessary pre-processing step.

The AO system performs wavefront calculation and correction of high-order ocular aberrations, but due to limitations of the wavefront corrector, such as the finite degree of freedom of the deformable mirror, the latency of the AO loop, the measurement error in the wavefront sensor and so on, the estimated correction is not perfect [137]. Therefore, there are residual errors in the AO system, resulting in blurry images, characterised by low contrast. Additional improvements in the contrast and resolution of retinal images can be obtained, by introducing deconvolution algorithms in the image post-processing framework, that are intended to recover the true image.

2.3 Image Registration

2.3.1 Classification

Image registration is a fundamental task in image processing. The registration process represents a computational method for determining a mapping function, which establishes the correspondence between a pair of images of the same scene taken at different times, from different viewpoints, and/or by different sensors. Components of the image registration process include test and reference image datasets, transformation model, similarity criteria, and optimization method. In order to perform registration, firstly a corresponding registration model should be established. After a transformation function is found, it is applied to the test image, thus mapping it onto the reference image. Then, these images are combined depending on the final task objectives.

Image registration transformation models are classified into two main categories: rigid and deformable (or non-rigid). Rigid image registration models assume that the transformation that maps the test image to the reference image consists only of translations, rotations and scaling. While such models are sufficient for many applications, it is clear that many registration problems, particularly in medical imaging, are non-rigid [145]. Non-rigid transformations are appropriate for structures that tend to deform naturally [146]. Due to the alterations in the eye between acquisitions, there can be subtle non-rigid deformations present in the fundus images that become apparent when performing rigid registration [147]. In the case of high-resolution retinal images, these non-rigid transformations are so minor that they do not appear to introduce any visible distortions in the registration process. For this reason, in most of the studies performed, registration methods recover rigid transformations only [71], [80], [148]. In some of the cases, only translation parameters were calculated so that the possible rotation and scaling deformations are omitted [72], [108], [129].

The next component of image registration – similarity measure – is used to establish the spatial correspondence between the pair of images. It represents a comparison measure to establish the closeness of fit between the two images under the current transformation. Then, the parameters of the spatial transformation that optimize the chosen similarity metric have to be determined.

Based on the similarity metric, image registration methods can also be classified into intensity-based and feature-based [149, 150]. Intensity-based approaches generally optimize a similarity metric function based on intensity differences, cross-correlation, gradient correlation, and mutual information of the images [149]. Usually, the optimization procedure in this approach requires high computation cost in order to find the global maximum or minimum, especially in the case of higher order transformation models. Besides that, intensity-based methods require information from the entire image to perform the registration process. If image quality is quite low or the overlap region between the images is small, intensity-based methods may fail to align the images. In high-resolution retinal images, frames with little overlap region are caused by large eye movements during image acquisition. These frames are usually characterized by a low quality and therefore discarded from a dataset prior to image registration.

Feature-based methods include a prior segmentation step, where the image features are firstly extracted. Examples of such features include vascular bifurcation points, intersection points, the entire vasculature network, and other feature points extracted by point detectors [149], [151]. The objective function of this group of methods is based on the correspondences of the extracted landmark points or feature curves that have to be optimized to find the best transformation parameters. Compared to intensity-based methods, feature-based methods are faster and more robust. However, feature-based methods are highly dependent on accurate and repeatable extraction of features [152]. Blood vessel bifurcation points are usually used for the control-point matching stage on fundus images and angiograms [153, 154]. Manual selection of control points is a less preferable but relatively straightforward approach in feature-based registration. This method of registration is best suited for images that have distinct common features that would allow the mapping of pixels at the same location [146], [155]. However, it is difficult to automatically choose adequate control points for the registration of high-resolution retinal images. This is because blood vessels lie in a different layer on the retina, thus extraction of blood vessels and image registration with reference to blood vessels will blur the photoreceptors [35]. Moreover, depending on the retinal eccentricity, the vascular structure differs in size and concentration, typically decreasing towards the fovea, which forms an avascular zone. The appearance of photoreceptor cells in each frame may also vary due to light scattering and the angle of incident light. As a result, in high-resolution retinal images which are not rich in detail and features are difficult to be distinguished from one another, the feature-based approach may not perform effectively. This problem can be overcome by the intensity-based approach. Therefore, intensity-based similarity metric is more appropriate for registration of high-resolution retinal images. However, intensity-based methods are generally based on pixel intensities and demonstrate poor performance in the case of varying illumination across the images. Thus, as previously stated, shading correction should be included in the pre-processing stage of high-resolution retinal images.

2.3.2 Image Registration in High-Resolution Retinal Imaging

The most common similarity measure used for high-resolution retinal images is cross-correlation [156]. This type of registration involves calculation of the cross-correlation between a template from the reference image and various parts of the test image. Since it is

purely a measure of the closeness of fit between the pixel intensities in two frames, it is only useful when lighting conditions remain reasonably constant over the images, there is little white noise, and the sensors are of similar nature. In the most recent works, where imaging of cones and rods with scanning ophthalmic instruments was performed [75], [131], [157], a well-established approach for registration was used [158]. As the scanning process of the retina in the AOSLO is very fast (~25 μs), a single scanline represents a snapshot of the retina, unaffected by fixational eye motions, and therefore it can be aligned on a line-by-line basis. To find the rigid translation, normalized cross-correlation between each strip of scanlines and the reference image was calculated. The position of the peak of normalized cross-correlation matrix corresponds to the translation shifts of the strip with respect to the reference frame. Another approach to control saccadic eye movements is to introduce an eye tracking system so that fixational eye movements in the horizontal and vertical axes are recorded and compensated afterwards [141].

In high-resolution retinal images acquired with an adaptive optics ophthalmoscope, a correlation-based registration algorithm was also used [13], [72], [129, 130], [159-160]. This method is able to track the retinal position with accuracy better than a fifth of the size of the smallest foveal cone photoreceptor. The retinal images are separately cross-correlated in the horizontal and vertical directions, achieving subpixel registration. Therefore, small shifts and any torsional eye motion between images are removed and then registered images are summed together, thereby reducing the photon noise. Although the cross-correlation approach shows successful results, there are a few drawbacks such as the flatness of the similarity measure maxima and high computational complexity, which make the performance of cross-correlation methods more sensitive to noise, changes in image intensity and the size of the overlapping area [71].

Another correlation similarity metric that is used for high-resolution retinal images is phase correlation. Unlike the cross-correlation technique, it uses the frequency-domain representation of the images to estimate the transformation parameters. It allows for more robust and computationally efficient image registration due to the use of the Fast Fourier Transform (FFT). Both correlation techniques tend to fail when there are large changes in scale and rotation between the reference and test images. The Fourier-Mellin approach proposes a combination of the phase correlation technique with the log-polar transform (LPT) that apart from translation allows the scale and rotation parameters to be retrieved

[161]. This method is based upon the rotation and scaling properties of the Fourier Transform. It consists of mapping the spectral magnitudes of both test and reference images onto log-polar coordinates and utilising them as inputs in the phase correlation. The location of the peak corresponds to the rotation and the logarithm of the scaling parameters. However, when used to calculate rotation, phase correlation produces false peaks near 0 deg, which may be higher than the true peak. As a result, the magnitude of the peak at the correct position is reduced due to the fact that the sum of the peaks is equal to unity in normalized phase correlation function. Therefore, presence of false peaks diminish the ability to discover small angular differences in images because they might be hidden within the false peak [162]. In order to minimize these effects, it is typical to perform a filtering operation before the FFT is employed. However, while attenuating low frequencies reduces aliasing errors, it also results in smoothing the edges in an image. This can adversely affect the accuracy of image registration as it is often dependent on tight registration of sharp edges [163]. Therefore, the Fourier-Mellin approach is suitable for recovery of large rotation and scale parameters, and insufficient when dealing with the finer transformations that are present in high-resolution retinal images.

Despite the wide range of correlation techniques combined with image transformation algorithms to recover and compensate for the presence of affine transformations [164-167], there has been little progress reported on their application in high-resolution retinal images. In [168], Li et al. proposed the use of the Scale-Invariant Feature Transform in order to automatically detect stable point features from retinal images and then perform their tracking using the Kanade-Lucas-Tomasi algorithm. With the tracked features, the image distortion in each frame is removed by the second-order polynomial transformation, and frames are averaged to enhance the image quality.

In the work of Kulcsar et al. [148], a new method for registration of high-resolution retinal images acquired with an AO flood illumination system was proposed. The Harris-Stephens interest point detector [169] was used to detect the feature points in the retinal sequence. The corresponding matches were found by using cross-correlation in small windows around the detected points in the test and reference images. In order to prevent false matches, forward-backward matching was performed and a voting system based on the Hough transform was used to account for the successful matches. The parameters which received the maximum number of votes were considered as a rough estimate of translation. Next, an affine motion

model was used to minimize a least-squares criterion between the reference and input images in order to estimate translation, rotation and scale.

Ramaswamy and Devaney [71] described a method where the registration process was divided into coarse and fine stages. In coarse registration, an initial estimate of the translation parameters was calculated using cross-correlation. Then, a peak tracking algorithm was used to locate the brightest points of the image and use their position as control points. The translation parameter was refined by parabolic interpolation about the brightest pixels and the angle of rotation was measured using a Procrustes transformation [170].

Another problem that has to be taken into account in image registration is the number of frames that have to be combined in order to calculate the resulting image. In general, this decision depends on the specific medical application and acquisition conditions. For example, parameters that need to be considered include eye motions, the SNR of each particular image series, the choice of image registration algorithm, the errors during AO correction, etc. [131]. The optimal number of images to register should be established experimentally and presents a compromise between computational cost, accuracy of registration method and other involved pre-processing filtering techniques. If the number of images is insufficient, assuming perfect image registration and AO correction, the image quality is limited by the noise introduced by the optical system and the acquisition process. If the number of averaged images is adequate, then only diffraction or residual aberrations would limit the resulting image resolution. Finally, when the number of images is too high, the accumulation of imperfectly registered images would blur the average frame of the registered images, and thus the resolution would be limited by the registration algorithm itself [131].

Based on the reviewed works, it can be concluded that although image registration is a popular topic in retinal imaging, a limited number of methods are applicable for AO high-resolution retinal images. High-resolution retinal images are characterised by large homogenous nonvascular regions that weaken the capabilities of both feature-based and intensity-based techniques. On the contrary, applying standard correlation techniques for registration of the retinal images with large scale features such as the blood vessels will blur the photoreceptors, since they lie at a different depth of focus. Therefore, more precise registration algorithms are required to bootstrap the ability of recovering individual

photoreceptors cells. Moreover, non-uniform contrast/intensity distributions due to imperfect illumination conditions, noise in the AO system and residual aberrations during image acquisition deteriorate the performance of intensity-based techniques. Thus, appropriate image processing techniques should be included prior to registration of retinal images.

2.4 Image Filtering

Due to the imperfections of imaging systems, a recorded digital image undergoes a degradation process, which results in a loss of spatial resolution, blur, noise, and aliasing effects. The factors that influence the quality of the resulting images are manifold: optical distortions due to camera misfocus or diffraction limit, motion blur due to limited shutter speed, sensor noise, insufficient sensor density and others [171]. Image restoration techniques are aimed at recovering a degraded image to produce a high quality image.

2.4.1 Noise Suppression

Image noise produces a random variation in image brightness or colour information that is not present in the real object being imaged. In imaging systems, there is a variety of noise, which originates from photoelectric components of the system, such as CCD camera, imaging screen, controller circuits, etc. Various classifications are used for the noise depending on its statistical characteristics, origin and type of imaging. The most common types of noise affecting digital images are photoelectronic, impulse and structured noise [172]. Photoelectronic noise such as photon noise refers to the variation of the incident photon flux. Photoelectrons collected by a CCD exhibit a Poisson distribution and have a square root relationship between signal and noise. The noise is therefore directly dependent on the number of photons recorded in a real image. A very bright feature emitting many photons have relatively little noise. A very dim feature has a "granular" appearance, revealing that not many photons were averaged during its acquisition. Impulse noise such as salt and pepper noise is caused by sudden changes in image signal due to dust particles in the image acquisition. This type of noise manifests itself as black and white dots in an image [173]. Line drop impulse noise presents itself as faint horizontal or vertical lines. Structured noise is caused by interference between electronic components, and characterized by a

varying or fixed amplitude, frequency and phase. As a result, images are corrupted by blotchy gradients and periodic patterning [174].

Noise can occur when the image is captured, transmitted or processed and may be dependent or independent of the image signal. When noise magnitude depends on the signal noise, this degradation is called multiplicative noise. Image independent noise can often be described by an additive noise model, where the recorded image is the sum of the true image and the noise [175]. In many cases, additive noise is evenly distributed over the frequency domain, whilst image content is prevailing in low frequencies. Hence, noise is dominant in high frequencies and its effects can be reduced using low-pass filters. This can be done using either a frequency filter or a spatial domain filter [176]. In practice, the noise model is usually more complex, but it is often simplified to the additive noise model, multiplicative noise model or Gaussian noise, which appear to be good approximations to noise that occurs in many practical cases [137].

In order to increase contrast and remove high-spatial-frequency noise, a band-pass filter can be applied. A band pass filter attenuates very low and very high frequencies, but retains a mid-range band of frequencies. Thus, it enhances edges by suppressing low frequencies, while reducing noise by attenuating high frequencies at the same time. In high-resolution retinal images, frequency filtering is a common tool for enhancing the microstructures of the retina. For example, Doble et al. [72] used the power spectrum of the image to obtain the cone and rod spatial frequencies. Using a Gaussian high-pass filter, the image was decomposed into a low-angular frequency background and a high-angular frequency image containing the cones and rods. The visibility of photoreceptor cells was equalized by using a power-law enhancement of angular frequency power [177]. Additionally, the 2D Chebyshev filter was applied to pass the desired structures and suppress noise-dominated spatial frequencies. Finally, the power was normalized and the enhanced image was added back to the background.

In other research studies, high-pass or band-pass filters were used in a similar way to supress the influence of noise in the system and enhance the contrast of retinal images [5], [65], [88], [178]. In order to compensate for the edge of the imaging field as well as eliminate the high frequency noise above the diffraction limited cut-off frequency of the eye's optics, a Difference of Gaussians can be applied to retinal images. Further visual improvement can

be done by stretching the grayscale histogram [129]. A problem with fixed-pattern noise in the retinal image was tackled by Nassif et al. [179]. For each image, two background spectra were generated, one by averaging all spectra from that image and the second by subsequently low-pass filtering this averaged spectrum to represent a smooth source spectrum. Each spectrum was then divided by the averaged background spectrum and then multiplied by the smoothed spectrum.

Another approach to image denoising was implemented by Rao et al. [137]. Assuming that the noise model in AO imaging is a "combined" type of noise, hybrid filtering techniques were used. Firstly, considering that combined noise in real applications is more in line with the characteristics of multiplicative noise, the logarithm of the image was taken to transform the noise model into additive noise type. Then, bilateral filtering [180] was applied to suppress large scale noise from the image. To remove noise efficiently, the parameter of this filter – the average noise intensity – was calculated from the background area of the retinal image. As a second step of image denoising, edge smoothing by coherent diffusion was performed. In order to smooth the photoreceptor cell edges corrupted by noise, linear geometric anisotropic diffusion controlled by a purpose-built, two-dimensional structure tensor was implemented. As a final stage of the filtering framework, image contrast was enhanced by merging image edges and image brightness into a coherent diffused image. The resulting images following hybrid filtering were compared to the images processed by frequency domain filtering, and demonstrated higher contrast.

2.4.2 Illumination Compensation

As it was mentioned in Section 2.2, retinal images are commonly corrupted by spurious intensity variations which relate to shading or intensity inhomogeneity [71]. As a result, the inhomogeneous illumination across the retina can limit the useful information accessible within the acquired image. Illumination correction methods are intended to remove the global shading from the images. They can be categorized in two groups, prospective and retrospective [143]. The prospective method requires an additional background image obtained during image acquisition. This can be either an image of the scene background acquired with no light or an image acquired with light but without objects. In case of post-processing of high-resolution retinal images, additional background images are not available, therefore retrospective illumination correction methods are required. In

retrospective shading correction, an illumination model has to be estimated from the information present in the image. Methods based on spatial filtering have the advantage of simple and fast implementation and they are widely used for recovering high-resolution retinal images. Assuming that the illumination is an additive and/or multiplicative component in the image signal and considering that illumination is low frequency spatial variations, the low-pass image is used as a rough estimate of a plain background. The background image is usually obtained by a low-pass filter with a very large scale: median filter, mean filter or Gaussian filter. By convolving the image with a kernel of a large scale high frequencies components in an image are attenuated, which results in a loss of edge definition and averaging of intensity values. Then, the smoothed version of the image is either subtracted from the original or the original is divided by the smoothed image in order to compensate for illumination variations and emphasize high-frequency content.

Despite the simplicity of shading correction methods based on spatial filtering, these methods tend to perform poorly in situations where the shading function and retinal features have overlapping spatial frequency content [144] and therefore, this type of illumination correction might affect the features within the image. Ramaswamy and Devaney [71] used a wavelet-based approach for correcting the uneven illumination. The Discrete Wavelet Transform (DWT) was applied to decompose the image into 'approximation' and 'detailed' information at different levels [172]. Image illumination was estimated by the approximation coefficients at the last level of decomposition, where they contain only low frequency information. The approximation coefficients were set to a constant value in order to impose a uniform background, and then the image with compensated illumination was reconstructed.

2.5 Image Restoration

2.5.1 Deconvolution from Wavefront Sensing

Direct observation of the retina suffers from various optical aberrations of the eye. A wavefront sensor in an AO instrument performs calculation and compensation of high-order ocular aberrations thus providing a high level of resolution when imaging the retina. Despite this, due to hardware limitations of the wavefront corrector, this correction is not perfect. Therefore, the acquired retinal images are still corrupted by residual aberrations resulting in blur. Additional improvements in the contrast and resolution of retinal images can be

obtained *a posteriori*, by using an image restoration technique such as image deconvolution. In AO, the degradation function of the system can be estimated partially from wavefront sensing (WFS), assuming that the measurements of the deformable mirror are accurate [137]. Based on the information about the residual errors after AO correction, the system's PSF and Optical Transfer Function (OTF) can be reconstructed and employed in the deconvolution process [181, 182]. If information about the residual errors after AO correction is accessible, then the OTF can be computed based on the residual Zernike coefficients. The image restoration can be performed using the Wiener filter [183], an inverse filter that works in frequency domain trying to minimize the noise impact when the image is deconvolved. Additionally, to avoid noise amplification a correction filter can be clipped to maximum complex amplitude while retaining its phase. The resulting filter is applied in the spatial frequency domain and Fourier-transformed back to the angular image space [72]. These algorithms which employ data measured by the wavefront sensor have been proposed as an alternative technique to adaptive wavefront corrections [184, 185].

However, the WFS is not a reliable source of data due to multiple types of noise in the AO imaging system, mentioned in Sections 2.2 and 2.4. Also, in practice the frame rate and exposure time of the camera taking the corrected image frames are different from those of the WFS camera. As a result, the obtained WFS data does not always correspond to the acquired set of frames. Therefore, ordinary deconvolution from WFS is not a suitable method for post-processing of AO images [137].

2.5.2 Blind Deconvolution

When the PSF is not available, 'blind' deconvolution (BD), a more general technique, can be applied to the images. This type of image deconvolution permits recovery of the object and the PSF distributions simultaneously from a series of measurements. This is made by the use of physical constraints about the target and knowledge of the imaging system [133].

Blind deconvolution approaches can be classified into two categories according to the stage at which the blur is identified: *a priori* blur identification methods and joint estimation, where the original image and blur kernel are identified simultaneously. The Bayesian framework is usually employed in order to present and compare different BD approaches. The main differences between them are the choice of the function to be optimized and the prior distributions used to model the original image and the degradation process. A

fundamental principle of the Bayesian approach is to regard all parameters and observable variables as unknown stochastic quantities, assigning probability distributions. Thus in BD, the original image, the blur and the noise are all treated as samples of random fields, with corresponding prior probability density functions [186].

A few blind deconvolution methods have been reported in the literature for restoring AO high-resolution retinal images. In the work of Blanco et al. [138], a joint estimation of PSF and original image within the Bayesian framework is used. The global PSF is modelled as an unknown linear combination of the PSF for each plane. To estimate the coefficients of this combination and the object, a marginal estimation of unknown hyperparameters (PSF coefficients, object Power Spectral Density and noise level) followed by a *Maximum a posteriori* (MAP) estimation of the object was employed. Despite such a marginal estimation proving to have better statistical convergence properties, the restored images appear to be oversmoothed.

In [137] Rao et al. proposed a hybrid deconvolution for the partially-corrected AO images, in which the WFS data was employed and revised while the AO system performs the closed-loop correction on the given object. As the actual PSF is related to the PSF measured by WFS, it was used to reduce the uncertainty of blind deconvolution. The criterion function was composed of fidelity term and two regularization functions, imposing smoothness to the estimated blur kernel and original image. The choice of the regularization function is critical for the convergence of the image deconvolution method as well as the accuracy of the restoration process itself. During the process of joint estimation, the PSF is revised using the blurred image and estimation of undistorted image; consequently, the revised PSF allows for a better estimation of undistorted image.

In the same paper, a method of multi-frame blind deconvolution was proposed for enhancing stellar images partially corrected by AO. In this method, the multiple short-exposure degraded images captured during AO closed-loop were used for the joint estimation of the real object and PSF. This algorithm does not use any *a priori* knowledge, it only imposes a positivity constraint and band-limit constraint to the iterative process for the convergence of the algorithm. The multi-frame joint estimation transforms the problem of "knowing one - deriving two" to the problem of "knowing M - deriving M+1", thereby reducing the degree of uncertainty. The greater the number of frames used, the greater the stability and

convergence of the blind deconvolution algorithm, and more importantly the greater the possibility that the recovered image approaches to the real solution. In order to ensure a good selection of frames, the Shannon entropy was taken as the quality evaluation standard [187].

Li et al. [188] report a blind deconvolution technique based on the Incremental Wiener Filter [189] to recover the AOSLO images in real time. The PSF measured by a wavefront sensor is only used as an initial value for the blur kernel. Then, the initial estimate for the restored image is calculated using the Wiener filter. Both estimates are updated iteratively while minimizing the fidelity term. For convergence, positive constraints are imposed on both, image and PSF.

Close examination of AO high-resolution retinal images reveals that raw images are also dominated by an important background. As a result, the blur caused by light scattering has a non-uniform effect on the recorded image. This can be explained by the fact that the object under examination, i.e. the retina, is a 3D volume, and thus a recorded image is in fact a result of superimposed retinal layers, each one interacting differently with the optics of the instrument, absorbing and reflecting the light. Therefore, out-of-focus planes of the object also contribute to the image formation, bringing additional blur and distortions in a recorded image. A deconvolution step, taking into account the 3D nature of the object, is therefore necessary to restore the lateral resolution of the retina images. Chenegros et al. [190] proposed a myopic 3D deconvolution method in the Bayesian framework in order to account for realistic PSF in AO retinal images. As opposed to blind deconvolution, in myopic deconvolution the PSF is partially known by making assumptions on a PSF model or providing an initial estimate. Following the Bayesian MAP approach, the deconvolution problem consisted of finding the most likely object, given the observed image and *a priori* information on the object, which was summarized by a probability density function. The noise component was modelled as nonstationary white Gaussian. A quadratic edge-preserving prior for small gradients and linear for large ones was chosen to avoid oversmoothing. A joint estimation of the true object and the PSF was performed for an N-plane 3D object, 3D image, and the 3D PSF. As the 3D PSF is composed of $2N-1$ layers, the problem is more underdetermined than in two dimensions. To overcome this, the whole 3D PSF was parametrized by a common pupil phase plus a known defocus phase that depends on the considered PSF plane. This helped to dramatically reduce the number of unknowns.

Although the latter method accounts for the true nature of the recorded AO high-resolution retinal images, it requires a 3D volume of the retina. So far, the proposed method [190] has been only validated on a synthetic retinal volume, generated so as to comply with the overall structure of a retina.

2.5.3 Learning Methods

While deconvolution methods that rely on the WFS data are highly restricted by the detection accuracy of the wavefront detector, conventional blind deconvolution has the drawback of being prone to getting stuck in a local minimum [137]. An alternative to conventional image deconvolution can be learning techniques. In [191], Fanello et al. proposed a method based on 'filter forests' which allows for predicting continuous variables given a signal and its context. The proposed framework is effective in different application domains, including image deconvolution, where an optimal convolution kernel is found with the use of Random Forest regressor [191]. During the learning stage, the image is partitioned into image patches such that within each partition a simple linear convolution produces the lowest error in the optimisation function. The cost function is composed of a fidelity term and a special data-dependent regularization term. During the training, the model learns to adjust the weights of the data-dependent regularization term so as to preserve the edges in the image. Random Forests are fast and efficient learners, particularly suitable for high dimensional data problems [192]. They are easily distributable on parallel hardware architecture and thus offer computational cost savings.

In the last years, deep convolution neural networks have become a new trend in computer vision. Deep learning models are representation-learning methods with multiple levels of abstraction. They are composed of simple non-linear modules that transform the representation of data at one level into a representation at a higher, slightly more abstract level [193]. Given the composition of enough such transformations, very complex functions can be learned. As a result, these models have made major breakthroughs in solving problems such as classification, pattern and speech recognition. In [194] Schuler et al. introduced a method for blind image deconvolution which utilizes deep layered architecture. The proposed deblurring network consists of three modules, feature extraction, kernel estimation and image estimation, which can be stacked several times. The neural network is

trained end-to-end with back-propagation, while learning different parameters of each module.

Despite showing impressive results, the aforementioned learning-based methods require a very large number of training samples. Moreover, they rely on generalized models and therefore their accuracy is limited to specific types of blur. In addition, in most of the reported methods the achieved resolution of the recovered blur kernel is often found to be restricted by size.

2.6 Automated Cone Detection

The disruption of the photoreceptor mosaic and loss of photoreceptor cells are considered early signs of retinal degeneration, which can lead to serious visual dysfunctions [106], [111, 112], [116]. Quantitative analysis of high-resolution retinal images provides vital information on the pathophysiology of various retinal degenerative conditions. The packing density, spacing distribution, and brightness of photoreceptor cells *in vivo* have been investigated in several studies, in an attempt to establish a correlation with the visual performance of the eye [83, 84], [86]. To date, manual interpretation of data with the aid of commercial graphics packages has commonly been used in clinical studies [77], [125], [129]. However, manual counting relies on the expertise of observers, and therefore the accuracy of this method is subject to human error. Moreover, this procedure is obviously time and labour intensive since it requires human resources. On the other hand, automation of the photoreceptor counting procedures will allow for a larger number of tests to be performed simultaneously and thus will help to strengthen the basis for objective judgment on the diagnosis. Figure 2.2 shows an example of automated cone counting using the commercially available software from Imagine Eyes (CK v0.1 and AO detect v0.1, Imaging Eyes, France).

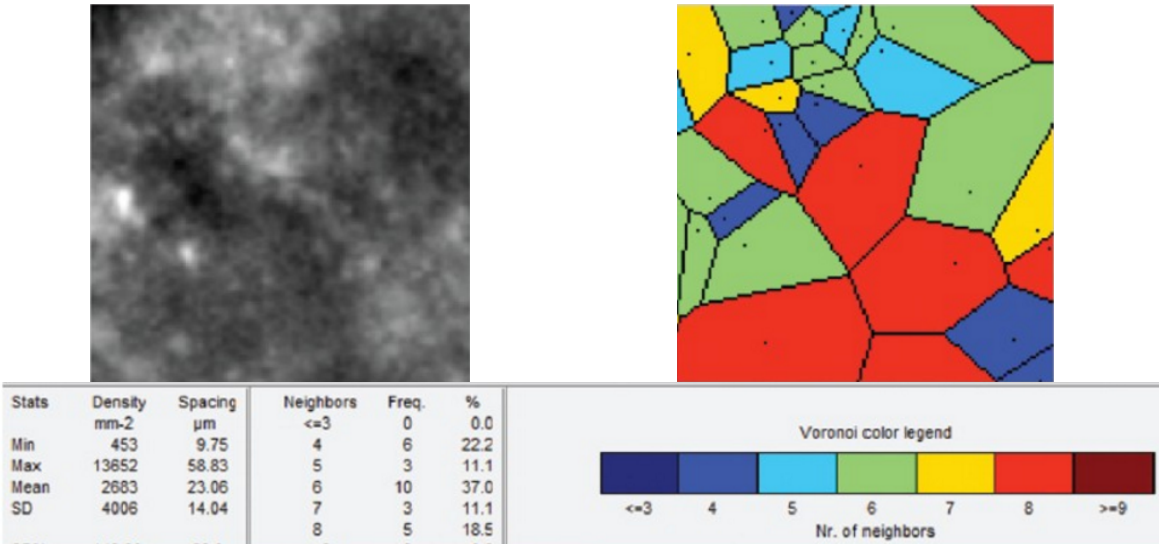


Figure 2.2 Illustration of cone packing density and Voronoi tessellation calculation using the software program provided by Imaging Eyes (CK v0.1 and AO detect v0.1, Imaging Eyes, France) in a patient with rod-cone dystrophy [195].

A number of algorithms have been reported in the literature for the automated identification of cones in AO-corrected images. Cones capture light based on the principles of optical waveguiding and support a single waveguide mode [79]. Therefore, they reflect a portion of the unabsorbed light back through the pupil, appearing as peaks with a higher intensity than other parts of the retinal image. Based on this optical property, Li and Roorda [79] and Xue et al. [80] identified the location of photoreceptor cells as the regional maxima of the image. In the Li and Roorda method [79] the local maxima are found using the *imregionalmax* built-in function of Matlab® (Mathworks Inc). If two or more maxima are closer than the minimum cone separation their centroid is taken as the final location. This is achieved with a dilation operator, which merges two closely located cones into a single one. This might introduce a systematic error in the identification of cone coordinates, especially in the images taken at areas closer to the fovea. Xue et al. [80] suggested to use a histogram analysis of the retinal images in order to find cone coordinates. The image histogram is divided into intensity ranges. For each intensity range, from the highest to the lowest, the algorithm searches for pixels with intensity values within the range. Once cone coordinates are established for a certain range, all the pixels within the square defined by the smallest center-to-center cone spacing are colour coded.

The aforementioned methods cannot be considered as fully automated as they require manual input for parameters, such as the intensity threshold and inter-cell spacing. This can adversely affect the inter-rater reliability of cone density calculations and thus objective judgment on the patient's diagnosis. Based on similar principles, Loquin et al. [196] developed an interactive tool based on watershed immersion algorithm which allows observers to adjust the parameters of the algorithm to achieve optimal cone detection. Although this is useful as it allows for the expert knowledge of physicians to be utilised, it is generally an impractical solution in regular clinical examination where a large number of images needs to be processed.

A recently proposed approach automatically calculates the photoreceptor cell density in retinal images by employing the frequency-based local content-adaptive filtering method [197]. A frequency domain of the retinal images is used to determine cell spacing. Based on the identified parameters, a circularly symmetric band-pass filter is designed for filtering the image. Once the AO retinal image is filtered cell coordinates are found as image maxima with constraints on cell separation based on the frequency domain analysis. Since the filter parameters are established automatically, this method is adaptable to different frequencies, which are indicative of various cell spacing in the image. However, the performance comparison of the results of this method with manual counts shows that there is a systematic error in the calculation of cone density [197].

2.7 Literature Review Synopsis; Motivation for Research in Retinal Image Enhancement

The above literature review showed that relatively little research has been done on image processing techniques in application to AO high-resolution images. In fact, little effort has been put in pursuing all sources of image degradation present in AO imaging system; therefore, there is potential to further develop and optimize image post-processing techniques, allowing for better distinction of photoreceptor cells.

Intensity-based registration techniques have been applied in order to compensate for eye motions during the acquisition of high-resolution retinal images. Retinal images are characterized by the presence of both, avascular regions and areas with large scale vessels;

therefore, appropriate image registration algorithm should perform well in both cases. The performance of intensity-based image registration can be weakened by the presence of large structures in the image. Blood vessels captured in high-resolution images do not have sharp edges as in fact they are the shadows cast by the blood vessels overlying the cone mosaic. This can cause inaccuracy in calculation of transformation parameters and as a result blur out photoreceptor cells on the resulting averaged image. Traditional approaches for recovery of rotation and scaling parameters, such as LPT and the Fourier-Mellin, cannot be used in high-resolution retinal images, as they fail to detect minor translation parameters. Therefore, a highly accurate image registration technique is necessary for recovering minor transformation parameters in high-resolution retinal images.

Given that intensity-based registration techniques are sensitive to noise and illumination variations, the calculation of transformation parameters requires additional image processing techniques prior to image registration, e.g., noise suppression, image enhancement and illumination correction.

In the literature, due to its simplicity, spatial filtering is the most common approach for shading correction. This type of illumination correction has a major disadvantage due to poor performance in cases when illumination and retinal features have overlapping spatial frequencies. This can cause a corruption of useful information in the image. Therefore, more realistic illumination models have to be taken into consideration, which allow preserving the integrity of retinal structures whilst correcting for uneven illumination.

Data from the WFS can be useful when deconvolving AO high-resolution retinal images. Nevertheless, image deconvolution methods that rely on this this data are subjected to the accuracy of wavefront sensor. The PSF reconstructed from measurements of the wavefront sensor is affected by various kinds of noise as well as the unsynchronized process of image capturing and wavefront calculation. In addition, wavefront measurements acquired with a Shack-Hartmann sensor lack information on the ocular scatter which may give rise to wavefront measure errors [198, 199]. Moreover, in AO high-resolution retinal images out-of-focus planes of the retina also contribute to the image formation, resulting in additional blur and distortion. Therefore, an adequate image deconvolution model is required for addressing complex distortion in AO high-resolution retinal images.

To assist the diagnosis of various retinal diseases, an automated procedure is required that can provide estimation of cone density distribution in agreement with statistical histological data or manual counting. The literature review on this subject has revealed that most state-of-the-art methods are solely based on the intensity information of image. In case of a good quality image of a healthy subject, these methods perform well. But when dealing with the images altered by blur and noise, more factors have to be taken into account. Moreover, these methods cannot be considered as fully automated as they require manual input for parameters, such as the intensity threshold and inter-cell spacing, thus affecting the agreement between the results obtained by different observers. Despite the rapid development of automated methods for cone density calculation, manual counting is still used as the reference for performance evaluation of automated cone counting methods [78], [200, 201]. Thus, the implemented model should correlate well with the results obtained by observers.

3. Techniques and Analysis: Image Pre-processing

3.1 About This Chapter

In this work, an image processing framework is developed that allows for enhancement of AO high-resolution retinal images and accurate detection of photoreceptor cells. In this framework, the visibility of retinal features is improved by tackling specific AO system components, which affect the quality of the acquired retinal data (Figure 2.1). The proposed image processing framework consists of several stages: uneven illumination correction, noise suppression, image quality assessment, image registration, image deconvolution, enhancement and detection of photoreceptor cells (Figure 3.1). Each step is designed to improve the quality of the retinal images while preserving retinal features content. As a result, accurate detection of photoreceptors cells is achieved. A comparative study of different image processing methods and evaluation of their efficiency on retinal datasets is performed by assessing image quality. The proposed set of algorithms is applied to datasets of high-resolution retinal images, obtained with a commercial AO-assisted flood illumination system, the rtx1 from Imagine Eyes (see Section 1.3.2 for the details). The proposed framework was implemented under Windows using MATLAB® 2015b (Mathworks Inc., USA).

In this chapter, a description of the chosen methodology for the image pre-processing steps is presented. This includes image quality assessment, uneven illumination correction, noise suppression followed by two-stage image registration. As a result, an averaged registered image is produced with a higher contrast.

3.2 Image Processing Framework

The proposed image processing framework consists of six stages designed to compensate for the variety of degradation processes in an AO system. At each stage the visibility of

photoreceptor cells is gradually improved thereby allowing for photoreceptor cell detection at the last stage of image processing framework. Figure 3.1 presents the block-diagram of the framework.

To facilitate the accuracy of image registration, firstly a dataset of 40 unprocessed frames is corrected for uneven illumination and noise. Thereafter, image quality assessment is performed on the enhanced dataset. The frame with the highest sharpness measure is chosen as the reference frame, used for mapping test frames at the following stage of image registration. The frames with a quality measure lower than the 0.15 quantile of the overall image quality distribution are eliminated from the image sequence prior to registration.

The obtained dataset with a reduced number of frames is further employed in two-stage image registration. At the coarse stage, only translation vectors are calculated. At the fine stage, the transformation model is refined by finding rotation angles and residual translation. The frames are compensated for the detected transformation parameters, and lucky averaging is performed on the aligned dataset. Consequently, a single image of a higher contrast is obtained.

At the next stage of image processing framework, the averaged image is used for predicting the PSF of a system. To compensate for the residual optical aberrations, the image is restored with the estimated blur kernel.

At the last stages of image processing framework, photoreceptor cell enhancement is performed on the deblurred image. Increased contrast between the cones and the background facilitates the next stage of cone detection. As a result, the proposed image processing framework produces a final retinal image with a significantly improved image quality which may assist in visual interpretation of retinal mosaic, and provide estimation of cone density distribution required for quantitative assessment of retinal images.

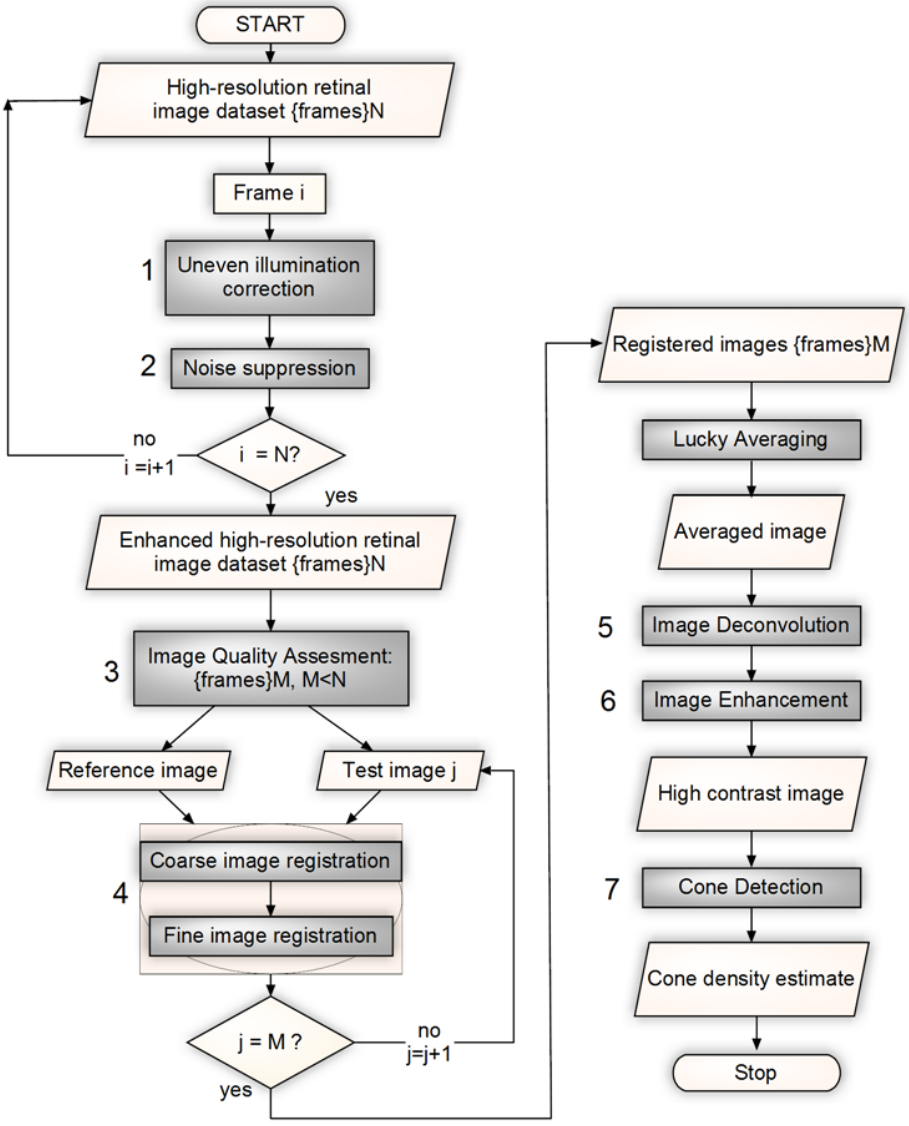


Figure 3.1: The block-diagram of the proposed image processing framework.

3.3 Image Quality Assessment

One of the most relevant issues in image processing and analysis is a choice of reliable image quality assessment. Image quality is a characteristic of an image that measures the extent to which the image data records the observed scene faithfully [202]. Objective evaluation of image quality has a fundamental importance for various image processing applications, where quantitative measures for automatic perception of the image are required. To this purpose, numerous image quality assessment methods have been proposed over the past years. These can be broadly classified into full-reference (FR) and no-reference methods

(NR). FR methods are based on comparison with a complete reference image that is assumed to be of perfect quality. NR quality assessment is a common method for many practical applications, where the reference image is not available. There is also a third type, where the reference image is given as a set of extracted features. This quality assessment method is known as reduced reference method [203].

Retinal images exhibit variations in contrast and blur due to multiple sources of distortion in the AO system. Even within a single dataset, the difference in image quality can be easily observed. Therefore, prior to the registration stage, it is important to exclude poor quality images from the sequence so as to avoid accumulation of noise and blur in the resulting averaged image. We also need a reliable measure to benchmark the image processing algorithms of the proposed framework, by evaluating the extent of image quality improvement achieved at each step. As the reference image is not available in this study, we focus on NR quality assessment metrics only.

The choice of an adequate image quality measure depends on the requirements of the considered application. The aim of this research project is to facilitate better distinction of photoreceptor cells. Therefore, while compensating for degradation effects present in the image the integrity of the photoreceptor edge has to be preserved. Following this requirement, we base our image quality assessment on the assumption that for a good quality image the intensity difference between adjacent regions must be very high. In case of blurry images, the intensity difference between adjacent regions will therefore be lower in comparison to sharper images. This quality measure model known as Blur Measure (BM) has been proposed by Kanjar and Masilamani [204] and proved to be close to human's perception of image quality.

Human beings are the ultimate users of most of the image processing applications, therefore evaluation of IQA models is commonly performed by comparing their performance with human visual perception [204, 205]. To this purpose, different image databases have been proposed. They contain reference images, their corresponding distorted images, and subjective scores which represent ground truth information obtained by human observers. Information on the perceived quality is reported as mean opinion scores or differential mean opinion scores [206]. In this work, the efficiency of BM is evaluated in high-resolution retinal images and compared with other well-known image quality measures. Since there is

no reference data available for high-resolution retinal images, the performance of IQA models is evaluated by assessing their correlation with average human ratings.

3.3.1 Blur Measure

Edges characterize the intensity discontinuities in an image and represent important features in computer vision [172], [207]. In [204], Kanjar and Masilamani estimated image sharpness from the edge information of the image I, using the following equation:

$$BM_1 = \frac{\sum_{I(x,y)\in E} \sqrt{\sum_{I(x',y')\in N_{xy}} \{I(x,y) - I(x',y')\}^2 / |N_{xy}|}}{\sum_{I(x,y)\in E} I(x,y)}, \tag{3.1}$$

where E is a set containing all edge pixels in the image computed with the Sobel filter; N_{xy} is a set of 8-neighbours of a pixel $I(x,y)$, where $I(x,y) \in E$; and $|N_{xy}|$ is a number of pixels in the set N_{xy}. The threshold in the Sobel filter is calculated automatically as $\sqrt{4\,\bar{I}}$, where $\bar{I}$ is the mean intensity of the image.

The higher the change in intensity around the edges of the image, the higher the BM_1 score gets, signifying higher sharpness. If the image is blurred, then the intensity variation along the edges of the image is low which results in low scores of BM_1.

A different approach for calculating the amount of blur in the image was proposed by Crete et al. [208]. This method works independently from any edge detector, based on the comparison between the original image and its low-pass filtered copy. If there is high variation between the original and the blurred image that means that the original image was sharp, whereas a slight variation between the original and the blurred image means that the original image was already blurred.

In order to calculate the blurred copy of the original image I of size of $M \times N$ pixels, horizontal H_{hor} and vertical H_{ver} strong low pass-filters are applied; thus two blurred images are modelled: B_{ver} and B_{hor}:

$$\begin{gathered} B_{ver} = I * H_{ver} \text{ and } B_{hor} = I * H_{hor}, \\ \text{where } H_{ver} = \frac{[1\,1\,1\,1\,1\,1\,1\,1\,1]}{9} \text{ and } H_{hor} = {H_{ver}}^T. \end{gathered} \tag{3.2}$$

In this manner, the absolute difference of the images ∇I_{ver}, ∇I_{hor}, ∇B_{ver} and ∇B_{hor} is calculated as follows:

$$\begin{aligned}
\nabla \mathrm{I}_{\mathrm{ver}}(x,y) &= |I(x,y) - I(x-1,y)|, for\ x = 1{:}M-1, y = 0{:}N-1 \\
\nabla I_{\mathrm{hor}}(x,y) &= |I(x,y) - I(x,y-1)|, for\ x = 0{:}M-1, y = 1{:}N-1 \\
\nabla \mathrm{B}_{ver}(x,y) &= |B_{ver}(x,y) - B_{ver}(x-1,y)|, for\ x = 1{:}M-1, y = 0{:}N-1 \\
\nabla \mathrm{B}_{hor}(x,y) &= |\ B_{hor}(x,y) - \ B_{hor}(x,y-1)|, for\ x = 0{:}M-1, y = 1{:}N-1.
\end{aligned} \tag{3.3}$$

In order to evaluate the extent of blur present in the image, the following variations are calculated:

$$\begin{aligned}
V_{ver} &= \max\big(0, \nabla I_{ver}(x,y) - \nabla B_{ver}(x,y)\big), for\ \ x = 1{:}M-1, y = 1{:}N-1 \\
V_{hor} &= \max\big(0, \nabla I_{hor}(x,y) - \nabla B_{hor}(x,y)\big), for\ \ x = 1{:}M-1, y = 1{:}N-1.
\end{aligned} \tag{3.4}$$

Variations in the original image are expressed as the sum of the coefficients as follows:

$$\begin{aligned}
s_I_{ver} &= \sum_{x,y=1}^{M-1,N-1} \nabla I_{ver}\,(x,y) & s_I_{hor} &= \sum_{x,y=1}^{M-1,N-1} \nabla I_{hor}\,(x,y) \\
s_V_{ver} &= \sum_{x,y=1}^{M-1,N-1} V_{ver}\,(x,y) & s_V_{hor} &= \sum_{x,y=1}^{M-1,N-1} V_{hor}\,(x,y).
\end{aligned} \tag{3.5}$$

In order to get the result measure in the range between 0 and 1, where 0 signifies sharp image and 1 blurred, normalization is used:

$$\begin{aligned}
blur_I_{ver} &= \frac{s_I_{ver} - s_V_{ver}}{s_I_{ver}} \\
blur_I_{hor} &= \frac{s_I_{hor} - s_V_{hor}}{s_I_{hor}}.
\end{aligned} \tag{3.6}$$

Following this logic, the blur value is calculated as the maximum of variations in horizontal and vertical direction:

$$BM_2 = \max(blur_I_{ver}, blur_I_{hor}). \quad (3.7)$$

3.3.2 Image Contrast

Contrast is defined as the difference in brightness values between two structures, such as regions or pixels [202]. There are various measures of contrast used in different situations, for example Weber contrast and Michelson contrast [209]. In this work, we use Root Mean Square (RMS) contrast, which is defined as image variance σ_I over average image intensity $\bar{I}$ [209]:

$$c_{RMS} = \frac{\sigma_I}{\bar{I}}. \quad (3.8)$$

3.3.3 Image Variance

The image variance measures the amount of variation of pixel brightness values in the image. Therefore, it can be used as a sharpness measure when image noise is assumed to be relatively constant. As the blurriness of the image increases, the edges are smoothed and the transitions between the grayscale levels in the image decrease, thus the variance decreases. The measure is expressed as the average of the square of the difference of each image pixel $I(x, y)$ from the mean $\bar{I}$ with the following expression:

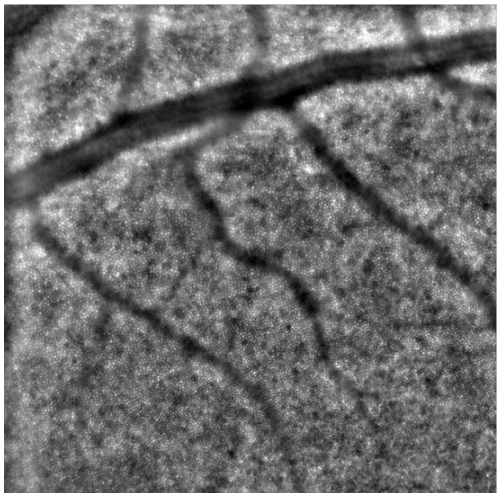
$$\sigma^2 = \frac{1}{MN}\sum_{x=1}^{N}\sum_{y=1}^{M}(I(x, y) - \bar{I})^2. \quad (3.9)$$

3.3.4 Evaluation of Image Quality Measures

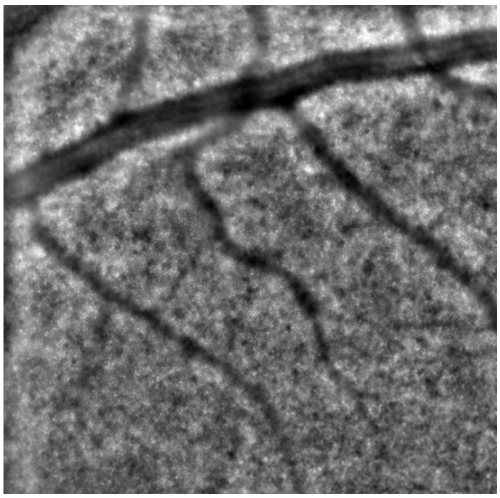
The effectiveness of the image quality assessment models has been tested on the high-resolution retinal images. In the first study, a rotationally symmetric Gaussian low-pass filter was applied to gradually blur the retinal image (Figure 3.2), using different values for the standard deviation σ (from 1 to 1.8) and kernel size k (from 2x2 to 10x10). The standard deviation controls the width of spread in the Gaussian function. Increasing the standard deviation results in more neighbourhood pixels used for averaging, and thus greater

smoothing of an image. To accurately represent the Gaussian shape of the filter, the total size of the kernel should be at least six times larger than the selected standard deviation. In this study, the aim was to produce a series of images with a small variation in blur comparable to what can be observed in AO retinal images. To this purpose, the size of the kernel was intentionally set to small values. To eliminate the ambiguity of the performance of image quality measures in the presence of noise and uneven illumination, the dataset of raw frames was processed with the software program provided by the system manufacturer (CK v0.1, Image Eyes, Orsay, France) as shown in Figure 3.2-a. For each of the blurred images, the image quality was calculated using the equations for image contrast (Equation (3.8)), variance (Equation (3.9)) and image blur (BM_1, Equation (3.1) and BM_2, Equation (3.7)). The resulting plots in Figure 3.3 show a similar trend for all four IQA models with a gradual decrease in image quality as the image becomes more blurred. For comparison purposes, the plot of BM_2 was inverted. Therefore, this test has not been able to reveal a significant difference between the tested image quality measures.

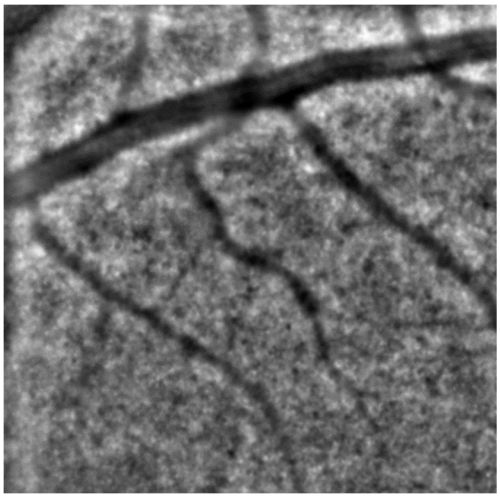
In the second study, in order to compare the chosen image quality measures with human visual perception, 10 independent observers (PhD students at School of Mathematics, Computer Science, and Engineering, City, University of London) were asked to visually rank four retinal datasets acquired with AO instrument and sort them in descending order in accordance to their perception of image quality. The obtained answers were averaged and compared against corresponding values calculated with the image quality measures (Table 3.1). To ease the evaluation process for the examiners, this task was simplified by reducing the sample to seven images in each dataset acquired from different retinal locations. For the sake of clarity, the images were processed to correct for uneven illumination and noise as described in Sections 3.4 and 3.5. Figure 3.4 shows the images from one retinal dataset which was used for evaluation by the observers and four IQA models.



a



b



c

Figure 3.2: Gradually blurred high-resolution retinal images. (a) Original high-resolution retinal image with corrected illumination; (b) image (a) blurred with the Gaussian low pass filter with k =4, σ = 1.2; (c) image (a) blurred with the Gaussian low pass filter with k =10, σ = 1.8.

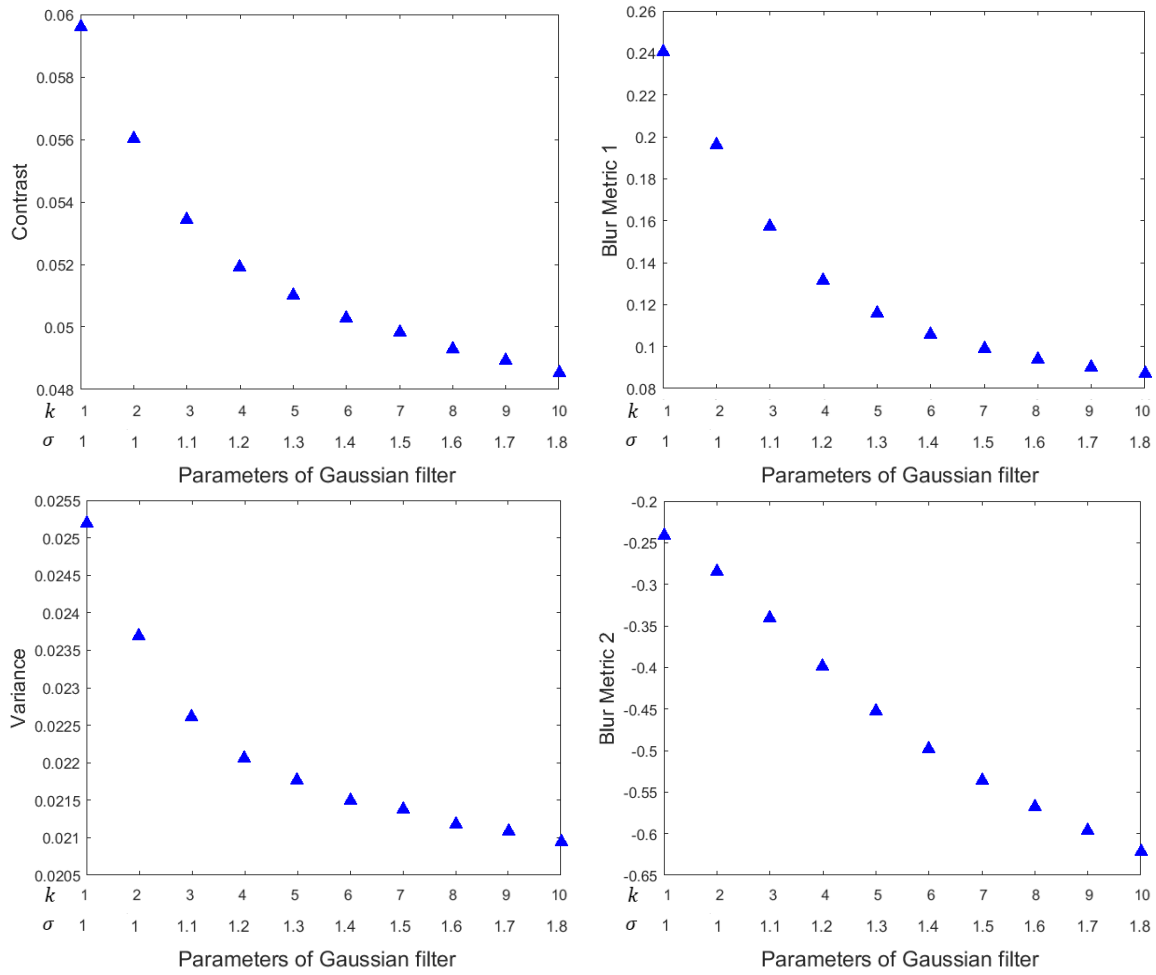


Figure 3.3: Image quality variations for the gradually blurred retinal image sequence calculated with four different IQA models.

Figure 3.5 illustrates scatter plots of image quality measures versus human ratings for four retinal datasets. The Spearman rank correlation coefficient was calculated for each comparison with the human ratings. The average human ranks were obtained by sorting the images in descending order where "1" represents the best image quality and "7" corresponds to the image with the worst quality for a given dataset. Therefore, the image quality model with the highest negative Spearman coefficient is expected to have the highest correlation with the human ratings. As it can be seen from Figure 3.5, only "blur measure 1" evaluates the images in accordance to the human choice except for images three and four in the retinal dataset 4 (highlighted with red in Table 3.1). This deviation can be explained by the fact that these images are very similar in quality and this difference is hardly distinguishable by human eye. This fact is also confirmed in Figure 3.6, by comparing the values of blur measure for image three and four.

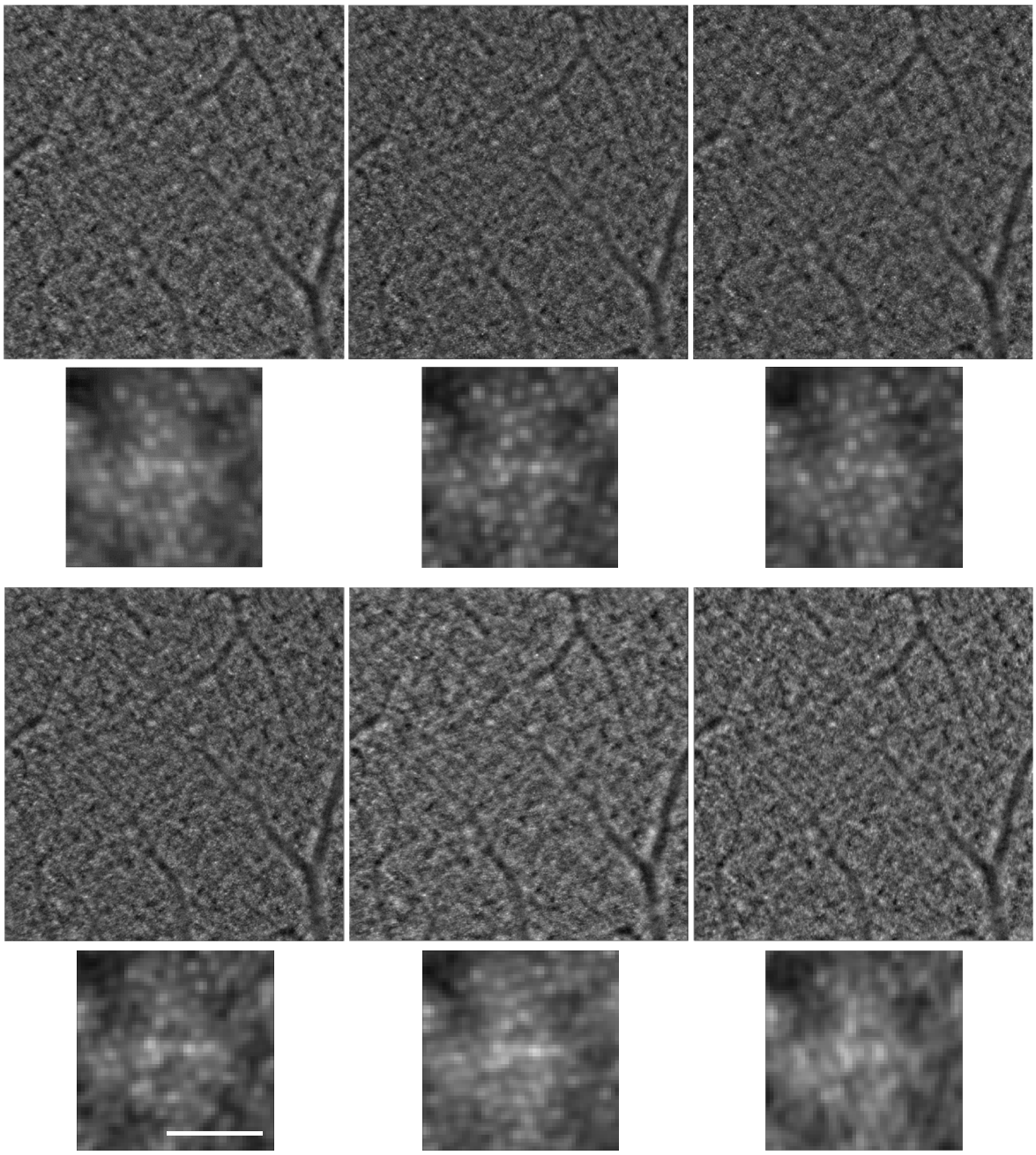


Figure 3.4: High-resolution retinal images selected from one dataset for image quality evaluation. The scale bar is 40 μm.

Image Number	Contrast Value (10^{-3})	BM_1 Value (10^{-1})	Variance Value (10^{-3})	BM_2 Value[1]	Human Ranking
Retinal dataset 1					
Im_1	0.1861	0.135	0.1675	0.2251	7
Im_2	0.1953	0.151	0.1708	0.2225	5
Im_3	0.1859	0.137	0.1650	0.2267	6
Im_4	0.2066	0.169	0.1806	0.2149	3
Im_5	0.1925	0.155	0.1681	0.2213	4
Im_6	0.2091	0.172	0.1843	0.2122	2
Im_7	0.2049	0.174	0.1775	0.2141	1
Retinal dataset 2					
Im_1	0.2821	0.2655	0.2067	0.1789	2
Im_2	0.2882	0.2649	0.2123	0.1821	3
Im_3	0.2936	0.2717	0.2175	0.1808	1
Im_4	0.2489	0.2070	0.2125	0.1728	6
Im_5	0.2555	0.2210	0.2046	0.1776	5
Im_6	0.2668	0.2358	0.2061	0.1794	4
Im_7	0.2485	0.2000	0.2259	0.1671	7
Retinal dataset 3					
Im_1	0.3503	0.2298	0.2964	0.2070	1
Im_2	0.3487	0.2294	0.2892	0.2096	2
Im_3	0.3338	0.2061	0.2897	0.2112	3
Im_4	0.3320	0.2044	0.2852	0.2145	4
Im_5	0.3007	0.1785	0.2716	0.2112	7
Im_6	0.3262	0.1976	0.2925	0.2085	6
Im_7	0.3346	0.2036	0.2936	0.2127	5
Retinal dataset 4					
Im_1	0.3723	0.2998	0.2600	0.2154	1
Im_2	0.3038	0.1951	0.2354	0.2501	6
Im_3	0.3642	0.2847	0.2596	0.2135	3
Im_4	0.3506	0.2835	0.2406	0.2183	2
Im_5	0.3249	0.2553	0.2375	0.2235	4
Im_6	0.1836	0.1611	0.1419	0.2383	7
Im_7	0.2524	0.2022	0.1868	0.2312	5

Table 3.1: Comparison of different image quality measures with human ratings in four retinal datasets acquired at different locations.

[1] For BM_2 the smaller the value the sharper the image is.

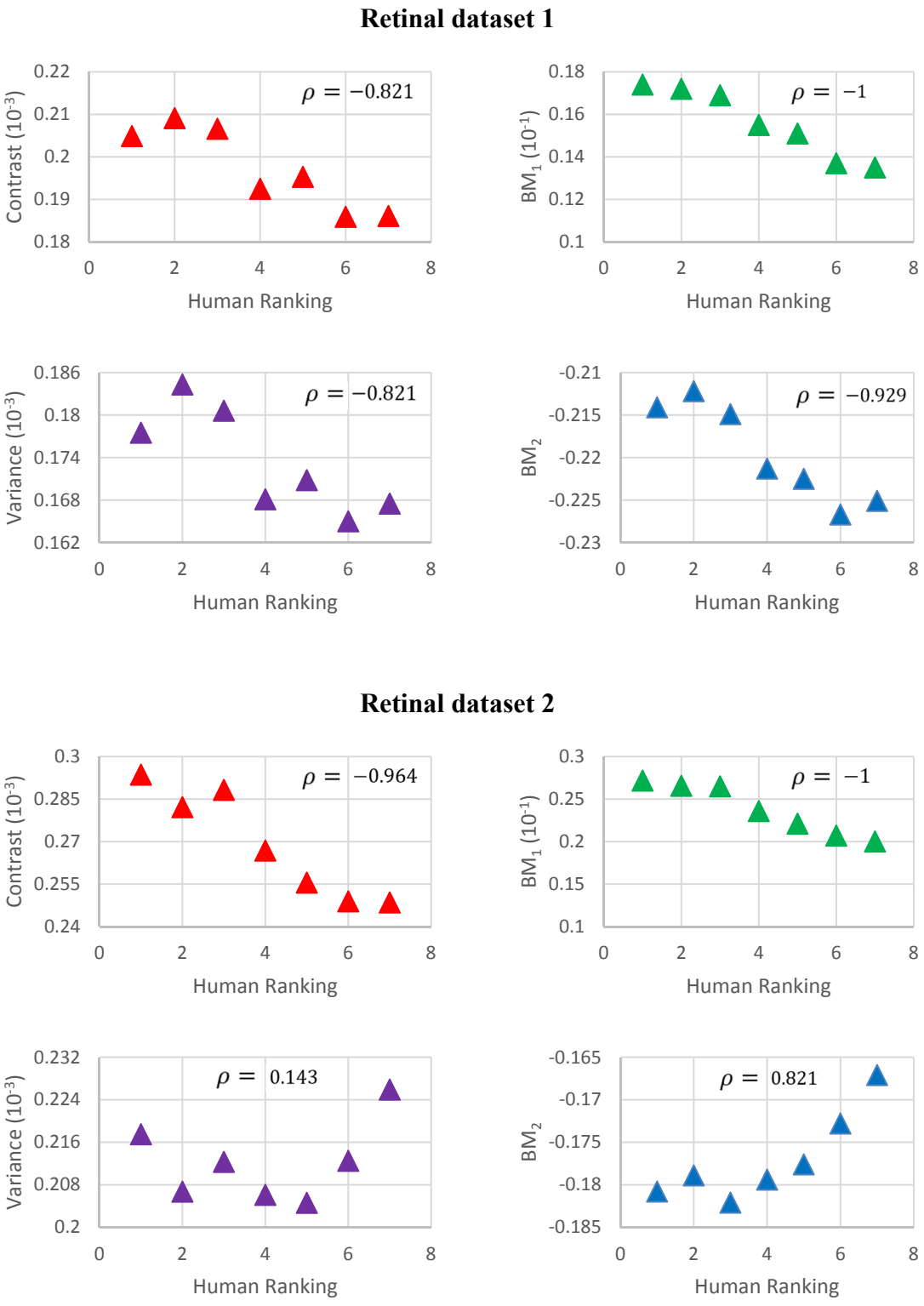


Figure 3.5: Scatter plots of different image quality measures versus human ratings for four retinal datasets acquired from different locations. Human ranking corresponds to the image quality sorted in descending order, from high (equal to one) to low (equal to seven).

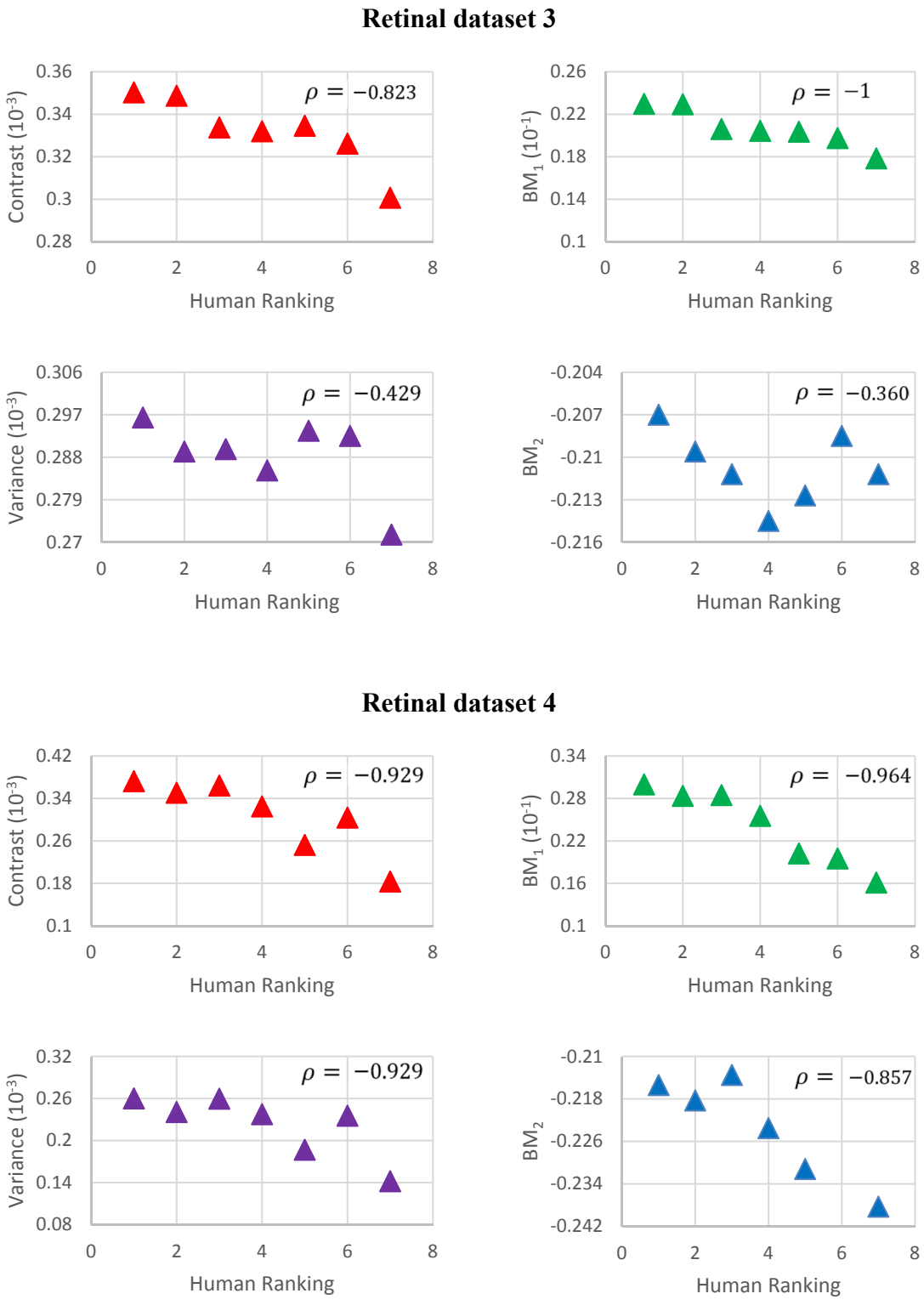


Figure 3.5 (Cont.): Scatter plots of different image quality measures versus human ratings for four retinal datasets acquired from different locations. Human ranking corresponds to the image quality sorted in descending order, from high (equal to one) to low (equal to seven).

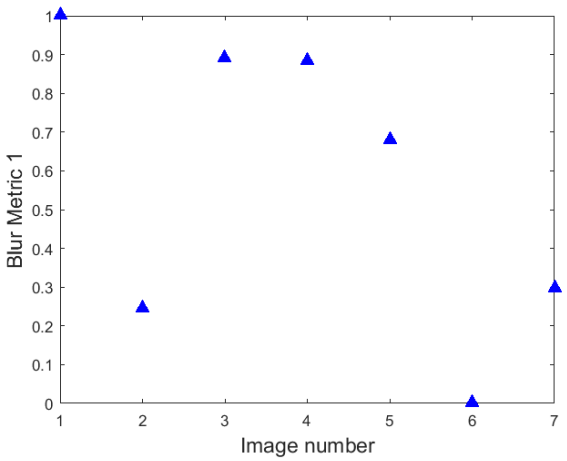


Figure 3.6: Retinal dataset 4 evaluated using BM_1.

Based on the results of the performed investigation, "Blur Measure 1" was chosen to perform quality assessment of high-resolution retinal images within the proposed image processing framework. Since BM_1 measures the extent of sharpness in the images, as opposed to BM_2 which calculates the amount of blur, we will call BM_1 metric as an image sharpness in the following chapters of this thesis.

3.4 Retrospective Illumination Correction

Due to imperfections in the imaging optics and image formation process in general, the visibility of retinal features is altered by the inhomogeneous illumination component of the AO-corrected retinal image. In order to improve visualization of retinal structures and to facilitate next steps of the image processing framework, correction of uneven illumination is required. Given that additional background images are not available for high-resolution retinal images, a comparative evaluation of retrospective illumination correction methods is performed.

3.4.1 Image Model

Illumination compensation requires estimation of various parameters of image models that consist of three essential parts: illumination of the scene by a light source, reflection of the light by the objects' surfaces and acquisition of an image by a camera. Existing shape-from-shading algorithms assume Lambertian reflectance, a uniform reflection of a light from the surface with no directional dependence on observer position. Under this assumption, in a

scene illuminated by a single distant light source, the observed luminance image $I(x, y)$ is the product of the reflectance image $R(x, y)$ and the shading image $S(x, y)$ [210]:

$$I(x, y) = R(x, y) * S(x, y). \tag{3.10}$$

The reflectance component characterizes physical properties of the object surfaces in the scene – the albedo of the object surfaces The shading component includes the geometric properties of the scene, for example, intensity of a light source which falling on the object [211]. By reducing the contribution of illumination, the details of the image can be enhanced. This requires a method which is able to separate two components of the image. Inference of shading and reflectance images is an ill-posed problem, because the observed image $I(x, y)$ can be produced by various combinations of $R(x, y)$ and $S(x, y)$. To this purpose various assumptions and simplifications were proposed for discriminating between illumination and reflectance components of an image. Most commonly, it is assumed that the shading component of an image is generally characterized by slow variations with no discontinuities, while the reflectance component is discrete sharply at the edges and varies abruptly. The frequency spectrum of shading component shows that this component prevails mostly in the low-frequency domain, while the high-frequency components are assumed to represent mostly the reflectance in the scene.

3.4.2 Retrospective Illumination Correction using Low-pass Filtering and Division/Subtraction

Assuming that the illumination component of an image is additive or multiplicative and considering that illumination variations mainly lie in the low-frequency band, the low-pass filter can be used to obtain an estimate of illumination component of an image. By convolving the image $I(x, y)$ with a Gaussian kernel of a large scale $H(x, y, \sigma)$, the spatial frequencies in an image are delimited, which results in a loss of edge definition and averaging of intensity values. The rotationally symmetric Gaussian function $H(x, y, \sigma)$ is defined by:

$$H(x, y, \sigma) = \frac{1}{2\pi\sigma^2} e^{-\frac{(x-x_c)^2+(y-y_c)^2}{2\sigma^2}}, \tag{3.11}$$

where x_c and y_c represent the mean of the Gaussian function, σ is the effective spread of the function; the larger the value of σ, the greater the smoothing effect. The optimal size of the

Gaussian filter is dependent upon the scale of the objects in the image and the size of the image.

After the smoothed version of the image is obtained, it is either subtracted from the original image or the original image is divided by the smoothed one, depending on the assumptions on the illumination component of an image. Hence, the image with compensated illumination variations $O(x, y)$ is obtained as follows:

$$O(x, y) = I(x, y) - I(x, y) * H(x, y, \sigma) \tag{3.12}$$

or

$$O(x, y) = \frac{I(x, y)}{I(x, y) * H(x, y, \sigma)}, \tag{3.13}$$

where symbol * represents convolution.

3.4.3 Retrospective Correction using Homomorphic Filtering

Homomorphic filtering is a generalized technique for image enhancement. It simultaneously normalizes the brightness across an image and increases the contrast [212]. Homomorphic filtering is based on the transformation of the multiplicative illumination component of an image into additive, by taking the logarithm of Equation (3.10):

$$I(x, y) = R(x, y) * S(x, y)$$

$$\log\big(I(x, y)\big) = \log\big(R(x, y) * S(x, y)\big) \tag{3.14}$$

$$\log\big(I(x, y)\big) = \log\big(R(x, y)\big) + \log\big(S(x, y)\big).$$

Using the assumption that illumination varies slowly across different locations of the image and the local reflectance changes quickly across different locations, high-pass filtering can be performed on the logarithm of the image $I(x, y)$. By adopting this process, we reduce the luminance part, which is the low frequency component of the image, and amplify the reflectance part, which corresponds to the high frequency component [213]. High-pass

filtering can be performed both in spatial and frequency domains. The processing may be described as shown below:

$$h * \log\big(I(x,y)\big) = h * \log\big(R(x,y)\big) + h * \log\big(S(x,y)\big), \tag{3.15}$$

where h is the kernel of the filter and * indicates convolution.

As a final step, the exponential function is applied to invert the log-transform and yield the enhanced image $O(x,y)$:

$$O(x,y) = \exp\big(h * log\big(I(x,y)\big)\big). \tag{3.16}$$

3.4.4 Wavelet-based Filtering

The Fourier transform (FT) is a fundamental tool used to analyse the frequency content of the signal. Although the FT provides information about the strength of individual frequencies present in the signal, it does not provide information regarding the point of occurrences of these frequencies in time. Lack of temporal information is a serious drawback of the FT when applied to non-stationary signals, therefore an alternative transformation which can give time-frequency representation is necessary to obtain time localization of the spectral components [214]. The wavelet transform has been introduced to solve this problem. Wavelet transforms are based on small wavelets with limited duration. The translated-version wavelets locate the differences in time, whereas the scaled-version wavelets allow analysis of the signal in different scales.

The wavelet transform is a multi-resolution image decomposition tool that provides a variety of channels representing the image feature by different frequency sub-bands at multi-scale [211]. A discrete signal can be approximated by [215]:

$$f[n] = \frac{1}{\sqrt{M}} \sum_{k} W_{\varphi}[j_0, k]\, \varphi_{j_0,k}[n] + \frac{1}{\sqrt{M}} \sum_{j=j_0}^{\infty} \sum_{k} W_{\psi}[j, k]\, \psi_{j,k}[n]\,, \tag{3.17}$$

where f $[n]$, $\varphi_{j_0,k}[n]$, $\psi_{j,k}[n]$ are discrete functions defined in the range $[0, M-1]$ with M points; k and j correspond to translation and scale values, respectively. $\psi_{j,k}$ is the wavelet function or the mother wavelet; it serves as a prototype for generating the daughter wavelets

which are the translated and scaled versions of the mother wavelet. $\varphi_{j_0,k}$ is the scaling function associated with the wavelet. The translation refers to the window location along the signal, while the scaling corresponds to either dilation or compression of a signal [216]. The scale parameter is defined as the inverse of the frequency, thus high scales (low frequencies) correspond to a global view of the signal, and low scales (high frequencies) correspond to detailed characteristics of the signal.

The sets $\varphi_{j_0,k}[n]$ and $\psi_{j,k}[n]$ are orthogonal to each other, thus the wavelet coefficients can be represented by their inner product:

$$W_{\varphi}[j_0, k] = \frac{1}{\sqrt{M}} \sum_{n} f[n] \varphi_{j_0,k}[n] \tag{3.18}$$

$$W_{\psi}[j, k] = \frac{1}{\sqrt{M}} \sum_{n} f[n] \psi_{j,k}[n] \, , j \geq j_0 \, . \tag{3.19}$$

Equation (3.18) defines approximation coefficients and Equation (3.19) defines detailed coefficients.

The DWT has the potential to decompose the signal into approximation and detailed information for analysing the signal at different frequencies and resolutions. For 2D signals like images, this kind of 2D DWT scheme provides a decomposition of the image into a low-frequency approximation component (LL) and a high-frequency detail component, which can be further divided into LH, HL and HH, known as horizontal, vertical and diagonal components, respectively. High-pass and low-pass filtering is used for decomposing the signal. The filtering operation changes the resolution of the signal, i.e. the amount of detailed information present. Up-sampling and down-sampling (subsampling) operations are used to control the scale, by increasing/reducing the sampling rate or adding/removing samples from the signal, respectively [216].

This first level of decomposition can be expressed as follows [211]:

$$LL_j(m,n) = \left[H_x * \left[H_y * LL_{j-1}\right]_{\downarrow 2,1}\right]_{\downarrow 1,2}(m,n)$$

$$\mathrm{HL}_{j\ vertical}(m,n) = \left[H_x * \left[G_y * LL_{j-1}\right]_{\downarrow 2,1}\right]_{\downarrow 1,2}(m,n)$$

$$\mathrm{LH}_{j\ horizontal}(m,n) = \left[G_x * \left[H_y * LL_{j-1}\right]_{\downarrow 2,1}\right]_{\downarrow 1,2}(m,n) \tag{3.20}$$

$$\mathrm{HH}_{j\ diagonal}(m,n) = \left[G_x * \left[G_y * LL_{j-1}\right]_{\downarrow 2,1}\right]_{\downarrow 1,2}(m,n)\ ,$$

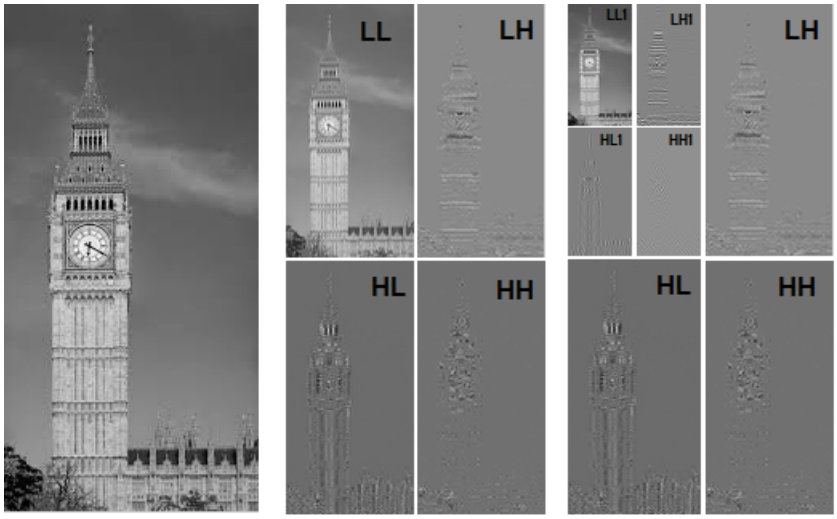
where * denotes the convolution operator, $\downarrow 2,1$ subsampling along the rows, $\downarrow 1,2$ subsampling along the columns and H and G are low-pass and high-pass filters, respectively.

When the original signal is convolved with a half band low-pass filter H, half of the frequencies are eliminated or in other words half of the information is lost. Thus, after the filtering operation the frequency resolution is reduced to half but the scale remains unaltered. Then according to the Nyquist's rule, half of samples in the signal can be eliminated with no loss of information. This decomposition subsamples the signal by two, as only half of samples are used to represent the entire signal. However, it doubles the frequency resolution for each frequency band as the corresponding range of the frequencies is reduced to half at the previous time interval. The above procedure is known as the sub-band coding and can be repeated for many levels [216]. Similarly, a half band high-pass filter G removes the low frequencies and after the process of subsampling produces the first level DWT coefficients or detail coefficients.

The low-frequency component can be decomposed again in the same manner, thereby producing even more sub-bands. After n applications of wavelet decomposition, this procedure results in one low-frequency component and n horizontal detail components, n vertical detail components and n diagonal detail components [217]. Figure 3.7 illustrates the process of 2-level wavelet decomposition.

In order to utilize wavelet decomposition in the illumination correction problem, the same assumptions are made as for the previously discussed methods, i.e. the illumination component is a low-pass component while the reflection component represents the detailed structure of the image. The logarithm function is applied to transform the product of illumination-reflection model into a sum with two components. To separate these

components, a multi-level DWT is applied. The more the decomposition scheme is being repeated, the more the approximation image concentrates in the low frequencies energy. At the last level of image decomposition, the approximation coefficients contain only low frequency information, which is expected to correspond to the image illumination. The coefficients in the wavelet approximation sub-band are set to a constant value in order to impose a uniform background. Consequently, the recovery process is performed using inverse of the DWT (IDWT) over the DWT and inverse of logarithm (exponential function) [211].



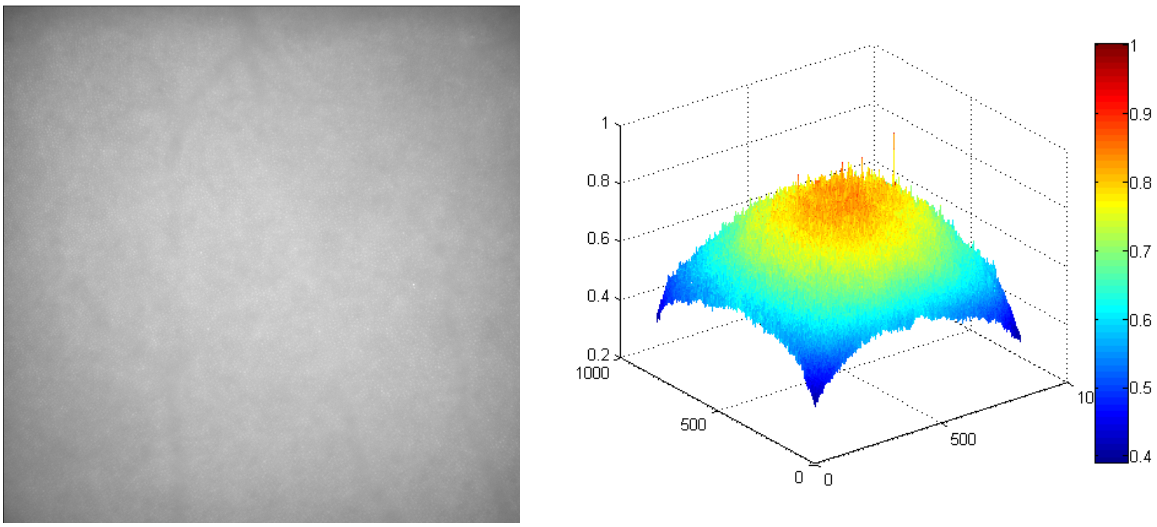
a b c

Figure 3.7: Wavelet decomposition of an image into sub-bands. (a) Original image; (b) 1-level wavelet decomposition; (c) 2-level wavelet decomposition. LL stands for the approximate image, the detailed information is represented by three components: horizontal (LH), vertical (HL), and diagonal (HH).

3.4.5 Implementation of Retrospective Illumination Correction Methods

High-resolution retinal images acquired with an AO instrument are characterized by a bright illumination pattern which gradually is falling off at the edges. The surface plot of unprocessed retinal image is illustrated in Figure 3.8. In order to choose the appropriate

method for illumination compensation in high-resolution retinal images, four retrospective illumination correction methods were implemented.



a b

Figure 3.8: (a) Original high-resolution retinal image and (b) its surface plot.

I. Illumination Correction using Low-pass Filtering and Division/Subtraction

For illumination correction using low-pass filtering, the optimal size of the Gaussian filter was firstly specified. Blood vessels are the largest object in retinal images. Depending on the retinal eccentricity, their scale varies and can reach the size of 750 pixels in length and 60 pixels in width (Figure 3.8-a). Therefore, a Gaussian filter with a large kernel needs to be used to eliminate detailed information corresponding to the vessels from retinal image. The standard deviation σ equal to 100 and kernel size of 100 pixels was used to produce an estimate of the illumination component. The obtained background was subtracted/divided from the original retinal image to compensate for illumination (Equation (3.12) and (3.13)).

II. Illumination Correction using Homomorphic Filtering

In the case of homomorphic filtering, a Gaussian high-pass filter was constructed directly in the frequency domain. The standard deviation of the Gaussian was set to 10 to eliminate the low frequency variations corresponding to the illumination component. The standard deviation in the frequency domain is the inverse of the standard deviation of the mask in the

spatial domain, and vice versa. That means that the standard deviation of 10 pixels corresponds to the cut-off frequency of 0.1 cycles/pixel. Given that photoreceptor cell spatial frequencies are in the range of 0.2 – 0.49 cycles/pixel (Section 3.5), this choice of cut-off frequency allows to preserve retinal features while compensating for illumination variations in low-frequency band. In frequency domain filtering, we have to deal with wraparound error which comes from the fact that DFT treats a finite-length signal (such as the image) as an infinite-length periodic signal, where the original finite-length signal represents one period of the signal. Therefore, there is interference from the non-zero parts of the adjacent copies of the signal. To avoid this, prior to filtering the original image was padded with a mirror reflection of itself.

III. Wavelet-based Illumination Correction

In order to successfully use the wavelet decomposition for illumination correction, the appropriate wavelet transform and the level of decomposition should be established. To this purpose, the original retinal image (Figure 3.8-a) was decomposed at ten levels using different wavelet families: Daubechies (DB); Coiflets, Haar, Symlets and Biorthogonal (bior), ReverseBio (rbio), implemented in Matlab® Wavelet Toolbox ™. Experimentally, it was found that Daubechies approximates illumination better, while other wavelet types introduce some obvious artefacts to the reconstructed image as it is shown in Figure 3.9. These artefacts occur as a result of the change in the approximation coefficients in order to impose a uniform background. The number next to the wavelet name defines the approximation order of the wavelet transform. In the wavelet family such as biorthogonal, there are two scaling functions, which may generate different multiresolution analyses, and accordingly two different wavelet functions. Therefore, there are two numbers defining the approximation order of the wavelet transform.

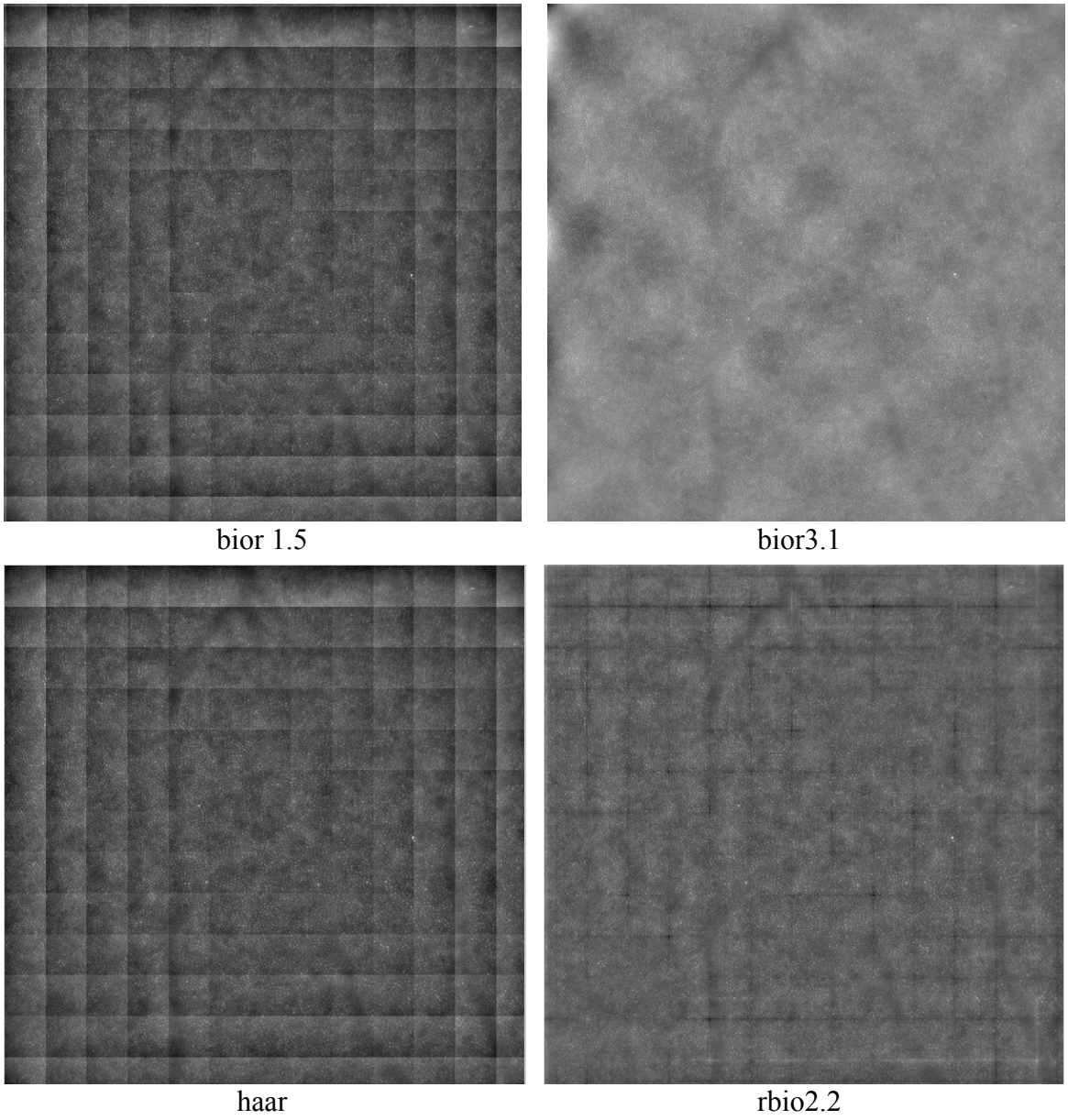
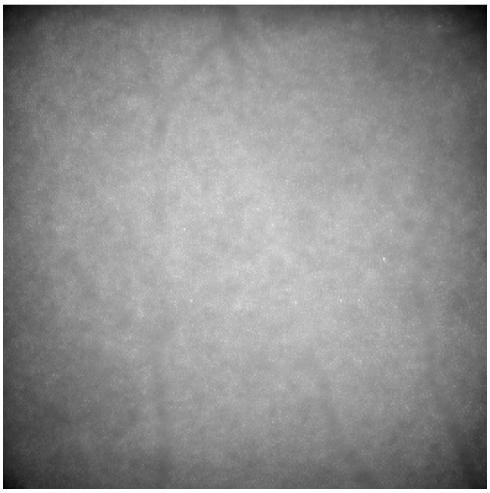
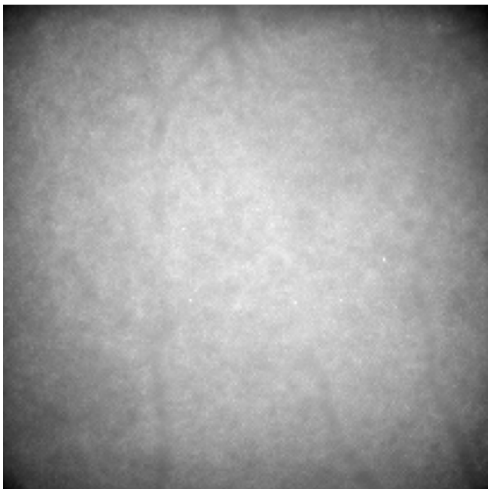


Figure 3.9: Retinal image reconstructed using different types of wavelet transform.

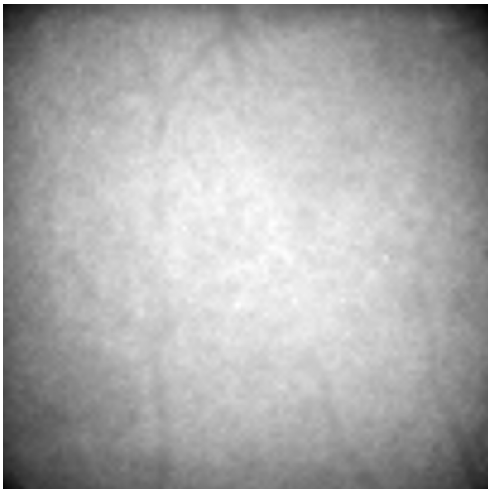
In Figure 3.10 the original retinal image is reconstructed using the approximation coefficients at different decomposition levels. Retinal features become more smoothed at each decomposition level, and at levels 6–10 the images do not contain any retinal features. Figure 3.11 shows the result of uneven illumination correction using DB6 wavelet at decomposition levels 1–10. As it can be observed uneven illumination correction at a single level of decomposition leads to elimination of most of the image information leaving only noise. Decomposing the images too far leads to almost a constant value in the approximation sub-band and thus does not allow for efficient illumination correction.



Level 1



Level 2



Level 3



Level 4



Level 5

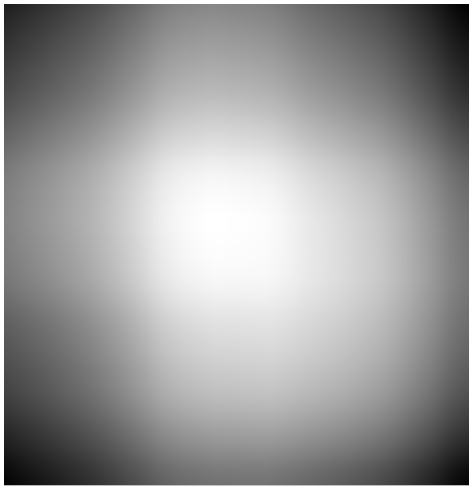


Level 6

Figure 3.10: High-resolution retinal images reconstructed using the approximation coefficients at decomposition levels 1-10.



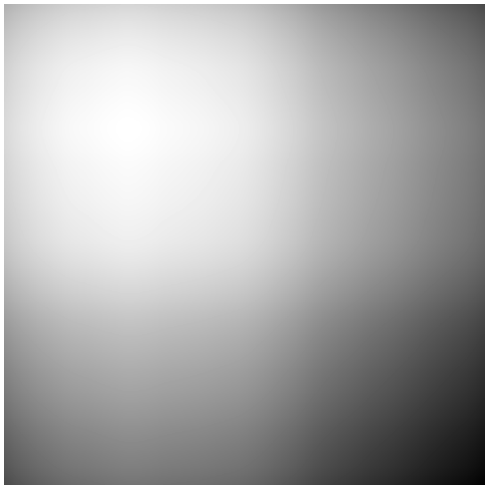
Level 7



Level 8



Level 9



Level 10

Figure 3.10 (Cont.): High-resolution retinal images reconstructed using the approximation coefficients at decomposition levels 1-10.

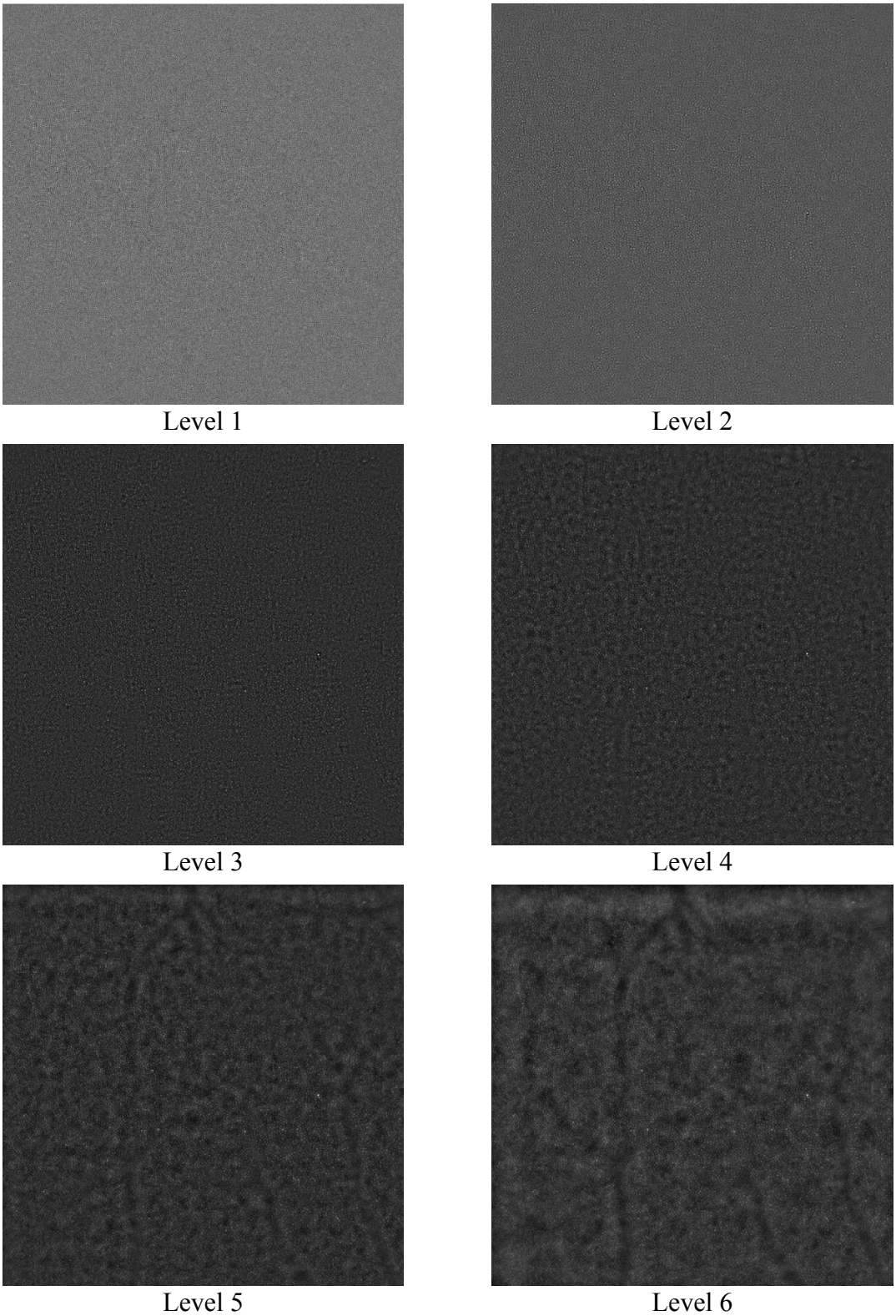
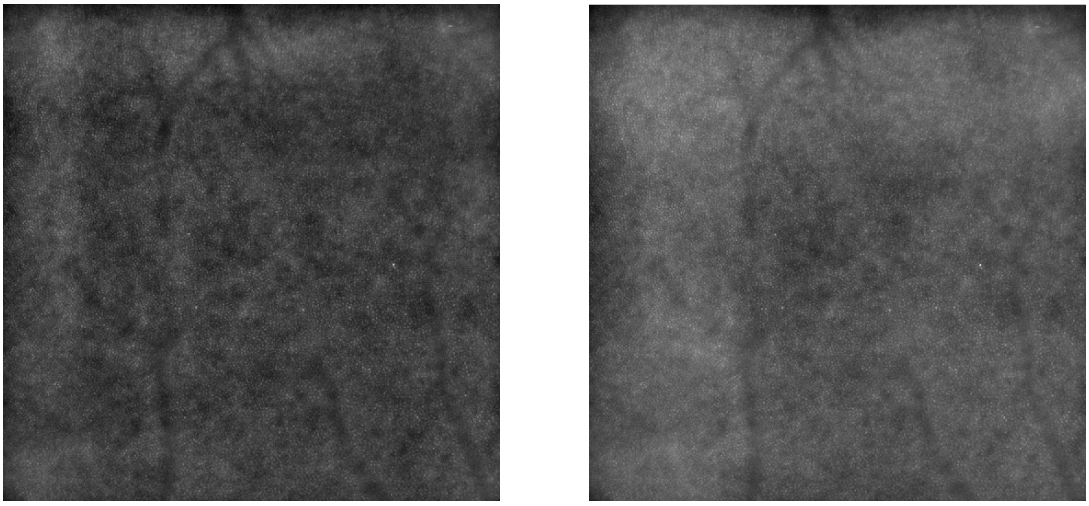
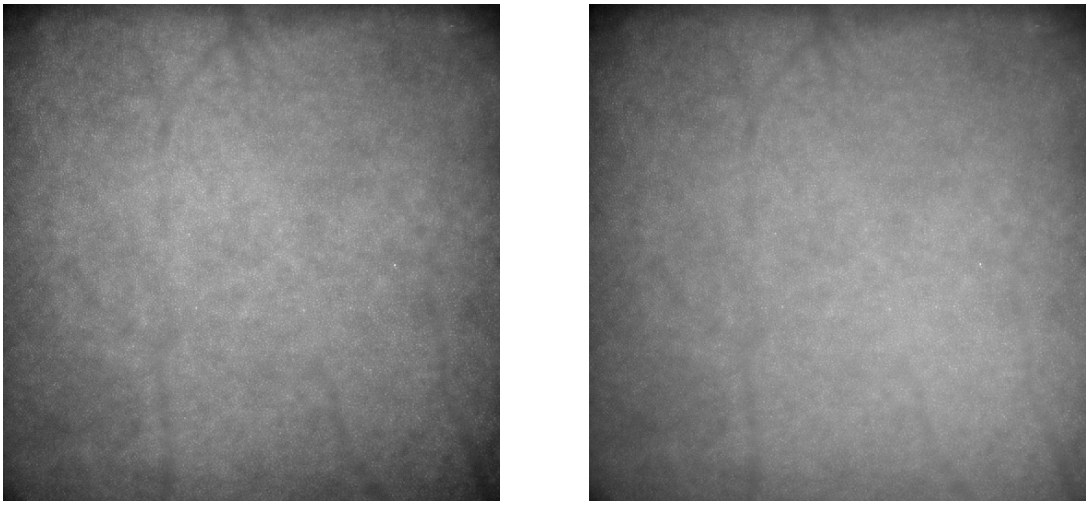


Figure 3.11: High-resolution retinal images with corrected illumination using DB6 wavelet at decomposition levels 1–10.



Level 7 Level 8



Level 9 Level 10

Figure 3.11 (Cont.): High-resolution retinal images with corrected illumination using DB6 wavelet at decomposition levels 1–10.

Since the purpose of illumination correction is to remove brightness variation from the images, a measure of local brightness variation [218] can be used in order to compare different illumination correction methods as well as to choose the appropriate level of decomposition in wavelet-based filtering. The local brightness variation is defined as follows:

$$\sigma_i = \sqrt{\frac{1}{N}\sum_i(\mu_i - \mu_\mu)^2}\,, \tag{3.21}$$

where $\mu_\mu = \frac{1}{N}\sum_i \mu_i$ is the mean brightness of the entire image, N is the size of non-overlapping blocks that the image is divided into and μ_i is the local mean image brightness

in the block i. In this work, the size of block was set to 20x20 pixels, which represents a local region with around 10 to 15 photoreceptor cells, depending on the retinal eccentricity. In this way, we were able to capture intensity variations of both, photoreceptor cells and the background.

Images reconstructed using the approximation coefficients represent the estimated background information, which would be removed from the original image in order to compensate for uneven illumination. Therefore, the level of decomposition at which background contains no retinal features is supposed to be appropriate for illumination correction. However, while decomposing the images at high levels may produce an estimate of the background with no retinal features (Figure 3.10, level of decomposition 7-10), reconstruction of the images at the corresponding levels does not necessarily allow for efficient illumination correction (Figure 3.11, level of decomposition 7-10). The process of finding the appropriate level of decomposition is therefore a trade-off between the local brightness variation of the reconstructed images (Figure 3.11), as a measure of illumination correction performance, and information encoded by the approximation coefficients at each level of decomposition (Figure 3.10), to ensure that the estimated background contains no retinal features. As homogeneity reflects the uniformity of the image intensity distribution, it was used as a measure of smoothness of the approximated background at each level of decomposition (Equation (3.22)).

$$\mathrm{H} = \sum_{i=1}^{N}\sum_{j=1}^{M}\frac{GLCM(i,j)}{1+(i-j)^2}, \tag{3.22}$$

where GLCM signifies the grey level co-occurrence matrix, the second-order histogram [219].

The appropriate level of decomposition was chosen as the level at which multiplicative combination of two parameters, homogeneity and the inverse of local brightness variation, reaches its maximum (Figure 3.12-c). In this way, the balance is found between effectively removing illumination background and preserving retinal features. Prior to the multiplication step, these values were normalized to the range of [0,1] (Figure 3.12-a, b). Experimentally, it was found that generally at the decomposition levels of $5-6$ the function of homogeneity and inverse local brightness variation reaches its peak. Figure 3.13 illustrates the process of

the proposed wavelet-based illumination compensation with the automated selection of decomposition level.

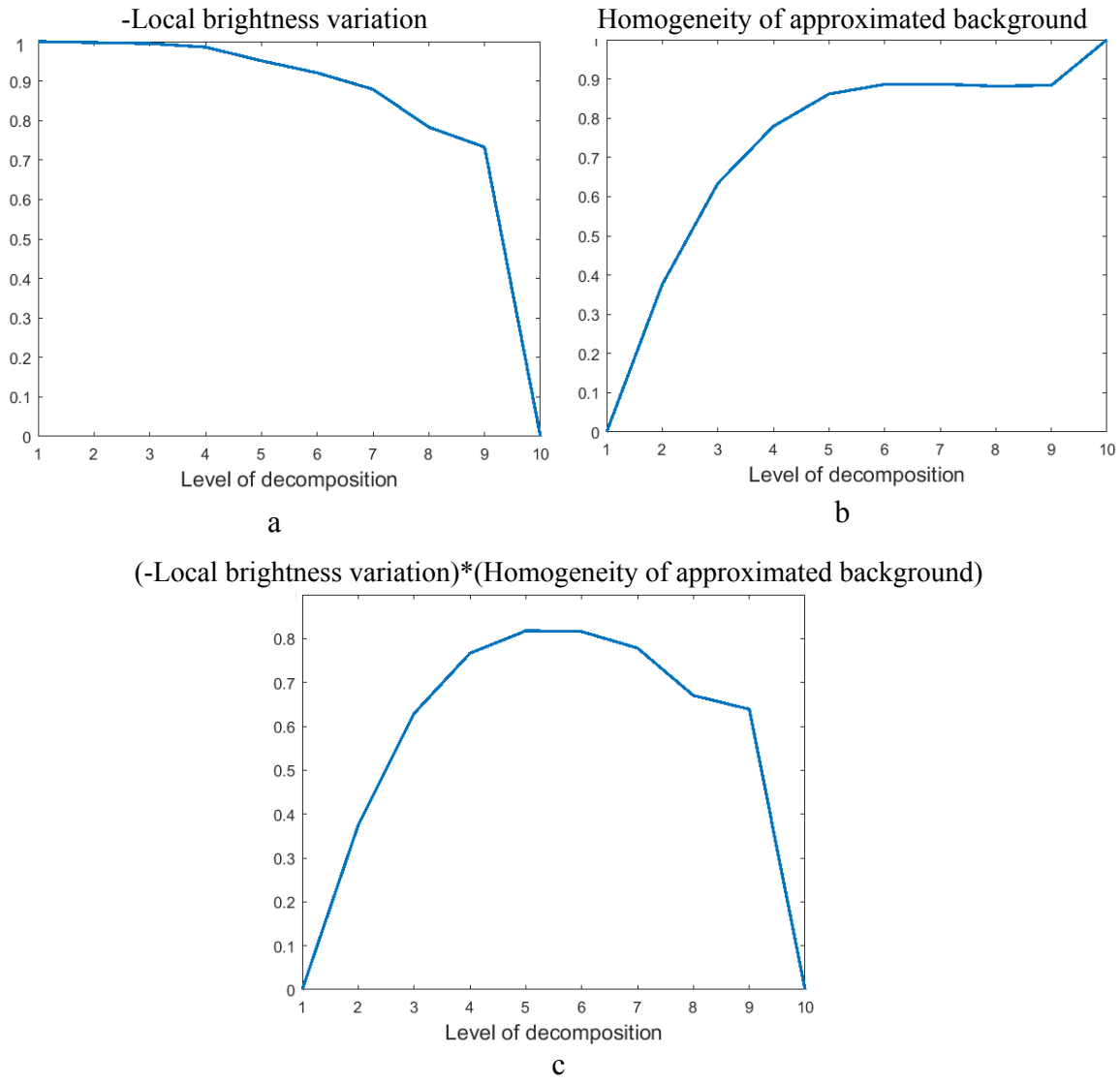


Figure 3.12: Calculating the appropriate level of decomposition using (a) negative of local brightness variation, (b) homogeneity of approximated background and (c) their multiplication.

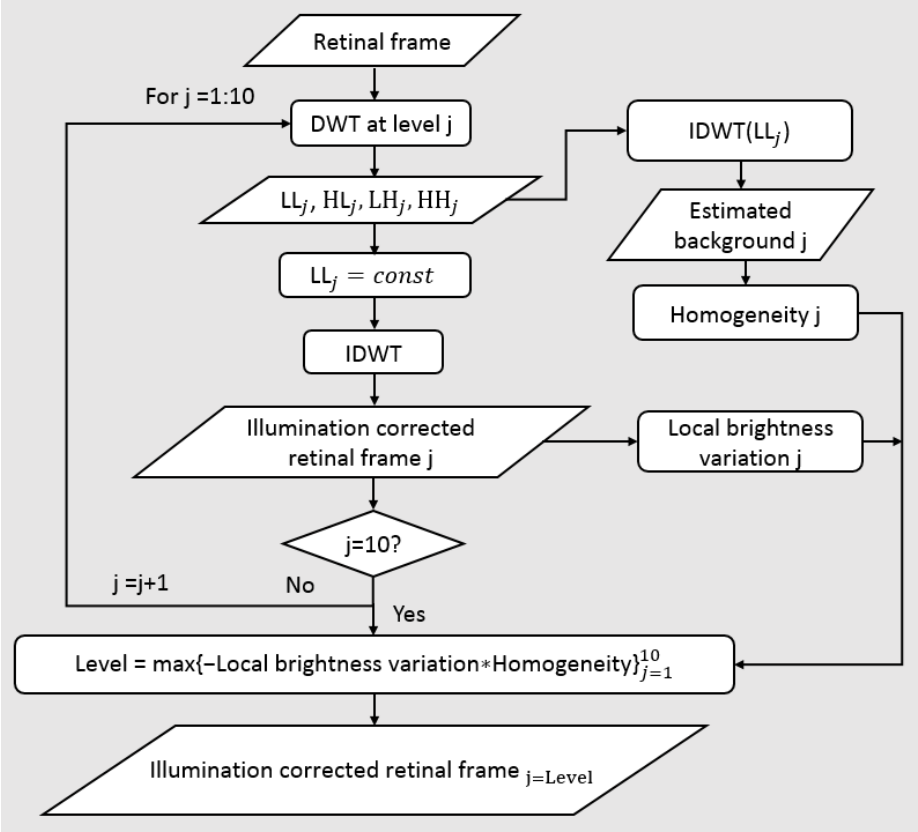


Figure 3.13: Flowchart showing the process of wavelet-based illumination correction with the automated selection of the decomposition level.

To test the approach, an artificial illumination pattern was modelled as a multi-variate Gaussian distribution, which was multiplied with the retinal image with corrected illumination (Figure 3.14-a, b). The surface plot of the resulting image (Figure 3.14-d) shows a similar appearance with the surface plot of the original raw image (Figure 3.8-b). The generated image (Figure 3.14-c) was decomposed with different types of Daubechies wavelet transform. The images reconstructed from the approximation coefficients were compared against the artificially created illumination pattern. Figure 3.15 shows the difference calculated between the predefined illumination pattern and the illumination component obtained with different types of Daubechies wavelets. As it can be noticed from the images, there are some artefacts introduced by the wavelet decomposition, which can be defined as horizontal/vertical stripes (DB3, DB6, DB10) and checkerboard pattern (DB3, DB45). Wavelet coefficients are calculated using iterative discrete operations with the non-ideal high and low-pass filters. Therefore, aliasing can appear. IDWT cancels aliasing as long as the coefficients are not changed. The idea of illumination correction using wavelet

transform is based on changing the low-pass band information of the image with no changes over the reflection component (high frequencies). But the recovered image is obtained using both approximation coefficients and detailed coefficients; therefore, it is obvious that changing the coefficients in the approximation sub-band to a constant value brings up the same artefacts to the recovered image. Figure 3.16 shows an example of the retinal image reconstructed using DB3, where horizontal and vertical stripe artefacts are apparent.

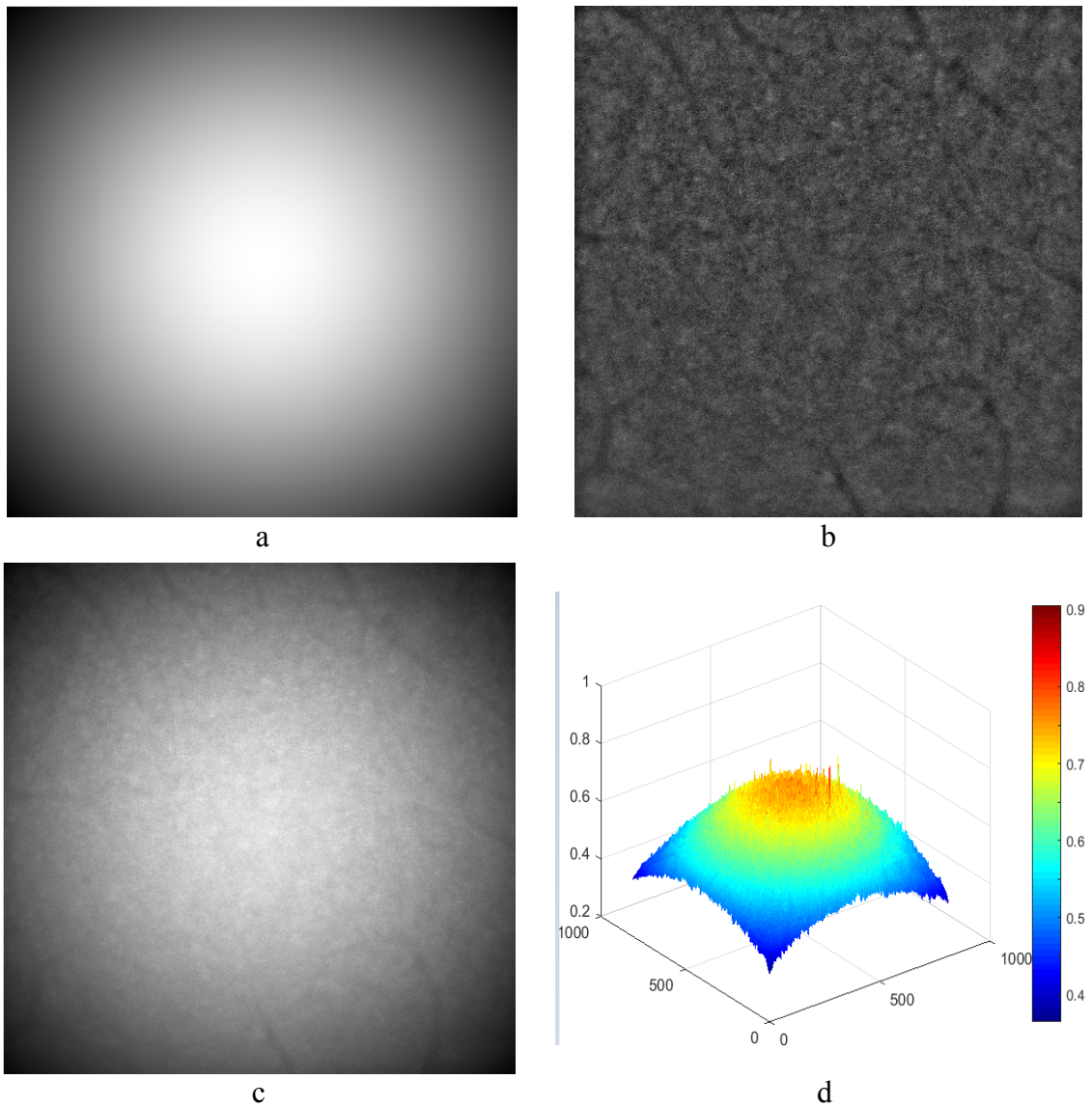


Figure 3.14: (a) Predefined illumination pattern; (b) high-resolution retinal image with no illumination background; (c) retinal image (b) multiplied with the illumination pattern (a) and (d) its surface plot.

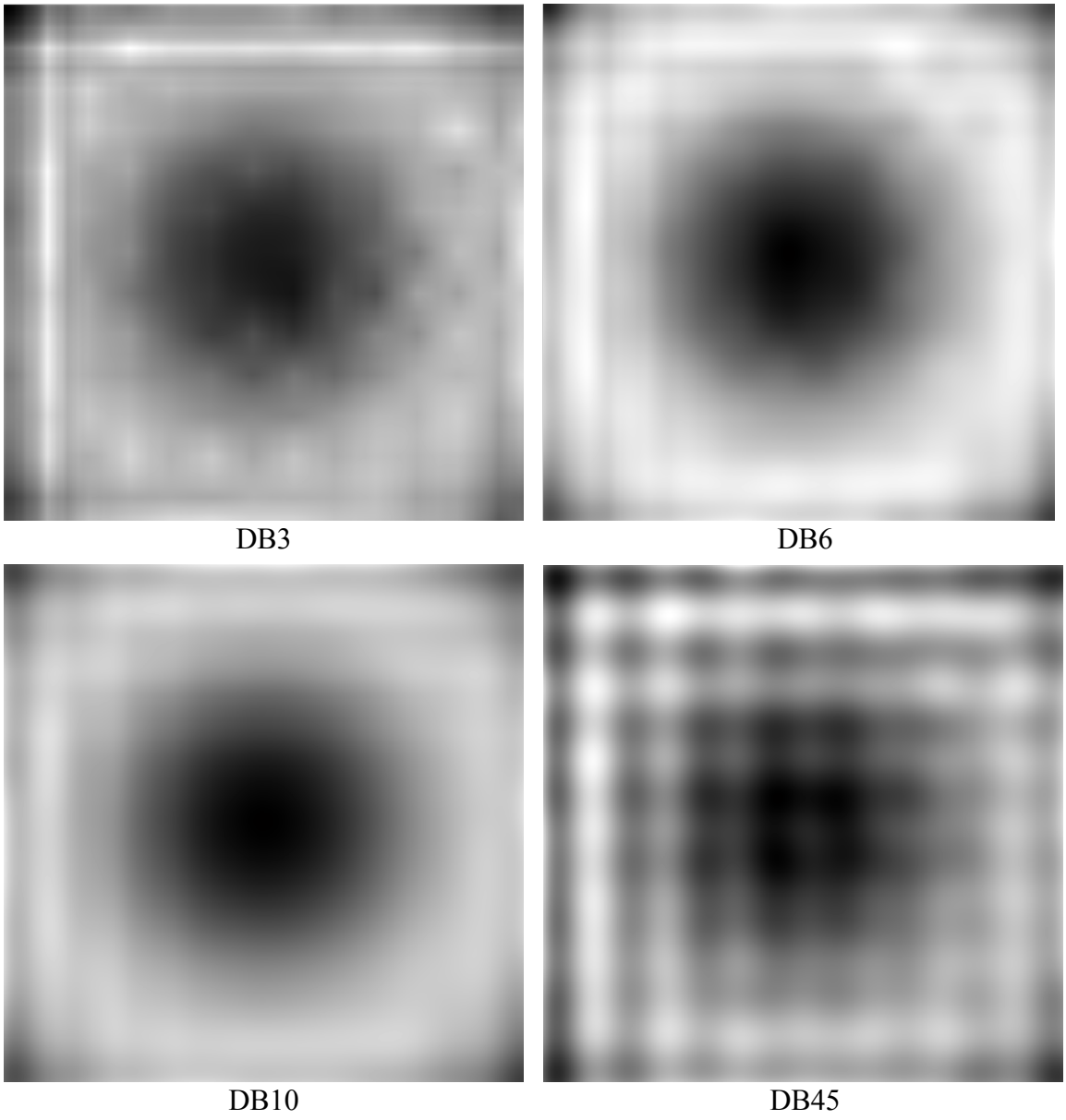


Figure 3.15: Difference between the predefined illumination pattern and illumination estimated using approximation coefficients at level 6 obtained with different types of Daubechies wavelet transform.

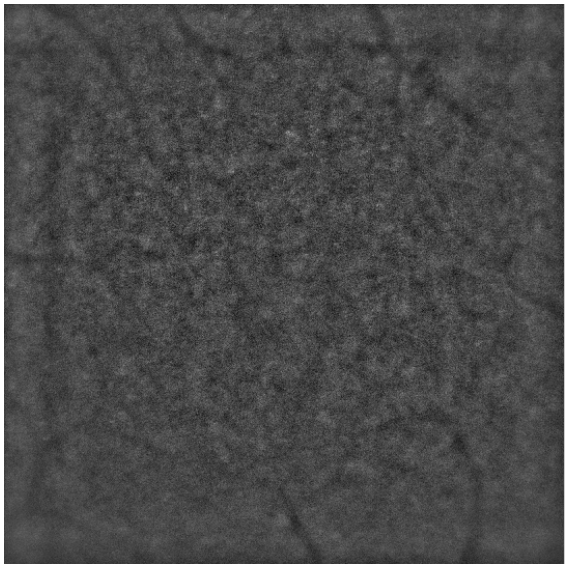


Figure 3.16: Retinal image reconstructed using DB3 showing horizontal and vertical artefacts.

IV. Wavelet-Fourier Filtering

Münch et al. [220] proposed a combined wavelet-Fourier filter for elimination of horizontal and vertical stripes in images. If an image impaired with vertical and horizontal lines is decomposed using wavelet transform, the information from vertical and horizontal stripes will concentrate in the vertical sub-band components HL_i and horizontal sub-band components LH_i at different resolution scales, accordingly. After applying the 2D Fourier transforms to these bands, the information of the striping noise will be completely condensed to the abscissa for vertical stripes and to the ordinate for horizontal stripes. By eliminating the Fourier coefficients at the abscissa and ordinate, the entire information arising from ideal vertical and horizontal stripes will be erased. For this purpose, vertical and horizontal components are transformed to frequency domain and multiplied with the Gaussian damping functions:

$$g(x,y) = 1 - \exp\left(-\frac{x^2}{2\sigma^2}\right) \text{ and } g(x,y) = 1 - \exp\left(-\frac{y^2}{2\sigma^2}\right). \tag{3.23}$$

The standard deviation σ defines the width of the filter in x and y-directions, accordingly, and is selected based on the spatial frequency spectrum of the stripes in vertical and horizontal directions, which correlates with the stripe width. At each level of decomposition, the Fourier transformed vertical and horizontal sub-band components of the image are

multiplied with the Gaussian functions (Figure 3.17). In this way, the coefficients close to the x and y-axis in the Fourier domain are eliminated. The recovery process is performed using inverse FFT (IFFT) and IDWT.

Figure 3.18 and Figure 3.19 illustrate this algorithm. For the presentation purposes, the wavelet-Fourier filter was applied to the illumination component of the retinal image, reconstructed from approximation coefficients. As the background image is smooth, the artefacts are more apparent. In the proposed framework, the wavelet-Fourier filter (with σ=2) is applied to the retinal image obtained after wavelet-based illumination correction (Figure 3.20).

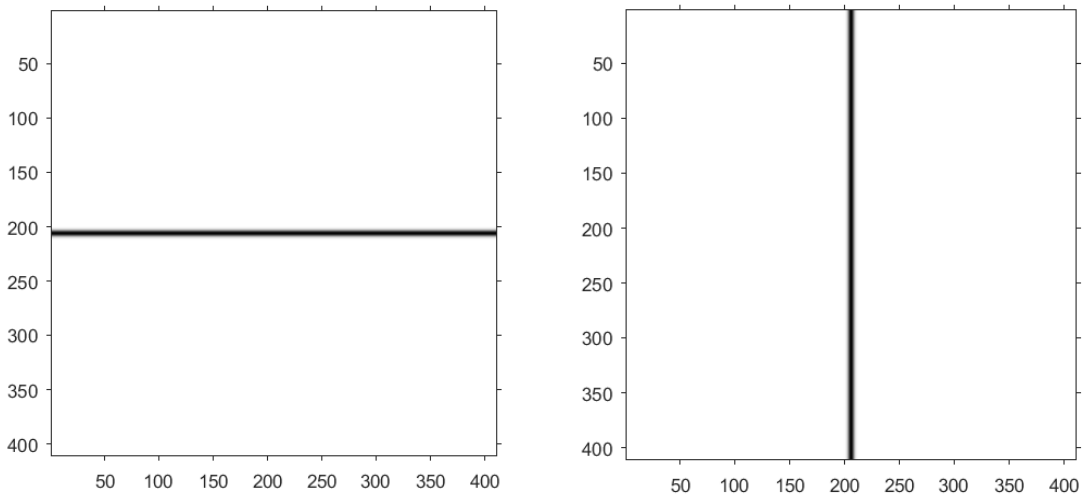
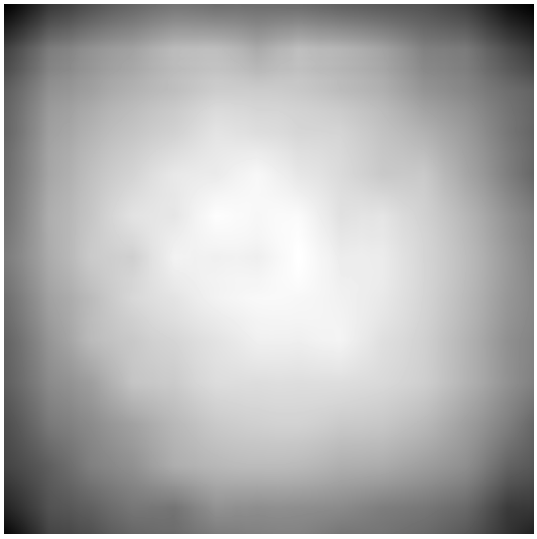
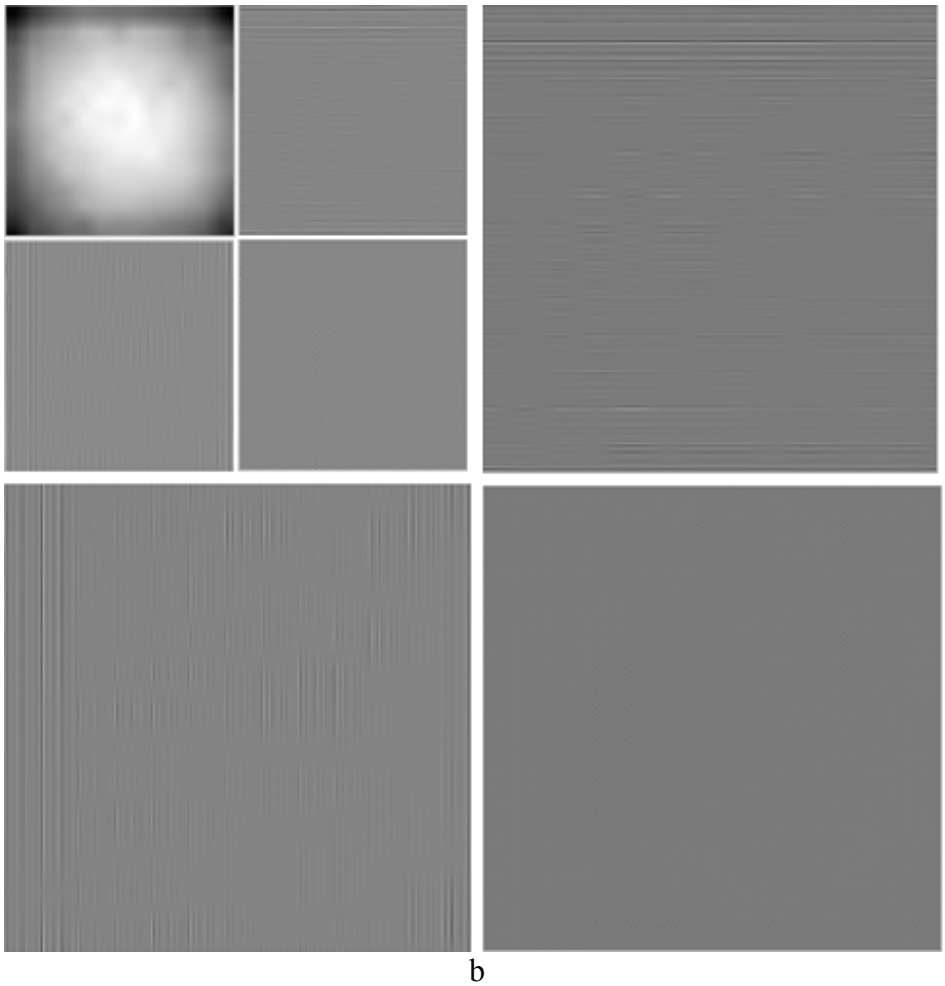


Figure 3.17: Gaussian filter used for eliminating the Fourier coefficients (a) at the abscissa for vertical stripes and (b) at the ordinate for horizontal stripes at the second level of decomposition.



a



b

Figure 3.18: Wavelet-Fourier filter applied to the illumination component of the retinal image. (a) Illumination component estimated using approximation coefficients; (b) 2-level wavelet decomposition of (a) showing that vertical and horizontal stripes concentrate in the vertical and horizontal sub-band components, respectively.

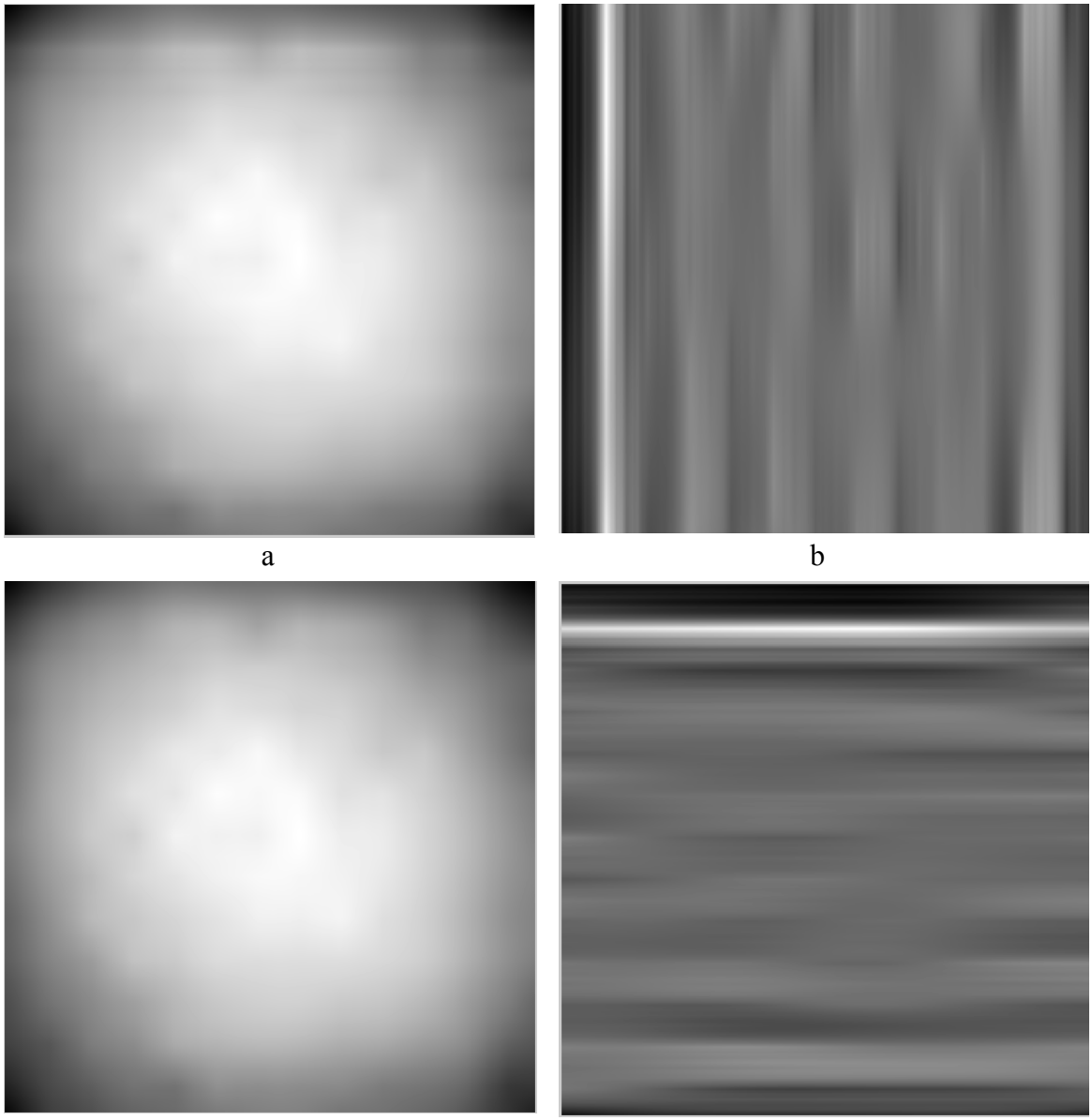
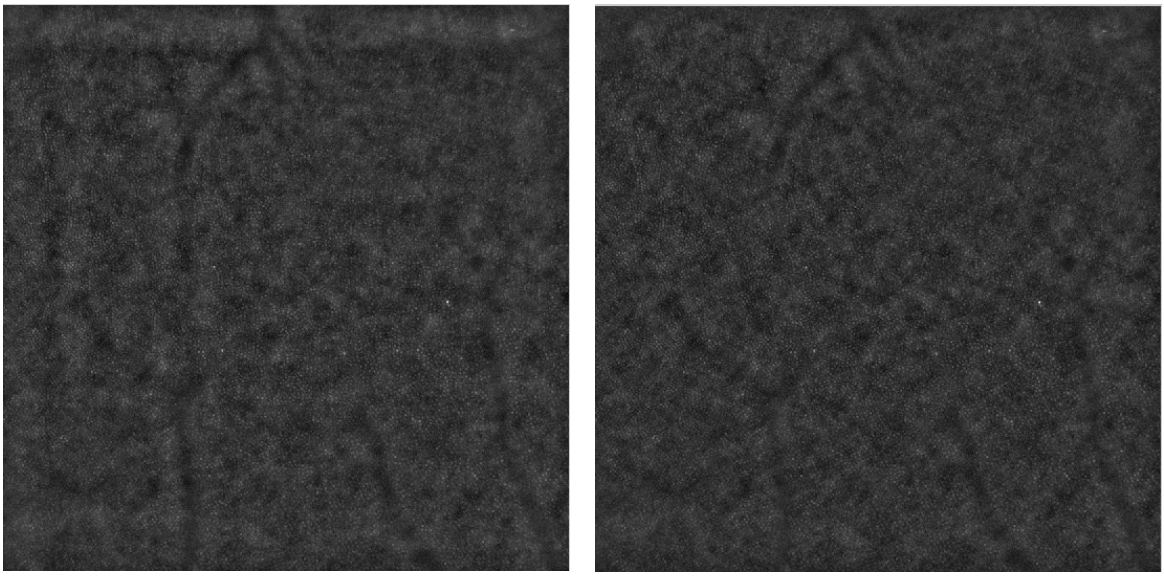


Figure 3.19: Result of wavelet-Fourier filter applied to the illumination component of the retinal image. (a) Illumination component with vertical stripes eliminated using the wavelet-Fourier filter; (b) vertical stripes that have been eliminated; (c) illumination component with horizontal stripes eliminated using the wavelet-Fourier filter; (d) horizontal stripes that have been eliminated.



a b

Figure 3.20: High-resolution retinal image (a) before and (b) after applying the wavelet-Fourier filter.

Experimentally it was established that DB10 introduces smoother vertical and horizontal artefacts on the reconstructed retinal image. Moreover, the image processed with DB10 yields a slightly higher sharpness for the restored retinal image. Therefore, in the proposed image processing framework DB10 wavelet is chosen for correcting uneven illumination where the level of decomposition is found automatically as a function of homogeneity and brightness variation.

3.4.6 Results of Uneven Illumination Correction

I. Visual Comparison of Uneven Illumination Correction Methods

An effective retrospective shading correction method compensates for the illumination component of the image without corrupting its information content. Figure 3.21 presents the results of illumination correction using four different methods: wavelet-based filtering, low-pass filtering and division, low-pass filtering and subtraction and homomorphic filtering. Even by visual comparison with the original unprocessed image, it can be seen that most of variation in the background illumination has been removed by all four methods.

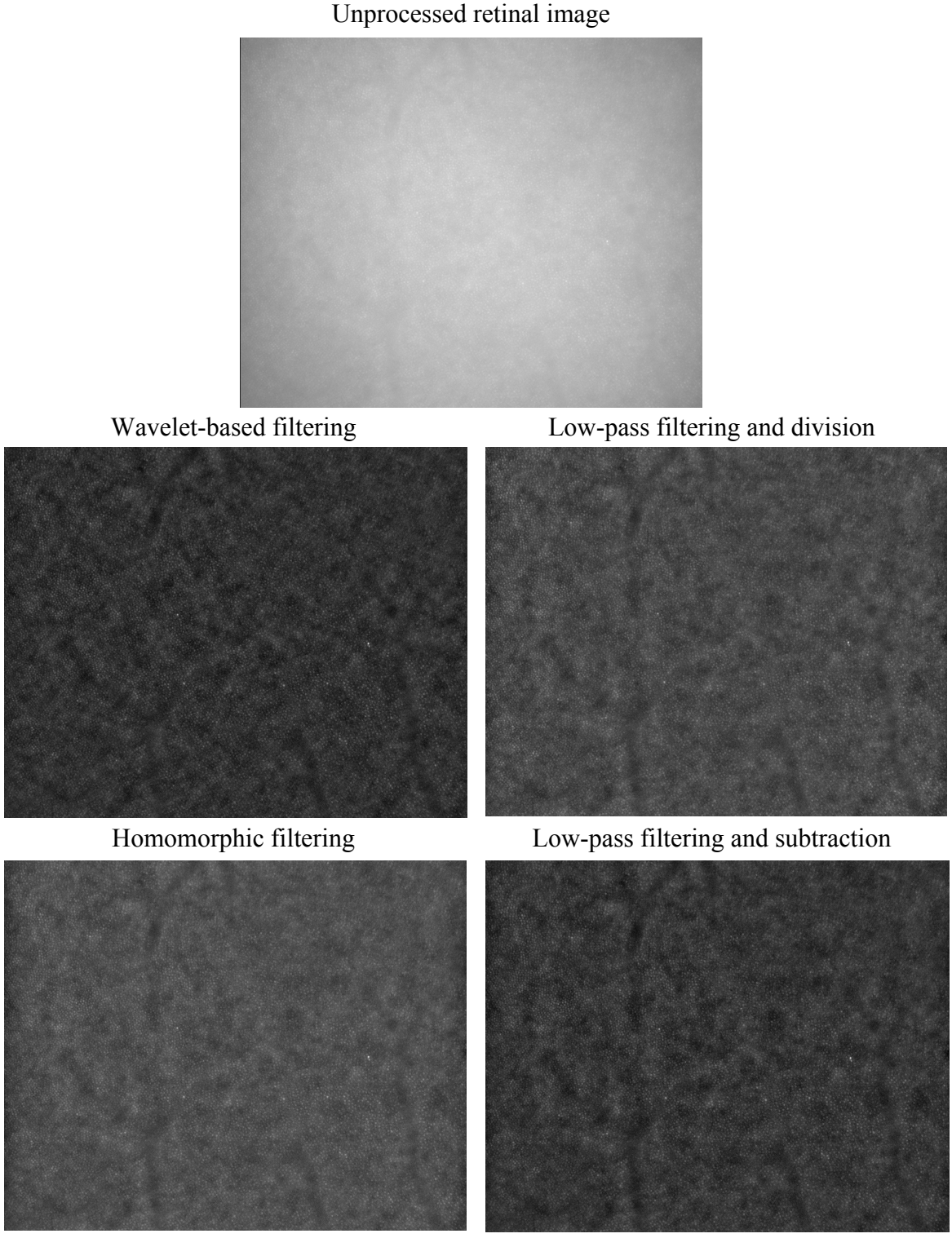
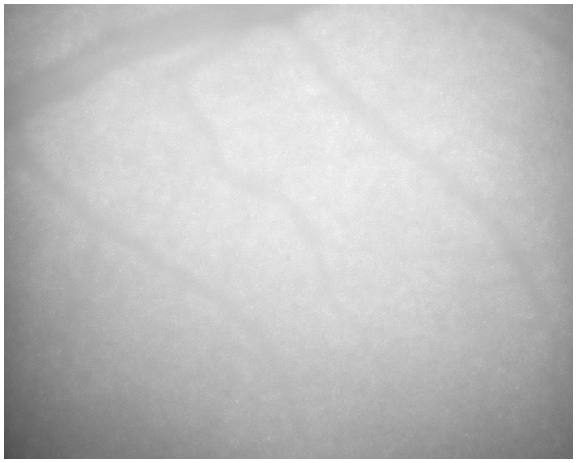
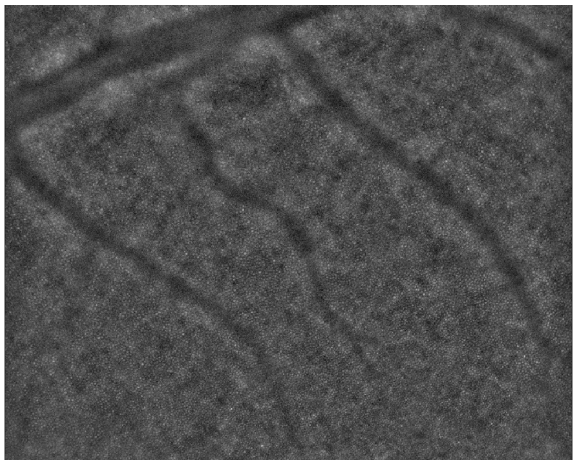


Figure 3.21: Results of illumination correction showed on a section of high-resolution retinal image using four methods: wavelet-based filtering, low-pass filtering and division, homomorphic filtering, low-pass filtering and subtraction.

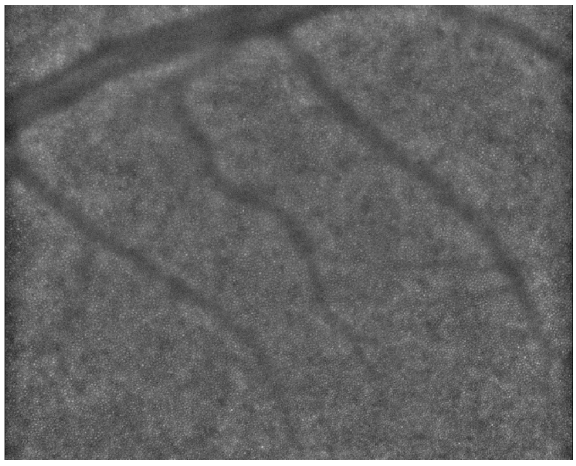
Unprocessed retinal image



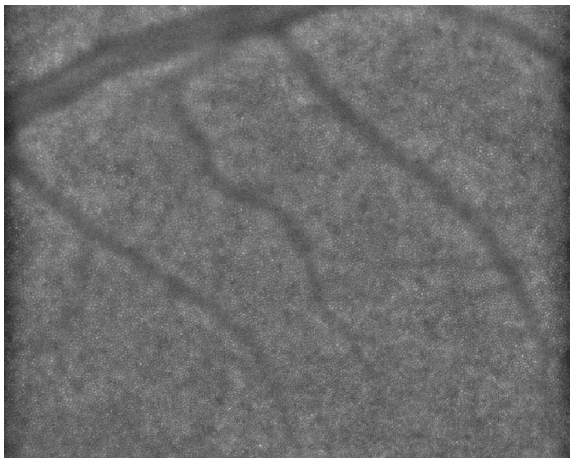
Wavelet-based filtering



Low-pass filtering and division



Homomorphic filtering



Low-pass filtering and subtraction

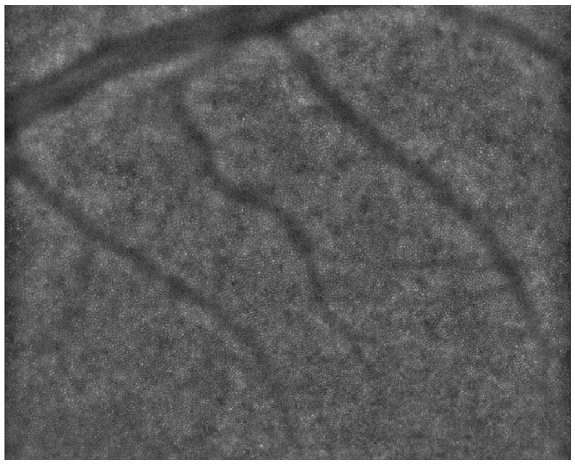


Figure 3.21 (Cont.): Results of illumination correction showed on a section of high-resolution retinal image using four methods: wavelet-based filtering, low-pass filtering and division, homomorphic filtering, low-pass filtering and subtraction.

Based on the surface plots in Figure 3.22 it can be concluded that the background of the resulting images became even after illumination correction performed by the four methods. The corresponding averaged intensity profiles in Figure 3.22 reveal the differences in illumination correction methods. The wavelet-based approach together with the method based on low-pass filtering and subtraction seem to remove background of a higher intensity in comparison with the rest of the methods, which yields a darker resulting image. The wavelet-based approach resulted in the highest range of intensity variations (peaks) in the average intensity profile. These peaks are the cumulative sum of the photoreceptor cones. This becomes clear if calculations of the image sharpness are considered (Figure 3.24). Given these results, it would be reasonable to presume that this method will facilitate better discrimination of cones for further segmentation and counting routines.

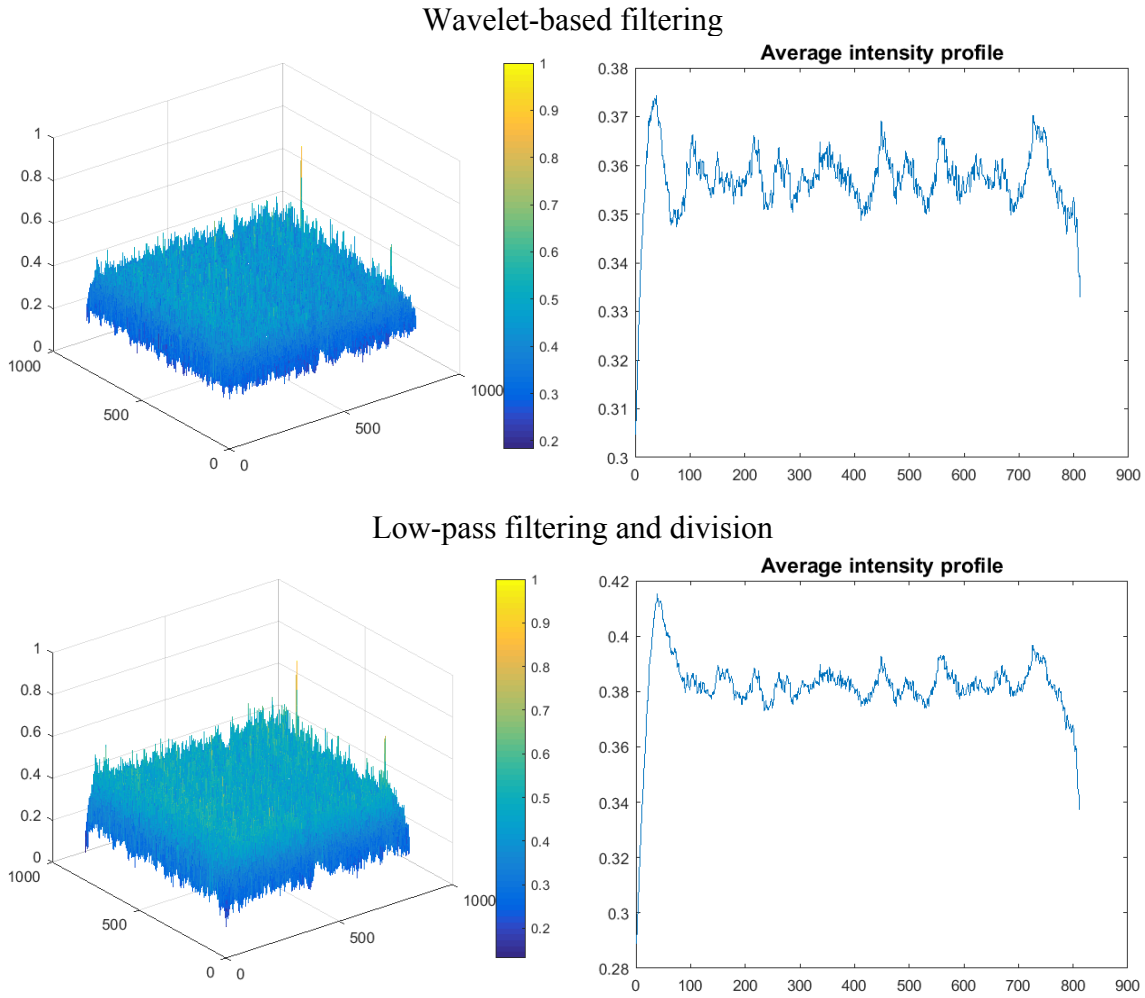


Figure 3.22: Surface plots and corresponding intensity profiles of retinal image processed by four different illumination correction methods.

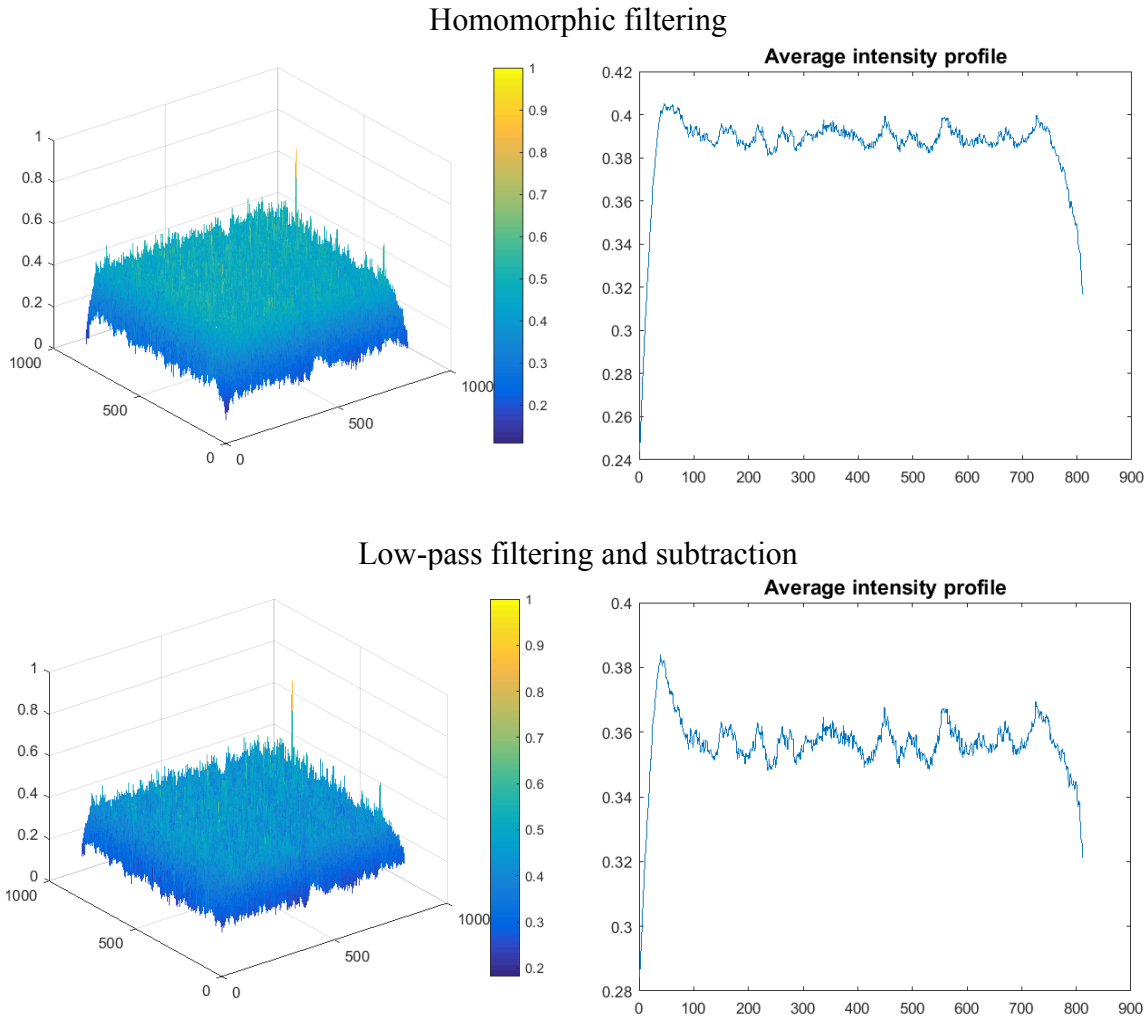


Figure 3.22 (Cont.): Surface plots and corresponding intensity profiles of retinal image processed by four different illumination correction methods.

II. Quantitative Assessment of Uneven Illumination Correction Methods

In order to compare different illumination correction methods and choose the appropriate scheme for our retinal image processing framework, a valid quantitative measure for evaluation of the performance of illumination correction is required.

Local brightness variation [218] introduced in the Subsection 3.4.5 is one of the measures that is used in order to quantitatively validate different methods of illumination correction. This measure is interpreted as the average amount of variation in each section of the image over the entire image. A lower value of local brightness variation corresponds to a more uniform image luminosity, and therefore it is expected that a successful illumination

correction would be associated with a reduction in the value of σ_i (Equation (3.21)). Calculating this measure for the four different illumination methods demonstrated that the wavelet-based approach provides the smallest value of local brightness variation than the rest of the methods (Figure 3.23).

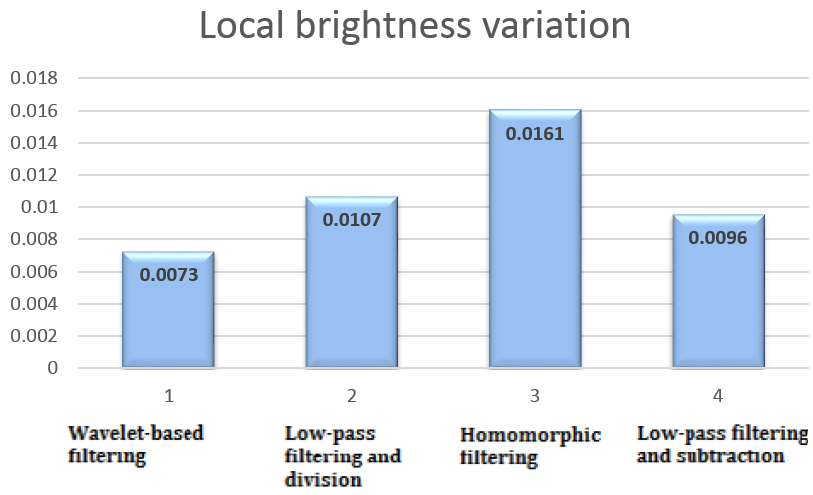


Figure 3.23: Local brightness variation of the images obtained with different methods of illumination correction.

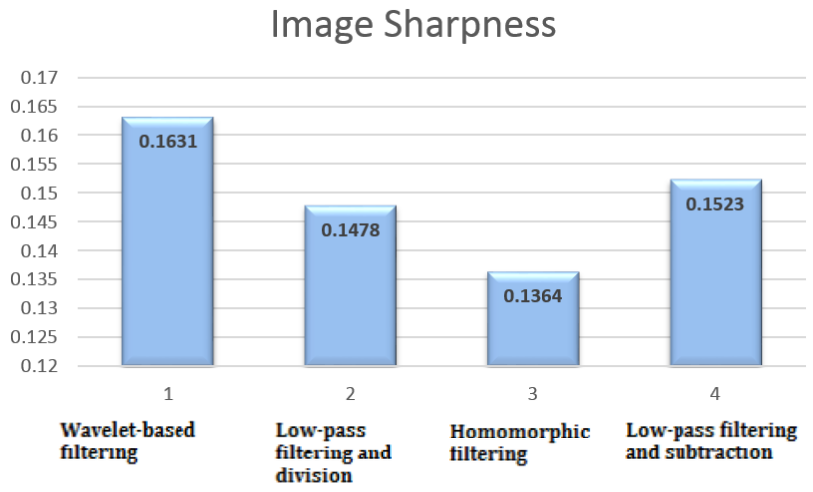


Figure 3.24: Sharpness measure of the images obtained with different methods of illumination correction.

A sharpness measure can be also used to evaluate the performance of the illumination correction methods. It is expected that successful illumination compensation increases the contrast between the object edges and the background, thus the sharpness of the image will

be improved. In Figure 3.24, wavelet-based filtering again provided the optimum results, showing the highest sharpness measure amongst the methods. To confirm the obtained results, this analysis was repeated for 10 different retinal images processed with four illumination correction methods (Table 3.2). Based on these calculations, the wavelet-based approach proved to be the most suitable method for correcting illumination in retinal images.

	Local brightness variation	**Sharpness measure**
Wavelet-based fileting	0.0162	0.2699
Low-pass filtering and division	0.0425	0.1887
Homomorphic filtering	0.0475	0.1732
Low-pass filtering and subtraction	0.0339	0.2191

Table 3.2. Performance evaluation of four illumination correction methods in terms of local brightness variation and sharpness measure averaged for 10 retinal images.

Overall, the results of shading correction show that all four methods significantly reduce uneven illumination present in raw high-resolution retinal images. The wavelet-based approach as well as low-pass filtering and subtraction correct retinal images better than other two methods, based on the quantitative measures of local brightness variation and sharpness. This implies that shading in high-resolution retinal images is mainly additive. Since the study indicated that the wavelet-based approach provided the best results according to the chosen metrics, we use this method to correct for uneven illumination in the proposed retinal image processing framework. As described in Subsection 3.4.5, it was found that Daubechies wavelets of type DB10 provide a good illumination correction with minimum artefacts introduced during the reconstruction of the image. Using the function of homogeneity and local brightness variation it is possible to automatically find the level of decomposition appropriate for approximating the background for each dataset. Additionally, a wavelet-Fourier filter is applied to the reconstructed retinal images in order to eliminate vertical and horizontal artefacts corrupting the retinal image content.

3.5 Noise Reduction

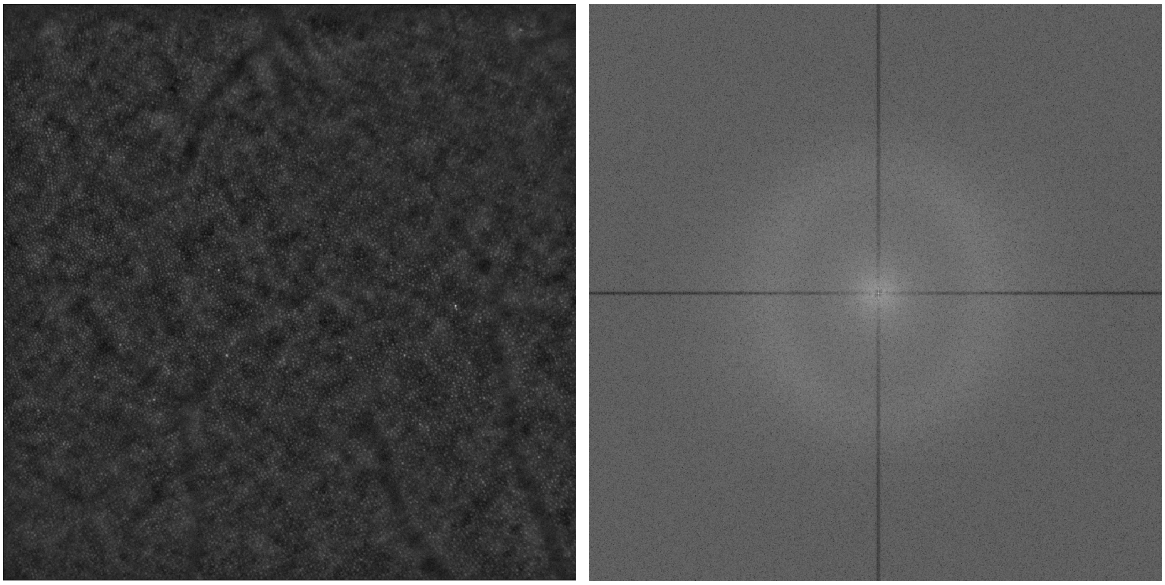
In an AO imaging system, there are many sources of noise that affect the quality of acquired retinal images. Correcting for uneven illumination is not sufficient to restore the true image signal; therefore, additional noise suppression methods should be included in the image processing framework.

Rao et al. [137] described the noise in retinal images acquired with an AO flood-illuminated instrument as a "combined" type of noise and assumed that it is additive. To estimate the noise intensity, a small section in the background of retinal image was cropped. The histogram of this area showed a Gaussian distribution. Therefore, it can be summarized that the noise model in AO instrument is an additive Gaussian noise.

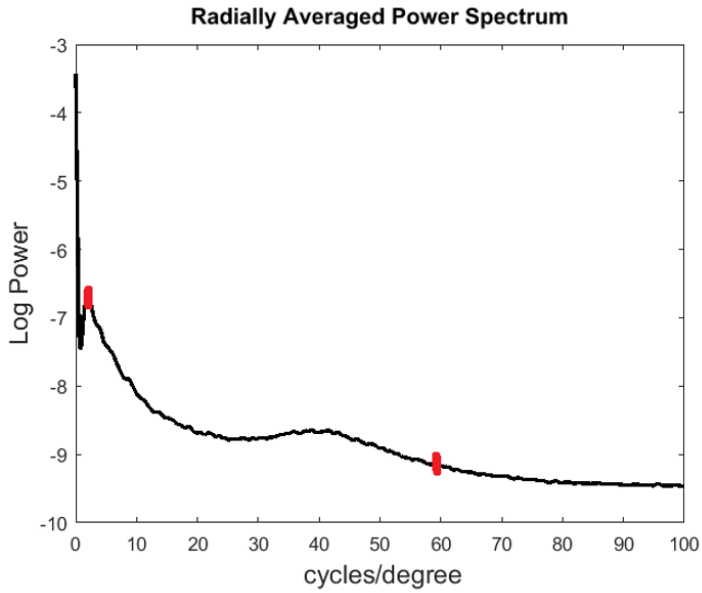
In this study, a frequency method is used in order to increase contrast and remove high-spatial-frequency noise. The choice of cut-off frequencies is very important in this processing step, as incorrect estimation of the spatial frequency of imaging objects can amplify the level of noise in the image. In high-resolution retinal images, the cone is the smallest object to be imaged; therefore the information beyond the cones' frequencies correspond to noise which should be filtered out. For the human eye, the spatial frequency of photoreceptor cones can be estimated based on the angular size of the photoreceptor cells, θ, as follows [137]:

$$f_c = \frac{1}{\theta} = \frac{1}{2\arctan(\frac{d_{cone}}{2\,F_{eye}})} * \frac{\pi}{180^\circ} \cong \frac{2F_{eye}}{d_{cone}} * \frac{\pi}{360^\circ} = \frac{2F_{eye}\tan 0.5^\circ}{d_{cone}} \left(\frac{cycles}{degree}\right), \quad (3.24)$$

where F_{eye} is the magnitude of the front focal length of the test human eye and d_{cone} is the photoreceptor cell diameter. F_{eye} is set to 17 mm, which is an average focal length for human eye. The photoreceptor cell diameter depends on the retinal eccentricity, where the image was taken. For the retinal images acquired at 1–4° eccentricity from the fovea, the cone diameter varies between 3–8 μm [30], which corresponds to 2–5 pixels (the camera pixel resolution is 1.6 μm). Therefore, the corresponding photoreceptor cell spatial frequencies are in the range of 40 – 100 cycles/degree or 0.2 – 0.49 cycles/pixel.



a b



c

Figure 3.25: Calculation of cut-off frequencies for the band-pass filter. (a) High-resolution retinal image after illumination correction; (b) its power spectrum, and (c) radially averaged power spectrum with cut-off frequencies for the Gaussian band pass filter shown with red markers.

Modal frequency of the cone mosaic can be estimated by analysing retinal images in Fourier domain [221]. Yellott [222] discovered that the power spectrum of the retinal mosaic has an annular appearance. The radius of this annulus corresponds to the modal frequency of the cone mosaic. This method was successfully used by Cooper et al. [223] to estimate the cell spacing in retinal images. The following correlation has been observed in Yellott's ring: the

power spectrum from more irregularly packed mosaics has a ring with a wider cross-sectional profile than that from more uniformly packed mosaics.

Figure 3.25-a and b shows the high-resolution retinal image after illumination correction and its power spectrum. In Figure 3.25-b, the dark lines along the abscissa and ordinate are the results of wavelet-Fourier filtering performed at previous stage for eliminating the vertical and horizontal stripes. Due to a relatively irregular cone mosaic, the power spectrum is characterized by a wide Yellott's ring. In Figure 3.25-c, a radially averaged power spectrum is shown, where Yellott's ring is represented by a small bump centred around 40 cycles/degree.

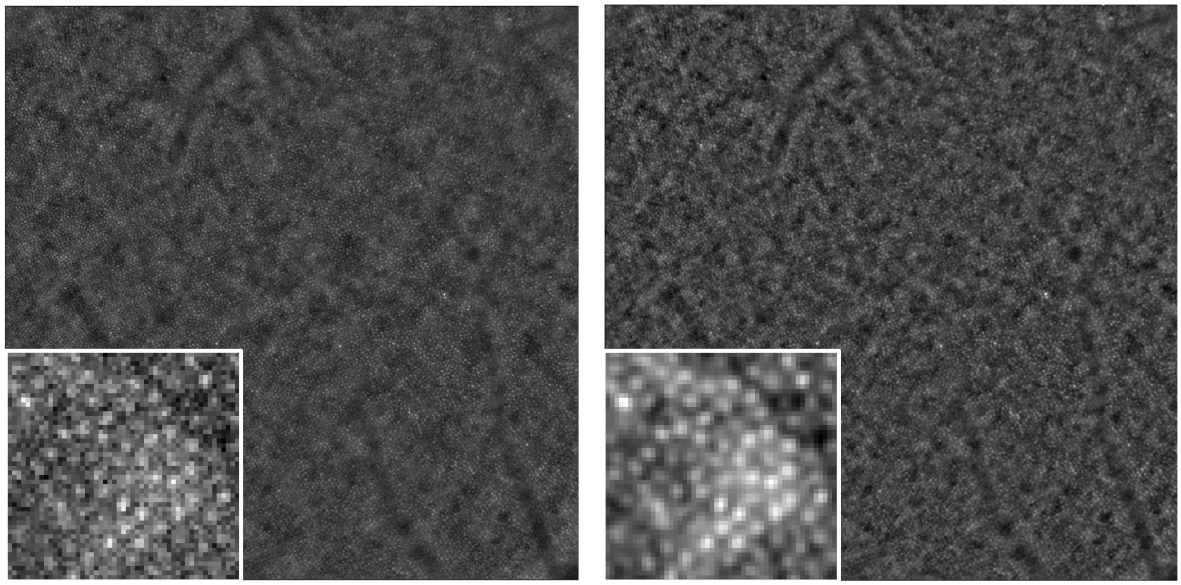
The Gaussian band-pass filter is employed to suppress high frequency noise, above photoreceptor cell stop frequency and enhance the image energy, within the start frequency. The Gaussian filters are rotationally symmetric filters with a smooth attenuation of desired frequencies. Moreover, Gaussian filters have weights specified by the probability density function of a bivariate Gaussian, or normal distribution which give higher significance to pixels near the edge, therefore reducing edge blurring [224]. These properties make the Gaussian filter a suitable choice for denoising retinal images. Since the retinal eccentricity is known based on the imaging protocol, the corresponding scale of photoreceptor cells d_{cone} can be found using the histological data of Curcio et al. [30]. Using Equation (3.24), we estimate the cone stop frequency which corresponds to the outer edge of Yellott's ring. Depending on the eccentricity where the image was taken, the stop frequency of the photoreceptors will vary. In the work of Cooper et al. [223], the inner edge of Yellott's ring was used for estimating the dominant low frequency of photoreceptor cells. However, in retinal images with a larger field of the view apart from photoreceptor cells, there are other large scale objects, such as vessels. Therefore, in the Fourier domain slow variations in intensity corresponding to the blood vessels are represented by the frequencies lower than the inner edge of Yellott's ring. This information is valuable and should not be discarded. After illumination correction, low frequency variation corresponding to the illumination component of the raw image has been removed from the image, resulting in a sharp cut of low frequencies. The peak located right after these frequencies is supposed to indicate the start point of the frequencies corresponding to the large scale variations. This point can be used as the start frequency for the Gaussian band pass filter and can be easily found from the plot of radially averaged power spectrum (Figure 3.25-c).

Figure 3.26 illustrates the result of band-pass filtering on four different retinal images which were corrected for uneven illumination. For visualization purposes, brightness of the images was increased. Qualitative comparison of the images before and after applying the Gaussian band-pass filter reveals that this process supressed the noise and improved the visibility of retinal features. However, the calculated BM_1 measure showed that image sharpness has been slightly decreased after the denoising step. This happens due to smoothing introduced by the Gaussian band-pass filter, which reduces the noise and thus the amount of edges detected by the Sobel operator. In order to evaluate the amount of noise suppressed during this stage, the Power Spectral Ratio was additionally calculated as a function of the frequency between the images before and after image denoising (Figure 3.27). A ratio greater than one indicates a higher spectral power for the images after noise suppression, at a given frequency. Overall, the improvement is within the range of cut-off frequencies; beyond the cut-off frequencies, the ratio is less than one, indicating that the high-frequency noise has been suppressed.

Retinal images after illumination correction

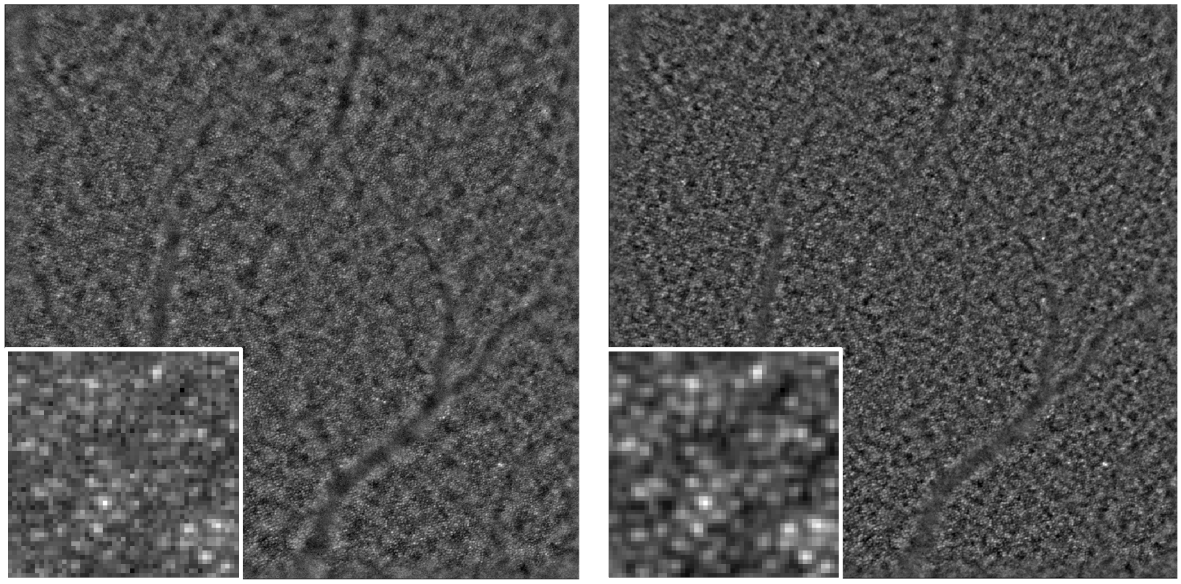
Retinal images after noise suppression

Retinal dataset 1



$BM_1 = 0.1631$ $BM_1 = 0.1244$

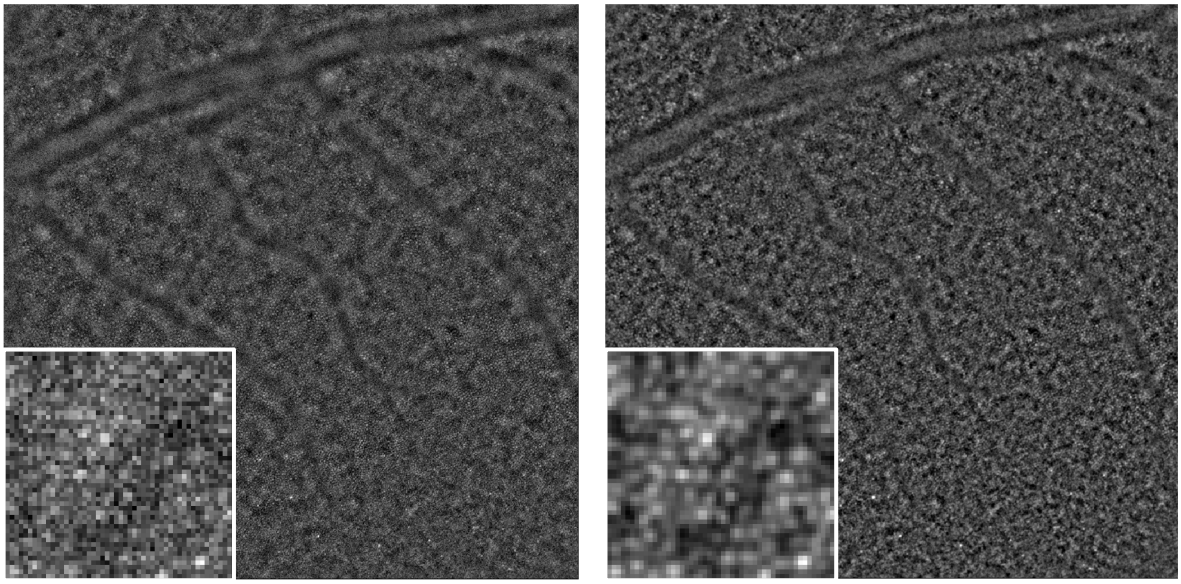
Retinal dataset 2



$BM_1 = 0.2028$ $BM_1 = 0.1701$

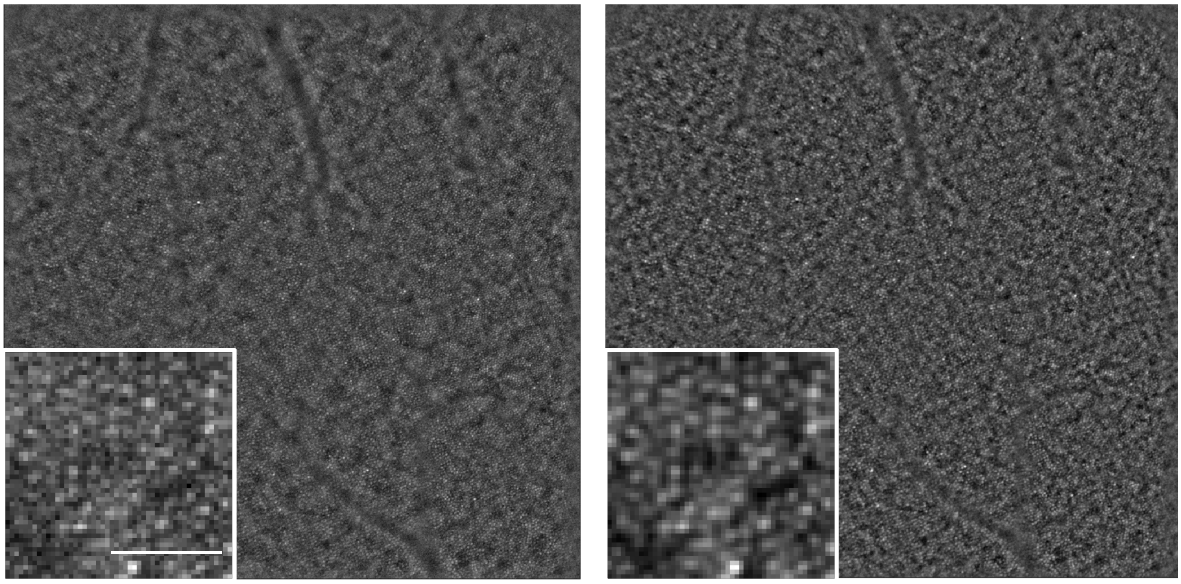
Figure 3.26: Retinal image frames before (left) and after noise suppression (right) in four representative datasets. The scale bar is 40 μm.

Retinal dataset 3



$BM_1 = 0.2891$ $BM_1 = 0.2082$

Retinal dataset 4



$BM_1 = 0.2065$ $BM_1 = 0.1753$

Figure 3.26 (Cont.): Retinal image frames before (left) and after noise suppression (right) in four representative datasets. The scale bar is 40 μm.

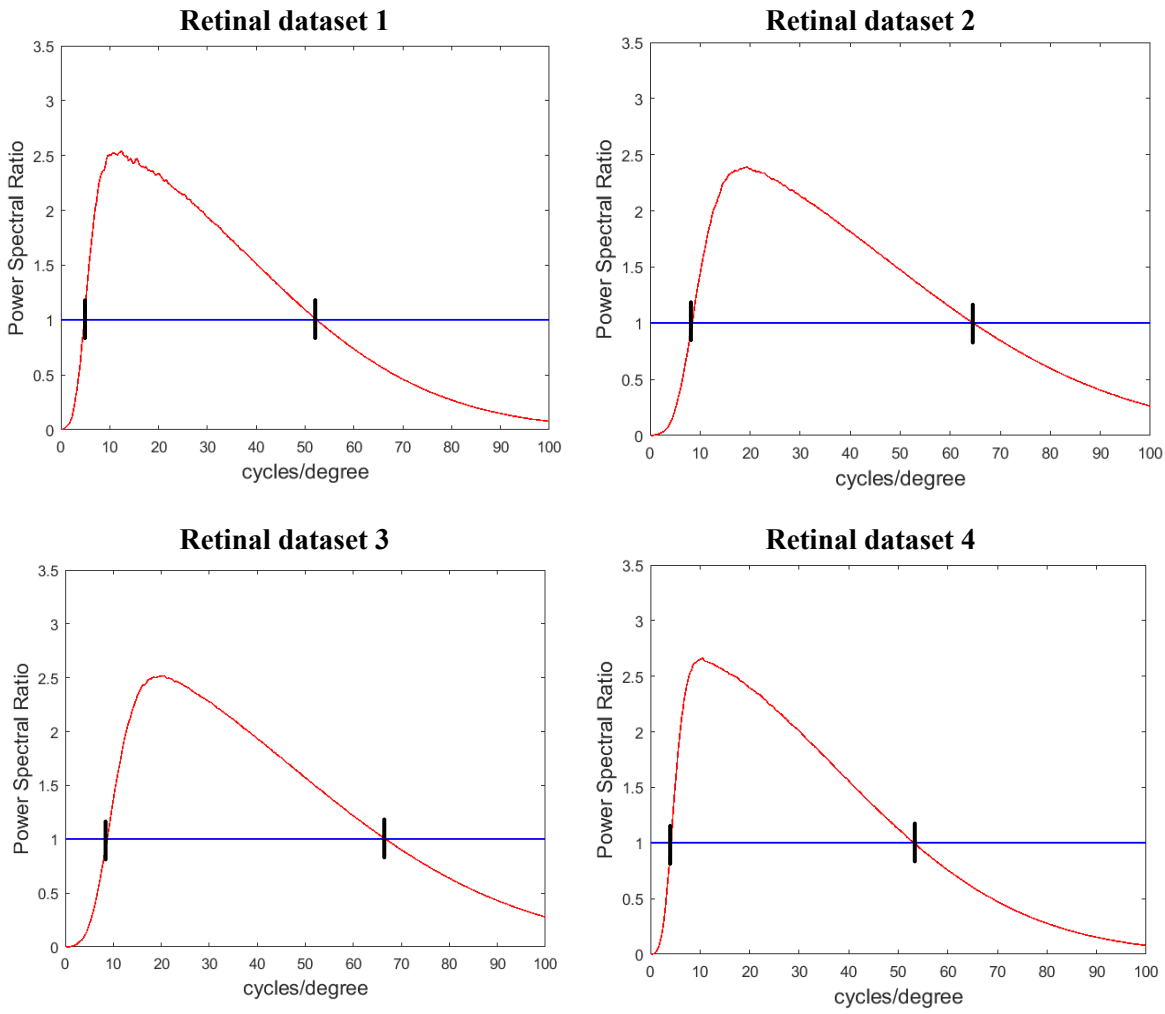


Figure 3.27: The spectral power ratio of the retinal images before and after image denoising. Black lines show the cut-off frequencies in the band-pass filter.

3.6 Image Registration

3.6.1 Introduction

The AO flood-illuminated instrument, rtx1, requires approximately four seconds for acquiring a retinal dataset of 40 frames. Despite fast acquisition, there are still geometric transformations in the acquired dataset due to fixational eye movements. Image registration is used to calculate the performed geometric image transformations and obtain a high quality image from multiple copies of the same retinal location. Moreover, registration of the images captured at different retinal eccentricities allow for a wide field-of-view which may assist

clinicians in visual inspection of a larger area of the patient's retina. Registration of the retinal images acquired at different times can help clinicians in tracking the progression of the patient's disease as well as monitoring the efficacy of specific therapy. Therefore, image registration is an essential image processing tool for the analysis of high-resolution retinal images which allows improvement in the image quality as well as facilitates patients' treatment process.

Mathematically, the registration process represents a mapping function T, which establishes spatial correspondence between the coordinates of the test image I_T and the reference image I_R, taken potentially at different times, from different viewpoints, and/or by different sensors. After a transformation function is found, it is applied to the test image in order to map the spatial coordinates onto the reference image such that [139]:

$$I_R(x', y') = T\{I_T(x, y)\}, \tag{3.25}$$

where (x', y') and (x, y) are the coordinate spaces of the reference and test images, respectively.

As discussed earlier, in high-resolution retinal images, due to multiple sources of noise and rapid eye motions, the quality of single frames may vary within an image sequence. Image registration does not only correct for the motion between the frames, but also compensates for the thermal and speckle noise. After the transformation model is applied to the sequence of frames, the final image of a higher contrast is produced by averaging co-registered frames.

A rigid transformation model is used to calculate the transformation function between the retinal frames. We consider scaling as a minor transformation that does not cause any distortions in the registration process, therefore in this study the transformation model consists of translation and rotation only. In order to establish spatial correspondence between the pair of retinal images, the Phase-Only Correlation (POC) similarity metric [225] is used. Phase correlation is a robust and computationally effective metric. It can be used for noisy images as it is resilient to changes in spectral energy as well as changes in brightness. Despite this, as a correlation technique, POC may fail if the reference and test images have large scale and rotation variations [225]. To this purpose, the registration process is divided into coarse and fine stages. At the coarse stage, translation parameters are calculated with sub-pixel accuracy using POC. At the fine stage, the Procrustes algorithm is employed to refine

the transformation model. By minimizing a least-squares criterion between reference and input image, rotation and remaining finer translation parameters are found.

3.6.2 Coarse Registration

During the coarse image registration stage, the POC technique is used to determine translation parameters between retinal frames. Let I_T be a translated replica of a reference image I_R , then I_T and I_R are related by the following transformation:

$$I_T(x, y) = I_R\left(\begin{bmatrix} x \\ y \end{bmatrix} - t\right), \tag{3.26}$$

where t – is translation vector: $t = \begin{bmatrix} x_0 \\ y_0 \end{bmatrix}$. Then:

$$I_T(x, y) = I_R(x - x_0, y - y_0). \tag{3.27}$$

The POC similarity metric is based on the Fourier transform and the Fourier Shift Theorem, which states that when a function is translated in the image domain, the magnitudes of its corresponding Fourier representation remain unaltered, but the phases in the frequency domain are translated proportionally to the translation in the image domain. Therefore, the translation vector t can be estimated from the Cross-Power Spectrum.

Let $F_T(\mathrm{u}, \mathrm{v})$ and $F_R(\mathrm{u}, \mathrm{v})$ be the Fourier transform of the test and the reference image respectively, represented as:

$$F_T(\mathrm{u}, \mathrm{v}) = \int_{-\infty}^{\infty} \int_{-\infty}^{\infty} I_T(x, y) e^{-2\pi j(ux+vy)} dxdy \tag{3.28}$$

$$F_R(\mathrm{u}, \mathrm{v}) = \int_{-\infty}^{\infty} \int_{-\infty}^{\infty} I_R(x, y) e^{-2\pi j(u(x-x_0)+v(y-y_0))} dxdy. \tag{3.29}$$

According to the Fourier Shift Theorem $F_T(\mathrm{u}, \mathrm{v})$ and $F_R(\mathrm{u}, \mathrm{v})$ are related by:

$$F_T(\mathrm{u}, \mathrm{v}) = F_R(\mathrm{u}, \mathrm{v}) e^{-2\pi j(ux_0+vy_0)} \tag{3.30}$$

and the Cross-Power Spectrum can be defined as:

$$C(u,v) = \frac{F_R(\mathrm{u},\mathrm{v})F_T^*(u,v)}{|F_R(\mathrm{u},\mathrm{v})F_T^*(u,v)|} = e^{2\pi j(ux_0+vy_0)}\,, \tag{3.31}$$

where * stands for complex conjugate. Taking the inverse Fourier Transform of the Cross-Power Spectrum, the result is a Dirac delta function centred at t, the location of the translation vector. This is mathematically expressed as:

$$\Im^{-1}\{C(u,v)\} = \delta(x + x_0, y + y_0). \tag{3.32}$$

Therefore, the POC is obtained by computing the IFFT of the cross-power spectrum, and the translational vector (x_0; y_0) is determined as the coordinates of the highest peak. Subpixel accuracy of the translation vector is achieved by performing parabolic interpolation of an array with finer sampling around the peak of the cross-power-spectrum [226]. The obtained vector is used as an initial estimate and progressively refined in the next stage of registration.

3.6.3 Fine Registration

At the fine stage of registration, similar to the work of Ramaswamy and Devaney [71], we use tracking of control points in order to calculate the residual displacements between the test and reference images. As control points, the brightest cones in the test and reference image pairs are used. There are various hypotheses with regards to the factors that influence the appearance of the brightest cones, such as molecular differences within the cones and differences in cone outer segment length [4]. From the visual inspection of retinal images of healthy patients, the location of the brightest cones within a dataset doesn't change. This allows us to use the brightest cones as control points at the fine stage of image registration.

It is assumed that the centre of cones can be represented by the brightest pixels; this way the coordinates with the highest intensities are tracked in the test and reference images. In order to refine the position of brightest cones, we crop small windows of size 20x20 pixels centred at the pixels with the highest intensities. Then, these windows are upsampled using parabolic interpolation and refined coordinates of the brightest cones are calculated. The size of the window is used as a distance criterion for finding the putative matches between two sets of cone coordinates in the reference and test frames. After the putative matches are established, the POC is employed to find the additional displacement between the corresponding cone windows. The obtained translation vector is used to refine the coordinates of the brightest cones in the test image. If for the selected control point in the reference frame more than one

cone candidate was found in the test image, the cone candidates with the lowest peak of cross-correlation are discarded.

After two sets of cone coordinates are found, the rotation parameters can be estimated by employing Procrustes alignment. In statistics, Procrustes analysis is a form of statistical shape analysis used to compare the distribution of two or more shapes. In the context of image processing, Procrustes alignment compares two shapes defined by landmark configurations [214]. In this work, landmark configuration is defined by two sets of cone coordinates. If the coordinates of the brightest cones from the reference image are stored in vector Y and corresponding coordinates of the brightest cones from the test image are stored in vector X, then the transformation parameters (rotation R, translation T and scaling C) can be found using the least squares estimation [227] as:

$$e^2(R,T,C) = \frac{1}{N}\sum_{i=1}^{N} \|Y_i - (CRX_i + T)\|^2. \tag{3.33}$$

As mentioned previously, in high-resolution retinal images the scaling parameter C is omitted in the registration process, thus it is set to 1 in Equation (3.33). The translation parameter T between the two shapes is defined by the differences in the coordinates of the control points. The rotation matrix R is given by VU^T, where U and V are obtained by singular value decomposition (SVD) of the matrix XY^T (i.e. $XY^T = USV^T$), where

$$S = \begin{cases} I & ,if\ \det(U)\det(V) = 1 \\ diag(1,1..1,-1), & if\ \det(U)\det(V) = -1, \end{cases}$$

with I denoting the identity matrix.

3.6.4 Lucky Averaging

Typically, after performing the registration the transformed frames are summed together to compensate for the photon and thermal noise and as a result produce a final averaged image with a better contrast. Given that image frames are of similar quality, the more frames used for the averaging, the greater the increase in signal to noise ratio [41]. However, in real time image sequences, image quality usually exhibits slight variations in both temporal and spatial dimensions. The common averaging scheme is frame-based and does not account for the intra-frame variation in contrast. As a result, averaging across the image sequence can

degrade the overall image quality, i.e. produce a final image with a contrast lower than the best images in the dataset.

The so called “lucky averaging” scheme was previously proposed for stellar images taken from a ground based telescope. The method selects only those image frames for averaging in which the atmospheric turbulence along the line of sight is minimal. Thus, this process takes advantage of lucky moments when turbulence has a minimal effect and has therefore been called “lucky imaging”. Huang et al.[41] adopted this method for averaging AOSLO retinal images. Due to the nature of the point-scanning mechanism of AOSLO, the image quality varies both across the dataset as well as within each frame. Thus, including the pixels with the best regional quality allows us to take the best advantage of inter and intra-frame variance and reduces regional variance in the final image.

Unlike in AOSLO, flood-illuminated images are instantaneous and do not measure the retina point-by-point. Nevertheless, the variance in local regions of one image can be attributed to dynamic changes in human eye aberrations such as the tear film, accommodation, local retinal shape changes due to ocular pulse, etc. Thus, this type of averaging can also be beneficial for high-resolution retinal images acquired with the AO flood-illuminated system.

After performing two-stage registration, the co-registered image sequence is analysed. Each image is divided into small blocks which can be considered as short-exposure areas with no intra-region quality variance. Based on the sharpness measure (BM_1), the region quality is evaluated across the image frame and sequence. As a result, a 3D quality measure is built. The final image is remapped by only including those regions that have the highest image quality. In this way, we can take advantage of the local variation in image quality and construct the final image without accumulation of blur in local regions.

3.6.5 Implementation and Results

I. Coarse Registration

The core of the image registration process consists of determining the horizontal and vertical translation vectors between the reference and test images. For this purpose, the FFT of both images is computed, then the cross-power spectrum is calculated and the POC is obtained by computing the IFFT of the cross-power spectrum. Finally, the highest peak is located and

its coordinates define the translation shifts. Figure 3.28-a, b illustrates the result of the cross-power spectrum calculation for the raw images (Figure 3.28-c) and images after illumination compensation and noise suppression (Figure 3.28-d). In this example the test image was translated by 18.5 pixels to the east and 3.7 pixels to the south. Due to noise and intensity variation present in the retinal images, the peak of power spectrum is less distinct (Figure 3.28-a). This can lead to inaccurate estimate of the translation parameters. This problem has been minimized by introducing uneven illumination correction and noise suppression at the previous stages of our image processing framework.

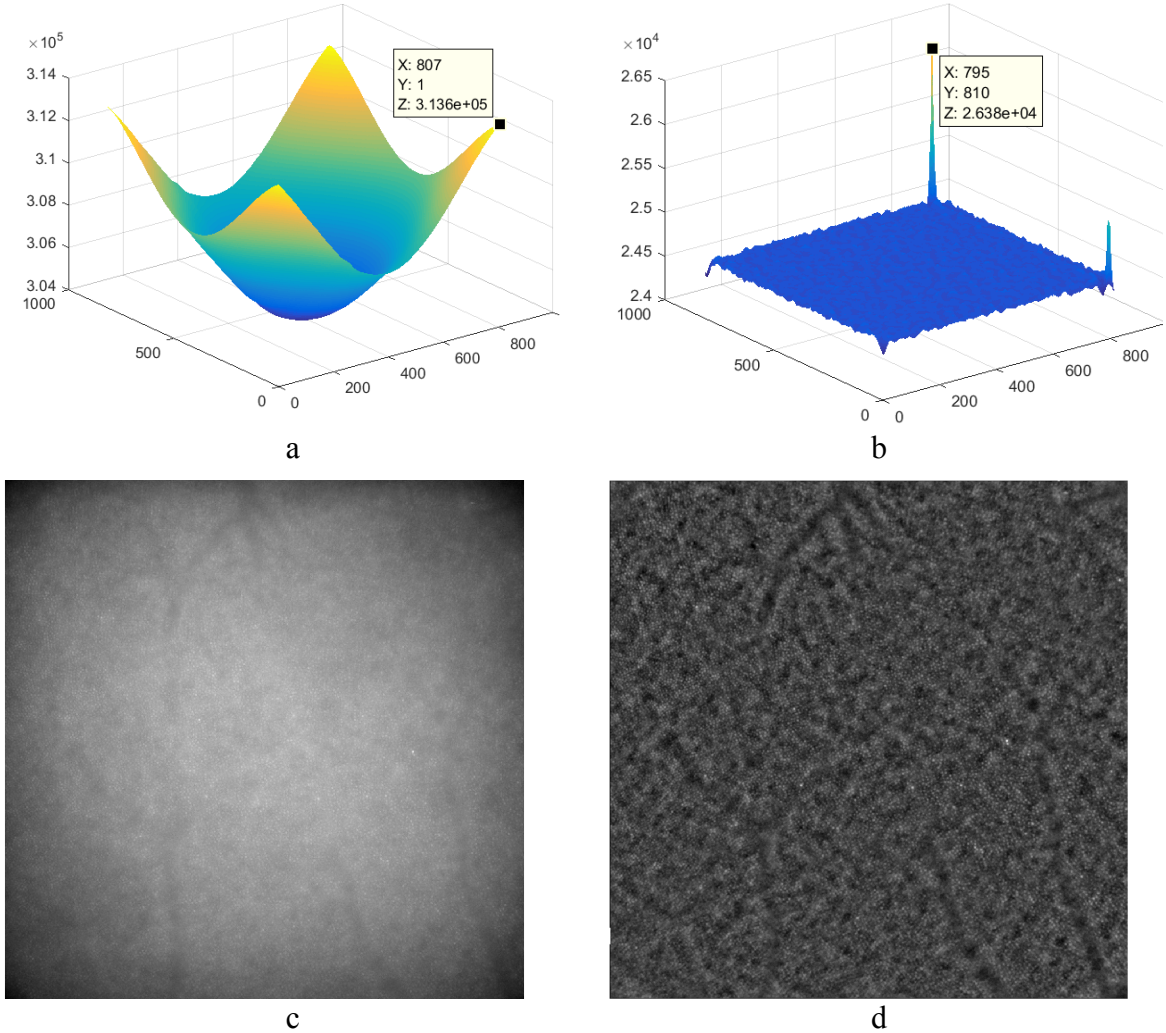


Figure 3.28: (a) Magnitude of cross-power spectrum for raw retinal images (c) and (b) for the images after illumination compensation and noise suppression (d).

The recovered translation parameters serve as an initial estimate and are further refined by upsampling only in a small neighbourhood of that estimate by means of a matrix-multiply

DFT [226]. Based on the new coordinates of the cross-power spectrum, residual translation parameters are found and added to the previous estimate. In this way, subpixel accuracy is achieved (Figure 3.29).

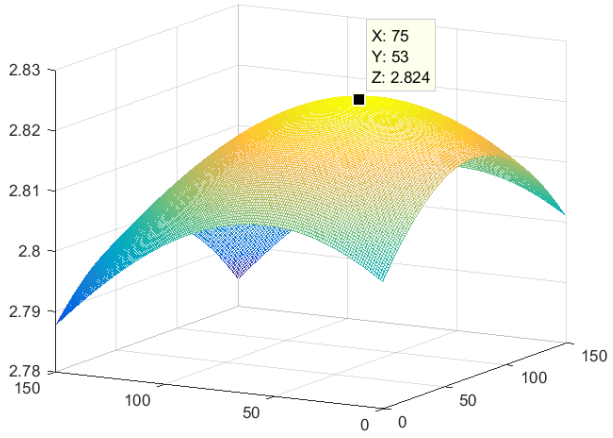


Figure 3.29: Magnitude of the cross-power spectrum interpolated onto an array with finer sampling.

The POC approach was tested by translating the test image by a known amount with subpixel accuracy. The POC approach shows good precision as long as the retinal images have relatively good quality. The average error for 100 predefined shifts, varying from 0.11 to 10 pixels, was found to be 0.01 which is within a range of values 0.002 – 0.02 previously reported in the study of Esteban and Torres [228]. In order to avoid miscalculations of the translation vector, as well as to prevent accumulation of blur at the stage of image averaging, retinal images with critically low quality were excluded prior to performing the coarse registration. The sharpness measure (BM_1), described in Subsection 3.3.1, was used in order to sort retinal datasets in descending order according to their quality (Figure 3.30). The image with the highest score is chosen as a reference frame for the POC registration. At this stage, only frames that do not contain any useful information are removed. The frames which have quality measure lower than the 0.15 quantile of the overall sharpness measure distribution are eliminated from the image sequence. Figure 3.31 gives an example the translation vectors found at the coarse stage of image registration for one of the retinal datasets acquired with the AO instrument.

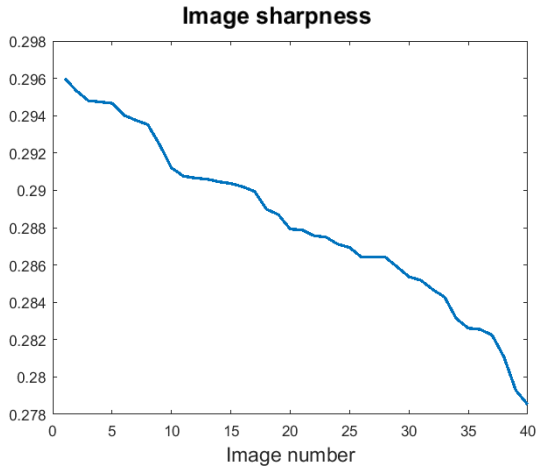
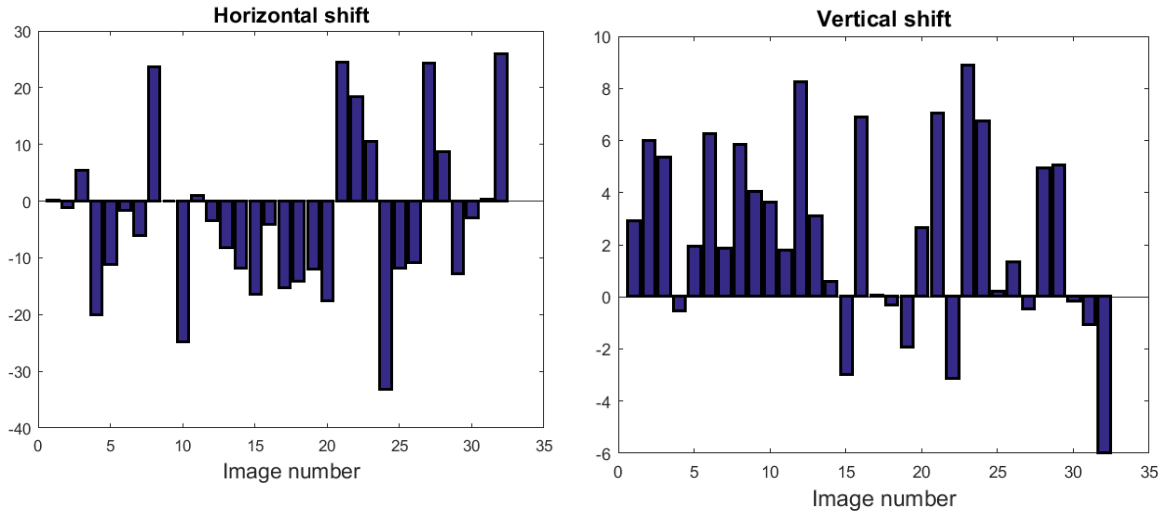


Figure 3.30: Sharpness measure for the sequence of images in the retinal dataset sorted in descending order.



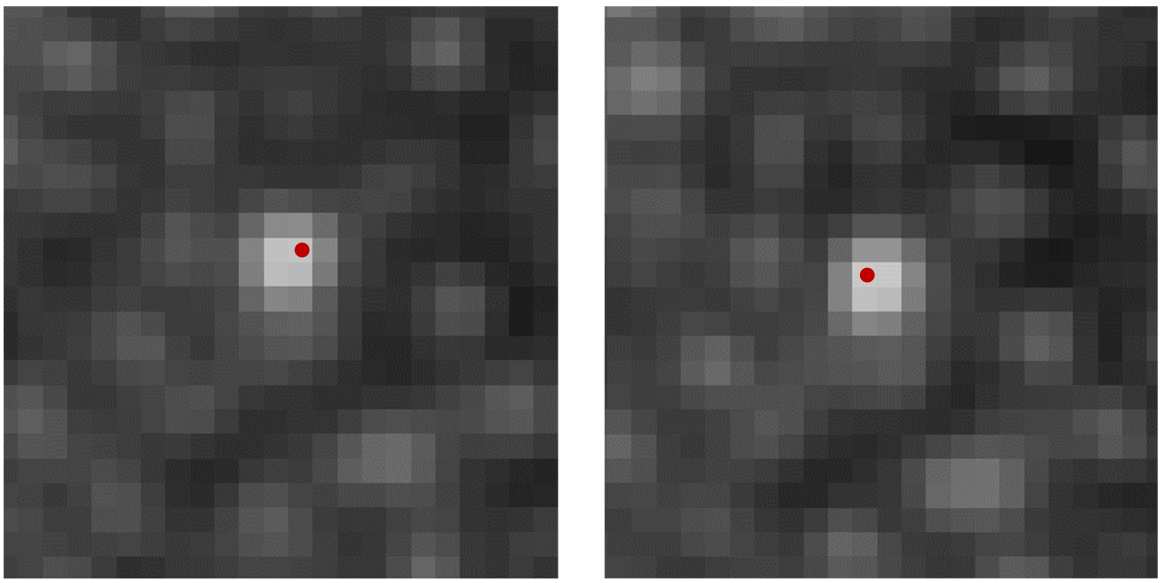
a b

Figure 3.31: Translation detected at the coarse stage of image registration in one of the retinal datasets: (a) horizontal and (b) vertical translation vectors.

II. Fine Registration

The fine stage of image registration includes tracking control points in order to recover the residual translation displacements and rotation angle between the test and reference images. As control points, the coordinates of the brightest cones in the image are used. To find the coordinates of the brightest cones we also tried the circular Hough transform [229] followed by centroid calculation and moment estimation (intensity weighted centroid). It was found that due to background noise and light scattering both methods fail to calculate the correct

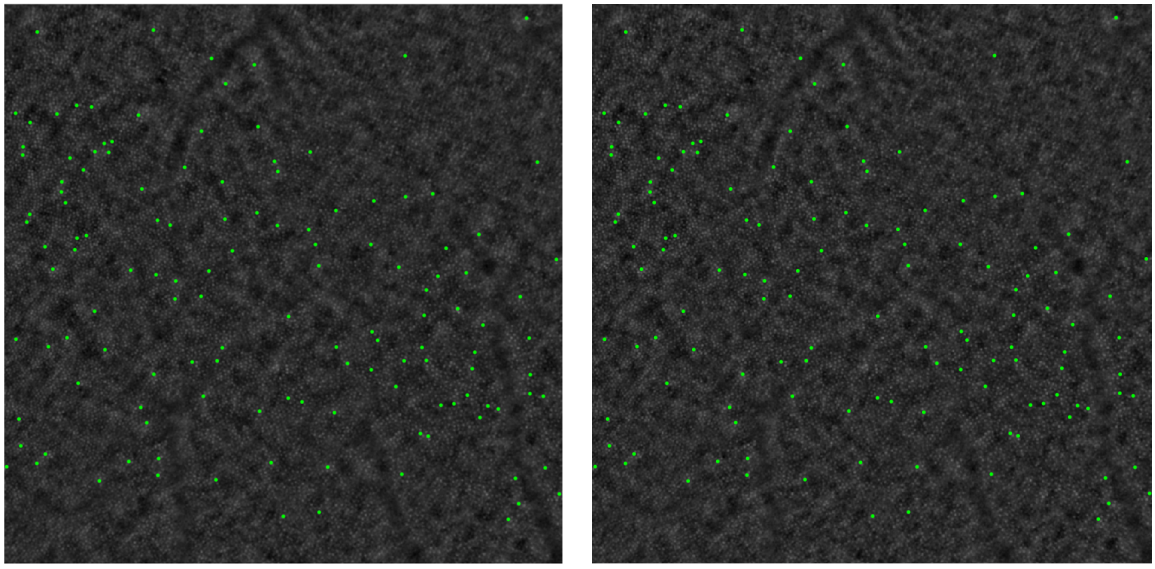
location of the cone centre. We can assume that the centre of cones can be represented by the brightest pixel and use these coordinates as control points. But again, due to scattering effects the intensity profile of the same cone can vary significantly from frame to frame. This implies that the coordinates of the detected brightest pixels cannot be used directly. Figure 3.32 shows an example when the coordinates of the brightest pixel (shown with the red circle) in the reference and test frame differ.



Reference image Test image

Figure 3.32: Control points in the reference and test image, showing the difference in coordinates of the brightest pixel.

Therefore, the coordinates of the brightest pixels are used only as initial estimate of the cone location. To refine the coordinates of the control points, the small regions (20-by-20 pixels) centred at the initial approximation of the brightest pixels are cropped from the reference and test images. Based on the minimum spacing between the cones defined by a window size, regions with matching cones from the reference and test images are established. Then, the POC is used to register matching windows with subpixel accuracy and update the coordinates of the control points in the test image accordingly. Finally, when two sets of control points are established for each pair of images (Figure 3.33) the rotation parameter and residual translation are found using the Procrustes alignment.



Reference image Test image

Figure 3.33: Control points for the reference and test images.

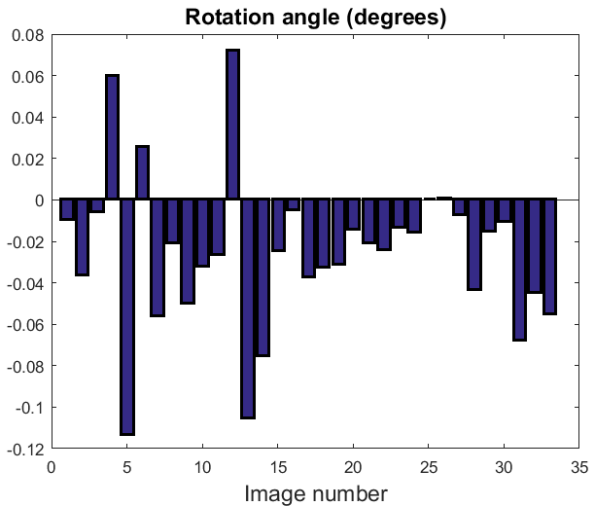


Figure 3.34: Rotation angles calculated at the fine stage of image registration for one of the retinal datasets.

In order to estimate the accuracy of the proposed approach, we performed a parametric study on images rotated by a predefined angle and compared this rotation angle with the one obtained using the proposed approach. The sampling rate and number of control points were varied in these experiments. In high-resolution retinal images the average rotation angle is around 0.1 degree, which would result in the shift of less than 1 pixel at the image border. Therefore, the up-sampling of the retinal images will facilitate the detection of even minor rotation angles. It was found that an upsampling rate equal to 5 using bicubic interpolation

around the brightest cones and 200 control points are sufficient parameters to precisely calculate the rotation angle with an error in the 4th significant figure (Table 3.3). In comparison with the fine registration performed on the original scale of the image, this sampling rate allows to increase the accuracy of detection on an average by 77%. The order of this error in the rotation angles implies that the corresponding translation error at the border of the image is reduced down to the 2nd significant figure. In this way, the information at the border of the image is preserved thereby facilitating calculation of a wide field-of-view obtained by montaging images at the adjacent retinal locations.

Using the aforementioned approach, the rotation angles and residual translations were detected (Figure 3.34) and retinal image sequence was corrected accordingly.

Sampling rate = 5, Number of points = 200		
Rotation angle	**Detected angle**	**|Error|**
1	0.9993	0.0007
0.5	0.4996	0.0004
0.4	0.4001	0.0001
0.3	0.2999	0.0001
0.2	0.1996	0.0004
0.1	0.0096	0.0004
0.05	0.0505	0.0005
0.04	0.0392	0.0008
0.03	0.0307	0.0007
0.02	0.0206	0.0006
0.01	0.0092	0.0008
0.005	0.0045	0.005
0.001	0.0013	0.0003
Average error:		0.0008

Table 3.3: Results of parametric study, showing rotation angle tests, model approximations and absolute error.

III. Lucky Averaging

Following the coarse and fine stages of image registration, the final image was calculated using the "lucky averaging" scheme. For each stack of retinal images, a 3D sharpness measure map was firstly created. Since in retinal images acquired with an AO flood-

illuminated instrument there is no pixel wise exposure difference, regional variation in image sharpness is related to residual optical aberrations and light scattering effects. Therefore, in a relatively small region, the image quality does not vary a lot. For this reason, instead of performing window sliding with a one pixel shift as in the work of Huang et al. [41], here a 3D sharpness measure map is calculated for non-overlapping regions of the size of 20-by-20 pixels. This also helps to significantly decrease computational costs. Figure 3.35 shows an example of a 2D sharpness measure map, calculated for each frame in the co-registered retinal dataset, thereby forming a 3D matrix. Once the sharpness measure map is built, the indexes of the frames are sorted in descending order in respect to the values of BM_1 of each block. The final image is remapped from the local regions with the best sharpness measure. The number of frames used for averaging of each block is also chosen based on the BM_1 measure. At each local region, the block of the next best frame is added for averaging as long as the overall BM_1 increases. Thus, for different regions there will be a different number of the best frames to be averaged. Figure 3.36 shows an example of a number of frames used for mapping a final image. The use of non-overlapping regions in lucky averaging may cause some border effects when there is a large difference between the number of blocks in the adjacent areas (Figure 3.36). To minimize these effects, histogram equalisation was performed in the retinal blocks. To avoid this problem, the final image should be composed by including the pixels with the best regional quality as in the original algorithm by Huang et al. [41].

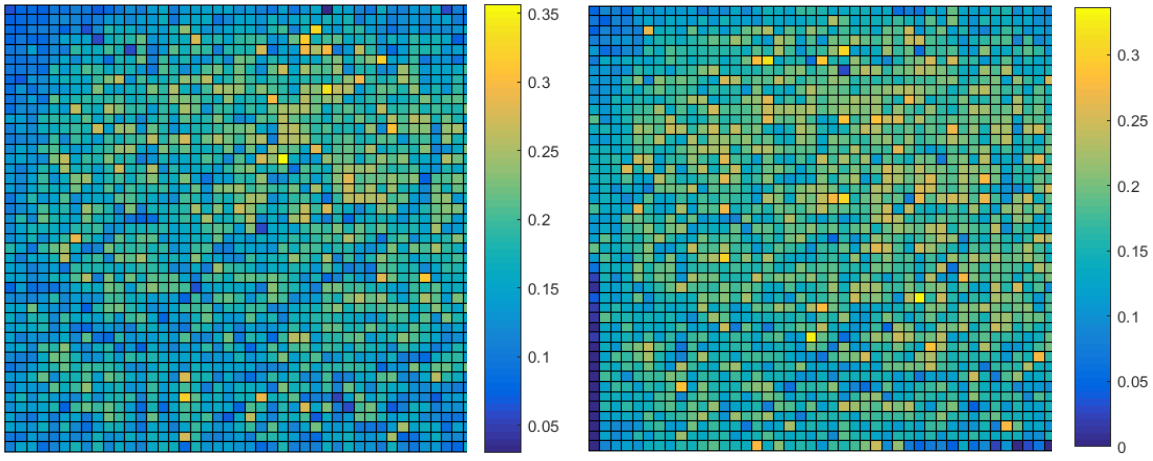


Figure 3.35: Sharpness measure map calculated in 20-by-20 pixel blocks for two retinal frames.

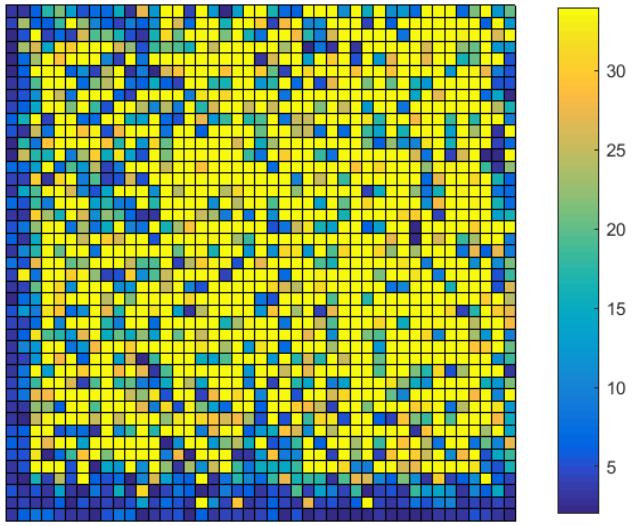


Figure 3.36: Image showing number of blocks used in the lucky averaging scheme for calculating one of the final images.

The proposed approach for image registration was validated on four representative retinal datasets, obtained after the illumination and noise compensation stages. The resulting images where only the translation vector was compensated were compared with the images where both rotation and translation were corrected in the retinal datasets (Figure 3.37). Figure 3.38 shows a difference between the normal averaging scheme and the proposed lucky averaging approach. Averaging of the frames leads to reduction of thermal and photon noise, therefore in addition to the sharpness measure, a peak-signal-to-noise ratio (PSNR) was calculated. Both, quantitative and qualitative comparison of the resulting images indicated that compensation for rotation is a necessary step in the registration of high-resolution retinal images and leads to an increase of sharpness in the images, especially at the edges of image. In comparison with the normal averaging of frames, the lucky averaging scheme provided additional improvement in the contrast of the retinal images. For visualisation purposes the intensity ranges in all resulting images were stretched. The final images were upsampled by the ratio of two using bicubic interpolation.

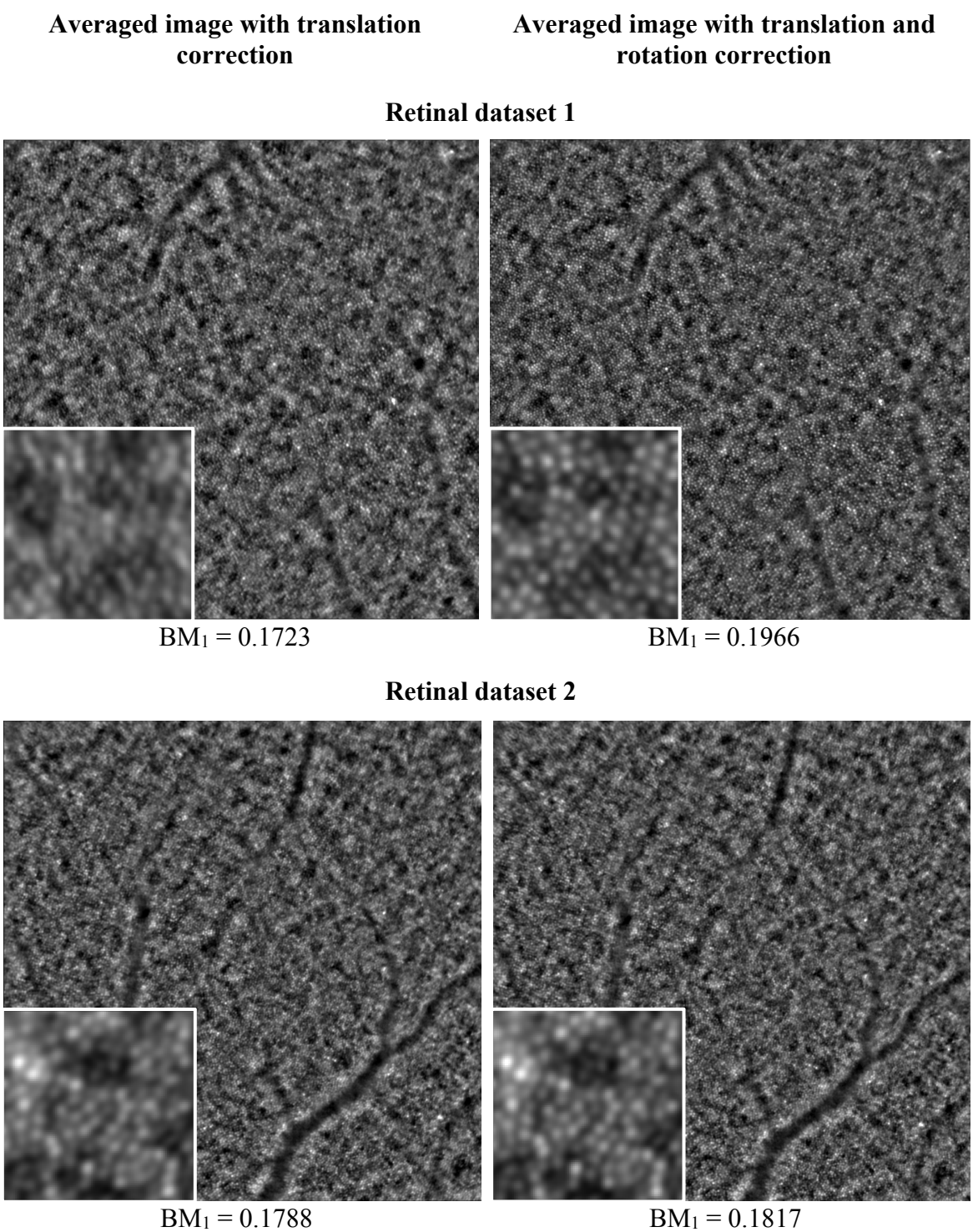
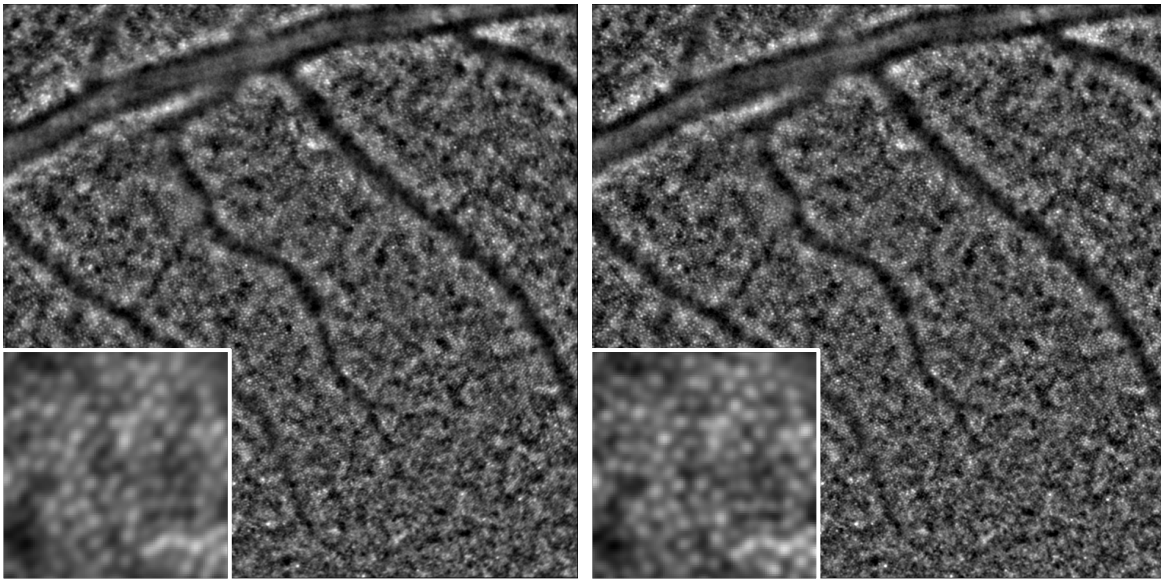


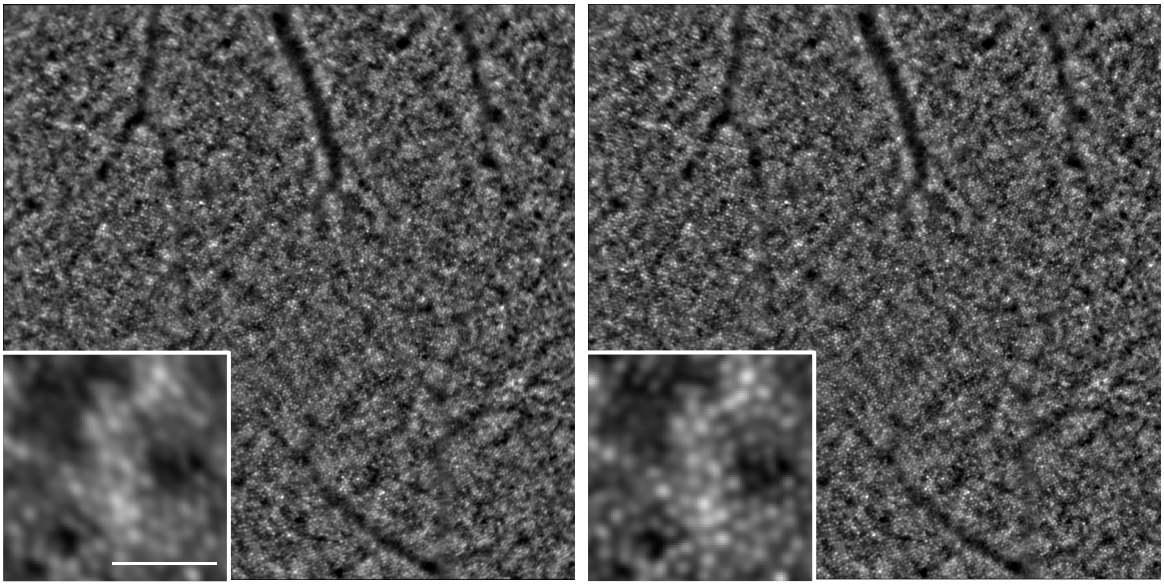
Figure 3.37: Average images after coarse registration (left) and fine registration (right) in four representative datasets. The scale bar is 40 μm.

Retinal dataset 3



$BM_1 = 0.2361$ $BM_1 = 0.2408$

Retinal dataset 4

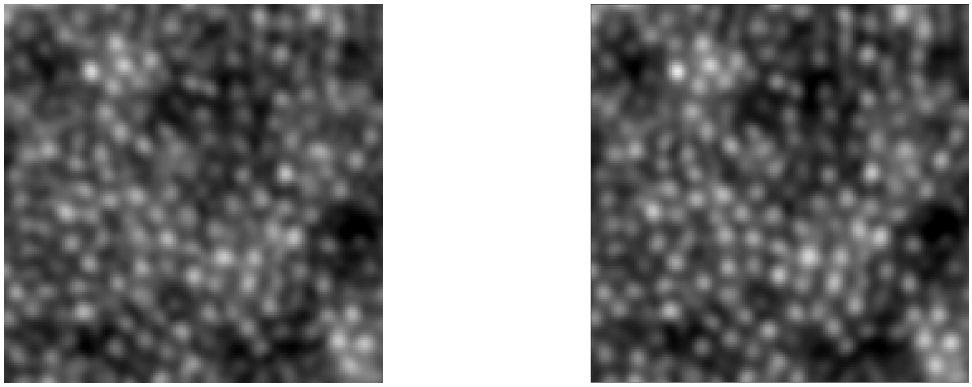


$BM_1 = 0.1973$ $BM_1 = 0.2073$

Figure 3.37 (Cont.): Average images after coarse registration (left) and fine registration (right) in four representative datasets. The scale bar is 40 μm.

Normal Averaging **Lucky Averaging**

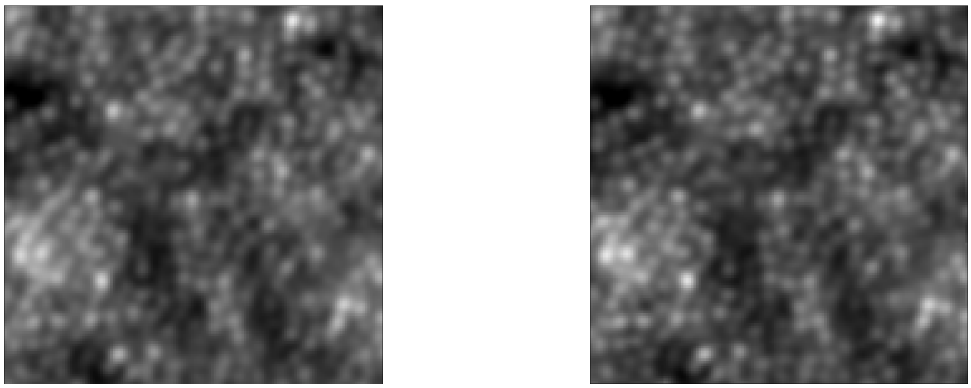
Retinal dataset 1



$BM_1 = 0.1966$ $BM_1 = 0.2110$

PSNR = 38.03

Retinal dataset 2

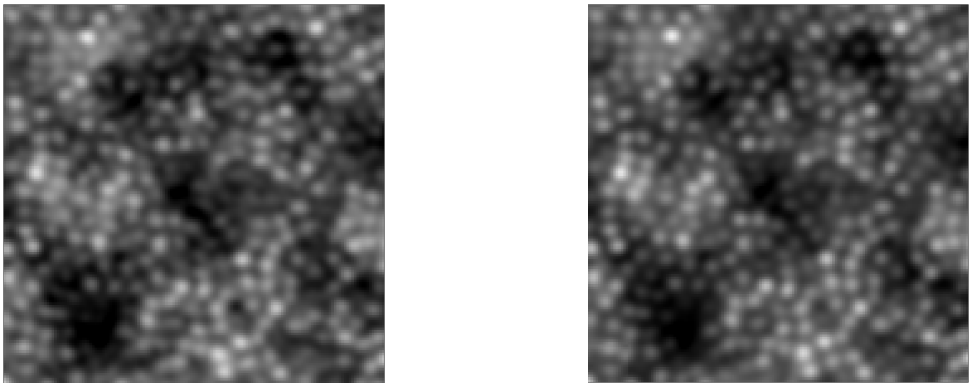


$BM_1 = 0.1817$ $BM_1 = 0.1892$

PSNR = 19.33

Figure 3.38: Sections of retinal images from each dataset showing the difference between normal averaging scheme (left) and lucky averaging (right). The scale bar is 60 μm.

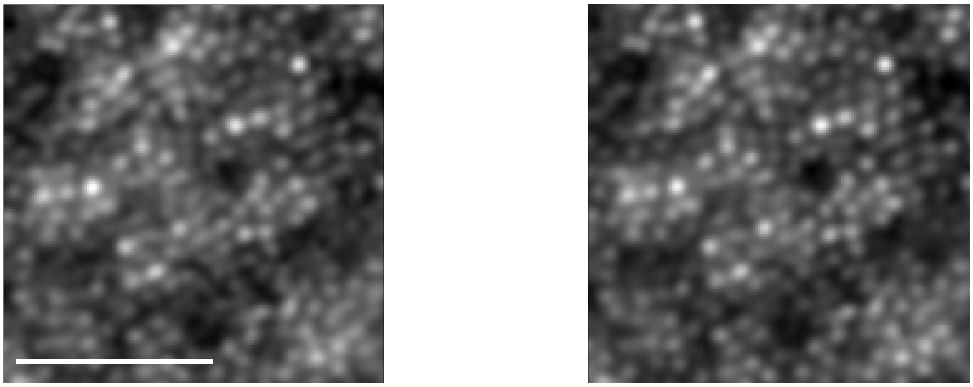
Retinal dataset 3



$BM_1 = 0.2408$ $BM_1 = 0.2471$

PSNR = 28.53

Retinal dataset 4



$BM_1 = 0.2073$ $BM_1 = 0.2085$

PSNR = 33.80

Figure 3.38 (Cont.): Sections of retinal images from each dataset showing the difference between normal averaging scheme (left) and lucky averaging (right). The scale bar is 60 μm.

3.7 Analysis and Discussion

In this chapter, we presented essential image pre-processing methods required for the enhancement of the retinal images. The improvement in image quality of retinal images is a prerequisite step since it allows better observation of retinal microstructures and thus facilitates the next stages of image processing framework. We gave a brief description of the chosen methodology, implementation details as well as quantitative comparison of the extent of quality improvement in the retinal images obtained at each stage.

Firstly, a comparison analysis of four IQA models was performed in order to establish the appropriate measure of quality improvement in retinal images. The effectiveness of the IQA models was tested on high-resolution retinal images. Sharpness measure based on Sobel filter (BM_1) showed the highest correlation with the human ratings and thus was chosen as a benchmark measure for quality evaluation in the proposed image processing framework.

In the second section of the chapter, four methods for illumination compensation were compared by assessing the local brightness variation and sharpness measure. The optimum parameters were found for each method. For the wavelet-based filtering it was established that the level of decomposition can be found automatically as a function of the local brightness variation and homogeneity measure of the estimated background. Based on the performed evaluation study, the wavelet-based approach proved to be the most effective in correcting the illumination component of retinal images. Nevertheless, this illumination correction method imposes artefacts in the restored images. In order to minimize distortion of the recovered images, the DB10 type of Daubechies wavelet was used. Amongst the tested wavelets, this type showed a higher sharpness measure as well as introduced minimum artefacts to the reconstructed images. The artefacts imposed by Daubechies wavelet decomposition can be described as vertical and horizontal lines. In order to eliminate these effects and thereby preserve the retinal features from corruption, the wavelet-Fourier filter was applied to the reconstructed retinal images.

To further increase the quality of high-resolution retinal images and thereby facilitate better distinction of photoreceptor cells, noise suppression was performed on the retinal datasets. To this purpose, a Gaussian band-pass filter was employed. Based on the scale of the retinal features the corresponding spatial frequencies of photoreceptor cells were calculated and used as the stop frequency of the band-pass filter. The start frequency was found automatically as the first peak in the plot of radially averaged power spectrum of the retinal images. The power spectral ratio was calculated between the images before and after image denoising. Overall, the images within the range of cut-off frequencies have been improved by 150%.

In the last section of the chapter, a two-stage image registration was performed on the retinal datasets. At the coarse stage, the translation parameters were found using the POC with subpixel accuracy. At the fine stage, the transformation model was refined by finding

rotation angles and residual translation with the use of Procrustes alignment, where landmark configuration was defined by the coordinates of the brightest cones in the test and reference frames. To ensure high accuracy of rotation detection, a parametric study was performed on the proposed image registration method. This study showed that upsampling the regions around brightest cones up to 5 times and 200 control points allow to detect even minor angles between the frames, dropping the error to the 4^{th} significant figure ($1e^{-4}$). In order to take advantage of intra-frame variability in image quality, a "lucky averaging" scheme was proposed for calculating the final averaged image. The calculated sharpness measures indicated that this approach outperforms the common averaging, allowing enhancement of the retinal image over the larger field of view.

In conclusion, the contribution of this chapter includes the proposed pipeline of image pre-processing methods designed for enhancement of AO retinal images. The wavelet-based illumination correction method has been automated by finding the optimal level of decomposition as a function of homogeneity of the approximated background and local brightness variation of the restored image. This essentially allowed us to minimize the number of input variables in the system for each retinal image. To preserve the integrity of retinal features, we proposed to apply a wavelet-Fourier filter to the restored images. The image registration stage was customized specifically for the compensation of even minor rotation and translation parameters in high-resolution retinal images. Through detailed experimentation the optimal parameters of the model were established such as number of control points and sampling rate. In order to take into account intra-frame variability in image quality, the "lucky averaging" scheme was proposed for calculating final averaged images. Figure 3.39 summarizes the results of this chapter by illustrating the transformation of retinal image at the proposed pre-processing stages.

Following the stages of illumination compensation, noise suppression and image registration, the obtained final images are restored with the proposed image deconvolution method. The next chapter of the thesis presents a model for blind image deconvolution specifically designed for AO high-resolution retinal images. The performance of the proposed method is validated on synthetically generated and AO retinal images.

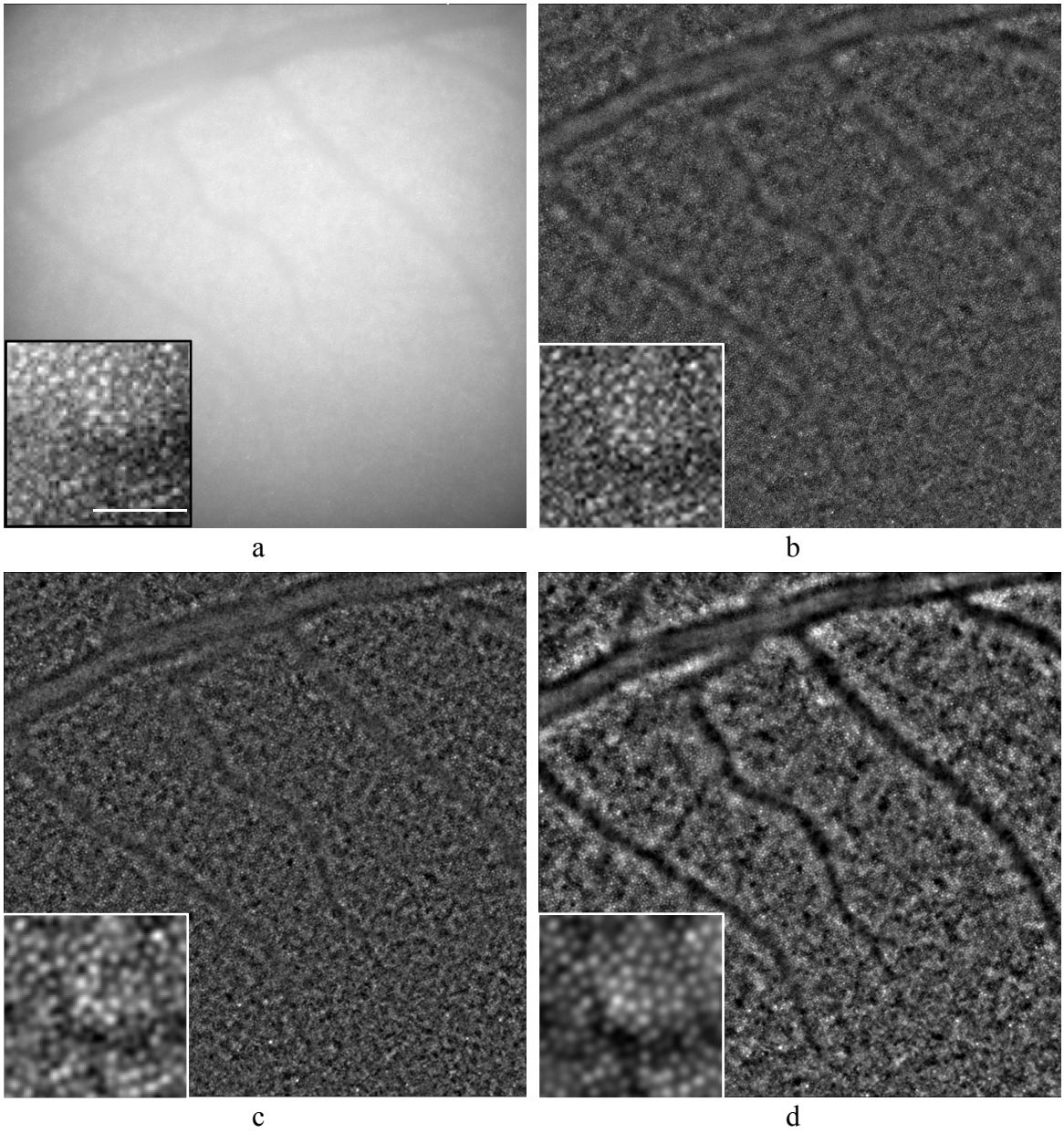


Figure 3.39: Comparison of retinal images obtained at the pre-processing stages: (a) raw image, (b) image after illumination compensation, (c) image after noise suppression and (d) averaged registered image. The scale bar is 40 μm.

4. Image Restoration

An AO instrument performs wavefront detection and correction of low and high-order ocular aberrations, which allows imaging at the cellular level. Yet, this correction is only partial due to hardware limitations of the wavefront corrector. As a result, the acquired retinal images are still corrupted by residual aberrations. This chapter describes a novel image restoration technique for image deconvolution that was included in the image processing framework. In theory, the information about the degradation function of the system can be partially obtained from WFS. However, due to lack of synchronization between image capturing and the wavefront calculation, the WFS data can be used only as an approximation to the real PSF of the system. Unfortunately, this data is not available in the commercial AO flood-illuminated instrument. Therefore, in this work we developed a blind deconvolution method for restoring high-resolution retinal images.

4.1 Introduction

Many tasks in image processing can be formulated as a regression problem where we learn a mapping function $f_w: X \to Y$ from the input space X to the output space Y, which is parametrized by a learned parameter or a vector of parameters w [191], [230, 231]. Ideally, in imaging, light from a single point in the scene should be mapped to a single position on the sensor. But this is not the case in real applications, where the imperfections of the optical system, or movement of the camera affect the quality of the recorded image. Thus, the degradation process can be described by the PSF, representing the response of the imaging system to a point input. In this sense, the task of image deconvolution requires estimation of an original image X from its degraded observations Y obtained as a result of convolution with the system's PSF w and additive noise, n. Mathematically, general image formation model can be expressed as follows:

$$Y = X * w + n\,. \tag{4.1}$$

In the simplest case, the image and noise are assumed to be uncorrelated random variables, which implies that their joint probability distribution does not change in time. In this case, the minimum mean square error estimator (Wiener filter) G can be used [172]:

$$X \approx \Im^{-1}\{G\,\Im Y\} = \Im^{-1}\left\{\frac{\Im\overline{w}\,\Im Y}{|\Im w|^2 + \frac{P_n}{P_x}}\right\}, \tag{4.2}$$

where the overbar denotes a complex conjugate and the Fourier Transform is indicated by variable $\Im$; P_n and P_x correspond to frequency-dependent power spectral densities of the noise and the signal, respectively. This filter assumes a circular convolution and that the system's PSF w is appropriately zero-padded to the size of X.

In many applications, neither the noise nor the PSF of the system are known. In this case, in order to restore the original image a blind deconvolution has to be performed. In addition to being ill-posed with respect to the image, blind deconvolution is also ill-posed with respect to the kernel. That means the solution to the problem may not exist or may not be unique. In practice, an approximate solution to the problem can be estimated; however, the non-uniqueness and the sensitivity of the solution to the noise are still serious problems [186].

One way to solve ill-posed inverse problems is by regularization. This process introduces additional information in the system that distinguishes between wanted and unwanted solutions. In blind deconvolution, regularization of both the original image and the kernel is required. Given a problem described by Equation (4.1), we want to find the optimal X and w knowing only Y. One solution to this problem is to find X and w such that they minimize the squared norm of the difference of the two sides of the equation:

$$min_{X,w}\|X * w - Y\|_2^2\,. \tag{4.3}$$

In order to find a feasible solution, additional regularization terms should be added to a fidelity term in Equation (4.3). A classic approach to this problem is to solve the following regularized minimization expression:

$$min_{X,w}\|X * w - Y\|_2^2 + \lambda\, J(X) + \gamma\, G(w)\,, \tag{4.4}$$

where the fidelity term enforces the data fitting, the regularization terms $J(X)$ and $G(w)$ are the smoothness priors for X and w, and λ and γ control the weight of their contributions. Increasing the parameter λ would make the recovered image smoother, at the expense of lower fidelity and a narrow kernel. Increasing the parameter γ results in a smoother kernel, at the expense of lower fidelity and ringing effects in the restored image [232] . Additional constraints on the system's PSF can be applied, such as positivity of its entries and integration to one.

A number of regularization constraint terms have been suggested in the literature: Tikhonov regularization [233], total variation [234], regularization introduced by Chan and Wong [235] and You and Kaveh [236]. Such approaches impose only mild constraints on the shape of the reconstructed kernel and as a result the distribution of edge directions in the image can affect the shape of the recovered kernel, via the trade-off between the fidelity and kernel smoothness terms.

In order to facilitate the recovery of the original image X, generally two approaches can be taken. One is to constrain the solution and the other is to add relevant data. Given that the ground truth (GT) is provided in the form of training data T composed of N input and output image pairs $(X_i, {Y_i}^{GT})_{i=1}^{N}$, the optimal convolution kernel w^* can be inferred by learning the mapping of blurred retinal images $\{{Y_i}^{GT}\}$ onto the space of corresponding PSFs $\{w_i\}$. In this work, we propose solving this problem with a multi-variate Random Forest regressor.

As already mentioned in Section 2.5, Random Forests are fast and efficient learners. In particular, due to good scalability they can be used to train large datasets as well as handle high-dimensional problems such as image deconvolution. Given the appropriate representation of the training data, Random Forest methods are capable of learning complex non-linear mapping with great accuracy and generalisation [237]. Randomness induced into the trees during the training stage (Section 4.2) makes them highly resistant to overfitting [238]. Moreover, they are easily distributable on parallel hardware architecture and can be easily deployed to real-time systems with no specialized hardware requirements. These properties render Random Forest an appropriate tool for learning a convolution blur kernel in AO retinal images.

Random Forest is an ensemble machine learning method that allows computers to learn without being explicitly programmed. Generally, machine learning techniques are classified

as supervised and unsupervised. In an unsupervised task, the training is done using only input data with no corresponding output variables, letting the algorithm model the underlying structure or distribution in the data itself. In a supervised task, the learning is performed on a training data of input and output variables, which allows the machine to produce an inferred function used for mapping new examples. In this work, a supervised type of learning is used. Since no GT data is available for AO retinal images, the training data is synthetically generated.

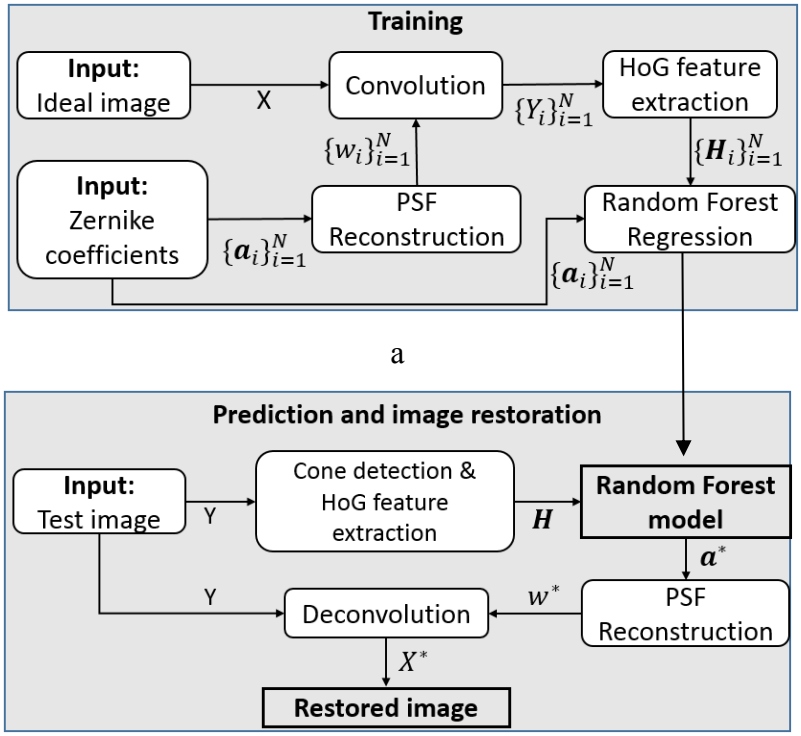


Figure 4.1: Flowchart showing (a) the process of training, (b) prediction and image restoration in the proposed model for blind image deconvolution based on Random Forest.

The training of the Random Forest is performed on large dataset of synthetically generated retinal images and blur kernels replicating the PSF of the flood-illuminated AO system. The blur kernel is modelled by the physics/optics of the AO flood-illuminated system and thus constrained as a member in a class of parametric functions. This allows us to significantly reduce the number of unknowns in the regression target, transforming the blind image restoration problem to a semi-blind restoration. Since the noise component in the AO instrument has been tackled in the previous stages of image processing framework (Sections

3.5 and 3.6), we can neglect term n in Equation (4.1) and assume that images are corrupted only by convolution blur kernel w. In this work, the PSFs of the AO system $\{w_i\}$ are defined by the vectors of Zernike coefficients $\{\boldsymbol{a}_i\}$[2] and the blurred images $\{Y_i\}$ are represented by Histograms of oriented Gradients (HoG) $\{\boldsymbol{H}_i\}$ [239]. A mapping function f_a: $\{\boldsymbol{H}_i\} \rightarrow \{\boldsymbol{a}_i\}$ is then learnt with the aid of the Random Forest. Figure 4.1 illustrates the flowchart of the proposed deconvolution method based on the Random Forest regressor. Details regarding the formulation of the implemented model are discussed below.

4.2 Multi-variate Random Forest

The forest can be realized as a collection of T decision trees which are trained independently using a training dataset $U = \{\boldsymbol{H}_i, \boldsymbol{a}_i\}$, where $\boldsymbol{H}_i$ is the input and $\boldsymbol{a}_i$ is the desired output variables. In this work, the training data is composed of a set of HoG feature vectors $\{\boldsymbol{H}_i\}$ extracted from the synthetic blurred images $\{Y_i\}$ (Section 4.4.1) and a set of Zernike coefficients $\{\boldsymbol{a}_i\}$, where each vector represents a combination of different types of optical aberrations in the eye. Each tree consists of non-terminal split nodes and terminal leaf nodes. The split nodes are responsible for performing a binary split on the input dataset, whereas the leaf nodes store the probability distribution of data arriving at their terminal position. This process is illustrated in Figure 4.2.

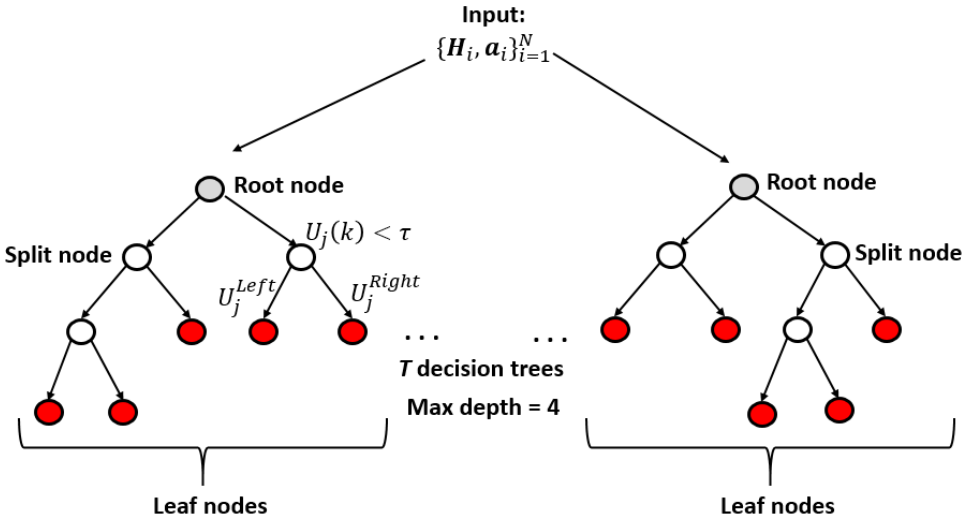


Figure 4.2: Basic notation in the Random Decision Forest Model.

[2] In this chapter, bold characters are used to represent a vector of variables.

At the j[th] split node, depending on the subset of the incoming training data, the splitting function $f(U_j, \Theta)$ learns the optimal parameter $\Theta = (k, \tau)$, where k is the index of the test image feature and τ is its corresponding learned threshold defining the split. The data arriving at the j[th] node is split using a splitting function $f(U_j, \Theta)$, defined as:

$$f(U_j, \Theta) = \begin{cases} left, & if\ U_j(k) < \tau \\ right, & otherwise. \end{cases} \tag{4.5}$$

During training, the optimal parameter Θ is selected from a pool of randomly generated parameters. For each candidate, the set of training data is partitioned accordingly into left and right child sets $\{U_j^{Left}, U_j^{Right}\}$. The problem of learning the "best" parameter θ is formulated as maximization of an objective function. In order to find an optimal split parameter at j[th] split node, an objective function is defined as the information gain $Q(U_j, \Theta)$:

$$Q(U_j, \Theta) = E(U_j) - \sum_{q \in \{left, right\}} \frac{|U_j^q|}{|U_j|} E(U_j^q), \tag{4.6}$$

where $E(U_j) = \log\left(\frac{1}{|U_j|}\sum_{i=1}^{N}\left(\boldsymbol{a}_i^j - \overline{\boldsymbol{a}^j}\right)^2\right)$ is the multi-variate differential entropy [240] for the target vector of Zernike coefficients $\boldsymbol{a}_i^j$ with mean $\overline{\boldsymbol{a}^j}$ of data U_j and q defines the data for child nodes.

Training continues until a maximum depth D is reached or the data arriving at j[th] node contains a minimum number of samples required for creating a leaf node. During the prediction stage (Figure 4.3), a given input feature vector $\boldsymbol{H}_i$ propagates down the branches of each tree T, where a leaf node gives a posterior probability $p_t(\boldsymbol{a}|\boldsymbol{H}_i)$. The prediction from all the trees is aggregated as:

$$p(\boldsymbol{a}|\boldsymbol{H}_i) = \frac{1}{T}\sum_{t=1}^{T} p_t(\boldsymbol{a}|\boldsymbol{H}_i). \tag{4.7}$$

Then, the optimal vector of Zernike coefficients $\boldsymbol{a}^*$ is defined by MAP estimate as:

$$\boldsymbol{a}^* = \arg\max_{\boldsymbol{a}} p(\boldsymbol{a}|\boldsymbol{H}_i). \tag{4.8}$$

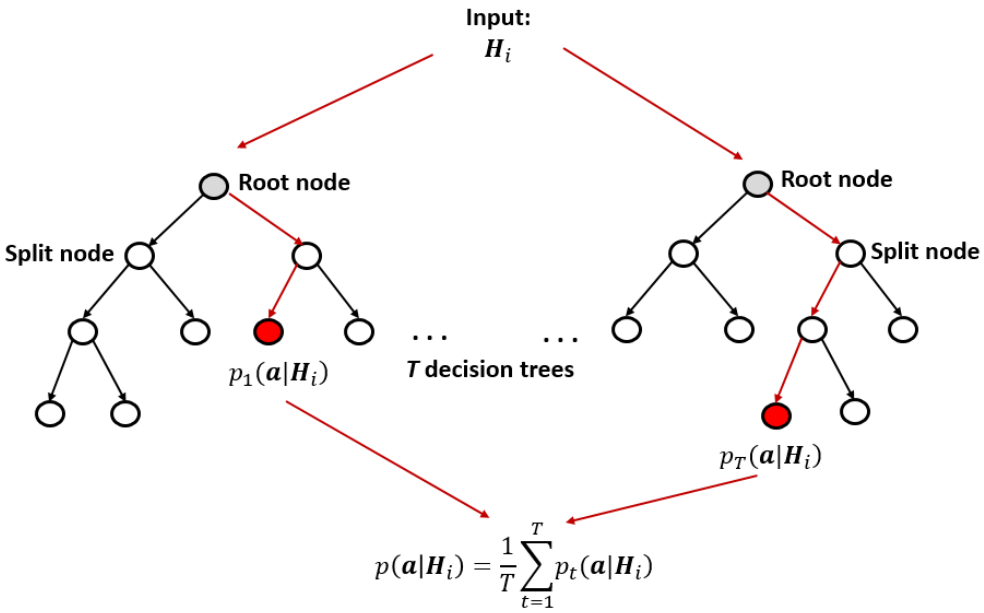


Figure 4.3: Prediction of target vector in the Random Forest Model.

The performance of the Random Forest depends on model parameters such as:

- the number of trees T;
- the maximum depth of the trees D;
- the choice of image features;
- the amount of randomness.

These parameters directly affect the accuracy of prediction, computational efficiency and inference of the target vector on previously unseen data, a property known as generalization [240]. It has been established that very deep trees can lead to overfitting, while shallow trees yield under-fitting [241]. In the work of Criminisi et al. [242], it was shown that the prediction accuracy increases monotonically with the forest size T.

Randomness is introduced into the trees during the training stage via bagging and randomized node optimisation. In bagging, a random subset of training data is selected for training of each tree. This helps to increase training speed, but more importantly, the controlled variation induced in a collection of decision trees makes them highly uncorrelated thus improves generalization and robustness. In the randomized node optimisation, instead of using the entire space of input data, only a random subset is made available for the splitting function at each node. This helps to significantly improve the efficiency of the optimisation

process and controls the amount of correlation between different trees in the forest. Together with bagging, randomized node optimisation introduces even more variability in the Decision Forest and makes the trees more diverse thus yielding better training accuracy [243].

The choice of image features usually depends on the application of the problem. The justification and details on the parameters used in Random Forest model for predicting blur kernels in AO system are explained in Section 4.4.

4.3 Model of Point Spread Function in AO System

The main sources of blur in AO high-resolution retinal images are caused by the residual errors of wavefront correction, light scatter and out-of-focus planes of the retina (Chapter 2). When AO system works in a closed-loop, the transfer error function is the transfer function of wavefront phase perturbation caused by optical errors of the eye. Low-order aberrations such as astigmatism, defocus and prism are usually well compensated with the Badal system embedded in the AO instrument [244]. These aberrations are represented by the first six Zernike polynomials (as defined by Noll [42]). In this manner, the pupil phase of the PSF is expanded on Zernike polynomials of higher order aberrations. An additional term corresponding to defocus is added so as to account for residual blur coming from different layers of the retina [190]. Mathematically this model of PSF is presented as:

$$w(\varphi, y) = \left| \Im \left\{ P(u)\, e^{-\mathrm{j}\left(\frac{2\pi}{\lambda l}\right) \mathrm{y\,u}} e^{\,j\,(\varphi(u)+\varphi_d(u))} \right\} \right|^2, \tag{4.9}$$

where

$$P(u) = \begin{cases} 1, & within\ the\ aperture, \\ 0, & otherwise \end{cases} \tag{4.10}$$

is the pupil function, λ is the central wavelength of imaging beam; l is the focal length of the optical system; y defines the coordinates of two-dimensional focal plane, $\varphi(u) = \sum_{m=7}^{M} a_m Z_m(u)$ is the wavefront phase error, $\varphi_d(u) = a_4 Z_4(u)$ is the defocus phase, a_m and Z_m are Zernike coefficients and Zernike polynomial.

The Zernike polynomials represent a complete set of orthogonal functions with angular harmonics over the unit disc. On a continuous unit circle, normalized Zernike polynomials (ZPs) are described as [245]:

$$Z_n^f(\rho,\varphi) = \begin{cases} \sqrt{2(n+1)}\, R_n^f \cos(f\varphi), & for\ f > 0, even\ ZPs \\ \sqrt{2(n+1)}\, R_n^f \sin(|f|\varphi), & for\ f < 0, odd\ ZPs \\ \sqrt{(n+1)}\, R_n^f, & for\ f = 0, \end{cases} \tag{4.11}$$

where R_n^f are radial polynomials, ρ is the radial distance $0 \leq \rho \leq 1$, φ is the azimuthal angle, $|f| \leq$ n and $\left|Z_n^f(\rho,\varphi)\right| \leq 1$. The radial polynomials can be computed as shown below:

$$R_n^f(\rho) = \sum_{k=0}^{\frac{n-|f|}{2}} \frac{(-1)^k (n-k)!}{k!\left(\frac{n+|f|}{2}-k\right)!\left(\frac{n-|f|}{2}-k\right)!} \rho^{n-2k}. \tag{4.12}$$

In this manner, Zernike polynomials are identified by two integers f and n representing azimuthal degree and radial order respectively. In this thesis, we use Noll's sequential indexing [42], which maps the two indices n and f to a single index m. Table 4.1 shows the relationship between single and double-index notation and corresponding Zernike terms expansion.

The wavefront aberration function is expressed as a weighted sum of Zernike polynomials, therefore each Zernike coefficient indicates a weight of a particular aberration in the wavefront. The RMS error is the most used pupil plane metric and is defined as the squared root of the sum of the squares of the deviation of the wavefront from the ideal wavefront. Since the normalized Zernike polynomials form an orthonormal basis, the squared root of the sum of the square of all non-zero coefficients of the Zernike terms is used to define the RMS wavefront error [246].

To our knowledge there is no data recorded on the residual optical aberrations of AO flood-illuminated instruments. For this reason, the values of the Zernike coefficients were sampled from a statistical model of the wavefront aberrations reported by Thibos et al. [247]. This model was obtained from 200 healthy eyes measured with a Shack–Hartmann wavefront sensor. Figure 4.4 presents the statistical behaviour of wavefront aberrations in a pyramid representation. Each histogram shows the frequency of occurrence of values for a specific

Zernike coefficient a_n^f. Each row specifies a given radial order n and column denotes meridional frequency (azimuthal degree) f of Zernike polynomial. A Gaussian probability distribution function was fit to each histogram.

Noll's index (m)	**Radial and Azimuth degree (n, f)**	**Zernike polynomial**	**Classical name**
1	(0, 0)	1	Piston
2	(1, 1)	$2\,\rho cos\varphi$	Tip (lateral position) (X-Tilt)
3	(1,-1)	$2\,\rho sin\varphi$	Tilt (lateral position) (Y-Tilt)
4	(2, 0)	$\sqrt{3}(2\rho^2-1)$	Defocus (longitudinal position)
5	(2,-2)	$\sqrt{6}\rho^2 sin2\varphi$	Oblique astigmatism
6	(2, 2)	$\sqrt{6}\rho^2 cos2\varphi$	Vertical astigmatism
7	(3,-1)	$\sqrt{8}(3\rho^3-2\rho)sin\varphi$	Vertical coma
8	(3, 1)	$\sqrt{8}(3\rho^3-2\rho)cos\varphi$	Horizontal coma
9	(3,-3)	$\sqrt{8}\,3\rho^3 sin3\varphi$	Vertical trefoil
10	(3, 3)	$\sqrt{8}\,3\rho^3 cos3\varphi$	Oblique trefoil
11	(4, 0)	$\sqrt{5}(6\rho^4-6\rho^2+1)$	Primary spherical
12	(4, 2)	$\sqrt{10}(4\rho^4-3\rho^2)cos2\varphi$	Vertical secondary astigmatism
13	(4,-2)	$\sqrt{10}(4\rho^4-3\rho^2)sin2\varphi$	Oblique secondary astigmatism
14	(4, 4)	$\sqrt{10}\,\rho^4 cos4\varphi$	Oblique quadrafoil
15	(4,-4)	$\sqrt{10}\,\rho^4 sin4\varphi$	Vertical quadrafoil

Table 4.1 Normalized Zernike polynomials in single (first column) and double-index notation (second column).

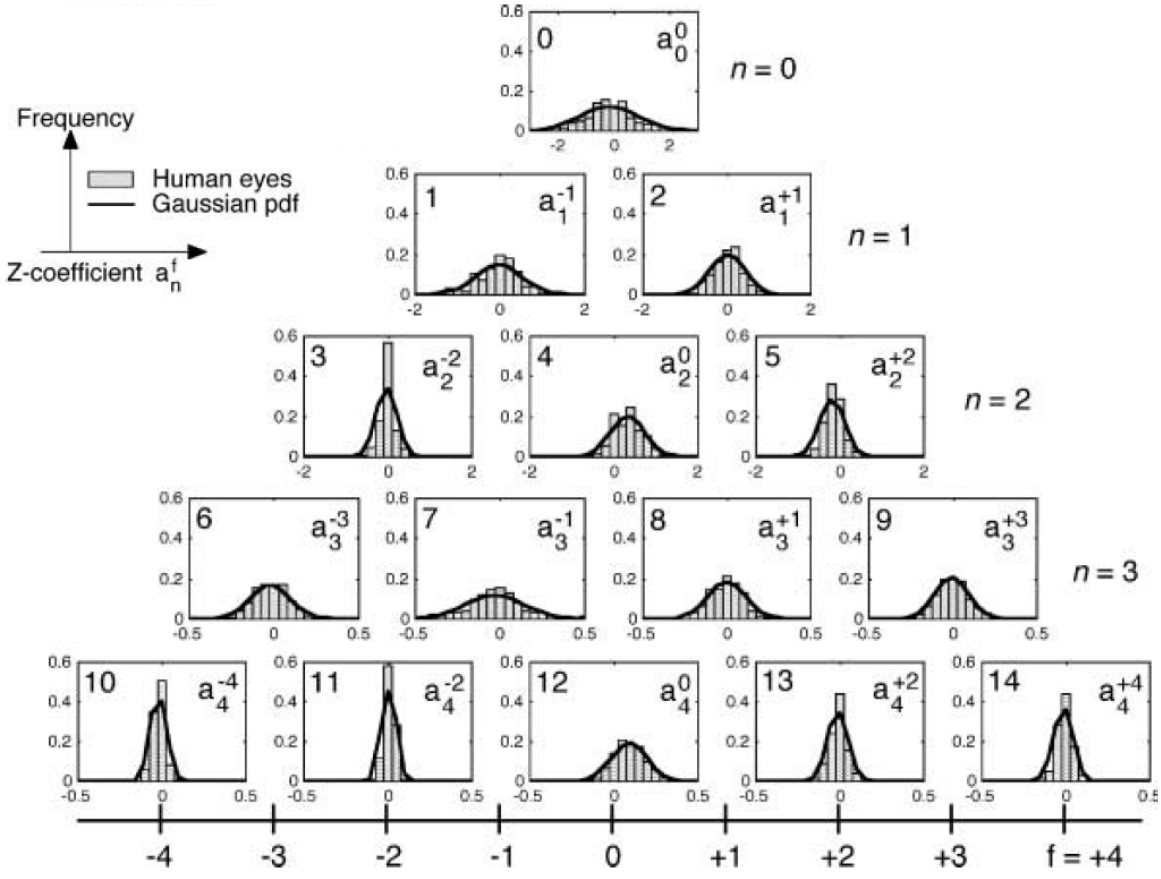


Figure 4.4: Frequency histograms of Zernike coefficients in a normal population of human eyes compared with Gaussian probability distribution (solid line). Physical units of Zernike coefficients are in μm. Pupil diameters is 6 mm [247].

Based on the values in the statistical model of ocular aberrations [247], the range of Zernike coefficients was quantized between $[mean - \frac{std}{2}, mean + \frac{std}{2}]$ with the step size of 0.01 μm. The range of values of Zernike coefficients was chosen so as to include the most likely combinations of optical aberrations which would produce synthetic images with the quality representative of those acquired with the AO flood illuminated instrument in healthy eyes. According to Valeshabad et al. [248] and Rha et al. [249], the RMS of the wavefront in healthy controls after AO correction fluctuates between $0.1-0.16$ μm; the chosen values fall within the specified range. In order to account for partial compensation of aberrations with the AO system, these values were scaled by 0.42 [248]. Imaging wavelength and focal plane sampling were set according to the specifications of AO instrument, rtx1 ($750\ nm$ and $1.6\ \mu m$, respectively). The pupil diameter was assigned to 6 mm and axial length to 24 mm.

Since all parameters defining the PSF were fixed to constant values, the PSF of the AO system can be represented by a vector of Zernike coefficients only, i.e. $\{\boldsymbol{a}_i\}$.

Figure 4.5 presents a few examples of PSFs of AO system generated using Equation (4.9).

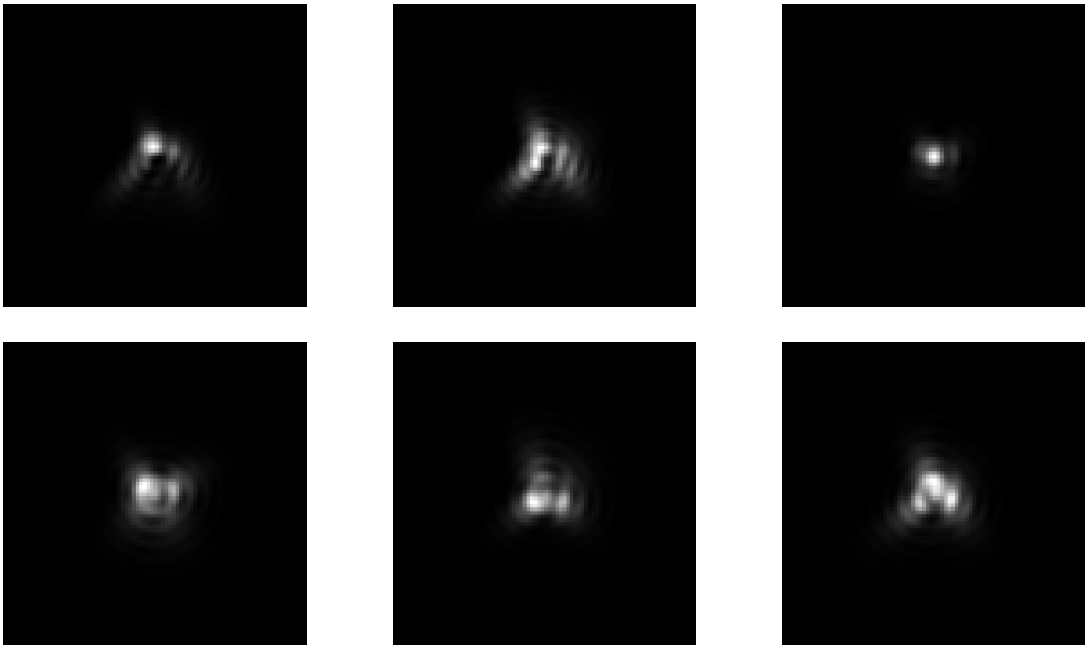
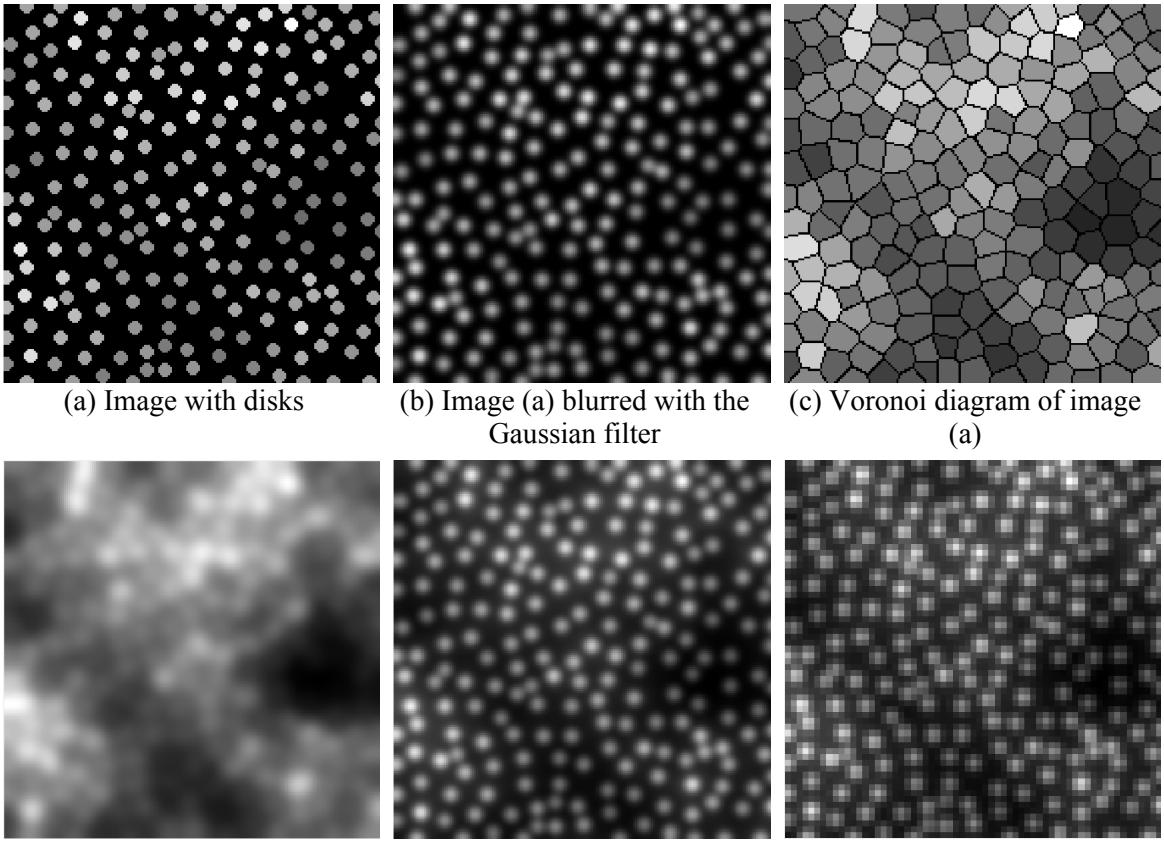


Figure 4.5: Example of simulated blur kernels replicating PSFs of the imaging system after AO correction.

4.4 Implementation

4.4.1 Generation of Training Data

The Random Forest was trained on a large dataset of synthetically generated blurred retinal images and blur kernels, replicating the PSF of the flood-illuminated AO system. For a training dataset U, a set of convolutional blur kernels $\{w_i\}$ was generated using Equation (4.9) so as to simulate optical aberrations of the eye. In order to generate a set of synthetic blurred retinal images $\{Y_i\}$, we created an ideal retinal image X of size 126x126 pixels (100 x100 μm on the retina), using the algorithm described by Mariotti and Devaney [250]. Figure 4.6 illustrates the process of synthetic data generation.



(a) Image with disks

(b) Image (a) blurred with the Gaussian filter

(c) Voronoi diagram of image (a)

(d) Image (c) blurred with the Gaussian filter

(e) Image (b) summed with image (d)

(f) Image (e) downscaled by a factor of 3

Figure 4.6: Step-by-step process of synthetic image generation.

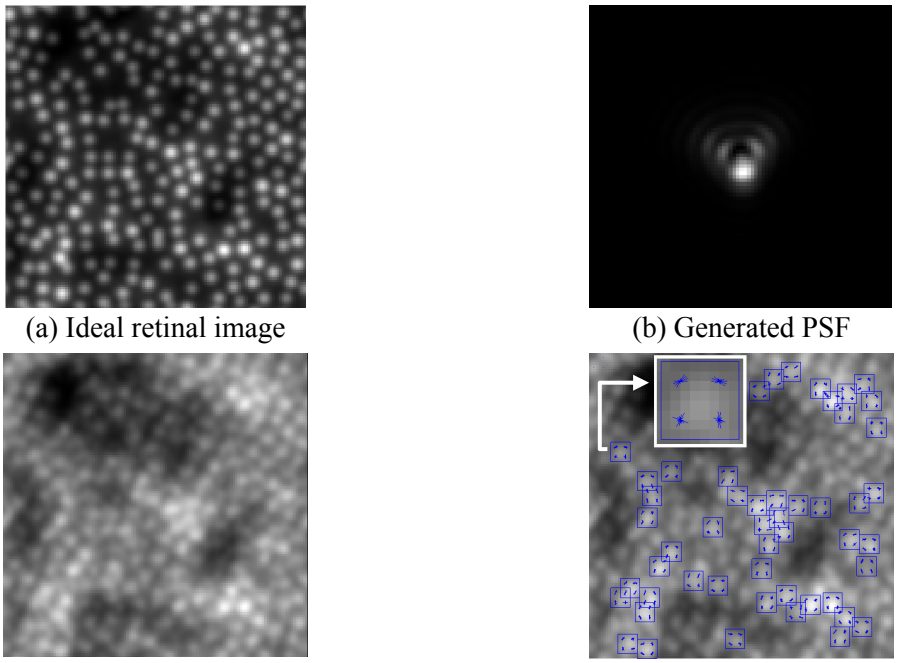
Initially, an image was created with disks placed in a hexagonal arrangement. The radii of the disks and the centre-to-centre distance were set according to the size of the photoreceptor cells and inter-cell spacing at the chosen retinal location [30], [75]. In order to simulate the regularity of cone packing so as to demonstrate characteristics similar to a real retina, a random displacement was added to each of the disks. In the next step, the overlapping disks were merged and their centroids were calculated and used as new coordinates of the cones (Figure 4.6-a). The intensity values of the disks were assigned to the values at the corresponding locations of the reference image. The reference image was chosen from a stack of retinal images, acquired with the AO instrument and processed with the proposed imaging framework. To emulate the background, a Voronoi diagram of the image with randomly distributed disks was used (Figure 4.6-c). The cells of this diagram were assigned to the corresponding intensity values of the reference image. Both the background and the image with disks were blurred with a Gaussian filter, before being summed together (Figure 4.6-b, d, e). The cut-off frequencies were set to 0.11 and 0.22 cycles/pixel, respectively.

Additionally, the intensity levels of the background image were multiplied by a factor of 0.5 in order to reduce its effect in the final image. In order to account for non-integer centring of cones, the initial image was generated three times larger, while retaining the parameters of the cone mosaic (disc radii and inter-cell spacing) in proportion. Finally, the last stage of synthetic data generation included resizing the image by a factor of three (Figure 4.6-f). A set of synthetic blurred retinal images $\{Y_i\}$ was obtained by convolving the generated ideal retinal image X with each PSF from the set $\{w_i\}$.

Depending on the application, various feature representations can be used for training the Random Forest. In this work, HoG was chosen as the image feature vector. This descriptor represents a local shape within an image subregion quantized into bins. Each bin in the histogram represents the number of edges that have orientations within a certain angular range. In this sense, the HoG representation captures edge or gradient structure that is characteristic of the local shape. Therefore, the HoG feature vector can capture the alterations in cone shape due to blur. Apart from HoG features, other descriptors were also tested, such as Gabor features and principal component analysis. However, these feature descriptors were not able to generalize on the training dataset. An advantage of the HoG features over other descriptors is that the this method is invariant to local geometric and photometric transformations [239]. These properties render the HoG an appropriate feature descriptor to discriminate between the blurred retinal images and thus allow their mapping onto the space of blur kernels.

HoG feature vectors were extracted around the strongest corners in small regions of size 10x10 pixels, centered at photoreceptor cell locations, using the *'extractHOGFeatures'* built-in function of Matlab® (Mathworks Inc). Since the cone coordinates are known through the process of synthetic image generation, locating windows with photoreceptor cells is straightforward. In addition to distinct variations caused by different types of optical blur, the retinal mosaic has a unique pattern, varying across the retina as well as human eyes. By extracting features from small windows containing a single cone, we limit the nature of variations down to the corruption of cone shape due to blur, thus assuring the inference of PSFs for any retinal image, taken at different locations of the retina. Moreover, due to light scattering and the angle of incident light, photoreceptor cells appear with different intensity levels in the acquired image. This phenomenon is called an optical Stiles–Crawford effect [97], the property of the photoreceptor cells that is related to the changes in their directional

sensitivity. To eliminate these variations, for each blurred image HoG features were extracted from 50 windows containing the brightest cones only. The resulting vector $\{\boldsymbol{H}_i\}$ of size 36x1 was obtained by averaging HoG features across 50 windows. In this way, the resulting vector characterizes the mean gradient structure of cone shape for a given blurred retinal image. The comparison analysis showed that including information from only brightest cones in the images significantly decreases the mean error between the training $\{\boldsymbol{a}_i\}$ and predicted target vectors of Zernike coefficients $\boldsymbol{a}_i{}^*$ by 82.5% in comparison with the results where HoG features were extracted from all photoreceptor cells. Figure 4.7 shows an example of synthetic data generation and image feature extraction.



(a) Ideal retinal image (b) Generated PSF

(c) Synthetic blurred retinal image (d) HoG features extracted from cone windows

Figure 4.7: Results of synthetic data generation and feature extraction, showing (a) ideal synthetic retinal image, (b) generated PSF, (c) the result of convolving image (a) with PSF (b), (d) HoG features extracted from windows centred at 50 brightest cones.

4.4.2 Training and Prediction

In this work, Random Forest consisted of $T = 80$ trees with a maximum depth $D = 15$. The parameters of the Random Forest were established by performing greedy optimization, where the mean error between the training $\{\boldsymbol{a}_i\}$ and predicted target vector of Zernike coefficients $\boldsymbol{a}_i{}^*$ was evaluated (Figure 4.8).

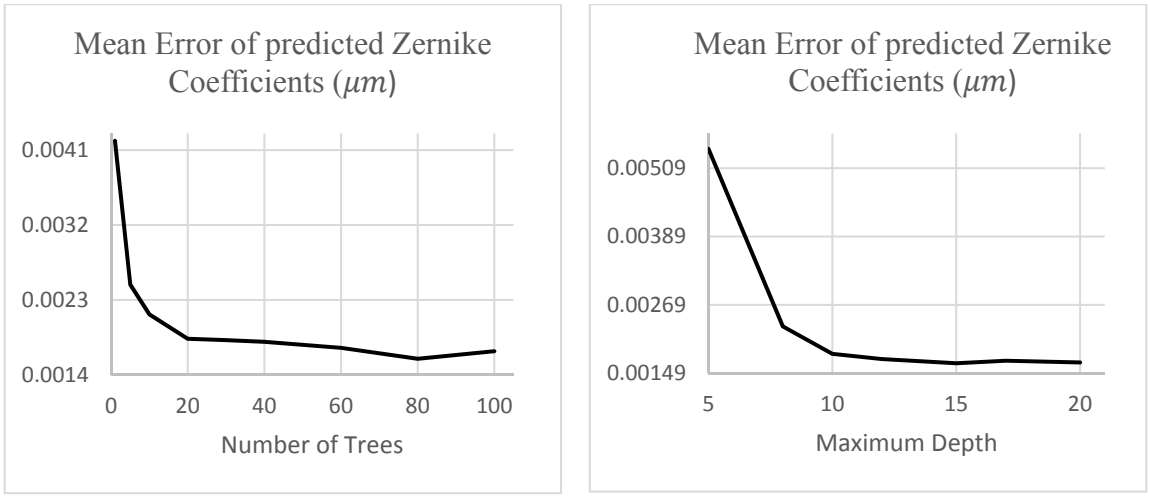


Figure 4.8: Mean error of predicted Zernike coefficients as a function of number of the trees in the Random Forest (left) and maximum depth of the trees (right).

Training is done offline using the training dataset: HoG feature vectors $\{\boldsymbol{H}_i\}$, extracted from a set of blurred retinal images $\{Y_i\}$ and Zernike coefficients $\{\boldsymbol{a}_i\}$, where each vector represents a combination of different types of optical aberrations in the eye (Figure 4.1-a). The choice of the number of terms to be retained in Zernike polynomials is a trade-off between computational time, allocated memory and the accuracy of prediction. In the case when the PSF is defined by 10 Zernike coefficients and the range of these values is equally quantized to 10 levels, we obtain 10^{10} combinations of optical aberrations. This means that the Random Forest would have to be trained on at least 10 billion synthetic blurred retinal images and blur kernels to cover all combinations. In order to reduce the computational time, the values of the Zernike coefficients were sampled with a fixed step size equal to 0.01 μm. Based on this, the number of values defining each type of aberration depends on the range of the Zernike coefficients in the statistical model [247]. According to this model, the probability density functions of oblique secondary astigmatism (Z_4^{-2}) and vertical secondary astigmatism (Z_4^2) have a low variance and a mean value which is lower than the sampling step size (0.0014 μm and -0.0056 μm after AO correction, correspondingly). For this reason, it was decided to approximate the corresponding Zernike coefficients with their mean values. Driven by compromise between the complexity of the PSF model and computation time, we have retained the first 15 Zernike terms, as defined by Noll [42]. Accordingly, the PSF model utilized in this work was approximated by 10 coefficients and consisted of the following combinations:

$$\varphi(u) = a_4 Z_4 + \sum_{m=7}^{15} a_m Z_m(u), \tag{4.13}$$

where a_4 was defined by 15 values, a_7 by 5, a_8 by 7, a_9 by 4, a_{10} by 4, a_{11} by 2, a_{12} by 1, a_{13} by 4, a_{14} by 1 and a_{15} by 2 values, resulting in 134,400 combinations of optical aberrations. Therefore, the target vector in the Random Forest model is of size 10x1 and the Random Forest is trained on 134,400 image pairs of generated PSFs and corresponding blurred retinal images.

During the training stage, the Random Forest learns the optimal split function by maximizing the information gain as defined in Equation (4.6). The branches in the tree terminate with leaf nodes that contain the probability distributions of the Zernike coefficients as a result of the splitting process and the corresponding data.

The prediction is done online using the same feature extraction method as for the training stage (Figure 4.1-b). In case of real AO retinal images, the cone coordinates are found automatically, using the algorithm based on the Hessian-LoG filter described in Chapter 5. Blob detection followed by the LoG filter is employed in order to enhance circular objects in the image. As a result, a binary mask is created, which is used for segmentation of photoreceptor cells from the image. The cone coordinates are calculated from the local maxima of the original image within the cone locations specified by the binary mask. From the set of identified cone coordinates, only the 50 brightest cones are used to calculate the averaged HoG feature vector. During the prediction, a given image feature vector $\boldsymbol{H}_i$ propagates down the branches of each tree where a leaf node gives a posterior probability $p_t(\boldsymbol{a}|\boldsymbol{H}_i)$ and the corresponding data. An optimal vector of Zernike coefficients $\boldsymbol{a}^*$ is usually found by averaging all tree predictions into a single forest prediction, as shown in Equation (4.7) and (4.8).

Figure 4.9 and Figure 4.10 show examples of calculating one of the Zernike coefficients in the target vector $\boldsymbol{a}^*$ at the prediction stage. In the first case (Figure 4.9), the posterior probability distributions of 80 regression trees were simply averaged. As a result, for a GT training defocus coefficient of 0.1992 μm, the predicted value was 0.2019 μm.

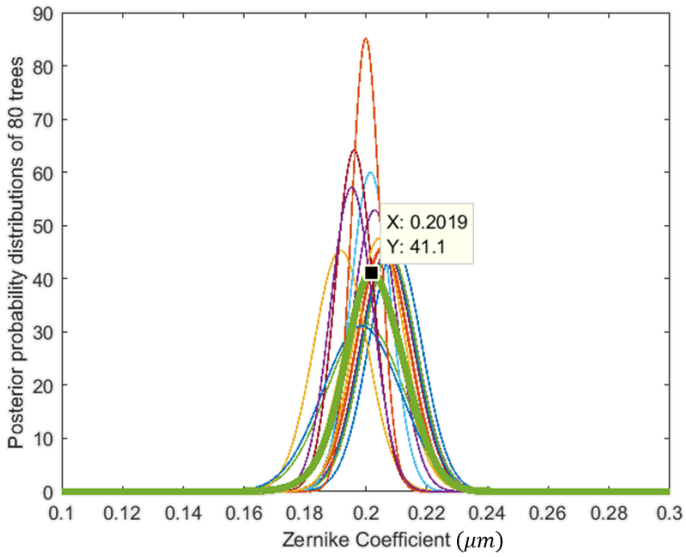


Figure 4.9: The posterior probability distributions of 80 regression trees (shown with different colours). The thick green line shows an ensemble posterior $p(\boldsymbol{a}|\boldsymbol{H}_i)$ obtained by averaging all tree posteriors with values showing the MAP (Y=41.1) and the corresponding predicted Zernike coefficient for defocus aberration (X=0.2019 μm).

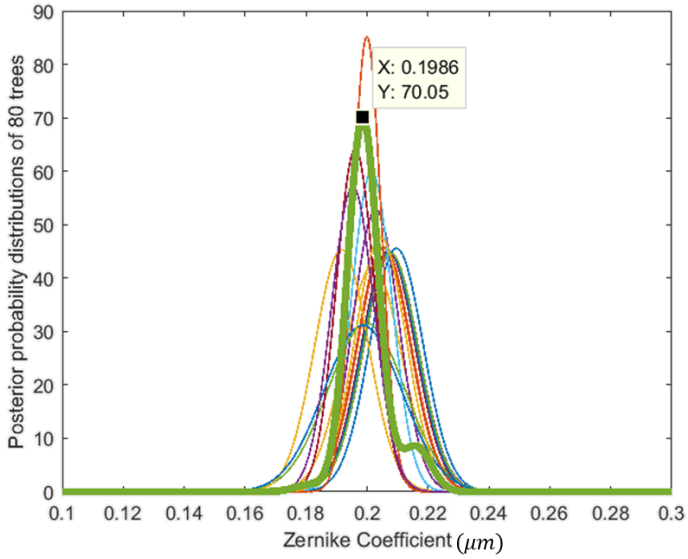


Figure 4.10: The posterior probability distributions of 80 regression trees (shown with different colours). The thick green line shows an ensemble posterior $p(\boldsymbol{a}|\boldsymbol{H}_i)$ obtained by performing KDE on the data from all the leaf nodes showing the MAP (Y=70.05) and the corresponding predicted Zernike coefficient for defocus aberration (X=0.1986 μm).

Alternatively, Kernel Density Estimation (KDE) can be used on the data aggregated from all the leaf nodes to find an optimal vector of Zernike coefficients $\boldsymbol{a}^*$ with the highest posterior probability (Figure 4.10). In this case, for a GT training defocus coefficient of 0.1992 μm, the predicted value was 0.1986 μm which is slightly closer to the target value than in Figure 4.9. Given a correctly chosen bandwidth for the kernel smoothing window, KDE can be useful in the case of outliers, produced by poorly trained trees. In this work, experimentally it was found that KDE performed on the data from all trees with the bandwidth of 0.005 generally gives better results than averaging, reducing prediction error by 39%.

4.4.3 Image Restoration

Following the aforementioned prediction stage, the corresponding PSF w^* was reconstructed with the estimated optimal vector of Zernike coefficients $\boldsymbol{a}^*$, using Equation (4.9). The obtained PSF was employed in the restoration of the blurred retinal image using the Lucy-Richardson deconvolution algorithm [251, 252], built in Matlab® (Mathworks Inc). The Lucy-Richardson algorithm is a well-known iterative procedure for image deblurring. The algorithm maximizes the likelihood of the restored image by using the expectation-maximization algorithm [253]. At each iteration step the previous estimate of the original image is multiplied by the correction factor C^i (Equation (4.14)). As a result, a more clearly deblurred image X^{i+1} is generated for each time of iteration.

$$C^i \approx \Im^{-1}\left\{\Im\overline{w}\,\frac{\Im Y}{\Im w\,\Im X^i}\right\}, \tag{4.14}$$

where w is the PSF, Y is the blurred image, the overbar denotes a complex conjugate and the Fourier transform is indicated by variable $\Im$.

Despite the fact that this method was originally developed for the restoration of astronomical images, where the noise is mainly Poisson-distributed, the Lucy-Richardson algorithm shows a sufficiently good performance with any type of noise in the image. Moreover, this algorithm does not require any prior knowledge of the original image.

4.5 Results and Evaluation

4.5.1 Experimental Validation using Synthetic Data

To evaluate the accuracy of the PSF estimation, the synthetic dataset was divided into two subsets used for training and testing. The training set was obtained by convolving blur kernels $\{Y_i\}$ with a single uncorrupted retinal image X, as described in Section 4.4.1. To test whether the trained Random Forest has generalized well for the inference of convolution blur kernels in any retinal images, test data was generated separately. Blur kernels were produced by taking random intermediate values from the range of Zernike coefficients and reconstructing corresponding PSFs. 10 ideal retinal images X were generated so as to reproduce mosaics at different retinal eccentricities and convolved with 100 PSFs obtained from the randomly generated vectors of Zernike coefficients. In this way, 1000 synthetic retinal images in the training dataset show variation in both, image quality and characteristics of cone mosaic. The HoG features were extracted from the obtained blurred images and stored for the prediction stage. This procedure provided test data composed of 1000 image pairs, representing the unseen data to evaluate the generalization of the Random Forest.

Table 4.2 presents a few examples obtained at the prediction stage, where vectors of Zernike coefficients predicted with the Random Forest are compared against the GT test data. The average absolute difference between the predicted Zernike coefficients and the GT was found to be 0.0061 μm.

Figure 4.11 illustrates few examples of the predicted PSFs, corresponding blurred images and restored retinal images. These results are compared with the GT data: the PSFs obtained from the training vectors of Zernike coefficients, corresponding blurred images and uncorrupted synthetic retinal images X. To evaluate the performance of the proposed method, quantitative assessment was performed on 1000 synthetically blurred retinal images in terms of the root-mean-square error (RMSE). All images were normalized from the original range of intensities to [0,1]. The mean RMSE between the predicted convolutional blur kernels and the GT PSFs was found to be 0.0051 across 100 samples of each synthetic image X. The mean RMSE between the restored retinal images and original synthetic images across 100 samples of each test data was 0.0464. This represents 0.5% and 4.6% of generalization error, respectively.

Randomly generated vectors of Zernike coefficients (GT)

Zernike coefficients	PSF number						
	1	2	3	4	5	6	7
a_4	0.0723	0.1340	0.1364	0.1071	0.1379	0.1656	0.1620
a_7	-0.0347	-0.0380	-0.0178	-0.0086	-0.0048	-0.0219	-0.0089
a_8	0.0107	0.0005	0.0101	0.0239	0.0249	0.0157	-0.0064
a_9	0.0048	0.0116	-0.0311	-0.0047	-0.0295	-0.0282	-0.0319
a_{10}	-0.0046	0.0106	-0.0091	0.0022	0.0085	0.0131	0.0123
a_{11}	0.0382	0.0349	0.0371	0.0369	0.0258	0.0259	0.0351
a_{12}	-0.0056	-0.0056	-0.0056	-0.0056	-0.0056	-0.0056	-0.0056
a_{13}	0.0014	0.0014	0.0014	0.0014	0.0014	0.0014	0.0014
a_{14}	-0.0087	-0.0088	-0.0115	-0.0166	0.0003	-0.0168	0.0000
a_{15}	-0.0122	-0.0079	-0.0164	-0.0157	-0.0021	-0.0091	-0.0120

Predicted vectors of Zernike coefficients

Zernike coefficients	PSF number						
	1	2	3	4	5	6	7
a_4	0.0687	0.1300	0.1348	0.1053	0.1351	0.1641	0.1627
a_7	-0.0349	-0.0362	-0.0178	-0.0058	-0.0045	-0.0229	-0.0097
a_8	0.0124	-0.0010	0.0123	0.0234	0.0249	0.0162	-0.0053
a_9	0.0057	0.0092	-0.0302	-0.0062	-0.0315	-0.0250	-0.0323
a_{10}	-0.0051	0.0107	-0.0077	0.0038	0.0097	0.0125	0.0120
a_{11}	0.0395	0.0338	0.0378	0.0354	0.0257	0.0253	0.0345
a_{12}	-0.0056	-0.0056	-0.0056	-0.0056	-0.0056	-0.0056	-0.0056
a_{13}	0.0014	0.0014	0.0014	0.0014	0.0014	0.0014	0.0014
a_{14}	-0.0120	-0.0070	-0.0129	-0.0155	0.0001	-0.0092	-0.0097
a_{15}	-0.0119	-0.0089	-0.0108	-0.0116	-0.0106	-0.0098	-0.0096

Table 4.2: Comparison between the GT and predicted vectors of Zernike coefficients. Each column represents a vector of 10 coefficients used for reconstructing the PSFs ($a_4, \sum_{m=7}^{15} a_m$) and the row gives a value of Zernike coefficient a_m for a corresponding type of aberration.

Absolute difference between the GT and predicted Zernike coefficients

Zernike coefficients	PSF number						
	1	2	3	4	5	6	7
a_4	0.0036	0.004	0.0016	0.0018	0.0028	0.0015	0.0007
a_7	0.0002	0.0018	0	0.0028	0.0003	0.001	0.0008
a_8	0.0017	0.0015	0.0022	0.0005	0	0.0005	0.0011
a_9	0.0009	0.0024	0.0009	0.0015	0.002	0.0032	0.0004
a_{10}	0.0005	1E-04	0.0014	0.0016	0.0012	0.0006	0.0003
a_{11}	0.0013	0.0011	0.0007	0.0015	1E-04	0.0006	0.0006
a_{12}	0	0	0	0	0	0	0
a_{13}	0	0	0	0	0	0	0
a_{14}	0.0033	0.0018	0.0014	0.0011	0.0002	0.0076	0.0097
a_{15}	0.0003	0.001	0.0056	0.0041	0.0085	0.0007	0.0024

Table 4.2 (Cont): Comparison between the GT and predicted vectors of Zernike coefficients. Each column represents a vector of 10 coefficients used for reconstructing the PSFs ($a_4, \sum_{m=7}^{15} a_m$) and the row gives a value of Zernike coefficient a_m for a corresponding type of aberration.

Qualitative analysis of the results indicated that most of the errors come from the images that were significantly distorted (e.g., the last column in Figure 4.11). In such cases, a larger number of iterations are required in order to reach convergence in the Lucy-Richardson deconvolution algorithm. In clinical practice, images with such poor quality would be rarely used for quantitative assessment of cone photoreceptor distribution. Retinal images where photoreceptor cells cannot be resolved are usually discarded from analysis or attributed to eye pathologies.

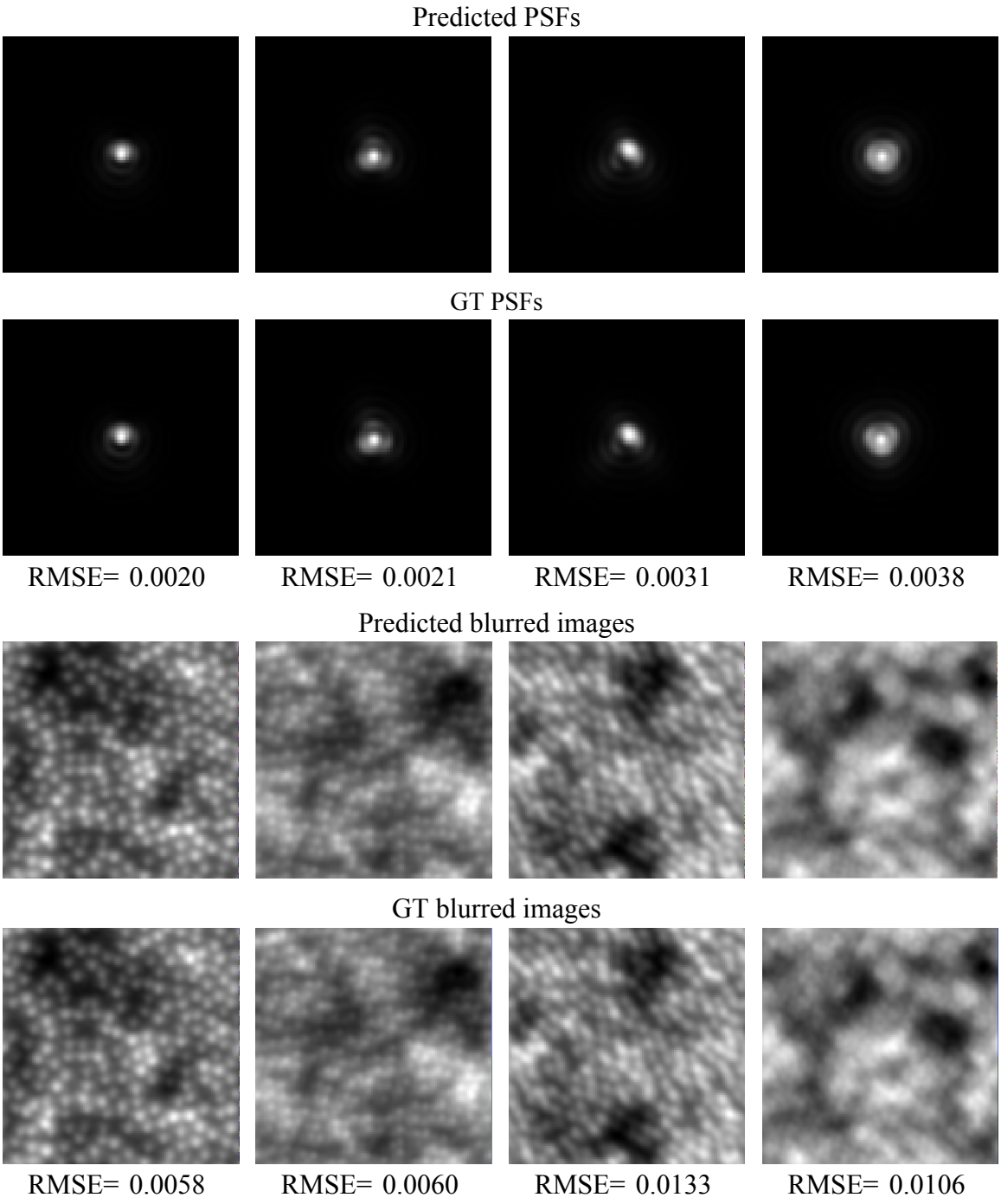


Figure 4.11: Results at the prediction stage showing the predicted PSFs, corresponding blurred images, images restored with the estimated PSFs and compared with the GT data in terms of RMSE.

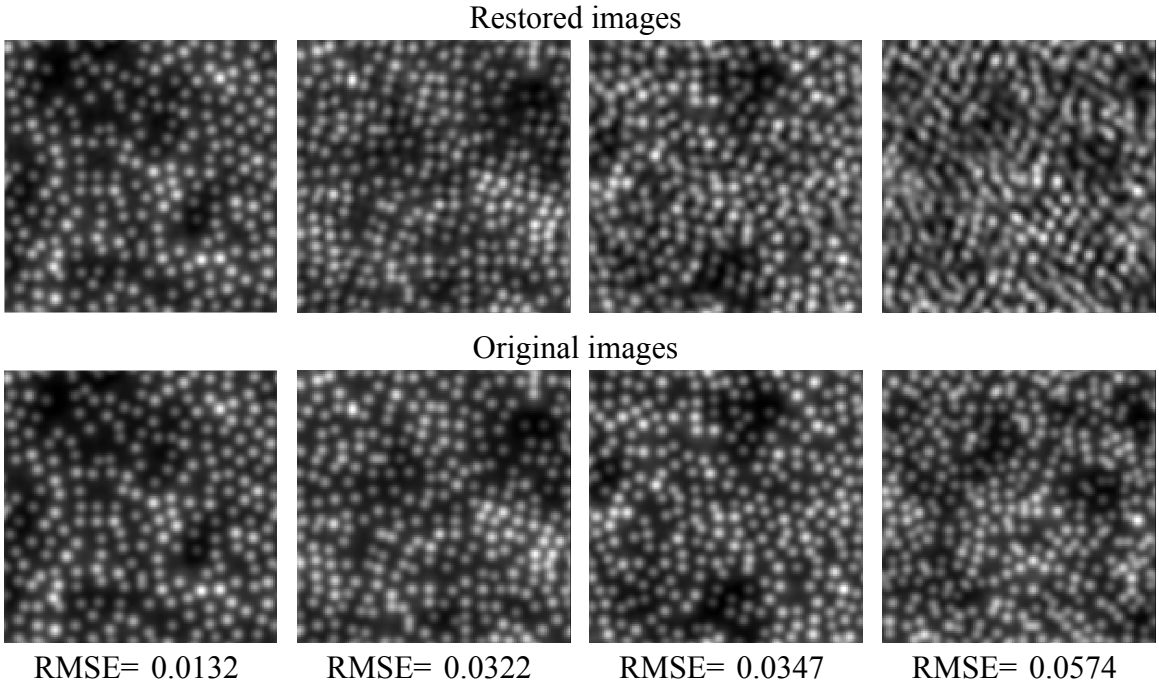


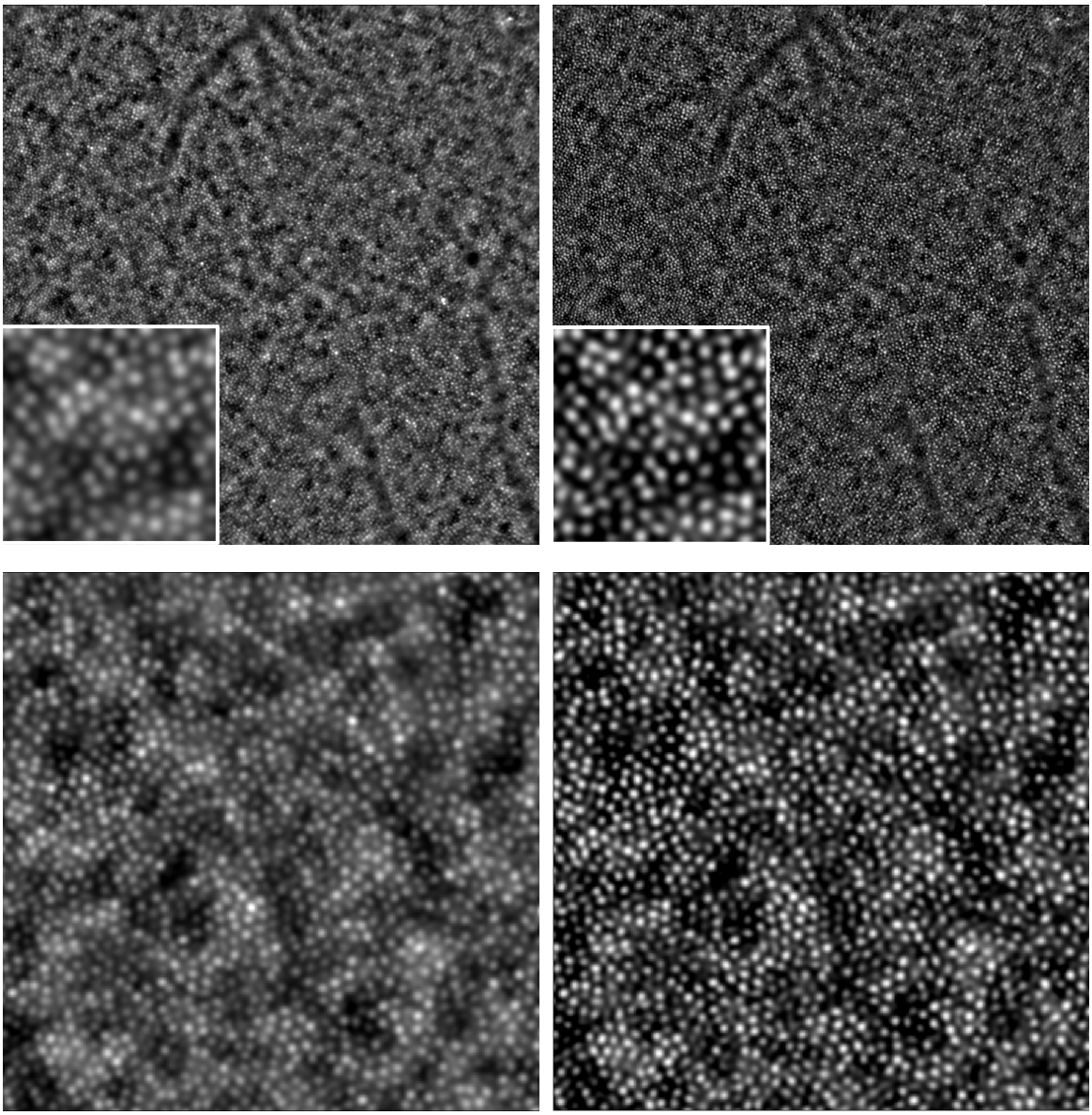
Figure 4.11 (Cont.): Results at the prediction stage showing the predicted PSFs, corresponding blurred images, images restored with the estimated PSFs and compared with the GT data in terms of RMSE.

4.5.2 Experimental Validation using Real AO Retinal Images

The trained Random Forest was used for predicting convolutional blur kernels for high-resolution retinal images, acquired with the flood-illuminated AO instrument. The generated synthetic retinal images of size 126x126 pixels represented 101 μm of the retina. For this data, it was established that 50 windows with cones of size 10x10 pixels is a sufficient number of samples for extracting information regarding the object shape. For the entire AO retinal image, which covers 1.2 mm of the retina, the aforementioned resolution analogously translates to 594 windows that need to be extracted. Figure 4.12 shows high-resolution retinal images before and after applying the proposed restoration process at different scales. As it can be seen from these images as well as the calculated image quality measures (BM_1 and PSNR), the visibility of the photoreceptor cells has been significantly enhanced and the image contrast improved.

Retinal images after image registration | **Retinal images after image deconvolution**

Retinal dataset 1

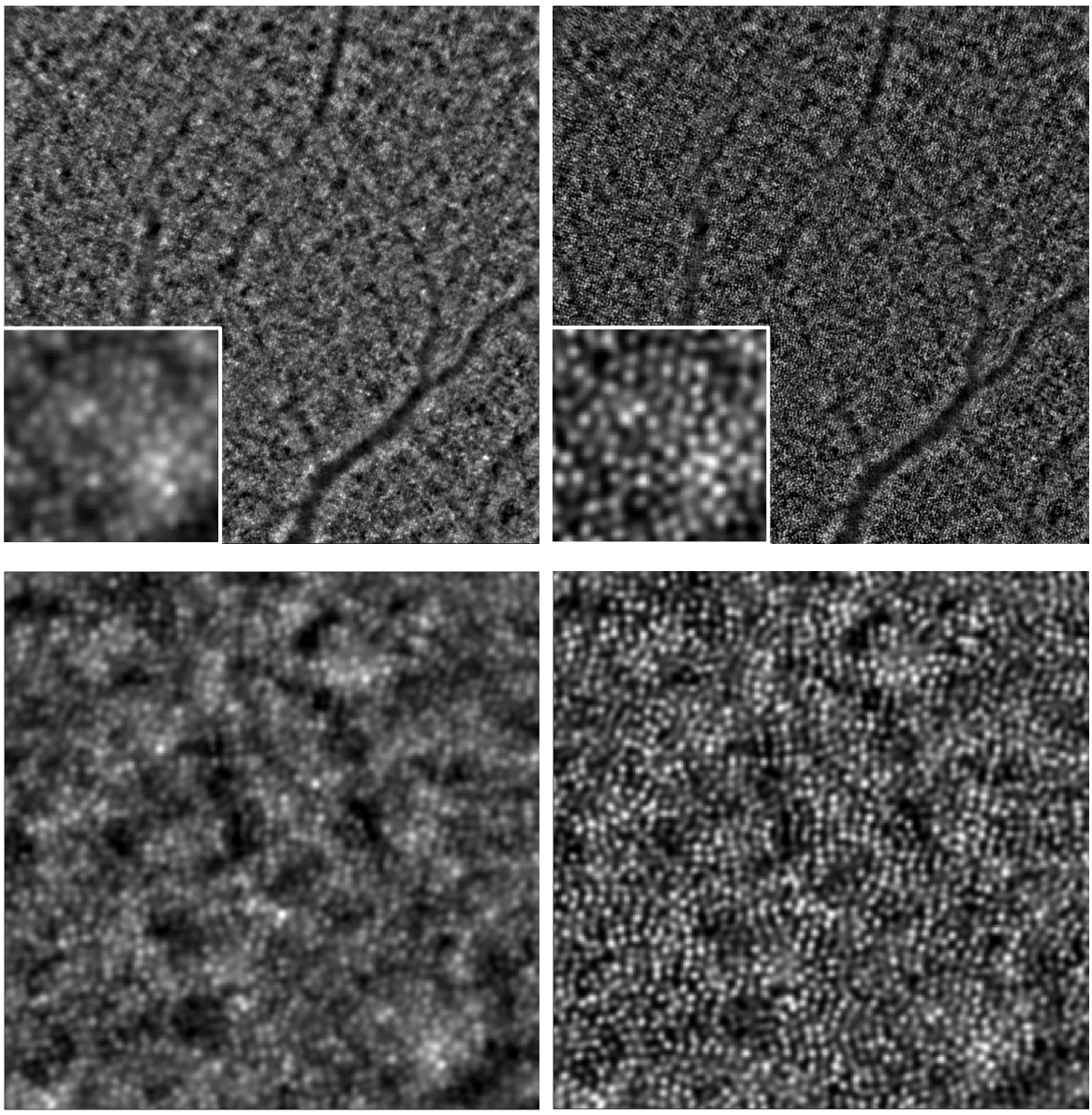


$BM_1 = 0.2110$ | $BM_1 = 0.3820$

PSNR = 14.71

Figure 4.12: Comparison between retinal images obtained after image registration (left) and image deconvolution (right) in four representative datasets in terms of sharpness measure (BM_1) and PSNR, showing retinal images at different scales: 1.2mm, 154 μm and 40 μm.

Retinal dataset 2

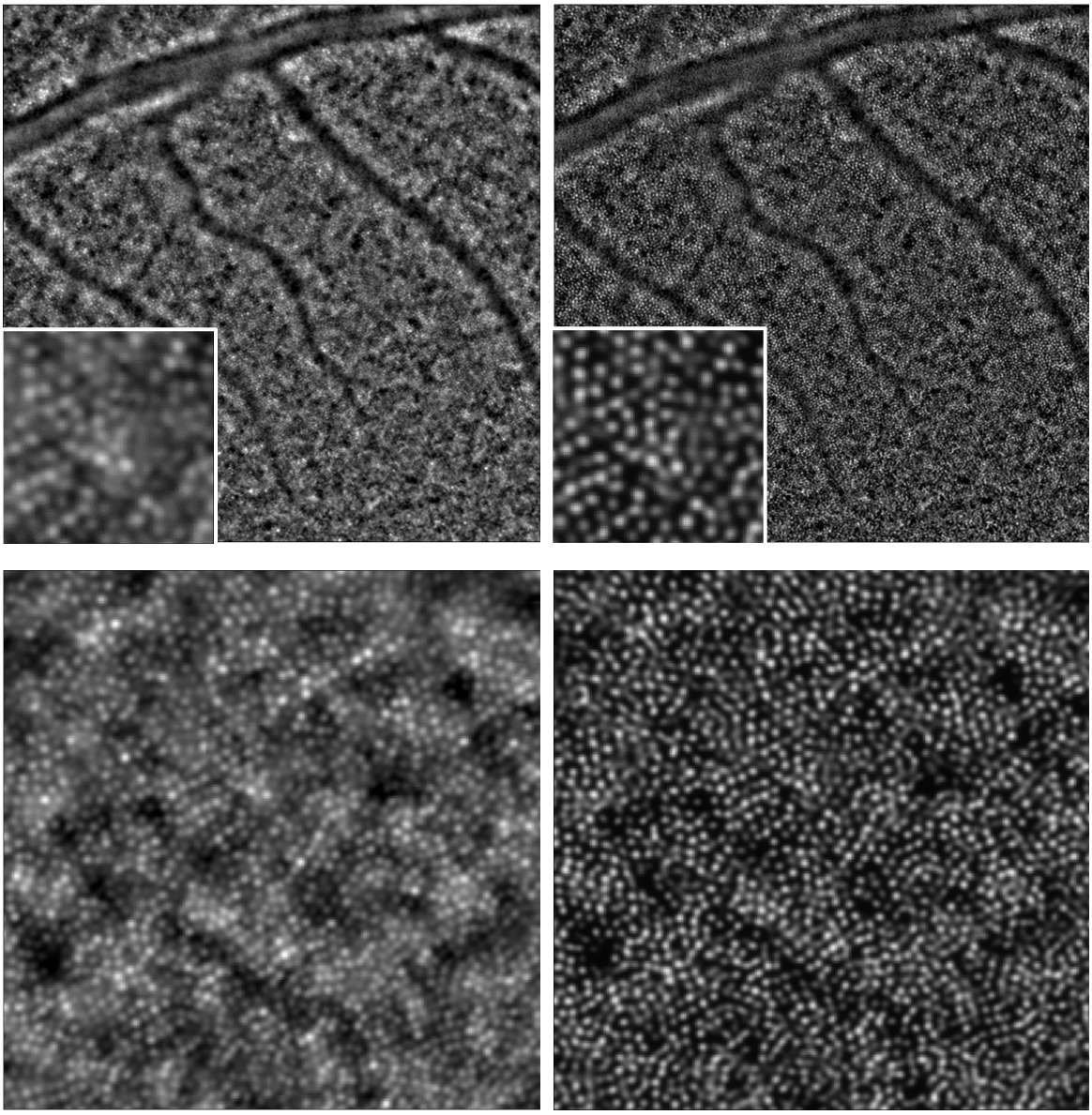


$BM_1 = 0.1892$ $BM_1 = 0.4129$

PSNR = 21.48

Figure 4.12 (Cont.): Comparison between retinal images obtained after image registration (left) and image deconvolution (right) in four representative datasets in terms of sharpness measure (BM_1) and PSNR, showing retinal images at different scales: 1.2mm, 154 μm and 40 μm.

Retinal dataset 3

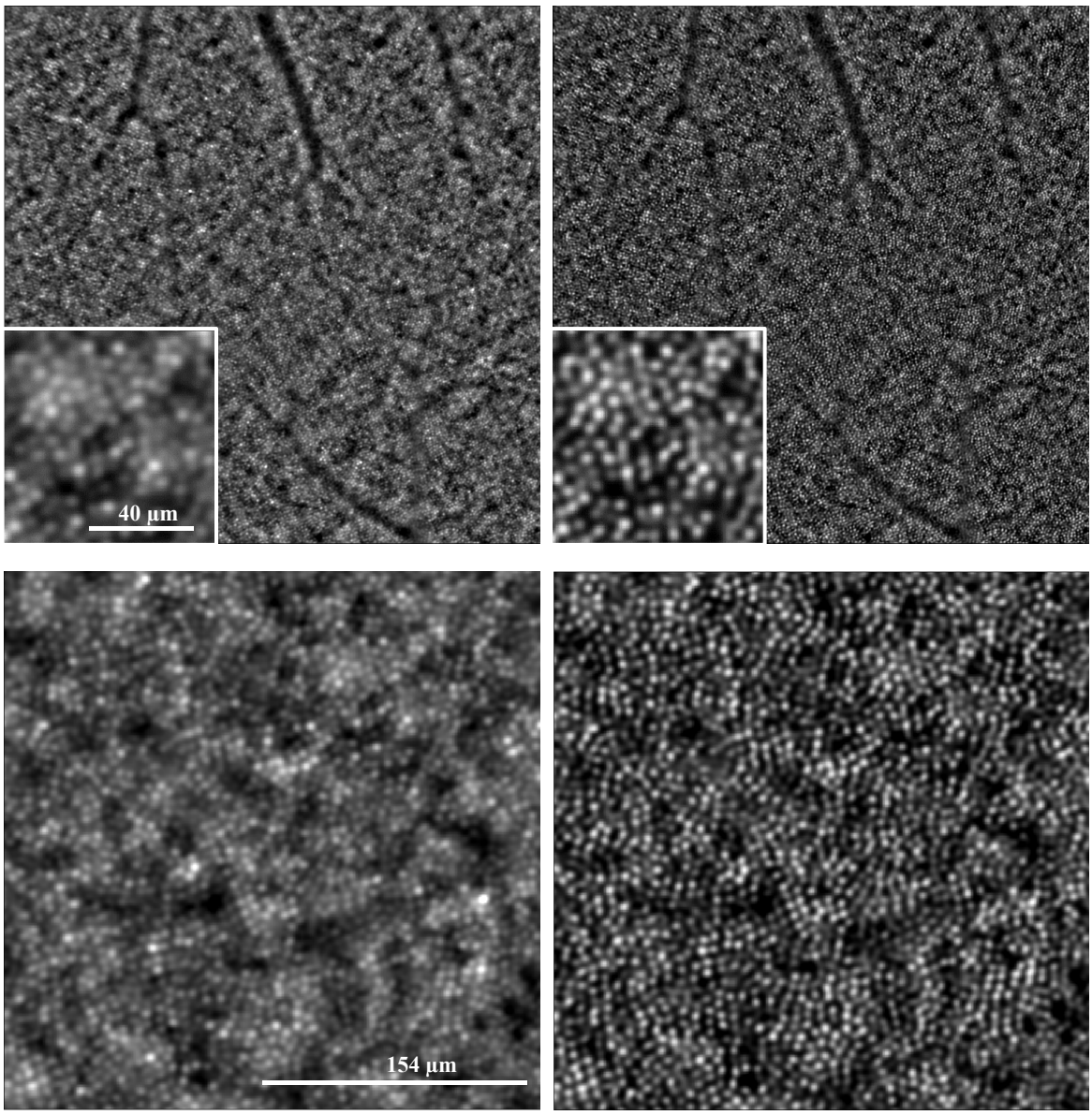


$BM_1 = 0.2471$ $BM_1 = 0.4714$

PSNR = 20.07

Figure 4.12 (Cont.): Comparison between retinal images obtained after image registration (left) and image deconvolution (right) in four representative datasets in terms of sharpness measure (BM_1) and PSNR, showing retinal images at different scales: 1.2mm, 154 μm and 40 μm.

Retinal dataset 4



$BM_1 = 0.2085$ $BM_1 = 0.4140$

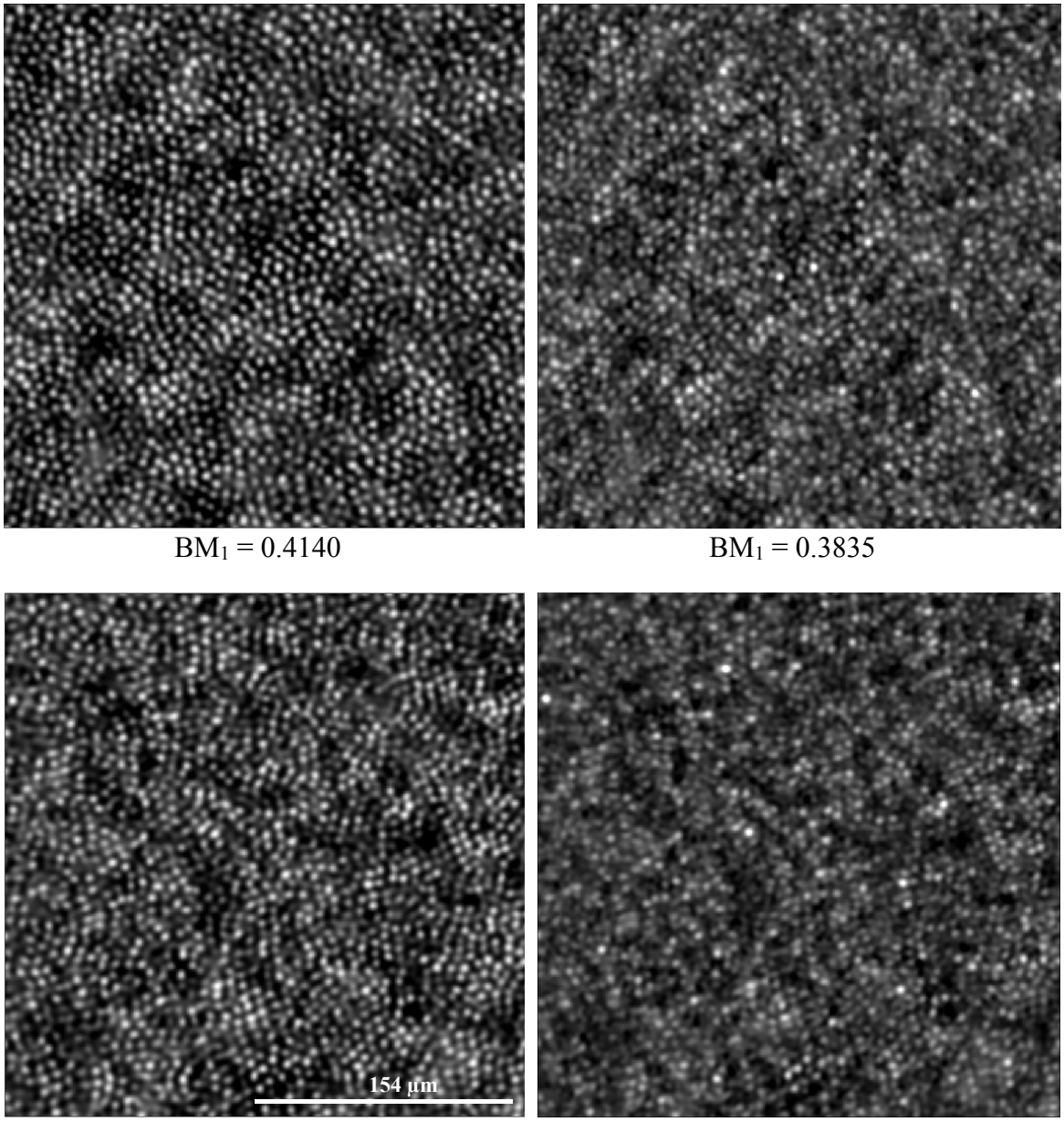
PSNR = 20.28

Figure 4.12 (Cont.): Comparison between retinal images obtained after image registration (left) and image deconvolution (right) in four representative datasets in terms of sharpness measure (BM_1) and PSNR, showing retinal images at different scales: 1.2mm, 154 µm and 40 µm.

In the case of real retinal images, there is no GT data for quantitative evaluation of the results. For this reason, we performed an extensive study, assessing the performance of the proposed method in terms of image quality measures in 25 processed high-resolution retinal images acquired from different subjects and at various eccentricities. Additionally, the obtained results were compared with the images restored with a blind deconvolution method by Sroubek and Milanfar [254]. In this method, blind deconvolution is represented as a l_1-regularized optimization problem, where a solution is found by alternately optimizing with respect to the image and kernel blurs. For a faster convergence, minimization is addressed with an augmented Lagrangian method (ALM) [255]. Table 4.3 presents the results of this study averaged for 25 AO retinal images. The ALM shows a higher PSNR than the proposed method. Despite this, the proposed method surpasses the ALM in terms of the image sharpness and contrast. From the retinal images processed with the two methods (Figure 4.13), it becomes apparent that the proposed method preserves better the edges of photoreceptor cells as well as achieves better differentiation of individual cells, while the ALM seems to blur the photoreceptor cells with weak edges. The power spectral ratio between the images restored with the two methods and images obtained after registration stage shows that the ALM gives a rise to the frequencies below and beyond the spatial frequencies of cone mosaic, which results in a lower contrast and sharpness (Figure 4.14).

	Images obtained after registration stage	**Images restored with the proposed method**	**Images restored with the ALM**
Image contrast	0.0216	0.0638	0.0479
Sharpness measure (BM_1)	0.2076	0.4100	0.3601
PSNR		19.66	25.09

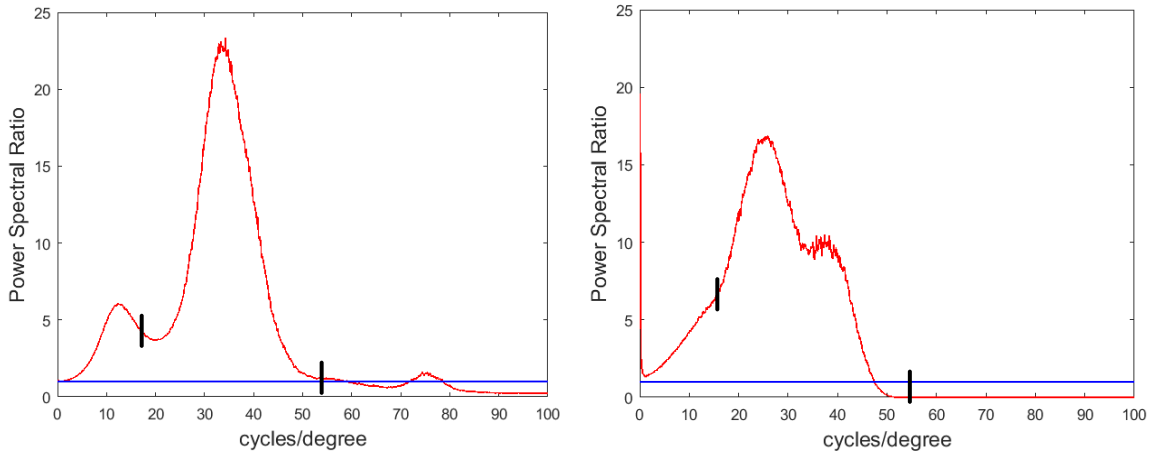
Table 4.3: Quality assessment of the AO retinal images obtained after image registration, image deconvolution performed with the proposed method and image restoration with the ALM averaged for 25 images.



$BM_1 = 0.4140$ $BM_1 = 0.3835$

$BM_1 = 0.3461$ $BM_1 = 0.3006$

Figure 4.13: Sections of AO retinal images restored with the proposed method (left) and the ALM (right). The proposed method shows better separation of individual photoreceptor cells, while the ALM seems to blur the photoreceptor cells with weak edges. The scale bar is 154 µm.



a b

Figure 4.14: Power spectral ratios (a) between the images restored with the ALM and obtained after the registration stage and (b) between the images restored with the proposed deconvolution method and obtained after the registration stage. Black lines show the spatial frequencies of cone mosaic.

4.6 Analysis and Discussion

In this chapter, we proposed a novel method for blind image deconvolution based on a multivariate Random Forest regressor designed for the restoration of AO high-resolution retinal images. A convolution kernel was estimated through non-linear regression of HoG features extracted from retinal images onto the space of PSFs expressed in terms of Zernike coefficients. This was achieved by training the Random Forest on a large dataset of synthetically generated retinal images and PSFs. The mathematical model of the PSF was parameterized through the pupil phase, retaining the first 15 Zernike terms. In AO high-resolution retinal images, out-of-focus planes of the retina also contribute to the image formation, resulting in additional blur and distortion. To account for this, apart from high-order aberrations the PSF's model also included the defocus phase. The parameters of the PSF model were set based on the specifications of the AO flood-illuminated system, rtx1 from Imagine Eyes. Such a compact representation of the PSF significantly reduced the degree of uncertainty in image deconvolution as well as allowed inference of convolution blur kernel for AO retinal images without compromising the resolution of the PSF.

Across the retina, due to light scattering and difference in incident light, photoreceptor cells exhibit variations in intensities. By extracting the information regarding the object shape from photoreceptor cells of similar intensities across the image, we limited the nature of variations present in retinal images down to the corruption of cone shape due to blur. This reduced the generalization error and allowed for the inference of PSFs from unseen retinal images of various quality, taken at different locations of the retina.

The proposed method has been tested on 1000 synthetic retinal images and 25 AO high-resolution retinal images. The validation study on synthetic data showed an average error of 0.0051 for the predicted blur kernels and 0.0464 for the reconstructed images, compared to the GT. Qualitative analysis of the results indicated that most of the errors come from the images which were significantly distorted (Figure 4.11). This happens when Zernike coefficients such as defocus and trefoil are set to the maximum values within their range. As a result, these coefficients have a dominating influence on the gradient structure of the local shape, masking the effects from other optical aberrations. This adversely affected the ability of the Random Forest to discriminate HoG features extracted from severely distorted photoreceptor cells. While in this study the Random Forest was trained on the model of healthy eyes, images with such a poorly resolved photoreceptors cells would be usually attributed to the diseased conditions. In case of pathological retinas, a different model may need to be used for setting the range of values of Zernike coefficients.

The obtained results proved that the proposed approach is applicable for the enhancement of real AO retinal images. We have shown how the images in four representative retinal datasets are transformed at this stage of the image processing framework (Figure 4.12). From the calculated image quality metric, we can see that the image sharpness has been improved by almost 100%. To benchmark the proposed method, a comparison analysis was performed using 25 processed retinal images restored with the proposed method and the ALM (Table 4.3). The results demonstrated that the method based on Random Forest regressor outperforms the ALM in terms of image contrast and sharpness. Visual comparison of the restored images (Figure 4.13) indicated that ALM method tends to blur photoreceptor cells with weak edges.

Despite significant improvement in the image quality, the proposed approach could not always restore the regularity of photoreceptor cell shape. This can be attributed to the

limitations of the proposed method, such as fixed axial length and pupil diameter as well as compensation of aberrations up to the 4th radial order of the Zernike polynomial expansion. Blur in the recorded retinal images, coming from multiple sources, also contributed to these residual distortions. However, even with these limitations the Random Forest was still able to generalize to most cases. This shows the promise of the proposed method, where future work can focus on modelling more complex blur kernels (see Chapter 6).

In conclusion, the contribution of this chapter includes the proposed framework for convolution blur kernel regression designed for the restoration of AO high-resolution retinal images. The performed validation studies showed that the proposed method can successfully restore even severely blurred images, thereby improving the differentiation of photoreceptor cells. As a result, this facilitates the next stage of image processing framework, allowing for more accurate detection of photoreceptor cells. To our knowledge, learning-based methods have not been previously used for AO retinal images.

In the next chapter, an automated algorithm is proposed, based on the use of the Hessian-LoG filter, which allows enhancement and detection of photoreceptor cells. The performance of the proposed technique is evaluated on both synthetic and high-resolution retinal images, in terms of packing density.

5. Enhancement and Detection of Photoreceptor Cells

5.1 Hessian-LoG Filtering

Histological images of *en face* sections of retinas demonstrate that photoreceptors cells resemble circular structures clustered in a hexagonal pattern [30]. However, light scattering during image acquisition as well as optical limitations of the AO system degrade the resulting image resolution when imaging in vivo. Thus, the observed structures suffer from blur and aliasing errors. In order to facilitate better distinction of photoreceptor cells and more accurate photoreceptor cell quantification, blob enhancement methods can be used.

Multiscale analysis of the Hessian matrix is a common tool in many biomedical applications, when enhancement or detection of specific geometric structures is required [256, 257]. For a 2D image $f(x, y)$, the Hessian matrix H is defined as a square matrix of second-order partial derivatives in orthogonal directions at each pixel (x, y):

$$H = \begin{vmatrix} f_{xx} & f_{xy} \\ f_{yx} & f_{yy} \end{vmatrix}, \text{ where } f_{xy} = f_{yx} \text{ for a symmetric matrix } H. \tag{5.1}$$

In 2D space, the two eigenvalues of the Hessian matrix can be calculated as follows:

$$\begin{aligned} \lambda_1 &= K + \sqrt{K^2 - Q^2} \\ \lambda_2 &= K - \sqrt{K^2 - Q^2}, \end{aligned} \tag{5.2}$$

where $K = \frac{(f_{xx}+f_{yy})}{2}$ and $Q = \sqrt{f_{xx}f_{yy} - f_{xy}f_{yx}}$.

The eigenvalues of the Hessian matrix contain geometric information of the image. Based on the relationships between the eigenvalues, a local pattern can be classified as plate-like, line-like or blob-like structure. Koller et al. [256] were the first to introduce this method for the purpose of segmentation and analysis of line structures. Lorenz et al. [258] and Frangi et al. [257] further refined and modified this method for enhancing vessel structures. Based on

the same principles, Sato et al. [259], and Li et al. [260] introduced selective enhancement filters for blob, line and plane structures.

The enhancement filters for blob structures described by Zhenghao et al. and Liu et al. [261, 262] require object scale calculation, prior to conducting the Hessian analysis. The object scale at every image pixel is defined as the radius of the largest hyperball centred at the pixel, such that all pixels within the ball satisfy a predefined image intensity homogeneity criterion [263]. The object scale is employed in a blobness response measure, in this way imposing constraints on both circularity and size of local structures. Thus, the detection response of any non-circular structure will have zero values at all pixels within the object. In our case, this method is not suitable, as the average cone shape is generally not sufficiently sharp for accurate detection and moreover the intensity homogeneity criterion does not hold within the local structure.

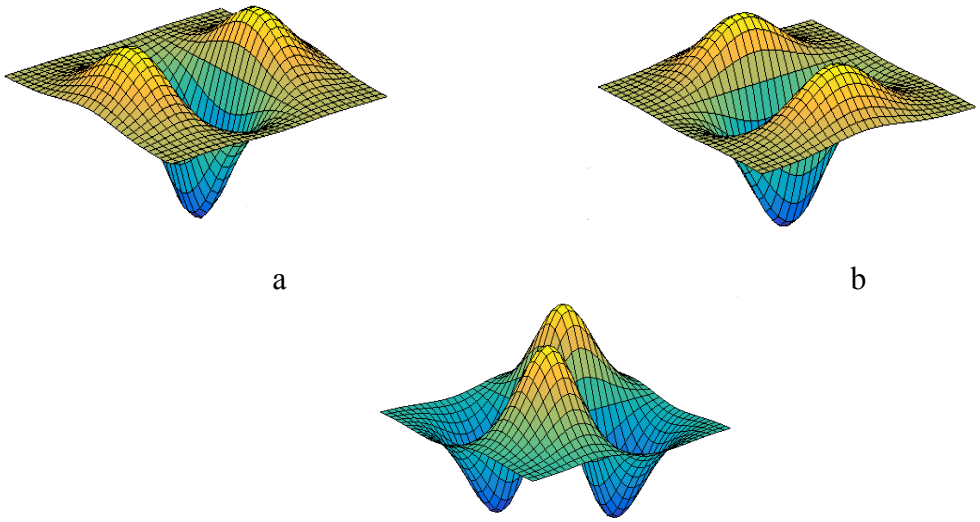
At this stage of the image processing framework, we use a blobness detection response measure, proposed by Li et al. [260]. Since there is prior knowledge on the size of objects to be enhanced, i.e. cone size distribution, this information can be utilised in the enhancement filter to compensate for the residual image noise and at the same time preserve objects with a defined scale. This can be achieved by convolving the object with a Gaussian smoothing function which can serve as a matched filter to preserve an object of the specific scale, as long as the appropriate Gaussian kernel is chosen. The optimum scale of the Gaussian function (i.e. Gaussian kernel) for an object of size d is defined as $d/4$ as it accounts for 95.4% of the area of the Gaussian function [260].

The size of photoreceptor cells depends on the retinal eccentricity. To make the method applicable for any retinal image, multiscale enhancement filter is required. If there are multiple objects in the image with the scale range $[d_0, d_1]$, then in order to enhance all objects within the scale range, the corresponding Gaussian kernels σ_i are calculated in the following way:

$$\sigma_1 = \frac{d_0}{4}, \sigma_2 = r\sigma_1, \sigma_3 = r^2\sigma_1, \dots \sigma_N = r^{N-1}\sigma_1 = \frac{d_1}{4}, \tag{5.3}$$

where $r = \frac{d_1}{d_0}^{1/(N-1)}$ and N is the number of smoothing scales.

For each scale σ_i , the original image is filtered with the second-order partial derivatives of the corresponding Gaussian function. Figure 5.1 illustrates the second-order partial derivatives of the Gaussian function f_{xx} , f_{yy} and f_{xy} with σ =5.



a b

c

Figure 5.1: Second-order partial derivatives of the Gaussian function: (a) f_{xx}, (b) f_{yy} and (c) f_{xy}. The scale of the Gaussian function, σ, is equal to 5.

The resulting smoothed images are corrected for scale by multiplying with ${\sigma_i}^2$. The two eigenvalues of the Hessian matrix are calculated using Equation (5.2) and the blob enhancement filter is computed as:

$$Z_{blob}(\lambda_1, \lambda_2) = \begin{cases} \frac{|\lambda_2|^2}{|\lambda_1|} \text{ , if } \lambda_1 < 0 \; and \; \lambda_2 < 0; \\ 0 \text{ ,} \qquad otherwise. \end{cases} \tag{5.4}$$

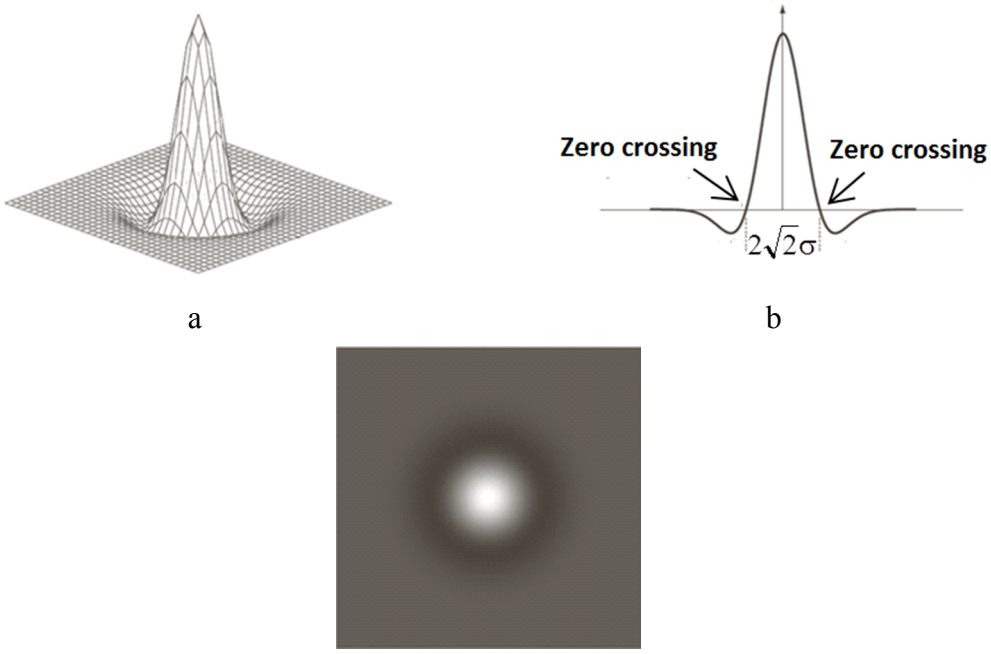
For each pixel, the final output is the maximum value from the results of applying the filters of all N scales.

In the multiscale object enhancement, excessive blurring can lead to low contrast between objects and as a result false detections. To avoid this problem, a LoG filter is proposed in the work of Zhenghao et al. [261]. After applying the blob enhancement filter, the resulting image is convolved with the LoG operator. This can significantly increase the contrast of circular objects and thereby facilitate more accurate object detection.

The LoG operator of an image $I(x, y)$ centered on zero is expressed as:

$$LoG_{\sigma}(x, y) = \frac{1}{\pi\sigma^4}\left(1 - \frac{x^2 + y^2}{2\sigma^2}\right)e^{-\frac{x^2+y^2}{2\sigma^2}}. \quad (5.5)$$

The LoG filter is a circular-symmetric filter with a high central lobe (Figure 5.2-a) which allows for a high intensity transmission. The filter has a shape of a circular centre region with positive weights, surrounded by another circular region with negative weights (Figure 5.2-b, c). As expected, the response of this filter is stronger for circular image structures with radii corresponding to the filter scale. Thereby, applying this kernel on images with circular objects increases the contrast between the region of interest and the background [207].



a b

c

Figure 5.2: The LoG filter. (a) 3D plot of the LoG; (b) cross-section of (a); (c) the LoG displayed as an image [264].

5.2 Implementation and Results

5.2.1 Hessian-LoG filtering on Synthetic Image

In order to verify the performance of the proposed enhancement algorithm, experiments were carried out on both synthetic data and real high-resolution retinal images.

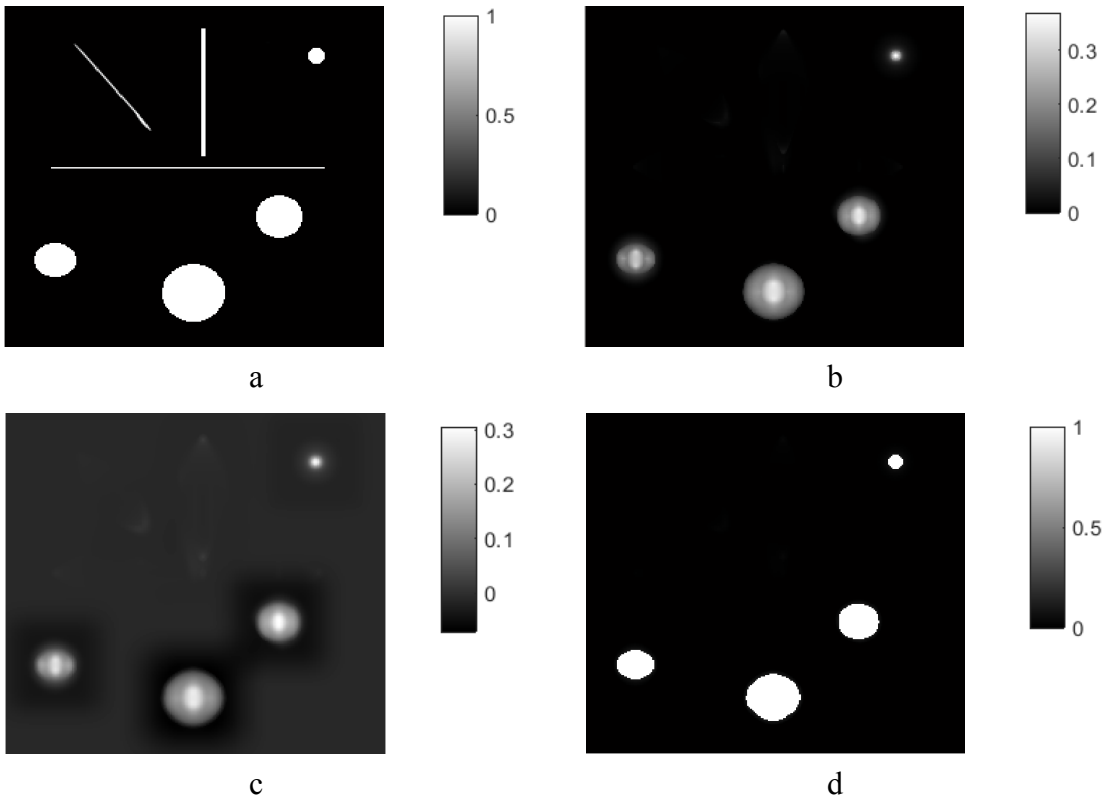


Figure 5.3: Hessian-LoG filter applied to a synthetic image. (a) Original image; (b) image processed with the Hessian enhancement filter; (c) LoG filtered image of (b); (d) binary image of (c) with the threshold equal to 0.09.

Firstly, an experiment was performed to test Hessian-LoG filtering on the synthetic image. Figure 5.3-a shows an example consisting of four idealized blobs of different scales and three lines with different thickness. In Figure 5.3-b the image processed with the Hessian-blob enhancement filter is illustrated. As expected, the filter produced output values mostly within the blob-like structures. To further increase contrast of circular structures, this image was processed with the LoG filter. The intensity values around the blob-like structures in Figure 5.3-c became negative, while the intensity values within the region of interest increased. Therefore, the contrast of blob structures was significantly improved with the use of LoG filter and blobs can be easily detected and segmented (Figure 5.3-d).

This experiment shows that while the multiscale Hessian-blob enhancement filter produces response for blob-like structures of various scales in the image, the following stage of LoG filtering facilitates their segmentation. Combining these two filters is essential for detecting photoreceptor cells, given that the objects to be detected are densely packed, vary in scale and have low contrast.

5.2.2 Synthetic Data Generation

The performance of the proposed cone counting method was validated on two sets of synthetic images. To this purpose, we employed the algorithm for artificial retinal image simulation described by Mariotti and Devaney [250]. The outline of this method was described in Subsection 4.4.1.

The density of the human photoreceptor mosaic peaks in the fovea and declines rapidly when moving away from the fovea [30]. Therefore, in the images representing the section of retina closer to the fovea, the cones are densely packed and image quality is generally poorer due to optical limitations, thus it is harder to identify photoreceptor cells [83], [200]. The amount of blur in the retinal images has a much greater effect on the accuracy of cone detection [250]. Therefore, in order to choose reference images for the synthetic data generation, the sharpness measure (BM_1) was calculated for each image in the processed AO retinal dataset. According to these calculations, we chose two images from two different retinal locations: the image with the lowest sharpness measure value taken at the area closer to the fovea and the image with the highest sharpness measure acquired in the parafoveal area. Based on these images, two sets of ten artificial retinal images of size 222 x 222 pixels were generated, resembling the properties of the retina at 0.59 mm (set A), i.e. closer to the fovea, and at 1.1 mm (set B) eccentricity from the fovea respectively, i.e. in the parafoveal area. In this way, we were able to perform evaluation of the cone counting methods at the two extremes, i.e. when retinal image quality is low and high.

To verify that the proposed method is applicable on retinal images of various quality, we neglected the previous stage of image deconvolution and as a reference took an image quality produced after the registration of retinal datasets. The discussion on how the image deconvolution facilitates the automated cone counting is presented in Subsection 5.2.6. Synthetic images were produced from the background image – a Voronoi diagram – and images with randomly distributed disks. Both the background and the image with disks were blurred with a Gaussian filter. To accommodate for the residual blur after AO correction, the cut-off frequencies were set to 0.11 and 0.17 cycles/pixel for the background and the image with disks correspondingly. The intensity levels of the blurred image with disks were scaled by 0.5 before being summed with the background image. To account for residual noise, Gaussian noise –with a mean of 0 and a variance of 0.0001 – was added to the resulting

image, which was normalized from the original range of [0, 2^{16}-1] to [0, 1]. Figure 5.4 shows an example of generated synthetic images with the corresponding AO-corrected retinal images, processed as described.

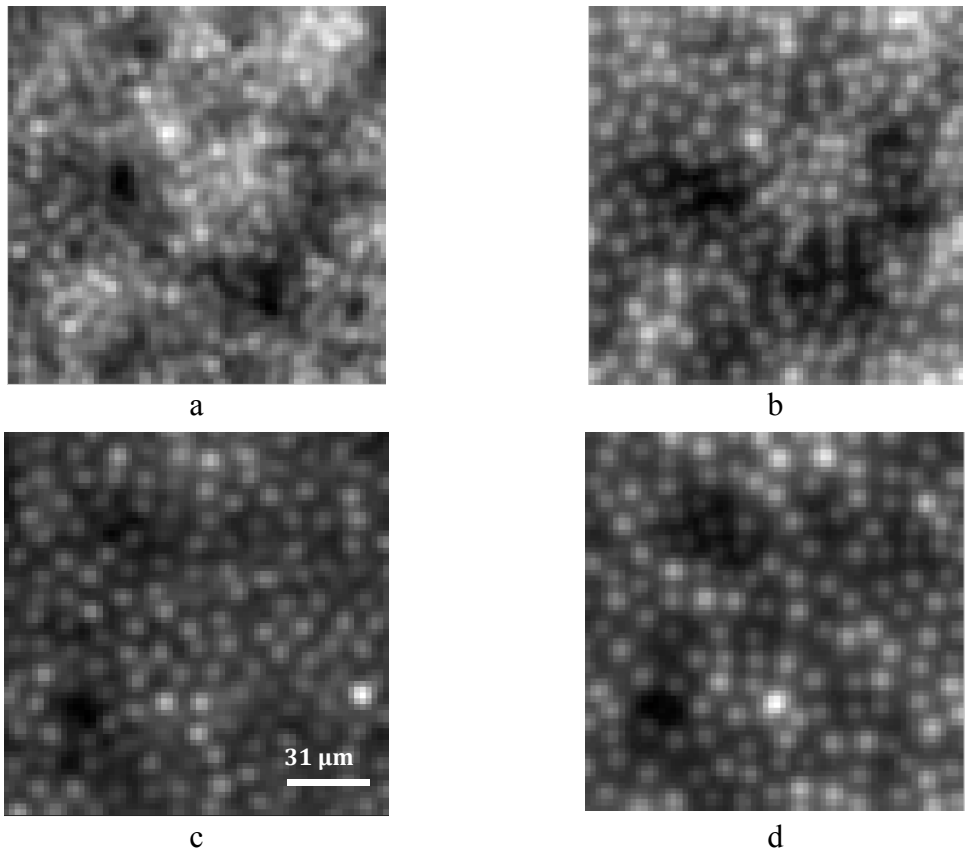


Figure 5.4: A set of processed AO-corrected and synthetic images at different retinal locations. (a) AO retinal image at 0.59 mm eccentricity; (b) synthetic image imitating the retina at 0.59 mm eccentricity; (c) AO retinal image at 1.1 mm eccentricity; (d) synthetic image imitating the retina at 1.1 mm eccentricity. The scale bar is 31 μm.

The generated stack of images was further analysed by calculating the sharpness measure [204], image contrast [209] and variance of the generated images for ten images in each set. Comparison between synthetic and reference AO retinal images, obtained after illumination compensation, noise suppression and image registration, shows a similar range of values for the two image datasets (Table 5.1).

In high-resolution retinal images, the scale of the photoreceptor cones varies across the retina. Depending on the retinal eccentricity, the cone diameter can be between 2 to 4 pixels, thus the corresponding Gaussian kernels of the smoothing function in Equation (5.3) are set

in the range of 0.5 to 1. It was found that N = 20 for a number of smoothing scales is sufficient to capture photoreceptor cells of all sizes. The kernel and the size of the LoG filter were set to 0.5 and 20, respectively.

	Image contrast (mean±SD)	**Image variance (mean±SD)**	**Sharpness measure (mean±SD)**
Retinal images, 0.59 mm	0.0179±0.0013	0.0072±0.0006	0.1680±0.0114
Synthetic images, 0.59 mm	0.0203± 0.0023	0.0081±0.0009	0.1632±0.0197
Retinal images, 1.1 mm	0.0176±0.0016	0.0024±0.0002	0.2815±0.0105
Synthetic images, 1.1 mm	0.0198±0.0017	0.0027±0.0002	0.2368±0.0131

Table 5.1: Quality assessment of 10 processed AO-corrected and 10 synthetic retinal images. The values are shown as mean ±standard deviation (SD).

Figure 5.5 illustrates the steps of the proposed blob enhancement filter applied to one of the synthetic retinal images. Initially, the synthetic retinal image (Figure 5.5-b) is generated from the image with randomly distributed disks (Figure 5.5-a) and processed with the blob enhancement filter (Figure 5.5-c). The obtained image is convolved with the LoG operator, resulting in negative values for the pixels surrounding the cones (Figure 5.5-d). By setting these values to zero, the photoreceptor cells can be easily segmented (Figure 5.5-e). A binary mask is obtained by thresholding the image. A global image threshold value was calculated using the Otsu's method [265]. Experimentally, it was determined that a choice of 60% of this global image threshold value suffices for cone segmentation from the background. The resulting binary image (mask), using 60% of the global threshold value, is shown in Figure 5.5-f. Finally, the corresponding cone coordinates are calculated as the local maxima of the original image (Figure 5.5-b) within the cone locations specified by the binary mask (Figure 5.5-f). The detected cones overlaid on the synthetic retinal image are presented in Figure 5.5-g. For visualization purposes, the detected cone locations are also shown on the image with disks, produced at the first step of the synthetic retinal image generation (Figure 5.5-h). The photoreceptor cells located at the boundaries of the image are excluded from the counting procedure.

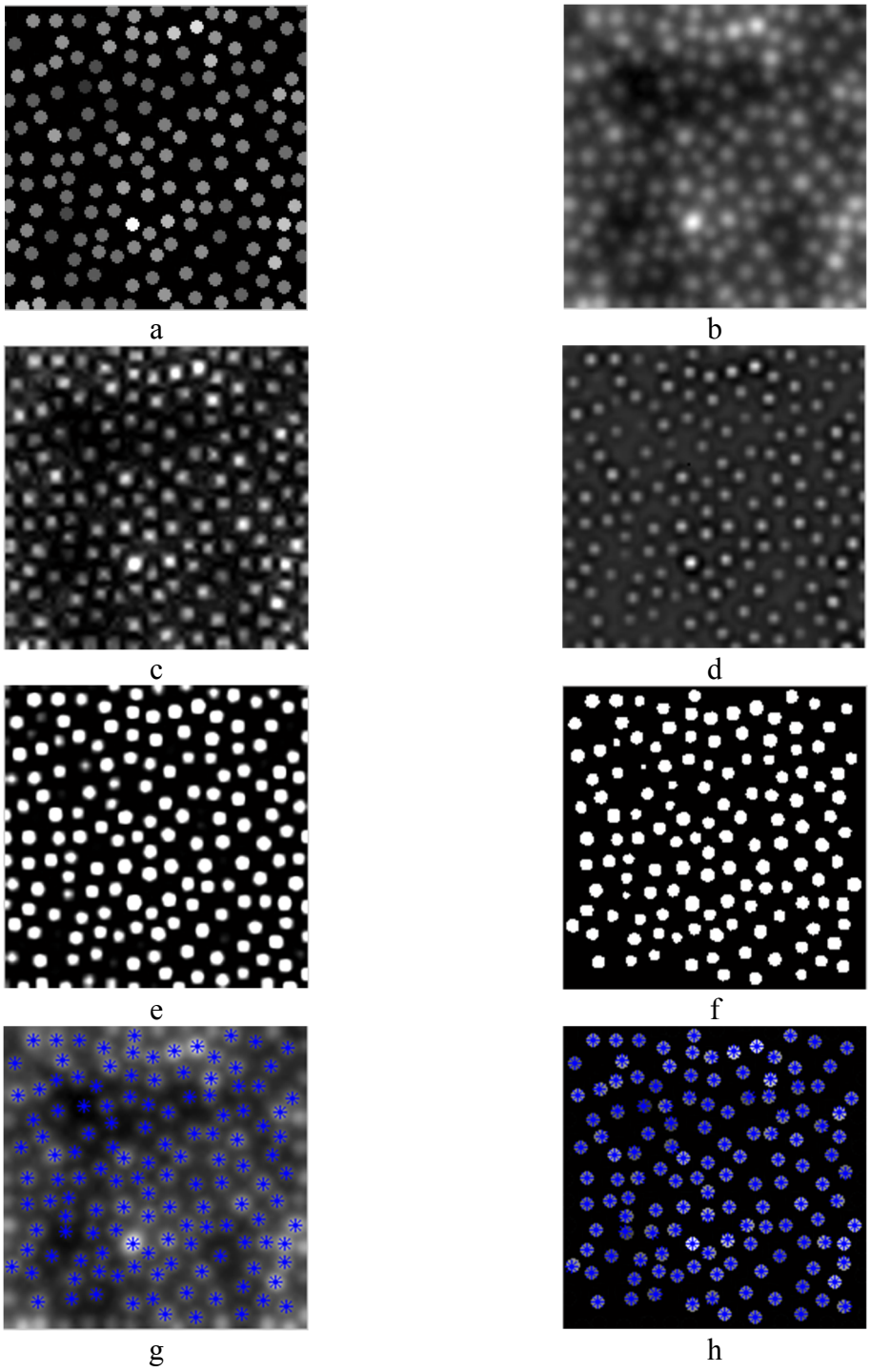


Figure 5.5: Step-by-step results of Hessian-LoG filtering for cone detection on a synthetic retinal image. (a) Image with randomly distributed disks; (b) synthetic retinal image; (c) image (b) processed with the blob enhancement filter; (d) image (c) convolved with the LoG operator; (e) image (d) with negative values set to 0; (f) binary mask with the boundary cones excluded; (g) result of cone detection overlaid on image (b) without the boundary cones; (h) result of cone detection overlaid on image (a) without the boundary cones.

5.2.3 Cone Counting on Synthetic Data

The proposed cone counting algorithm was tested on two sets of 10 synthetic images (each of size 222 x 222 pixels which corresponds to 178x178 μm on the retina), imitating the properties of the retina at 0.59 mm (set A) and 1.1 mm (set B) eccentricity from the fovea. The calculated cone density estimates are compared against the results obtained with the Li and Roorda algorithm [79]. This method was chosen as a benchmark for this study as it is one of the most commonly used cone counting methods. Moreover, a comparison study carried out by Mariotti and Devaney [250] using the free response operating characteristic curves showed that the Li and Roorda algorithm performs better than the method of Xue et al. [80] and a software package used for stellar imaging IRAF/DAOPHOT [266]. As the cone density and cone location are known through the process of synthetic image generation, it is straightforward to evaluate the accuracy of cone detection methods. The number of correctly identified cones (true positives, TP), the number of missed cones (false negatives, FN) and the number of objects that have been incorrectly identified as cones (false positives, FP) were calculated for each image in the two sets using the proposed method and the Li and Roorda algorithm. The image with randomly distributed disks (Figure 5.5-a) was used to discriminate between the TP and FP counts as shown below:

$$\begin{aligned} \text{If} \quad & I(x_i, y_i) > 0, \qquad i = 1{:}M \\ & TP = TP + 1 \\ \text{Else} \quad & FP = FP + 1, \end{aligned} \tag{5.6}$$

where I is the image with randomly distributed disks used for the generation of synthetic image, (x_i, y_i) stands for the i-th set of the detected cone coordinates, defined as the local maxima of the original image within the cone locations specified by the binary mask, and M is the total number of cones detected by the algorithm.

Despite the rapid development of automated methods for cone density calculation, manual counting is still used as the reference for performance evaluation of automated cone counting methods [78], [200, 201]. For this reason, four qualified researchers from Leipzig University Hospital were asked to carry out manual counting on the generated synthetic datasets (sets A and B). Equation (5.6) was used for calculating the number of TPs and FPs in the automated cone counting methods. However, it is not applicable for the manually labelled images. Due to the difficulty of accurate localization of cone coordinates by the observers,

a visual comparison between manually labelled synthetic images and the images with disks used for generation of the corresponding synthetic images (as shown in Figure 5.5-a) was used to calculate the number of TPs and FPs. The values of TPs, FPs and FNs obtained from four observers were averaged and compared with the results of the automated cone counting methods.

The corresponding percentages of TP, FP and FN were calculated according to Equation (5.7) and averaged for each set:

$$TP_{ratio} = \frac{TP}{N} \times 100\%,$$

$$FP_{ratio} = \frac{FP}{N} \times 100\%, \qquad (5.7)$$

$$FN_{ratio} = \frac{N - TP}{N} \times 100\%,$$

where N is the predefined number of cones in the synthetic image. Table 5.2 summarizes the results for sets A and B.

	TP ratio	**FP ratio**	**FN ratio**
Proposed method, set A	98.1%	0.06 %	1.9%
Li and Roorda, set A	89.8%	2.3%	10.2%
Manual Counting, set A	95.6%	0.009%	4.4%
Proposed method, set B	99.4%	0.2%	0.6%
Li and Roorda, set B	97.9%	1.7%	2.1%
Manual Counting, set B	98.5%	0.001%	1.5%

Table 5.2: Average TP, FP and FN ratios for sets A and B obtained by the proposed method, the algorithm of Li and Roorda and manual counting.

As shown, in set B where the cone distribution is sparser and the image quality is generally better, the accuracy of correct cone identification is very high for both automated methods. Out of an average of 1521 cones, 1513 are correctly detected by the proposed algorithm and 1489 cones are detected by the Li and Roorda algorithm, which is equivalent to 99.4% and 97.9% accuracy, respectively. In set A, the photoreceptor cells are closely clustered and the image sharpness is significantly poorer. This results in a lower detection rate for both

automated cone counting methods. Out of 2179 cones, 2138 are detected by the proposed method and only 1957 by the approach of Li and Roorda, which corresponds to 98.1% and 89.8% accuracy, respectively. Apart from having a significantly lower detection rate, the Li and Roorda algorithm produces a high number of false positives. Figure 5.6 illustrates the results of cone detection using both methods on a section of two synthetic images. False negatives and false positives are marked with white solid and white dotted circles, respectively.

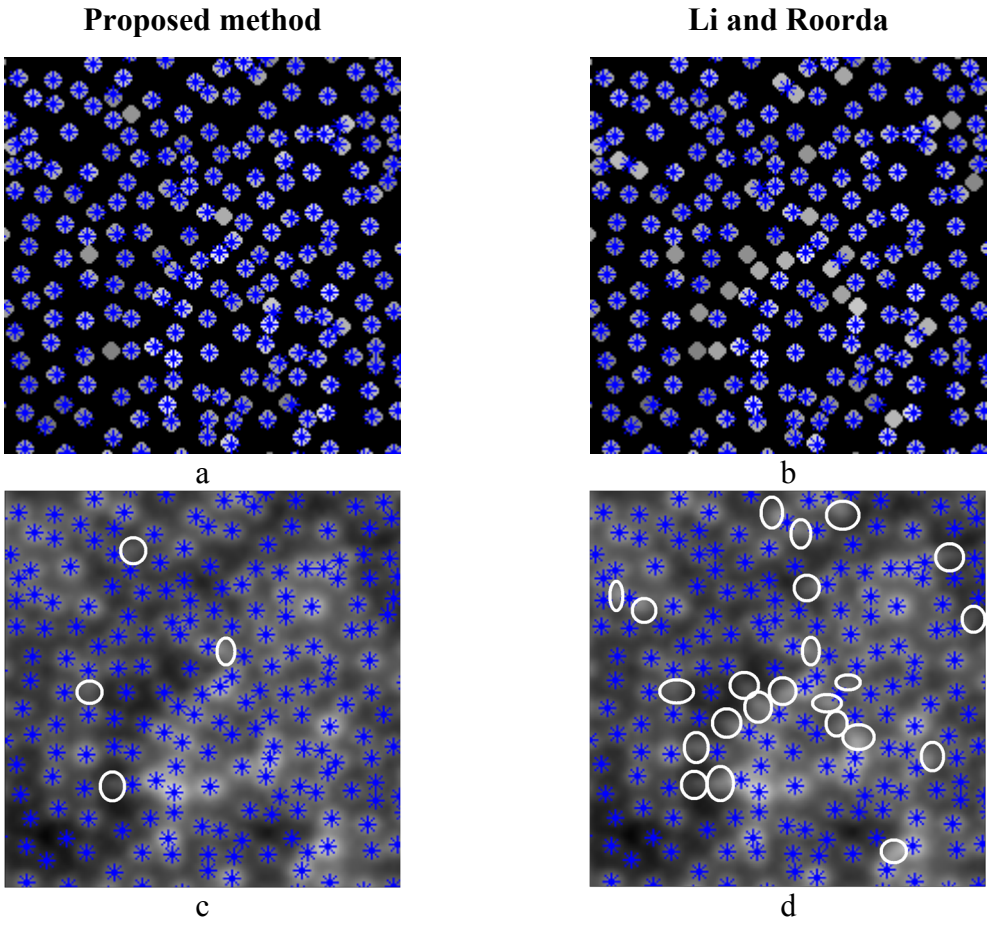


Figure 5.6: Results of cone detection obtained by the proposed method and the algorithm of Li and Roorda; (a) and (b) cone coordinates overlaid on the image with disks from set A; (c) and (d) cone coordinates overlaid on the synthetic retinal image from set A; (e) and (f) cone coordinates overlaid on the image with disks from set B; (g) and (h) cone coordinates overlaid on the synthetic retinal image from set B.

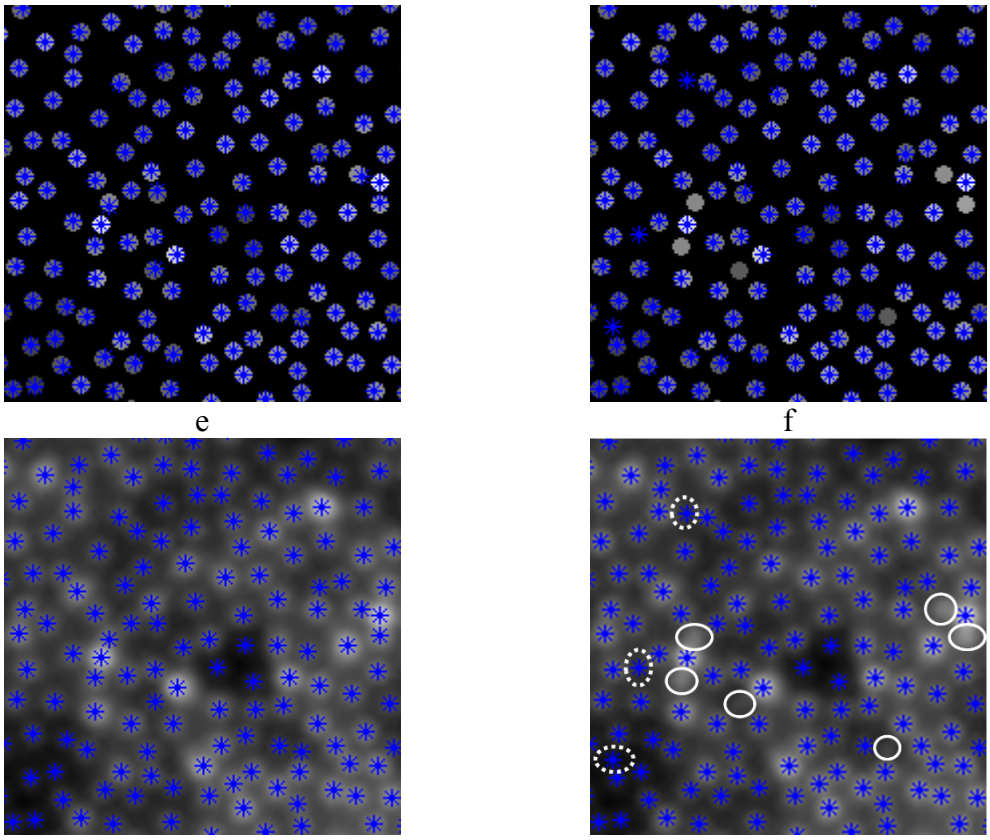


Figure 5.6 (Cont.): Results of cone detection obtained by the proposed method and the algorithm of Li and Roorda; (a) and (b) cone coordinates overlaid on the image with disks from set A; (c) and (d) cone coordinates overlaid on the synthetic retinal image from set A; (e) and (f) cone coordinates overlaid on the image with disks from set B; (g) and (h) cone coordinates overlaid on the synthetic retinal image from set B.

The manual counts obtained by the observers showed a similar dependency between detection rate and retinal location. Overall, the performance of manual counting appeared to be lower than the proposed Hessian-LoG filter, but higher than the Li and Roorda algorithm. This can be explained by human error as well as the difficulty of differentiating between the cones in the human eye, particularly in the images with densely populated cones (set A). In order to assess the inter-observer reliability in this experiment, the coefficient of variation (CoV), defined as the ratio of the standard deviation to the mean, and Cronbach's alpha coefficient [267] were calculated for the manual counts from four observers in set A and B. The CoV defines the amount of dispersion in the observers' ratings. Cronbach's alpha coefficient is useful for understanding the extent to which the ratings from a group of

observers hold together to measure a common dimension. The inter-observer counts demonstrated a moderate variation and reliability, with the CoV of 2.4% and Cronbach's alpha coefficient of 0.77 for set A. In set B, the inter-observer variation was found to be lower, with the CoV of 1.3% and reliability coefficient of 0.95. This correlates with the fact that in set A, cones are harder to be identified due to their dense arrangement, therefore a larger variation between the observer's counts is expected.

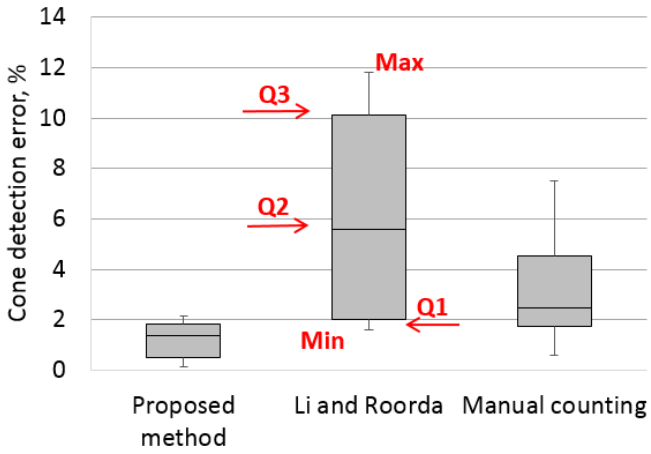


Figure 5.7: Box-and-whisker plot showing the cone detection error expressed as percentage difference between the proposed method, the Li and Roorda algorithm, manual counting and GT. The size of each bar is defined by a minimum (Min) and a maximum (Max) cone detection error. Q2 represents the median error; Q1 and Q3 are the lower and upper quartiles, respectively.

Box-and-whisker plot was used to further analyse the performance of the examined cone counting methods. The cone detection error was calculated for each image and expressed as percentage difference between the number of TPs obtained by the proposed method, the Li and Roorda algorithm, manual counting and GT (Figure 5.7). The proposed method appeared to have the smallest median error in cone detection (1.4%) as well as the smallest variance. The upper quartile of the detection error (Q3) by the proposed method, corresponding to 75% of the data, is well beyond the median values produced by the Li and Roorda algorithm and manual counting. Due to a large number of FNs obtained in the set A, the algorithm of Li and Roorda showed the largest variance and median detection error (5.6%) amongst the tested methods. The results obtained by the observers showed a moderate detection error of 2.5%.

	Proposed method	Li and Roorda	Manual counting
ρ_c	0.996	0.858	0.959
p-value	p<0.001	p<0.001	p<0.001
95% CI	0.993–0.997	0.781–0.909	0.930–0.977
(a)			
CoV	0.6%	3.2%	1.5%
(b)			
t-value	6.43>2.09	5.72>2.09	6.14>2.09
t_{crit}	2.09	2.09	2.09
p-value	p<0.001	p<0.001	p<0.001
Mean Difference	2.46	12.68	5.85
95% CI	1.66–3.26	8.04–17.31	3.86–7.84
(c)			

Table 5.3: Results of the reproducibility test showing (a) the concordance correlation coefficient ρ_c with p-values and confidence intervals (CI); (b) CoV; (c) results of the paired t-test showing associated t-test statistics and mean differences for the cone count estimates obtained by the proposed method, the algorithm of Li and Roorda and manual counting in respect to the GT.

To evaluate the reproducibility of the measurements, Lin's concordance correlation coefficient [268] was calculated for cone counts obtained by the tested methods and GT (Table 5.3-(a)). The advantage of this measure over the Pearson correlation is that in addition to assessment of how close the data points are distributed about the line of best fit, concordance correlation also measures how far that line is to equality, i.e. 45-degree line representing perfect agreement. Overall, the tested models displayed good agreement with regards to the GT counts, with the concordance correlation coefficients of 0.996, 0.858, 0.959 ($p<0.05$) and CoV of 0.6 %, 3.2% and 1.5% for the proposed method, the Li and Roorda algorithm and manual counting, respectively. In addition, a paired t-test was performed in order to analyse whether there is a systematic difference between the measurements obtained with the examined methods and the GT (Table 5.3-(c)). This test checks for acceptance or rejection of the null hypothesis which states that any differences between the sets of measurements are due to random rather than systematic errors. In all

cases, the calculated t-test statics appeared to be higher than the corresponding t-critical values, t_{crit}, with p-values < 0.05. Significant outcome implies that the null hypothesis is rejected thus there is an evidence of a systematic difference in the cone density measurements. Table 5.3-(c) summarizes the estimated mean differences and corresponding CIs for each pair of measurements. As in previous studies, the mean difference between the cone counts obtained with the proposed methods and the GT appeared to be smaller than those estimated by the Li and Roorda algorithm and manual counting.

5.2.4 Cone Counting on AO Retinal Images

The proposed algorithm was tested on ten datasets of AO high-resolution retinal images. Each set of images was processed in order to compensate for the noise in the system with the proposed image processing framework as described in Chapter 3. Cone density was calculated on sampling windows of 120 x 120 μm in 10 processed high-resolution retinal images acquired at different retinal locations. The performance of the proposed method was compared with the algorithm of Li and Roorda [79] and a proprietary software from Imagine Eyes (AOdetect v0.1, Imagine Eye, Orsay, France). As manual counting was used as a reference for performance evaluation on the synthetic data, the results obtained by the three methods on the AO retinal images were also validated against manual counts of cone density, calculated by four independent observers. The cone counting method developed by Imagine Eyes was chosen as a benchmark for this study as there is a growing number of clinical studies based on the first commercially available compact AO instrument (rtx1, Imagine Eyes,Orsay, France) and its dedicated software for automated cone counting. Due to the proprietary nature of the software, only retinal images acquired with the AO instrument can be processed with the automated cone counting procedure of Imagine Eyes software. Hence, this method was excluded from the previous evaluation study on the synthetic data.

The cone density estimates obtained by the three automated methods and average numbers of manual cone counts for each image are presented in Table 5.4. The inter-observer counts showed a CoV of 2.7% and Cronbach's alpha coefficient of 0.99. However, a high reliability measure in this experiment might be attributed to unequal variances in the scores across the images, due to difference in retinal eccentricity.

Image number	Retinal Location (mm)	Imagine Eyes	Proposed method	Li and Roorda	Manual counting
1	1.27 N[a]	215	215	194	205
2	0.75 N	207	208	212	210
3	0.67 N	228	219	227	218
4	0.59 N	289	307	264	296
5	0.59 N	304	301	270	302
6	0.84 N	231	227	230	220
7	0.84 T[b]	339	344	311	346
8	0.89 N	259	267	245	242
9	0.89 N	250	260	244	262
10	0.89 T	334	326	294	319

[a] Nasal retina

[b] Temporal retina

Table 5.4: Cone density estimates obtained by the three automated methods and the average values of manual cone counts from four observers for 10 AO-corrected retinal images.

Image number	Imagine Eyes, %	Proposed method, %	Li and Roorda, %
1	4.9	4.9	5.4
2	1.4	1	1
3	4.6	0.5	4.1
4	2.4	3.7	10.8
5	0.7	0.3	10.6
6	5	3.2	4.5
7	2	0.6	10.1
8	7	10.3	1.2
9	4.6	0.8	6.9
10	4.7	2.2	7.8

Table 5.5: Percentage differences between cone density estimates obtained by the three automated methods and average manual cone counts for 10 AO-corrected retinal images.

Table 5.5 shows cone detection errors expressed as percentage differences between cone density estimates obtained by the three automated methods and average manual cone counts

for 10 AO-corrected retinal images. Amongst the evaluated images, the proposed cone counting method showed the largest error with respect to manual counting for the image number eight (Table 5.4). This can be explained by the low contrast of the image and therefore difficulty for the observers to identify some poorly resolved cones, while the proposed method as well as Imagine Eyes software were able to detect more cones. To ease the interpretation of the results, the performance of the automated cone counting methods was evaluated as a function of the error expressed as percentage difference with respect to manual counting and presented as a box-and-whisker plot (Figure 5.8). It can be seen that the proposed method has the smallest median error in cone detection (1.6%). The software of Imagine Eyes has the smallest variance, thus showing a more consistent detection rate amongst the tested methods with a median detection error of 4.6%. The upper quartile of the detection error by the proposed method, corresponding to 75% of the data, is well beyond the median values produced by the Li and Roorda algorithm and the Imagine Eyes software. Overall, the tested models displayed good agreement with regards to the cone counts obtained by the observers, with the concordance correlation coefficient of 0.975, 0.979 and 0.876 ($p<0.05$) and CoV of 1.8%, 1.3% and 3.2% for the Imagine Eyes software, the proposed method and the Li and Roorda algorithm, respectively (Table 5.6-(a), (b)).

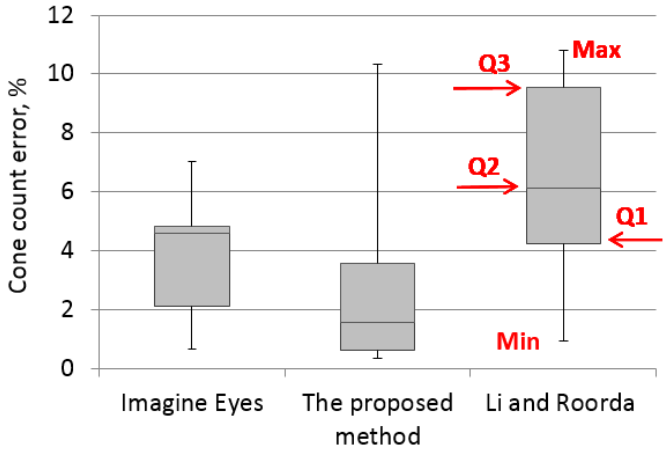


Figure 5.8: Box-and-whisker plot showing the cone detection error expressed as percentage difference between the proprietary software of Imagine Eyes, the proposed method, the Li and Roorda algorithm and manual counting. The size of each bar is defined by a minimum (Min) and a maximum (Max) cone detection error. Q2 represents the median error; Q1 and Q3 are the lower and upper quartiles, respectively.

A reproducibility study performed using a paired t-test (Table 5.6-(c)) resulted in insignificant t-statistics for the cone densities obtained by the software of Imagine Eyes and the proposed method, with the mean differences of 3.6 and 5.4 cones, respectively. Therefore, there is no evidence to reject the null hypothesis that the mean difference is zero, and the observed variations between the manual counts and the cone estimates obtained by the two methods are due to a random error. However, the Li and Roorda algorithm showed a statistically significant error in respect to manual counts, with the mean difference of 12.9 cones. This means that in comparison with the proposed method and the software of Imagine Eyes, the Li and Roorda algorithm produces a systematic bias in the cone density measurements in respect to manual counts.

	Imagine Eyes	**Proposed method**	**Li and Roorda**
ρ_c	0.975	0.979	0.876
p-value	p<0.001	p<0.001	p<0.001
95% CI	0.926–0.992	0.937–0.993	0.744–0.942
	(a)		
CoV	1.8%	1.3%	3.2%
	(b)		
t-value	1.10	1.98	2.28
t_{crit}	2.26	2.26	2.26
p-value	0.29	0.078	0.048
Mean difference	3.6	5.4	12.9
95% CI	-3.79–10.99	-0.76–11.56	0.11–25.68
	(c)		

Table 5.6: Results of the reproducibility test showing (a) the concordance correlation coefficient ρ_c with p-values and CIs; (b) CoV; (c) results of the paired t-test showing associated t-statistics and mean differences for the cone density estimates obtained by the three automated methods and average manual counts.

To conclude, the proposed method and the software of Imagine Eyes showed a similar performance in terms of agreement with manual counting. While the software of Imagine Eyes produces more consistent results, with low variance and mean cone difference, the cone

estimates obtained by the proposed method are in closer agreement with the manual counting, based on the concordance correlation coefficient and median detection error expressed as a percentage difference.

In Figure 5.9 a few examples are presented of cone detection using the proposed method and the algorithm of Li and Roorda. White circles highlight the cones detected by one of the examined methods but missed by another. From these images, it becomes apparent that the algorithm of Li and Roorda tends to merge two closely located cones into a single one, due to the use of the dilation operator and therefore introduces a systematic error in the identification of cone coordinates.

The information content in the image produced after Hessian-LoG filtering is solely related to the photoreceptor cones (Figure 5.10-b), and therefore it can be used to produce an image where other retinal features remain preserved, while the contrast of photoreceptor cones is significantly increased. For this purpose, the intensity levels of the Hessian-LoG filtered image were firstly shifted by unity and the resulting image was multiplied with the corresponding retinal image obtained after following the stages of illumination compensation, noise suppression and image registration. Figure 5.10 illustrates the result of this process. Visual inspection of the images enhanced with the Hessian-LoG filter and the corresponding retinal images confirms that the intensity values are increased at the cone locations after adopting this process.

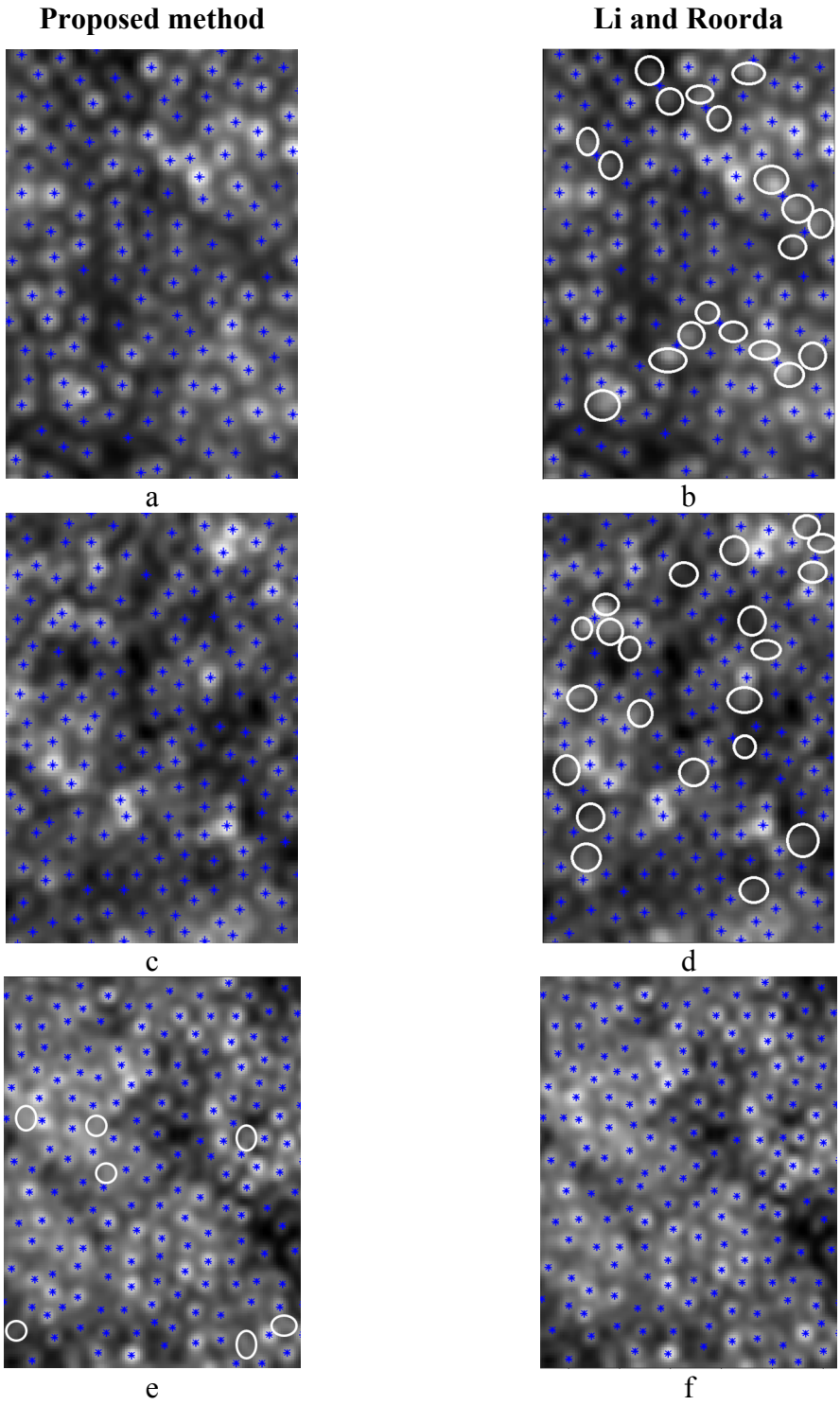


Figure 5.9: Results of cone detection on the AO high-resolution retinal images with the proposed method and the Li and Roorda algorithm at different retinal locations: (a) and (b) at 0.89 mm Nasal, (c) and (d) at 0.89 mm Temporal eccentricity, (e) and (f) at 0.6 mm Nasal. White circles correspond to the cones missed by one of the examined cone counting methods but detected by another one.

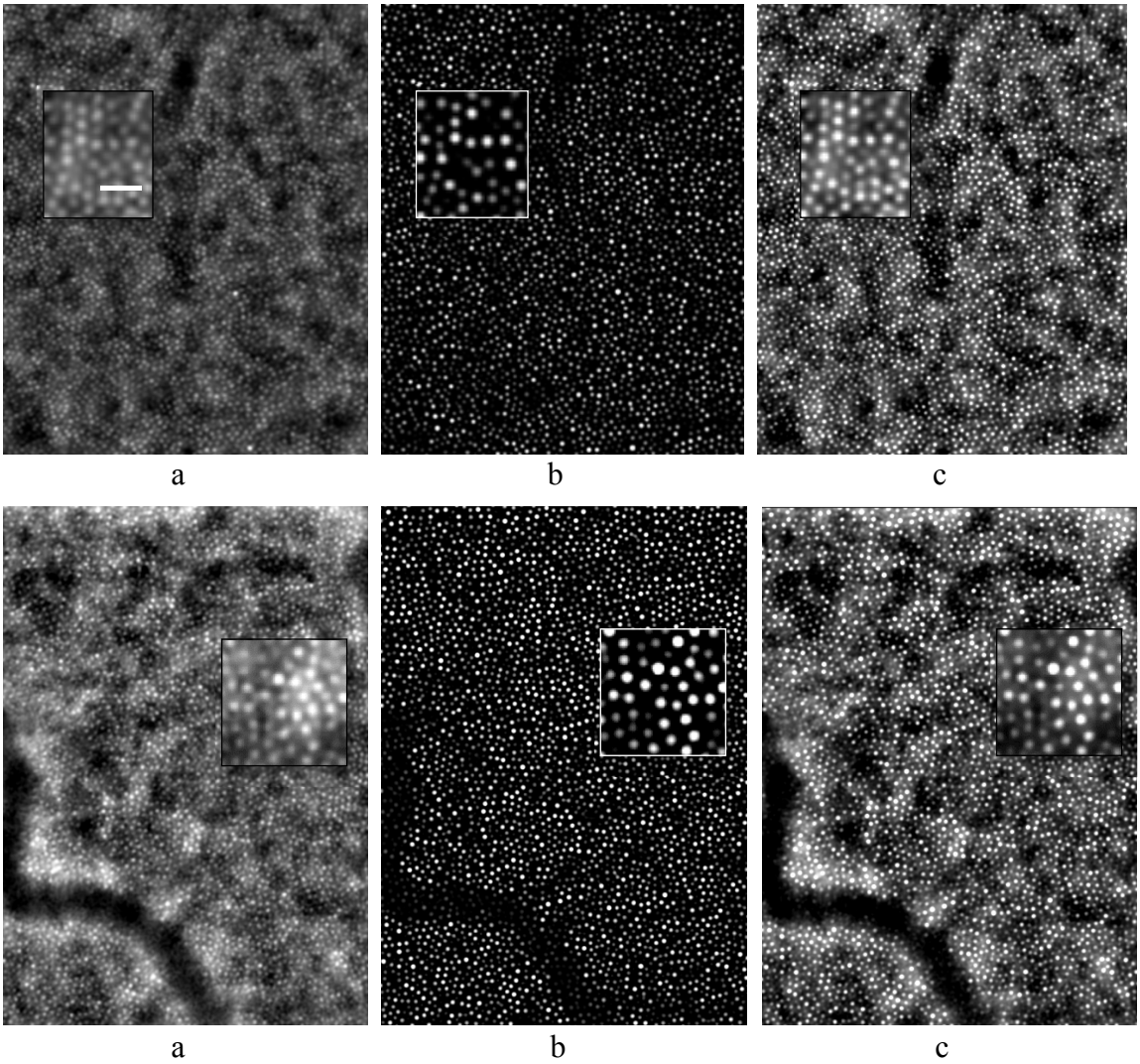


Figure 5.10: Image enhancement with the Hessian-LoG filter. (a) Processed retinal image; (b) Hessian-LoG filtered image; (c) image (a) multiplied with image (b). The scale bar is 21 μm.

5.2.5 Validation of Hessian-LoG Filtering on the Emmetropic Data Population

As part of the LIFE Child study conducted in Leipzig, Germany [269], cone packing arrangement was investigated in children and adult populations in order to reveal any differences in two groups related to age and retinal development. The thirteen subjects that participated in this study were classified into two groups based on their age. Group 1 was composed of nine healthy children (age range 9-18 years, mean 13.7) and group 2 consisted of four healthy adults (age range 30-34 years, mean 32.5). All subjects in groups 1 and 2

received a complete eye examination. Exclusion criteria for the participation in this study were any retinal pathology or media opacity and myopia/hyperopia. Spherical equivalent (calculated as mean spherical equivalent of three measurements per subject) refractive errors ranged from +0.50D to -0.50D with astigmatism less than -0.50D when referenced to the spectacle plane. All subjects had visual acuity of at least 20/20 or better, obtained with result of wavefront-based autorefraction.

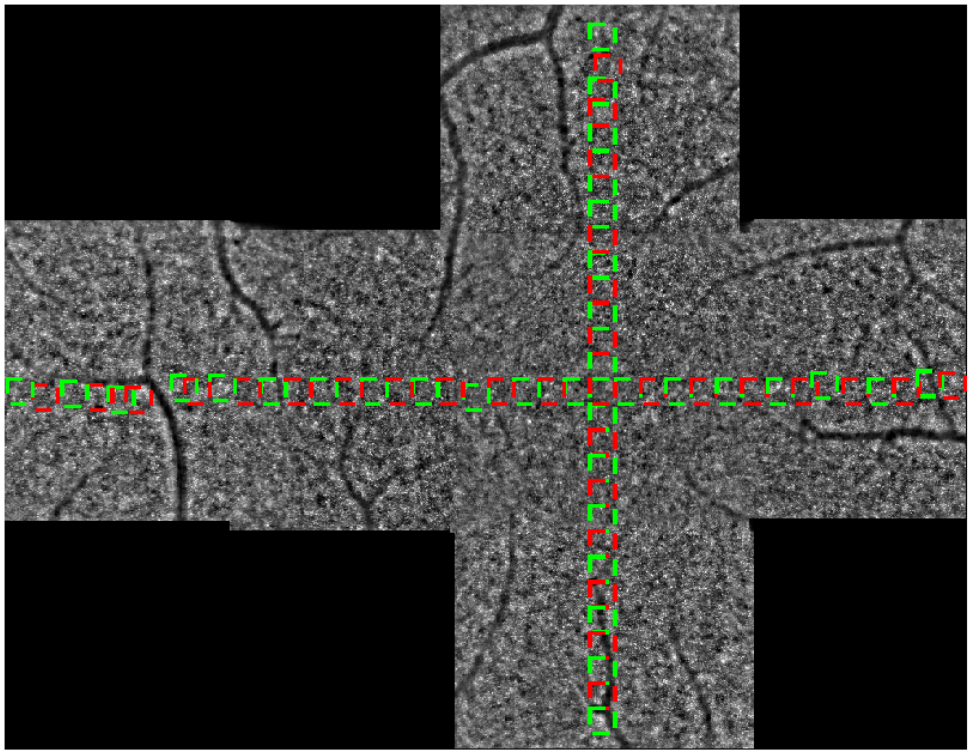


Figure 5.11: Example of retinal montage composed of six AO high-resolution retinal images. Sampling windows where cone packing density was assessed are shown with red and green rectangles.

An AO flood-illuminated instrument (rtx1, Imagine Eyes, France) was used to acquire high-resolution retinal images. To examine the distribution of cone packing arrangement across the retina, for each subject six images were taken at 3° eccentricity in the superior, inferior and nasal quadrants and at 0°, 3° and 6° eccentricities along the temporal meridian. A stack of raw images was processed with a software provided by the system's manufacturer (CK v0.1 and AOdetect v0.1, Imagine Eyes). Using that software, image frames were registered using a cross-correlation method [156] and averaged to produce a final image of a better contrast. Image frames affected by an eye blink or saccadic movements therein were

automatically excluded from the averaging. Then, images of adjacent areas were stitched with the use of pairwise stitching tool in Image J package (version 1.48v, NIH, Bethesda, MD). The obtained retinal montages were used to collect the associated retinal statistics with the proposed Hessian-LoG filter.

The number of cones and cone spacing were measured in windows of size 100x100 μm sampled at 0.3-1.2 mm along the nasal, superior and inferior meridian and 0.3-2.2 mm in temporal meridian, with the step of 0.1 mm. For each subject, eccentricity was computed as the distance between the center of each window and the fovea in pixels (fixation coordinates: x = 0°, y = 0°) and converted to mm based on the pixel to object size ratio, provided by the manufacturer for a reference axial length. Figure 5.11 shows an example of a montage image with the sampling windows where cone density was assessed.

A number of factors influence the accuracy of cone density estimation [270], one of which is the size of a sampling window. Even a slight shift in retinal location can adversely affect the reliability of this correlation. In this study, a smaller sampling window was chosen. This allowed easy localisation of an area on the retina that is not obstructed by any blood vessels without deviating too far from the designated eccentricity. The sizes of the windows were corrected for differences in axial length of each subject, based on the derived individual pixel to object size ratio.

The sampling windows were processed with the Hessian-LoG filter. As a result, a binary image was produced and the cone coordinates were calculated as the local maxima of the original image within the cone locations specified by the binary mask. The photoreceptor cells located at the boundaries of the image were excluded from the counting procedure. The obtained cone counts per window were then recalculated as cone density in cell/mm^2 by multiplying a cone number by the proportion of the 1mm^2 to the sampling window size. The inter-cell distance (ICD) was determined under the assumption that photoreceptor cells are hexagonally arranged [84]. In this way, the cone spacing can be calculated based on the cone density as follows: $ICD = \left[1000\frac{\sqrt{3}}{2D}\right]^{1/2}$, where D is the number of cones per square millimetre.

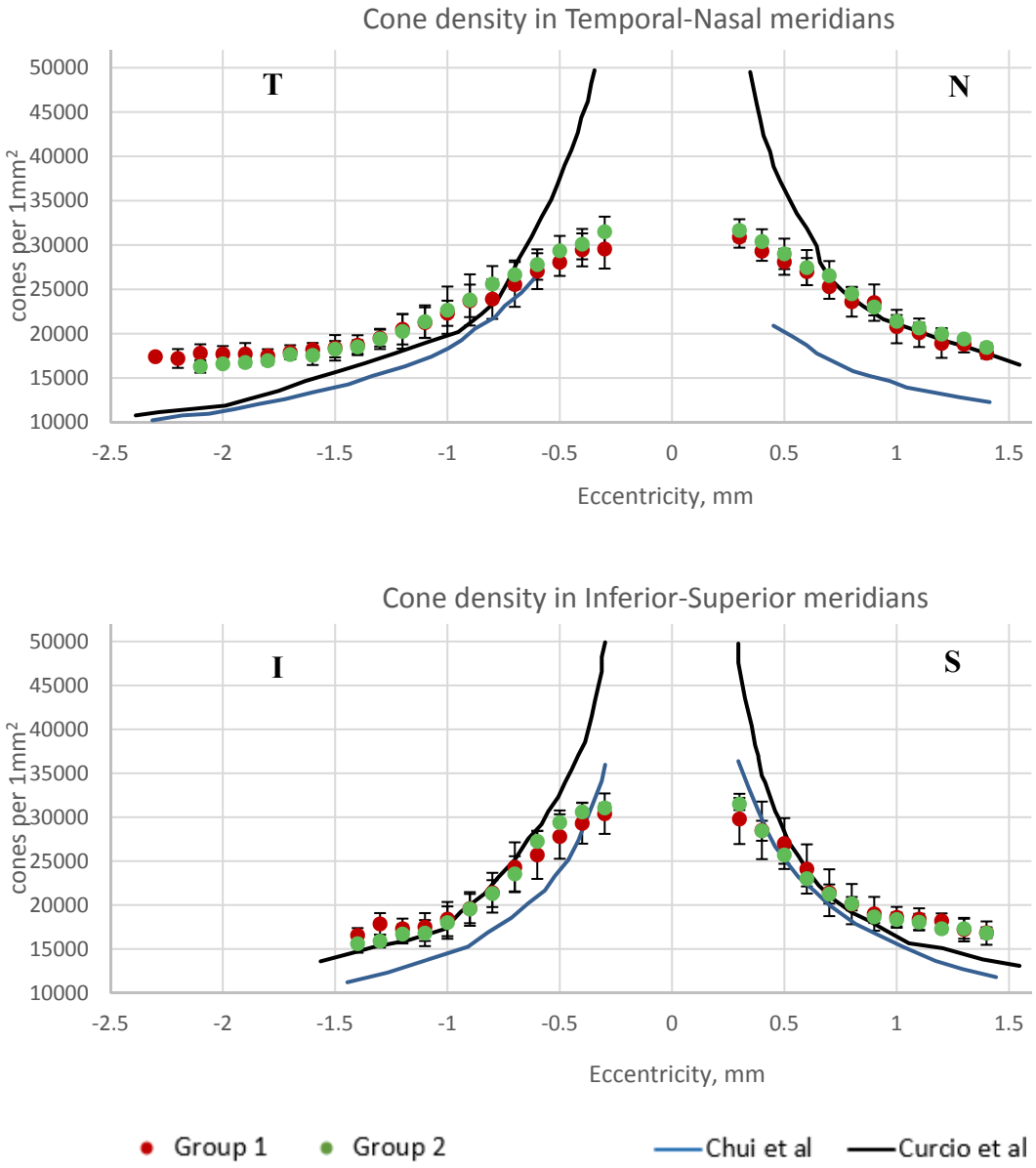


Figure 5.12: Variation of cone packing densities with eccentricity in the nasal (N), temporal (T), superior (S) and inferior (I) quadrants obtained from the study of Curcio et al. [30] (black line), Chui et al. [84] (blue line) and data from the two age groups.

The variation of cone packing density with retinal eccentricity averaged for subjects in group 1 and group 2 is shown in Figure 5.12. The data for the children and adult population showed a significant decrease in cone density at the retinal eccentricities of 0.30 mm to 1.40 mm along the nasal, superior and inferior meridians, respectively, and at the retinal eccentricities of 0.30 mm to 2.20 mm along the temporal meridian (Table 5.7). Overall, the cone

distribution of the two investigated groups appeared to be very similar, with the average CoV of 1.6%, 1.6%, 2% and 1.1% and p-values < 0.05 in the nasal, temporal, superior and inferior quadrants, respectively.

	0.3 – 1.4mm Nasal	**0.3 – 2.1mm Temporal**	**0.3 – 1.4mm Superior**	**0.3 – 1.4mm Inferior**
Group 1, cells/mm^2	17 800 ± 618 – 30 900 ± 1 205	17 200 ± 1 066 – 29 550 ± 2 211	16 850 ± 607 – 29 800 ± 2 860	16 550 ± 826 – 30 400 ± 2 302
Group 2, cells/mm^2	18 450 ± 476 – 31 650 ± 1 258	16 300 ± 698 – 31 500 ± 1 699	16 800 ± 1 329 – 31 500 ± 694	15 600 ± 1 023 – 31 050 ± 512

Table 5.7: The range of cone densities for group 1 and group 2 at the retinal eccentricities of 0.30 mm to 1.40 mm along the nasal, superior and inferior meridians, respectively, and at the retinal eccentricities of 0.30 mm to 2.20 mm along the temporal meridian. The values are expressed as mean ± SD.

Since the ICD was calculated based on the cone density measurements, the cone spacing distribution graphs showed the same trends but inversely proportional to the ones of cone density. The ICD values (expressed as mean ± SD) varied from 5.36 ± 0.19 μm to 7.04 ± 0.16 μm for retinal eccentricities of 0.30mm to 1.40mm as an average across four meridians in group 1 and from 5.25 ± 0.09 μm to 7.08 ± 0.18 μm in group 2.

In order to verify the results obtained with the Hessian-LoG filter, the data in the current study was compared with cone density established based on the histology data of Curcio et al. [30] (black line in Figure 5.12) and results of an AOSLO study by Chui et al. [84] (blue line in Figure 5.12). The measurements in the study of Curcio et al. were collected from the retinas of 49 healthy eye bank donors (age range 20-44 years). Eye examination performed prior to the surgery showed visual acuity of 20/20 in each eye. Cone counts were made using NDIC-video images of the photoreceptor layer at the level of inner segments. In the study of Chui et al., eleven healthy subjects (age range 21–31 years, mean, 26.6) participated in the experiment. A complete eye examination showed that all subjects had best corrected visual acuity of 20/20 or better. Spherical equivalent refractive errors varied from +0.50 to −7.50 D with astigmatism less than −1.00 D when referenced to the spectacle plane. In order to investigate the correlation between the refractive error and cone density distribution, subjects were separated into three groups –five subjects with emmetropia, four subjects with low-to-

moderate myopia and two subjects with high myopia. Refractive errors in three groups ranged from −2.75 to −4.50 D, −2.75 to −4.50 D and −6.00 to −7.50 D, respectively. For comparison purposes, we used only measurements acquired from emmetropic eyes in the study of Chui et al. Therefore, it can be concluded that the data in three studies is comparable since cone density was measured in healthy emmetropic subjects of similar age at the same retinal eccentricities.

		Chui et al.	Group 1	Group 2
Nasal	ρ	0.255	0.810	0.839
	p	p<0.001	p<0.001	p<0.001
	95% CI	0.091–0.405	0.657–0.899	0.725–0.909
	CoV	20.0%	2.2%	2.7%
Temporal	ρ	0.937	0.664	0.749
	p	p<0.001	p<0.001	p<0.001
	95% CI	0.879–0.968	0.502–0.782	0.597–0.850
	CoV	4.6%	10.6%	9.9%
Superior	ρ	0.889	0.869	0.872
	p	p<0.001	p<0.001	p<0.001
	95% CI	0.759–0.951	0.717–0.942	0.768–0.931
	CoV	5.8%	4.5%	4.3%
Inferior	ρ	0.609	0.809	0.807
	p	p<0.001	p<0.001	p<0.001
	95% CI	0.359–0.777	0.589–0.918	0.567–0.921
	CoV	12.7%	7.9%	8.2%

Table 5.8: Results of the reproducibility test showing the concordance correlation coefficient ρ_c with p-values and CIs, and CoV for the measurements acquired in the study of Chui et al. and two age groups in respect to the histology data of Curcio et al. at four retinal meridians.

According to Curcio et al. [30], cone density falls steeply with increasing eccentricity and is an order of magnitude lower 1 mm away from the foveal center. The slope of the obtained cone distribution data follows the Curcio graph well, showing a steep decrease in the central area and a slow change rate at parafoveal eccentricities. Due to resolving power limitations of the AO instrument used in the current study, the foveal cones are very difficult to capture due to their small size, thus there is a larger difference in the data when compared to 0.3 - 0.5 mm eccentricities. If this area is excluded (0.3-0.5 mm), the average concordance correlation coefficient for the two age groups and histological data of Curcio et al. is 0.825,

0.707, 0.8705 and 0.808 ($p<0.05$) in the nasal, temporal, superior and inferior quadrants, respectively (Table 5.8). The data from the study of Chui et al. showed a lower agreement with the histological measurements, with the correlation coefficients of 0.255, 0.937, 0.889 and 0.609 ($p<0.05$). When the Pearson correlation is used, the correlation coefficients for the measurements of Chui et al. are higher than in two groups which means that there is a stronger linear association between the two sets of cone density measurements. Indeed, as can be seen in Figure 5.12 the cone density measurements of Chui et al. follow the curve of histological data in a more linear fashion. However, it can be also observed that the data obtained with the AOSLO has a larger error margin than the cone density distribution in groups 1 and 2, apart from the temporal meridian. This resulted in a lower concordance correlation, as this reproducibility index also accounts for the distance of regression line to a line of equality. To quantitatively analyse these differences, the CoV was calculated for the two studies (Table 5.8) in four retinal meridians. The average CoV between the results of Curcio et al. and the examined groups of the current study was found to be 2.5%, 10.2%, 4.4%, 8% in the nasal, temporal, superior and inferior quadrants, respectively. The corresponding results published by Chui et al. [84] showed the average CoV of 20%, 4.6%, 5.8%, 12.7% in the nasal, temporal, superior and inferior quadrants, respectively.

	Chui et al.	**Group 1**	**Group 2**
t-value	-7.54	-4.08	-4
t_{crit}	2.017	2.017	2.017
p-value	$p < 0.001$	$p < 0.001$	$p < 0.001$
Mean difference	-3865	-1744	-1828
95% CI	-4899 – -2830	-2606 – -881	-2608 – -1048

Table 5.9: Results of the paired t-test showing associated t-statistics and mean differences for the cone density distribution obtained in the study of Chui et al. and two age groups in respect to the histology data of Curcio et al. across four retinal meridians.

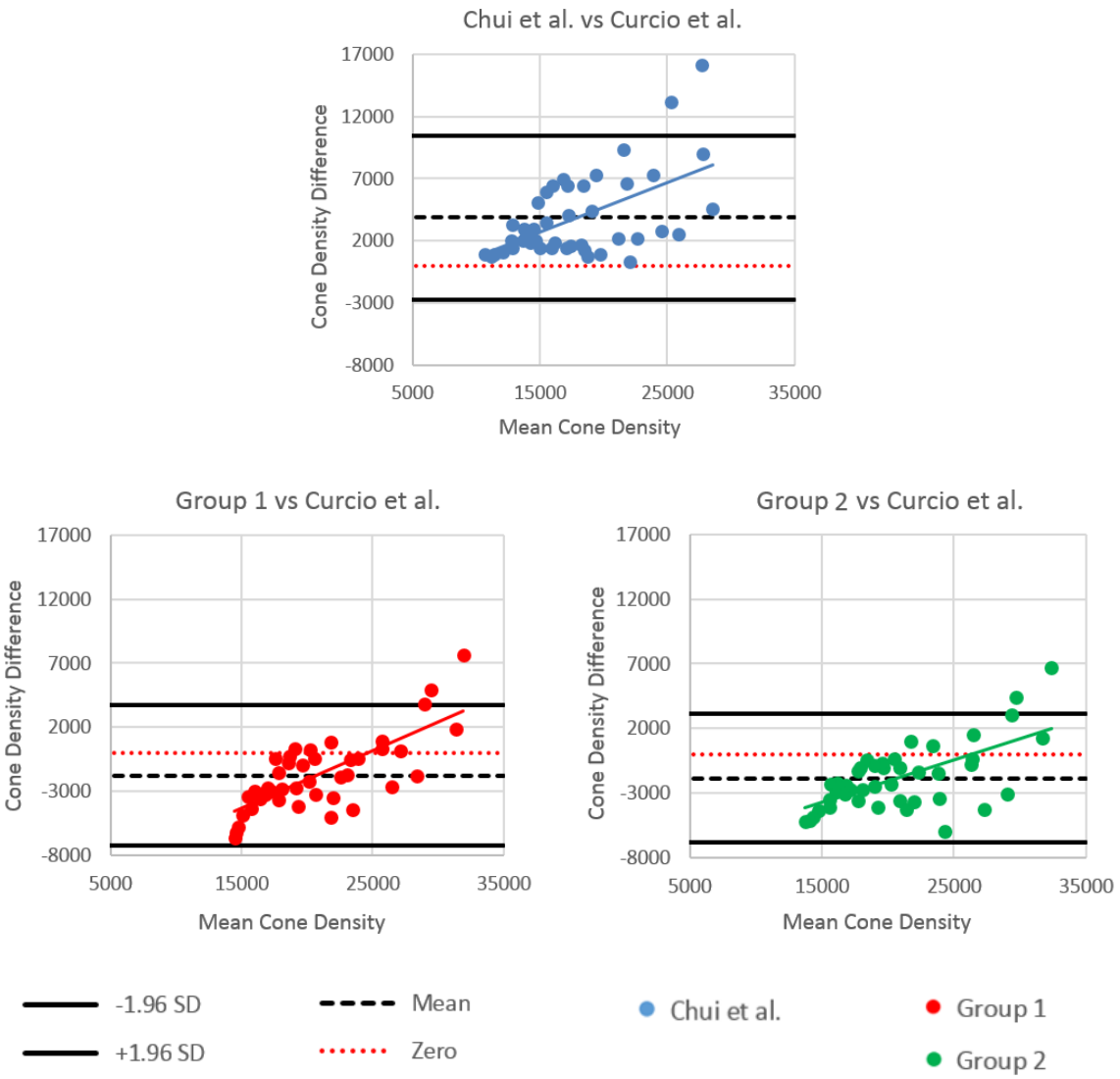


Figure 5.13: Bland-Altman plots showing differences between cone density measurements obtained from the study of Chui et al. and two age groups in respect to the histology data of Curcio et al.

Bland-Altman plots were employed to further analyse the agreement between the measurements of our study, results of Chui et al. and histological data of Curcio et al. Figure 5.13 shows the difference of the two paired measurements plotted against the mean of the two measurements. In all cases, most of the data points lie within ± 1.96 SD of the mean difference. The positive trend in the Bland-Altman plots (inclined line of the corresponding colour) implies that the higher the expected cone density the larger the error between two sets of measurements. The bias is represented by the gap between the x-axis, corresponding to the zero differences (red dotted line) and the mean difference in each pair of measurements (black dashed line). The bias in the measurements of Chui et al. (3865 cones) is larger than

in the group 1 and 2 (1744 and 1828 cones, respectively). Also, the limits of agreement defined as the mean difference ± 1.96 SD of differences (black lines) in the measurements of Chui et al. are higher than those in group 1 and 2. This correlates with the previously calculated values of CoV for the study Chui et al. and two age groups with respect to the histology data of Curcio et al. A paired t-test confirmed the significance of the bias in the measurements of Chui et al. and two age groups (Table 5.9).

The obtained cone densities in the measured parafoveal region showed a slower decrease rate than the data by Curcio et al., resulting in higher cone counts for the current data. Curcio et al. noted that at 1.3–1.4 mm cones are larger and circular in shape and rods encircle these cones. Due to resolution of the rtx1 AO device it is difficult to delineate the rods at these eccentricities. However, when examining further away from the fovea (1.5-2.2mm), rods are easier to be distinguished based on their larger size and therefore can potentially be detected by the automated cone counting algorithm. Moreover, when comparing in-vivo cone counting as presented here with histology findings of postmortem tissues, one should take into account a shrinkage effect commonly present as part of the preparation for histology. As the shrinkage does not have a uniform effect on the retina, it is difficult to factor it out during post-processing. Retinal tissue can shrink up to 10-20% during the measurements [271], thus the cone densities in the Curcio et al. paper could potentially represent data for the retina at eccentricities shifted by 0.1-0.2 mm towards the fovea. These two effects, the presence of rods and the shrinkage effect of histology, could have possibly contributed to a larger difference in parafoveal locations (1.5-2.2 mm) between the cone density estimates obtained in this study and the histology data.

In summary, the results presented here provide a baseline for analysis of cone photoreceptor packing distribution in an emmetropic child and adult population. Based on the calculated cone packing densities, further statistical correlations can be derived, such as correlation of cone packing density with axial length, age and spherical refractive error as well as investigation of regularity of cone packing arrangement. These analyses allow us to quantitatively assess the differences in cone distribution attributed to the age and retinal development in an emmetropic child population. The obtained results can be used for comparison with the data related to pathological photoreceptors in pediatric eyes.

5.2.6 Image Deconvolution followed by Hessian-LoG Filter

To evaluate how the proposed image deconvolution stage (Chapter 4) facilitates the automated cone counting we performed two studies, on the synthetic retinal data and real AO images. For the first part of this study, the test data generated for the performance evaluation of the Random Forest was used (see Section 4.4.1 and 4.5.1). The cone counts were estimated with the use of the Hessian-LoG filter in 1000 synthetically blurred images of size 126x126 pixels. Then, these images were restored with the trained Random Forest as described in Section 4.4 and the cone counts were estimated again. The number of TPs, FPs and FNs were calculated for each image as described in Section 5.2.3. Table 5.10 summarizes these results averaged for 1000 images.

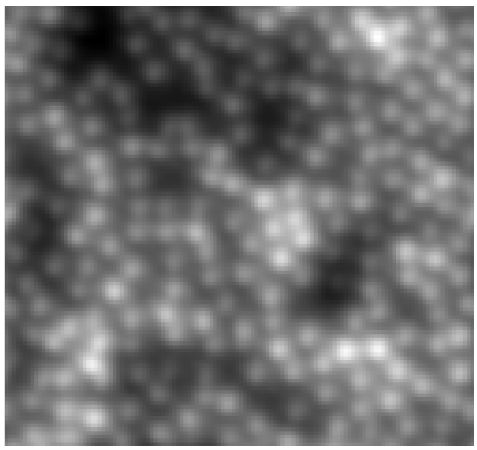
	TP ratio	**FP ratio**	**FN ratio**
Cone Counting before Image Deconvolution	97.9%	0.69 %	2.1%
Cone counting after Image Deconvolution	98.4%	0.44%	1.6%

Table 5.10: Average TP, FP and FN ratios for 1000 synthetic images obtained by the proposed cone counting method before and after image deconvolution stage.

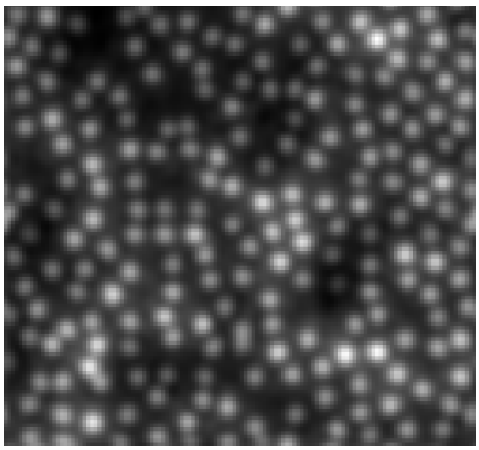
Despite the images being significantly distorted by convolution with the randomly generated blur kernels, the proposed cone counting method still performs well in both cases, with and without image deconvolution step. Successful restoration of synthetically blurred images facilitates better differentiation of cones and thus helps to reduce number of FPs and FNs, especially in the images where cones are more densely packed (Figure 5.14-g). Figure 5.14 illustrates the process of cone detection in two images, imitating the retina at 1.2 mm (Figure 5.14-a) and 0.9 mm (Figure 5.14-g) before and after performing image deconvolution. To ease interpretation, the obtained results are overlaid on the images with disks used for synthetic data generation. FNs and FPs are marked with red solid and red dotted circles, respectively. In this experiment, the boundary cones, excluded from the counting procedure, were found based on the distance criterion from the edge of the image. A shift during image deconvolution led to a few number of false positives related to the missed boundary cones. Despite that, the proportion of FPs is still low according to Table 5.10.

Cone detection in the synthetic images before image deconvolution

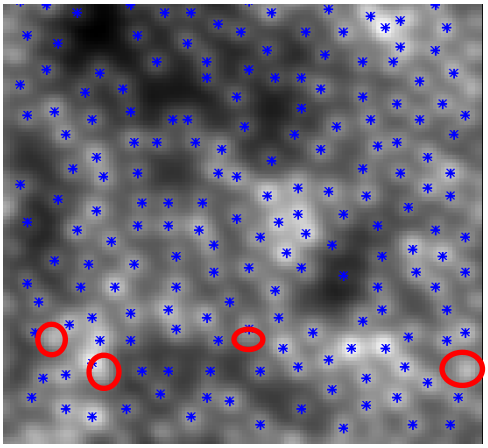
Cone detection in the synthetic images after image deconvolution



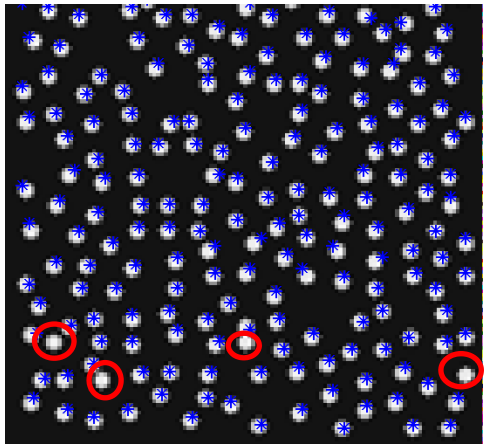
(a) Synthetic image at 1.2 mm



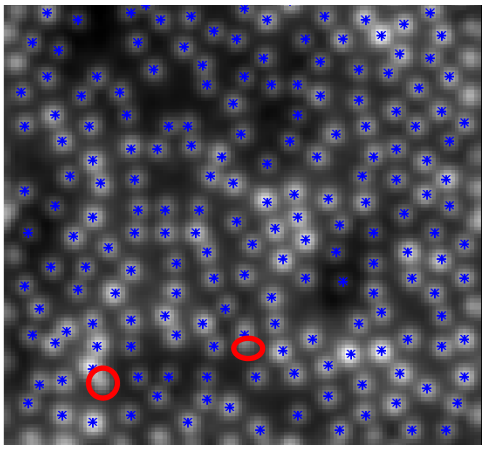
(b) Restored image (a)



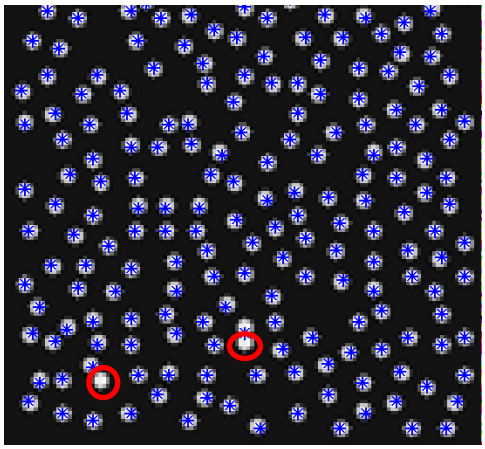
(c) Cone coordinates detected in the image before deconvolution (a)



(d) Cone coordinates detected in the image (a) and overlaid on the image with disks

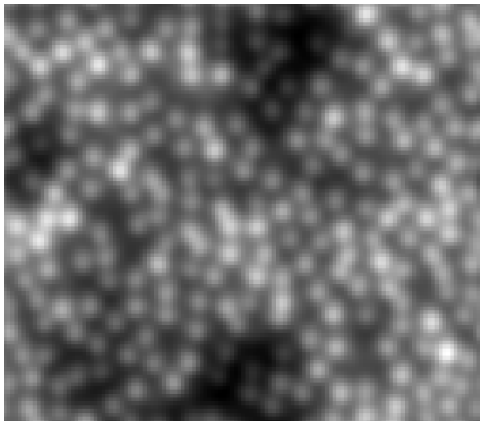


(e) Cone cone coordinates detected in the image after deconvolution (b)

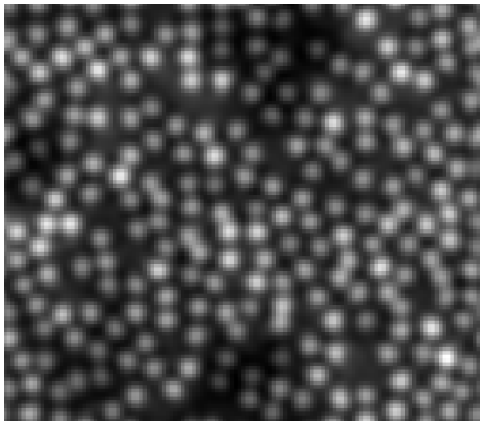


(f) Cone coordinates detected in the image (b) and overlaid on the image with disks

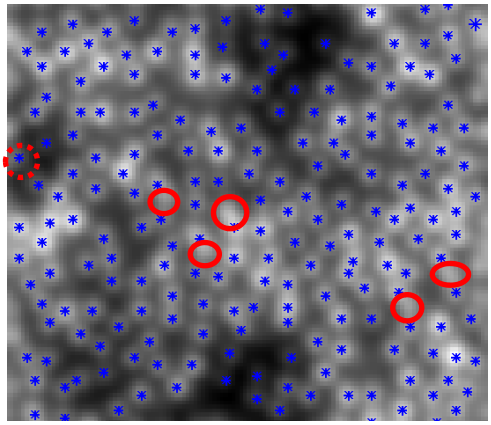
Figure 5.14: Cone detection in two synthetic images, imitating the retina at 1.2 mm and 0.9 mm eccentricity before and after image restoration. Solid red circles and red dotted circles indicate FNs and FPs, respectively.



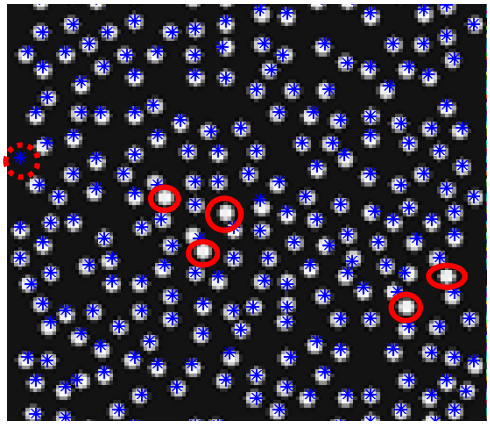
(g) Synthetic image at 0.9 mm



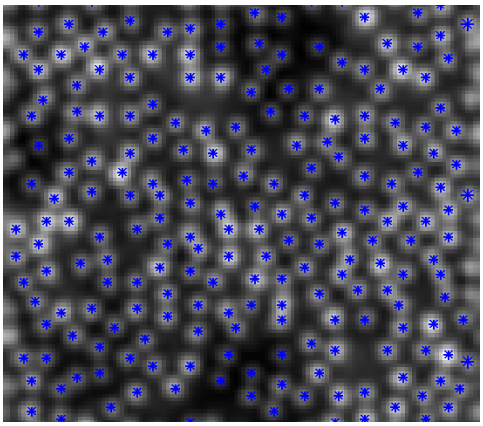
(h) Restored image (g)



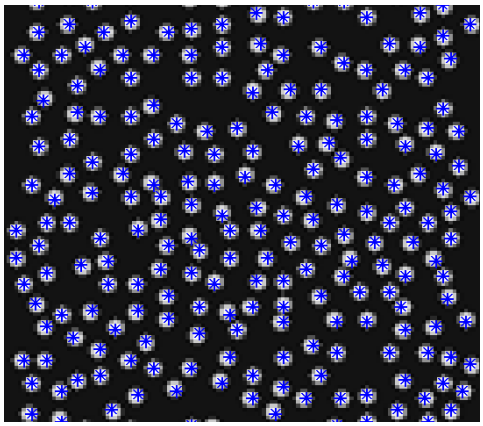
(i) Cone cone coordinates detected in the image before deconvolution (g)



(j) Cone coordinates detected in the image (g) and overlaid on the image with disks



(k) Cone cone coordinates detected in the image after image deconvolution (h)



(l) Cone coordinates detected in the image (h) and overlaid on the image with disks

Figure 5.14 (Cont.): Cone detection in two synthetic images, imitating the retina at 1.2 mm and 0.9 mm eccentricity before and after image restoration. Solid red circles and red dotted circles indicate FNs and FPs, respectively.

In addition, the cone density distribution was analysed in retinal datasets of four adult subjects processed with the proposed image processing framework. The cone density was

estimated in a window of size 100x100 μm taken at 0.9 - 2.1 mm temporal meridian with the step size of 0.3 mm. The window size was adjusted according to the axial length of each subject. For comparison purposes, the sampling windows were cropped from the images obtained after the image registration and image deconvolution. The cone density was estimated in two sets of images and the obtained cone counts per window were then recalculated as cone density in cell/mm^2. The photoreceptor cells located at the boundaries of the image were excluded from the counting procedure. In Table 5.11 the results of this study are presented and validated against the histology data of Curcio et al. [30] at the same eccentricities. Measurements acquired from the image before and after image deconvolution step are in close agreement with the histological values, with the concordance correlation coefficients of 0.99 and 0.982, correspondingly. The calculated CoV between the measurements before image deconvolution and histology data of Curcio et al. appeared to be lower than that obtained after image deconvolution. The CoV increased from 0.9% to 1.7% when cone density was assessed after performing image deconvolution. However, given a small number of samples, it is difficult to interpret the differences in the measurements with statistical significance. Despite that, as in the previous study on synthetic images, here the image deconvolution stage detects a slightly higher number of cones. Figure 5.15 shows an example where the cone counts in the restored image outnumber those obtained from the image after registration stage

	Before image deconvolution (mean ± SD)	**After image deconvolution (mean ± SD)**	**Curcio et al. (mean)**
0.9 Temporal	20 825 ± 746	21 550 ± 568	21 184
1.2 Temporal	17 750 ± 250	18 225 ± 238	17 786
1.5 Temporal	15 137 ± 491	15 600 ± 291	15 603
1.8 Temporal	13 225 ± 843	14 375 ± 834	13 542
2.1 Temporal	11 400 ± 809	12 550 ± 712	11 613

Table 5.11: Comparison of cone density estimated in the images at different retinal eccentricities before and after image deconvolution with the histological data of Curcio et al. [30].

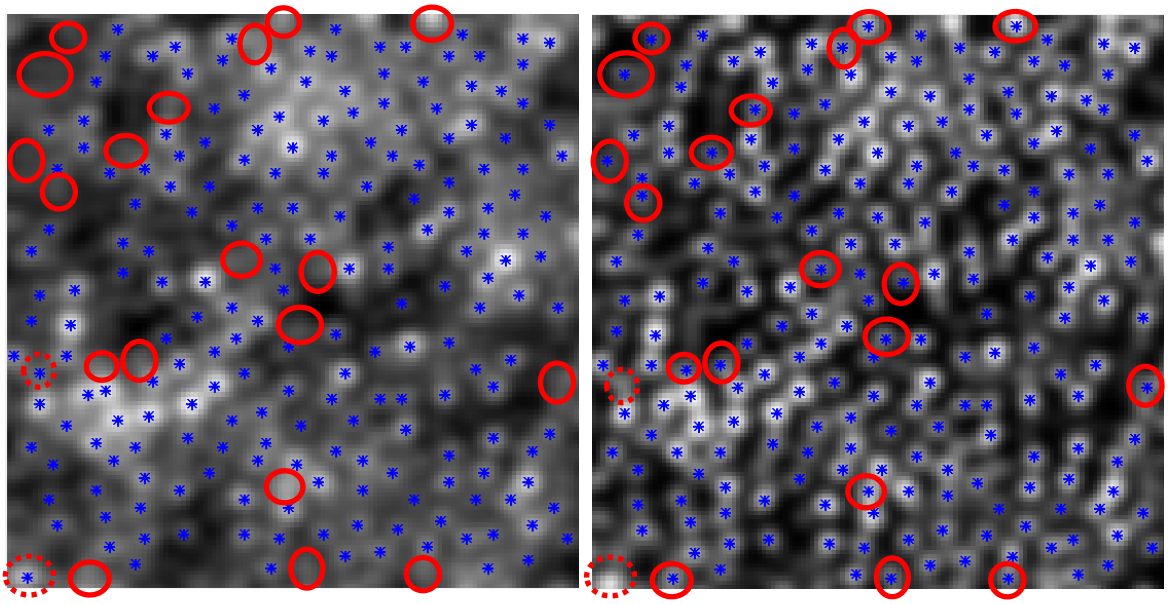
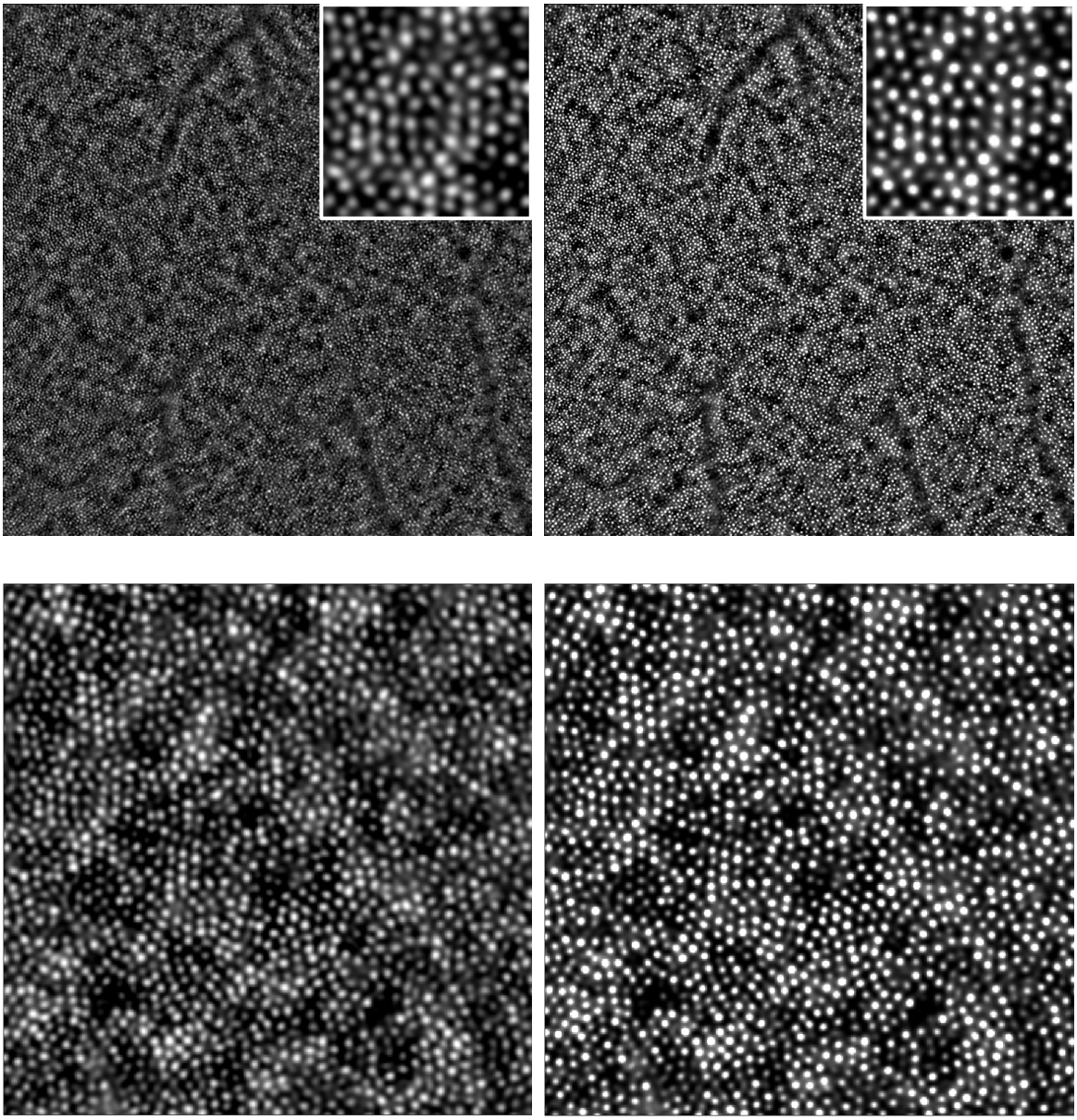


Figure 5.15: Cone coordinates detected in the retinal images before (left) and after image deconvolution (right) and overlaid on the AO retinal image acquired at 0.9 mm. Red solid circles show the cones detected after image deconvolution but missed in the image after registration stage. Red dotted circles show the cones detected before image deconvolution but missed after the image was restored.

Figure 5.16 presents the results of image enhancement with the Hessian-LoG filter performed on four representative AO retinal images, obtained after image deconvolution. These images are compared with those obtained at the previous stage of image processing framework in terms of sharpness measure. As it can be noticed, the enhancement with the Hessian-LoG filter further increases the image sharpness and facilitates more circular appearance of photoreceptor cells.

Retinal images after image deconvolution | **Retinal images enhanced with Hessian-LoG filter**

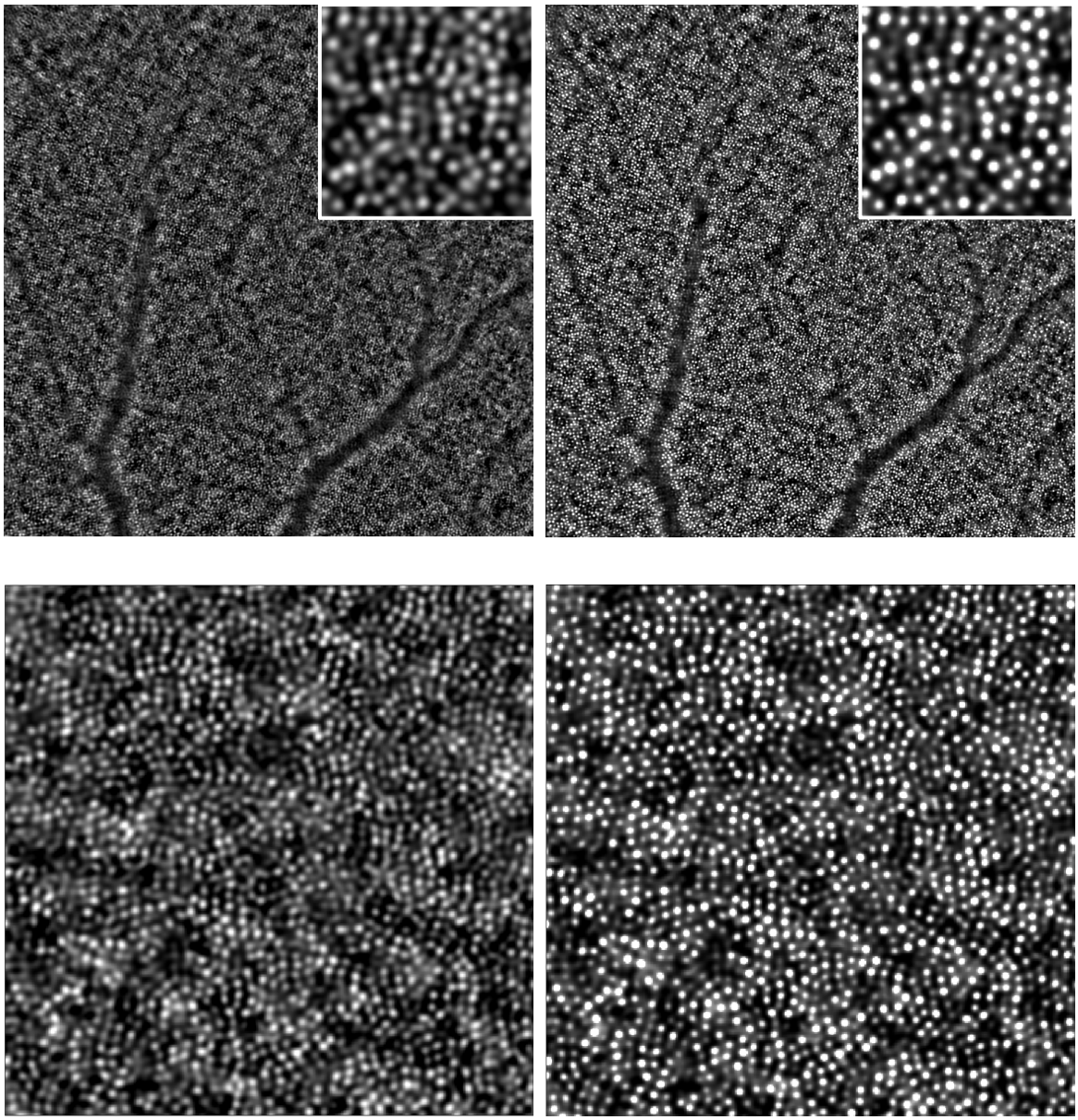
Retinal dataset 1



$BM_1 = 0.3820$ | $BM_1 = 0.6097$

Figure 5.16: Comparison between retinal images obtained after image deconvolution (left) and enhancement with the Hessian-LoG filter (right) in four representative images in terms of sharpness measure (BM_1), showing retinal images at different scales: 1.2mm, 40 μm (upper row) and 154 μm (bottom row).

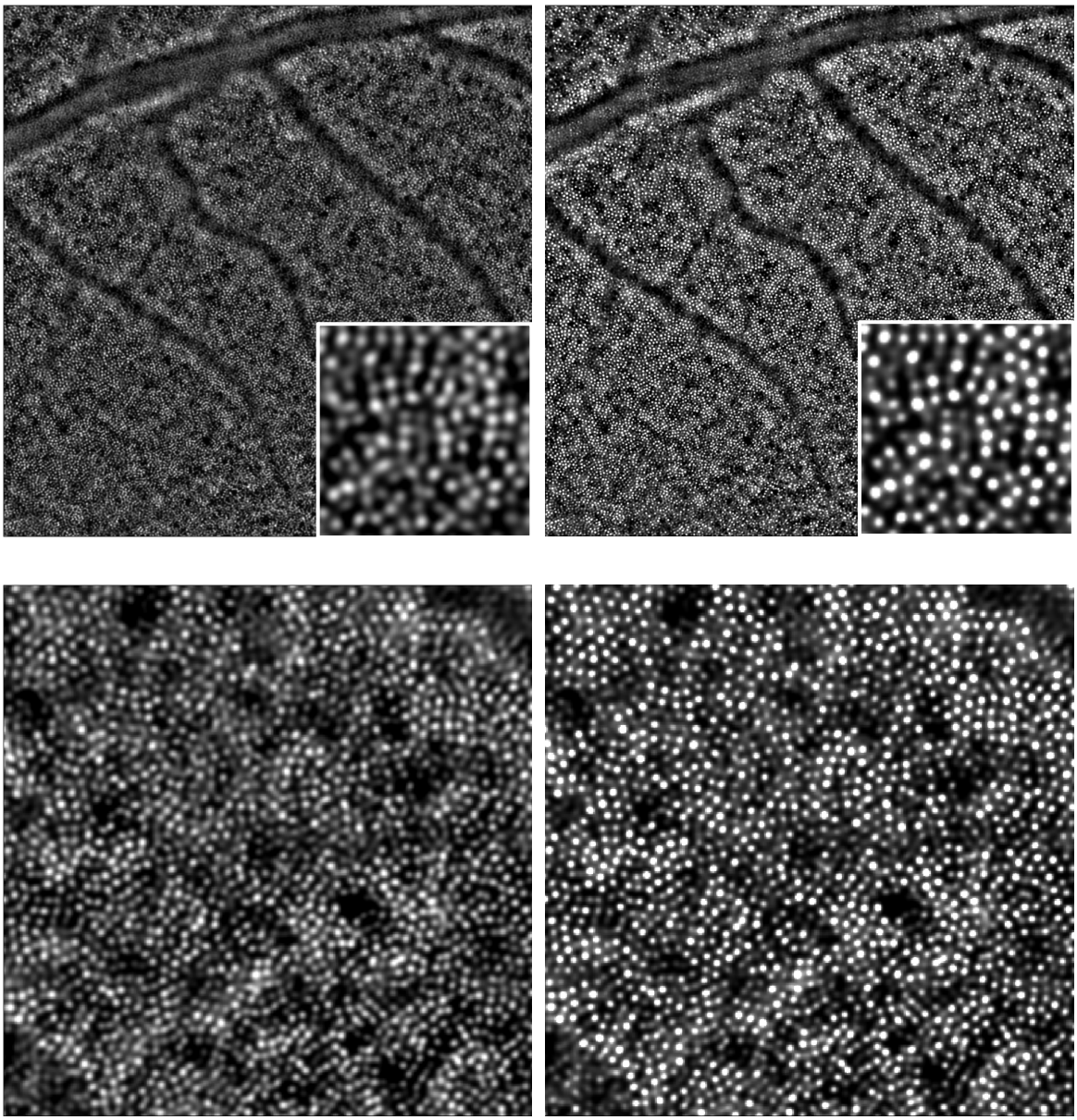
Retinal dataset 2



$BM_1 = 0.4129$ $BM_1 = 0.6218$

Figure 5.16 (Cont.): Comparison between retinal images obtained after image deconvolution (left) and enhancement with the Hessian-LoG filter (right) in four representative images in terms of sharpness measure (BM_1), showing retinal images at different scales: 1.2mm, 40 μm (upper row) and 154 μm (bottom row).

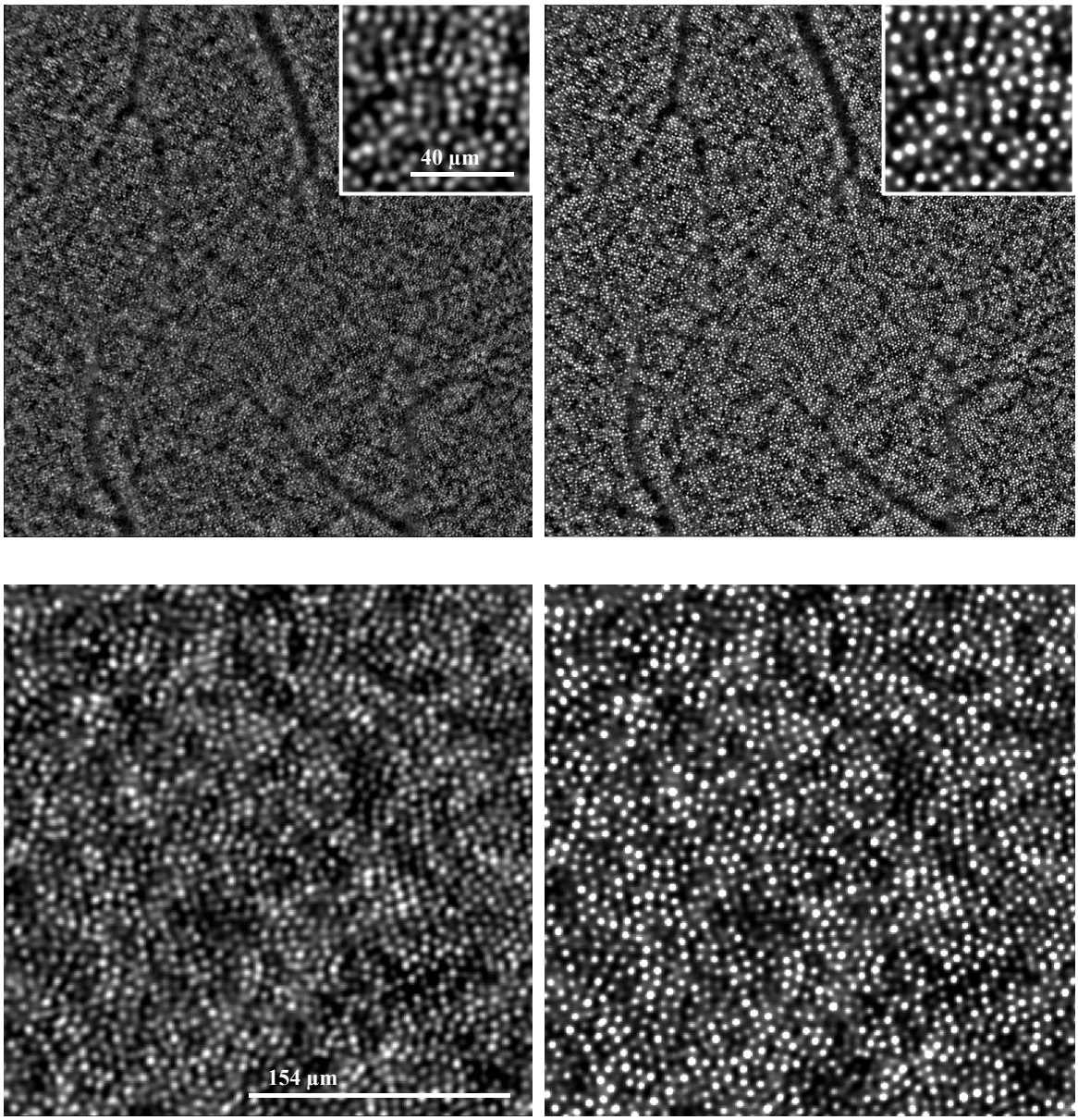
Retinal dataset 3



$BM_1 = 0.4714$ $BM_1 = 0.6247$

Figure 5.16 (Cont.): Comparison between retinal images obtained after image deconvolution (left) and enhancement with the Hessian-LoG filter (right) in four representative images in terms of sharpness measure (BM_1), showing retinal images at different scales: 1.2mm, 40 μm (upper row) and 154 μm (bottom row).

Retinal dataset 4



$BM_1 = 0.4140$ $BM_1 = 0.6129$

Figure 5.16 (Cont.): Comparison between retinal images obtained after image deconvolution (left) and enhancement with the Hessian-LoG filter (right) in four representative images in terms of sharpness measure (BM_1), showing retinal images at different scales: 1.2mm, 40 µm (upper row) and 154 µm (bottom row).

5.3 Analysis and Discussion

In this chapter, an automated algorithm is proposed for the detection of photoreceptor cones in high-resolution retinal images. Blob detection followed by LoG filtering are employed in order to enhance circular objects in the image. As a result, a binary mask is created, which is used for segmentation of photoreceptor cells from the image. This subsequently transforms cone counting into a straightforward process. The corresponding cone coordinates are calculated as the local maxima of the original image within the cone locations specified by the binary mask. In comparison with state-of-the-art automated methods, the Hessian-LoG filter allows for both geometric and intensity image information to be integrated in the process of cone density estimation.

Two sets of synthetic images were generated to assess the performance of the automated cone counting methods. The calculated image quality measures (sharpness measure, image contrast and variance presented in Table 5.1) indicated that the generated synthetic images resemble characteristics of real AO high-resolution retinal images. The validation tests on the synthetic data showed that the proposed approach performs better than the algorithm of Li and Roorda, with an average TP ratio of 98.8% in both synthetic sets. When testing the images where cones are densely packed, the algorithm of Li and Roorda does not only show a lower number of correctly identified cones but also a high number of false positives. This generally occurs as a result of merging closely located cones due to the use of the dilation operation, employed in this method. Overall, the average TP ratio of the Li and Roorda algorithm was found to be 93.9% , which is within a range of 93% - 96% reported in the original study [79].

In order to benchmark the manual counting procedure implemented in this part of the thesis, four observers carried out manual labeling of cones on the synthetic data. The average performance of manual counting appeared to be lower than that of the proposed Hessian-LoG filter, but higher than the one of the Li and Roorda algorithm. In set A, where the differentiation between cones proved to be harder especially for the human eye, the detection rate of correctly identified cones by manual counting falls to 95.6% in comparison with 98.1% by the proposed method. In set B, all the methods showed satisfactory detection rates with a variance of 0.38%.

The cone packing density was calculated on ten AO high-resolution retinal images acquired at different retinal eccentricities using the proposed cone counting algorithm, the algorithm of Li and Roorda and the proprietary software of Imagine Eyes. The results were compared against manual counts provided by the four observers. To ease the interpretation of the results, the data were presented with a box-and-whisker plot as a function of the error with respect to manual counting. Amongst the methods under consideration, the proposed approach demonstrated the closest agreement with manual counting, with an average CoV of 1.3%. The results obtained by the software of Imagine Eyes showed the smallest variance in the box-and-whisker plot, thus proving to be more consistent, with an average CoV of 1.8%. The Li and Roorda algorithm produced the highest detection error as well as the highest variance amongst the methods, with an average CoV of 3.2%.

The main advantage of the proposed method is that the Hessian-LoG filter can be used for enhancement of high-resolution retinal images as well as cone detection. By multiplying the Hessian-LoG filtered images with the corresponding retinal images obtained after the stages of illumination compensation, noise suppression and image registration, the contrast of photoreceptor cells can be significantly enhanced. The corresponding improvement in the quality of the retinal images will ease visual interpretation, thus facilitating clinicians in the visual examination of the living retina and the diagnosis of different types of eye diseases.

The proposed cone counting method was further tested in a clinical study investigating cone packing distribution in children and adult emmetropic population. It was found that results obtained from both age groups were in good agreement with the histology data reported by Curcio et al. [30], once again proving the accuracy of the proposed automated cone counting method.

In this chapter, we also investigated how the image deconvolution influences the accuracy of the cone detection. The evaluation studies on the synthetic and real retinal images confirmed that the restoration process allows for a higher number of cones to be correctly identified with the automated method based on the Hessian-LoG filter. By removing the residual blur from the retinal images during the deconvolution process, a better separation of the photoreceptor cells is achieved. This facilitated further improvement in the image sharpness when the restored images were enhanced with the Hessian-LoG filter (Figure 5.16), increasing the sharpness measure on average by 50%.

Interpretation of the results reported in this chapter should also account for a number of limitations, attributed to the methods as well as the lack of validation studies in this field. To our best knowledge, there are limited validation results available on the proprietary software of Imagine Eyes. Moreover, the Imagine Eyes software only processes custom-made image files, acquired by the Imagine Eyes AO instrument, and therefore it has not been possible to test this method on synthetic images. In regards to the proposed method, the main weakness and cause of the variability in the produced results lies in the use of a user-defined thresholding for localization of photoreceptor cells. While in the retinal images used in this research, 60% of the global threshold was sufficient to successfully segment the cones from the background, this parameter may need to be adjusted for the images acquired in pathological cases.

In conclusion, the contribution of this chapter includes the proposed automated cone counting algorithm. Our goal was to employ both geometric and intensity image information in order to ensure correct identification of photoreceptor cells. Various validation studies confirmed that in comparison with the state-of-the-art methods the proposed algorithm achieves better detection rate in the retinal images of various quality and can provide quantitative statistics of cone packing density close to histologic reference data.

The next chapter concludes the work presented in this thesis, provides limitations of the framework, suggests refinements for optimisation of the implemented methods and proposes further steps for future research.

6. Discussion and Conclusions

6.1 Summary of the Thesis Work

In this work, we have presented an automated computer vision system developed for enhancement of high-resolution retinal images acquired with the AO flood-illuminated instrument and accurate detection of photoreceptor cells. The AO instrument is a complex system, which includes a number of photoelectric components, corrupting the quality of acquired retinal images. The human factor and dynamic nature of eye optics also contribute to distortions in the retinal images. The proposed image processing framework was developed in attempt to tackle each of identified sources of degradation in the AO system and thereby gradually improve the quality of AO retinal images at each step in order to recover the true image. To this purpose, the implemented framework included a number of different image processing procedures such as illumination compensation, noise suppression, image registration, image deconvolution, enhancement and detection of photoreceptor cells.

In order to objectively evaluate the extent of improvement in retinal images at each stage, a reliable image quality assessment method is required. To this end, four different image quality measures were examined: two blur measures, image contrast and image variance. The aim of this research project is to facilitate better distinction of photoreceptor cells which potentially can assist clinicians in the examination of the living retina. In this manner, the fidelity of an image quality measure is effectively appreciated according to human visual perception. In the performed experiments, the measure based on the edge detection operator – Blur Measure, BM_1 (or sharpness measure as we refer to it in the thesis) – showed the ability to predict image quality in a manner that agrees with human ratings (Section 3.3). Therefore, it was chosen as the quality assessment measure for high-resolution retinal images in the proposed image processing framework. We were able to successfully use this sharpness measure to evaluate the level of improvement at each stage of the proposed image processing framework and benchmark different image processing methods. The sharpness

measure was also used to eliminate bad quality frames prior to image registration as well as select local regions for mapping the final image in lucky averaging scheme.

However, this measure is not suitable for measuring the noise levels, as generally, the noisier the image the more spurious intensity variations it contains and therefore the more edges are detected by the Sobel filter. This problem occurred at the stage of noise suppression, when the quality measure of processed retinal images appeared to be lower than the one resulted after the stage of illumination compensation (Section 3.5). To this purpose, apart from evaluating the amount of blur we also need to correctly quantify the amount of noise in the image. To achieve this, the Power Spectral Ratio was calculated between the images before and after applying a band-pass filter in order to evaluate the amount of improvement at the image denoising stage. Ideally, a generalized measure which is sensitive to both noise and blur, should be used for accurate estimation of image quality in the proposed image processing framework. Such measure is especially needed for processing images depicting pathological retinas, where the AO loop does not function perfectly and thus the acquired frames in dataset are generally much noisier than those acquired in healthy subjects.

High-resolution retinal images acquired with AO instrument are characterized by a bright illumination pattern which is gradually falling off at the edges. This impairs the visibility of retinal features, and moreover, adversely affects the next steps of the image processing framework. To surpass this problem, a retrospective illumination correction method was embedded in the proposed image processing framework. Spatial filtering is typically used for correction of uneven illumination in images. However, despite its simplicity and fast implementation, this type of illumination correction can perform poorly when illumination and reflectance content have overlapping spatial frequencies. In this thesis, the existing wavelet-based illumination compensation model was adopted in order to correct for the intensity inhomogeneity present in high-resolution retinal images (Section 3.4). The comparative study showed that this method provides the minimum of local brightness variation and the highest value of sharpness measure amongst other methods, thus proving to successfully decompose the retinal image into the luminance and reflectance components. To ensure high fidelity estimation of the illumination component, the level of decomposition and the type of wavelet were carefully chosen. The optimal level of decomposition was found based on homogeneity of the approximated background and local brightness variation of the restored image, in an automated manner. This allowed to minimize the number of

input variables in the system for each retinal image. Generally, five to six levels of decomposition are appropriate for approximating the background of retinal images since at these levels the recovered image shows the lowest local brightness variation and the estimated background has the highest homogeneity.

Daubechies wavelets are the popular choice in many image processing tasks as they are real and continuous in nature and have least RMS error compared to other wavelets [272]. Nevertheless, the decomposition of the image into approximation and detailed sub-bands with this type of wavelets still imposes some aliasing errors. By changing the coefficients of approximation component to a constant value the same artefacts appear in the recovered image. The artefacts caused by Daubechies wavelet decomposition can be described as vertical and horizontal lines (Subsection 3.4.5). DB10 type of Daubechies wavelets was chosen for decomposition of retinal images in this framework as it showed a slightly higher sharpness measure as well as introduced minimum artefacts to the reconstructed images. To prevent even a minor corruption of the integrity of the retinal features, a wavelet-Fourier filter was applied to reconstructed retinal images in order to eliminate block artefacts, imposed during the reconstruction process.

In order to compensate for the eye saccadic motions inflicted between the frames as well as suppress thermal and photon noise, image registration was performed on the dataset of retinal frames. Feature-based methods are not suitable for the registration of high-resolution retinal images as it is not feasible to choose adequate control points. Since blood vessels lie in a different layer of the retina, extraction of these features and performing image registration in reference to them will blur the photoreceptor cells. Therefore, the phase correlation method known as the POC was used to calculate transformation parameters in retinal images.

However, in high-resolution images large scale vessels can negatively affect the performance of correlation-based image registration method as well. Located in a different layer of the retina, these vessels do not have sharp edges and this can cause inaccuracy in calculation of transformation parameters. Moreover, as a correlation technique, the POC may fail when there are large changes in scale and rotation between reference and test frames. For these reasons, the registration process was divided into coarse and fine stages (Section 3.6). At the coarse stage, the POC with sub-pixel accuracy was employed to find

the translation parameters between the frames. At the fine stage, the transformation model was refined by calculating rotation angles and residual translation with the use of Procrustes alignment, where landmark configuration was defined by the coordinates of the brightest cones in the test and reference frames. While finding the matching control points in unregistered frames is a challenging task, after performing coarse registration it becomes possible. Now, the minimum cone spacing can be used to establish the matches between the brightest cones in test and reference frames. However, due to the angle of incident light and light scattering, the coordinates of the brightest pixel within the photoreceptor cell may change from frame to frame. For this reason, the coordinates of the brightest pixels in the reference frame were updated with the translation vector found using the POC performed on the windows cropped around candidate cone locations in the reference and test frames. Final matching points were used in Procrustes algorithm to refine the transformation model with the rotation and residual translation vectors.

Both stages of the image registration approach were tested by translating and rotating the image by a known amount. In both cases the proposed image registration method showed good accuracy as long as the examined pair of frames is of good quality. To this purpose, the retinal image sequence was sorted according to the sharpness measure. The frames with quality measure lower than the 0.15 quantile of the overall sharpness measure distribution were eliminated from the retinal dataset prior to the image registration. To ensure high accuracy of rotation detection, a parametric study was performed on the model of fine registration. It was established that sampling the regions around brightest cones up to 5 times and 200 control points allow for high fidelity estimation of transformation model, dropping the error to the 4^{th} significant figure ($1e^{-4}$) (Subsection 3.6.5). Qualitative comparison of the averaged images where only the translation vector was compensated with the images where both rotation and translation were corrected showed that the details in the latter are sharper, especially at the edges. Calculated image quality metric confirmed that the sharpness has been increased by 6% for all the images where rotation was additionally corrected.

To account for intra-frame variability in image quality, the “lucky averaging” scheme was employed. The final retinal image was constructed by averaging the local regions with the best sharpness measure in co-registered frames. The calculated sharpness measure indicated that a “lucky averaging” approach provides an additional improvement of 4% in the contrast of the retinal images in comparison to a typical averaging of frames.

In the images of pathological retinas, the use of brightest cones as control points can be problematic. Often, the brightest pixels correspond to the part of retina which was severely distorted due to the disease. This is caused by the changes in the reflectance properties of the photoreceptor mosaic in pathological retinas [112]. For example, in patients with DR it was found that the parafoveal cone photoreceptors appeared to have a higher variation in intensity, especially in the areas of intraretinal focal oedema [113]. Also, due to poor correction with AO, the retinal content may vary even more from frame to frame than in healthy retinas. Thus, it becomes more difficult to find appropriate matches. To facilitate this process, an additional criterion for choosing control points can be added in the framework, such as circularity of the photoreceptor cells. This will guarantee that the chosen cones are the least damaged by the disease and thus have more regular appearance in the recorded frames.

Given that intensity-based registration techniques are generally sensitive to the noise and illumination variations, the calculation of transformation parameters requires additional image processing techniques prior to image registration. In the proposed model, the fine stage of image registration is highly sensitive to the image noise, therefore the prior stage of noise suppression has a great impact on the resulting image and success of rotation detection in general. In this study, a Gaussian band-pass filter was used in order to increase contrast and remove high-spatial-frequency noise (Section 3.5). The choice of cut-off frequencies is very important in frequency processing, as wrong estimation of the spatial frequency of imaging objects can amplify the level of noise in the image. In high-resolution retinal images the cone is the smallest object to be imaged; therefore, the frequencies beyond the cones' frequencies correspond to the noise and should be filtered out. Based on the scale of the retinal features the corresponding frequencies were calculated and used as the stop frequency of the band-pass filter. The start frequency was found automatically as a first peak in the plot of radially averaged power spectrum of the retinal images.

In this work, the spatial frequencies of photoreceptor cones were derived from visual angles, as a projection of the image on the retina [137]. This formula requires knowledge of the focal length of human eye and photoreceptor cell diameter. This adds up two variables in the image processing framework, on which the accuracy of image restoration depends. Alternatively, the spatial frequency of photoreceptor cones can be estimated directly from the radially averaged power spectrum of the retinal image. However, in pathological cases, the Yellott's

ring will be less defined due to irregularly of cone packing, which makes it harder to automatically estimate the cones' spatial frequency.

The sharpness measure and image contrast were calculated before and after image denoising. While image contrast was significantly improved, the sharpness measure was slightly decreased due to smoothing introduced by the Gaussian band-pass filter. Therefore, in order to evaluate the amount of noise suppressed, the Power Spectral Ratio was calculated between the images before and after image denoising. Overall, the signal within the range of cut-off frequencies has been improved by 150%.

Even though the AO system performs wavefront detection and correction of high-order ocular aberrations, due to hardware limitations of the wavefront corrector, the acquired retinal images are still corrupted by residual aberrations. Therefore, an image restoration technique such as image deconvolution was included in the image processing framework. Prior knowledge on the blur kernel can significantly improve the accuracy as well as convergence of the deconvolution method. In AO, the degradation function of the system can be estimated partially from WFS. However, due to lack of the synchronization between image capturing and wavefront calculation, the WFS data cannot be used directly. However, it could serve as initial estimate of the true PSF of the system in the deconvolution process. Unfortunately, this data is not available in the commercial AO flood-illuminated instrument. Therefore, in this work a blind deconvolution method was proposed.

Conventional blind deconvolution methods are more prone to getting trapped in local minima, especially when there is only a single blurred image to be restored. In this work, for computational cost-saving, the restoration process was performed on final images obtained after registration of retinal frames. To this purpose, we developed a learning method based on a multi-variate Random Forest regressor (Section 4.2). Although a number of learning-based techniques have been proposed in the literature for the purposes of image deconvolution [193, 194], [237], these methods rely on generalized models and therefore their accuracy is limited to specific types of blur. In addition, in most of the reported methods the achieved resolution of the recovered blur kernel is often found to be restricted by size. In our work, the system's PSF was modelled by the physics/optics of the AO flood-illuminated system and thus constrained as a member in a class of parametric functions (Section 4.3). Parametrization of the PSF through the pupil phase allowed to significantly

reduce the degree of uncertainty in image deconvolution. The mathematical model of the system's PSF was defined through the wavefront phase error retaining the first 15 Zernike terms, where all parameters were fixed according to the specifications of the AO flood-illuminated system, rtx1. This allowed to represent the blur kernel in a compact form as a vector of Zernike coefficients in the implemented framework, and thus estimate a convolution blur kernel for AO retinal images without compromising resolution. In AO high-resolution retinal images, out-of-focus planes of the retina also contribute to the image formation, resulting in additional blur and distortion. To account for this, apart from high-order aberrations the PSF's model also included the defocus phase.

Across the image and the retinal dataset, single cones imaged with AO show a certain variability in reflectance, appearing with different intensity levels. This is caused by the changes in their directional sensitivity, the so-called optical Stiles–Crawford effect [97]. In addition, the visibility of the retinal features is also altered by other factors, which are more difficult to single out. As mentioned previously, the retina is a 3D volume, where retinal layers interact differently with the optics of the imaging instrument. This results in a non-uniform blur across the recorded retinal images.

Due to the aforementioned variations in image quality it is difficult to restore retinal image with a single PSF. In the proposed method for image deconvolution, we attempted to tackle this problem by extracting the features from small windows containing a single cone. In order to capture structural changes in the local shape caused by blurring, the HoG features were used (Subsection 4.4.1). To limit the nature of variations down to the corruption of cone shape due to blur, the HoG features were extracted from only the brightest cones and then averaged across the image. Experimental analysis showed that this approach reduced the generalization error by 82.5% in comparison with the case where HoG features were extracted from all photoreceptor cells. Moreover, this feature extraction technique allowed for the inference of PSFs from unseen retinal images of various quality, taken at different locations of the retina.

In the proposed model, a convolution kernel was estimated through non-linear regression of HoG features extracted from retinal images onto the space of PSFs expressed in terms of Zernike coefficients. This was achieved by training the Random Forest on a large dataset of synthetically generated retinal images and PSFs. For the estimation of the target vector of

Zernike coefficients, KDE was used on the data aggregated from all the leaf nodes of the trained Random Forest (Subsection 4.4.2). In comparison with the commonly used averaging of the posterior probablity distributions, the KDE allowed to further decrease the prediction error by 39%.

The proposed deconvolution method was validated on 1000 synthetic retinal images (Subsection 4.5.1). This study showed an average error of 0.5% for the predicted blur kernels and 4.6% for the reconstructed images, compared to the GT. The performance of the proposed deconvolution method was also tested on 25 AO retinal images, processed with the proposed image processing framework (Subsection 4.5.2). In comparison with the previous stage of the image processing framework, the deconvolution stage significantly increased the image sharpness by almost 100%. These results were also compared with the images restored with the state-of-the-art method by Sroubek and Milanfar [254]. The qualitative comparison indicated that the proposed deconvolution approach preserves better the edges of the photoreceptor cells as well as facilitates better separation of individual cells, while the ALM method seemed to blur the cones with poorly defined edges. This was confirmed also by the higher values of sharpness measure and contrast in the images restored with the proposed method.

Overall, the validation studies showed that proposed image deconvolution method can successfully restore synthetic retinal images and significantly improve the quality of the real AO images. Despite that, the implemented model provides only an approximation to the real PSF of the AO system, as it does not account for all the spectrum of variations present in AO retinal images. Fixed parameters in the PSF model, such as axial length and pupil diameter, also contribute to the limitations of the proposed method. As there is no statistical model of the residual aberrations in pathological retinas, the implemented model is designed to restore images of healthy retinas.

For enhancing photoreceptor cells in AO high-resolution retinal images the Hessian-LoG filter was employed (Chapter 5). This method allows for segmentation and detection of photoreceptor cells, thus providing the means for quantitative analysis of retinal images. In comparison with state-of-the-art automated methods, the proposed method integrates both geometric and intensity image information in the process of cone detection. As a result, the proposed method provides highly accurate estimation of cone density. Visual analysis

revealed that the proposed cone counting method can detect photoreceptor cells even in the areas where image is significantly blurred or obstructed, such as borders of the image and vessels.

The performance of the Hessian-LoG filter was evaluated on both synthetic and high-resolution retinal images, in terms of packing density. The results on the synthetic data were compared against the GT as well as cone counts obtained by the Li and Roorda algorithm (Subsection 5.2.3). For the synthetic datasets, our method showed an average detection accuracy of 98.8%, compared to 93.9% for the Li and Roorda approach. The approximated packing density, calculated on the retinal datasets, was validated against results obtained by a proprietary software from Imagine Eyes and the Li and Roorda algorithm (Subsection 5.2.4). To quantify the accuracy of cone detection, four independent observers performed manual counting on the corresponding high-resolution retinal images. Among the tested methods, the proposed approach demonstrated the closest agreement with manual counting, with an average percentage difference of 2.7%.

With the use of the proposed cone counting method, the cone packing distribution was investigated in children and adult emmetropic populations (Subsection 5.2.5). The cone density was calculated across the retina in four meridians for all subjects in two age groups. In order to verify the results obtained with the Hessian-LoG filter, the calculated density distributions were compared with cone density established based on the histology data by Curcio et al. [30] and results of AOSLO by Chui et al. [84]. The cone density distribution obtained with the proposed cone counting method appeared to be in closer agreement with the postmortem measurements, than the data obtained with AOSLO. The average CoV between the results by Curcio et al. [30] and the examined two age groups of the current study was 2.5%, 10.2%, 4.4%, 8% (with $p < 0.05$) in the nasal, temporal, superior and inferior quadrants, respectively.

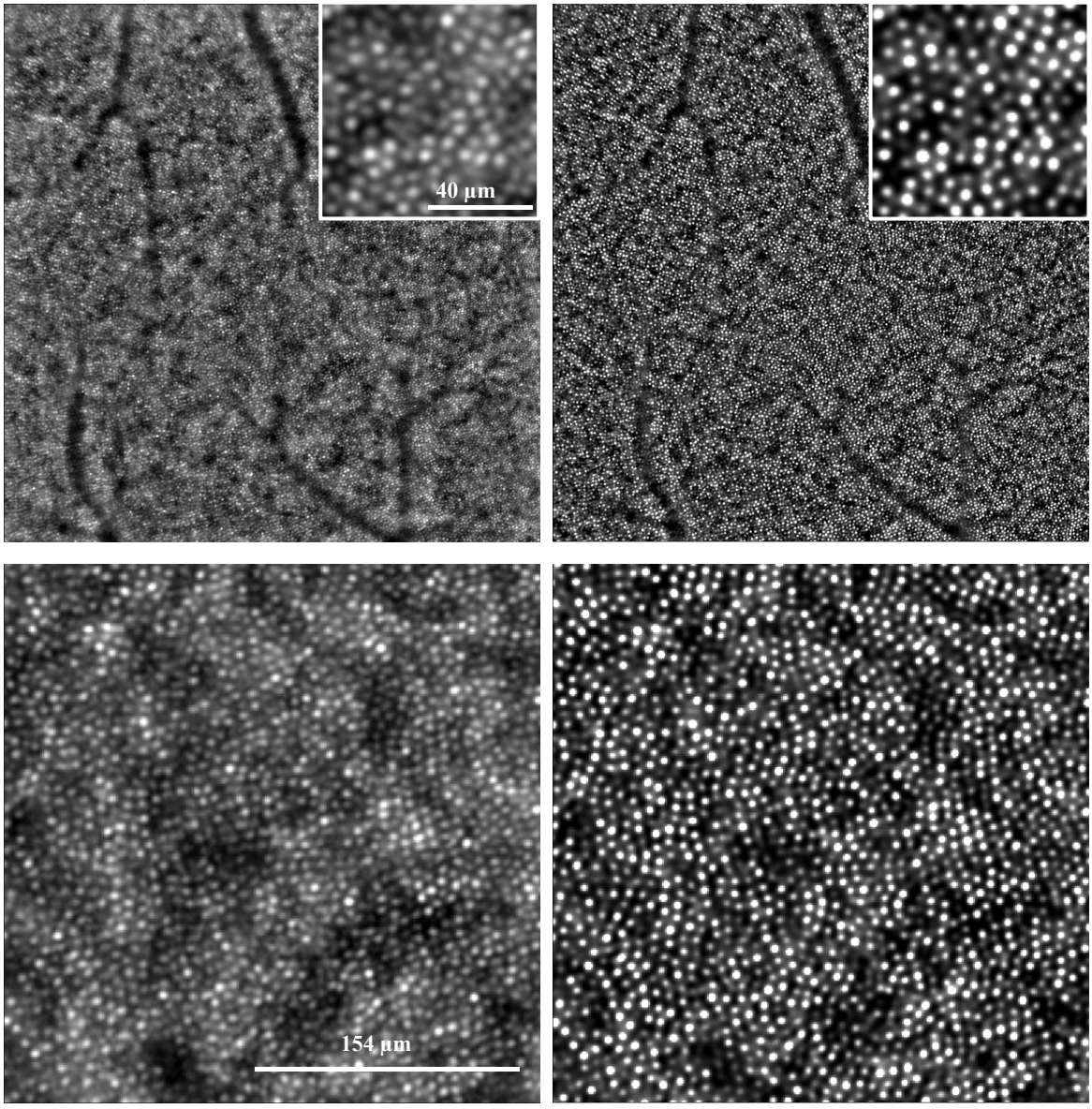
To verify that the image deconvolution stage is beneficial for the image processing framework, two studies were performed where cone counts were calculated on synthetic and real retinal images before and after image deconvolution (Subsection 5.2.6). Both studies proved that the restoration of the images with the proposed method based on the Random Forest allows for a better separation of the photoreceptor cells and as a result leads to a higher

number of cones to be correctly identified with the automated method based on the Hessian-LoG filter.

The main advantage of the proposed cone counting method is that the Hessian-LoG filter can be used for the enhancement of high-resolution retinal images as well as cone detection. The images produced after Hessian-LoG filtering were used as a mask multiplied with the images obtained at the previous stage of image processing framework. Adopting this process resulted in a more circular appearance of photoreceptor cells and facilitated further improvement in the image quality, increasing sharpness measure on average by 50%.

Most of existing methods for cone detection methods cannot be considered as fully automated as they require manual input for parameters, such as the intensity threshold and intercell spacing, thus affecting the agreement between the results obtained by different observers. Due to the use of multi-scale Hessian filtering, the proposed cone counting method can be successfully used on a wide range of retinal images, taken at different retinal locations. However, the choice of a threshold value for localization of photoreceptor cells can play an important role. While in the retinal images used in this research, 60% of the global threshold was sufficient to successfully segment the cones from the background, this parameter needs to be thoroughly investigated on a larger dataset, including images of varying quality, spanning over retinas with different pathologies.

The execution time of the implemented framework on an average PC with two cores is around seven minutes, which makes it suitable for performing image post-processing in clinical practice. The most expensive functions in the framework are rotation detection and lucky averaging. The runtime complexity of rotation detection is $O\left(M(N^2 + K^2L^2)\right)$, where M is the number of frames to be registered, N is the size of the image, K is the number of control points and L is the dimension of the window centred at cones. The runtime complexity of lucky averaging is $O\left(M(N^2 + P^2) + P^2(MlogM + MP^2)\right)$, where M is the number of frames to be averaged, N is the size of the image, P is the size of the blocks. Further optimisation steps could be made in order to cut the computation time, such as use of parallel loops in lucky averaging and registration stage.



$BM_1 = 0.3619$ $BM_1 = 0.6097$

Figure 6.1: Comparison of retinal images produced by the commercial software of Imagine Eyes (left) and the proposed image processing framework (right).

In comparison with the existing image processing frameworks designed for AO-corrected retinal images [71, 72], [80], [137, 138], the proposed framework was implemented in an attempt to compensate for the variety of possible degradation sources, interfering with the system. One of the commercially available programmes for the enhancement of AO retinal images is CK v0.1 from Imagine Eyes. To justify the potentials of the proposed image processing framework, the output image of the developed processing framework was compared with the image produced by the commercial software of Imagine Eyes (Figure

6.1). Based on the calculated image quality measure, the proposed image processing framework produces the final image with sharpness higher by 68%. Sharpness measure map, calculated for the retinal images produced by the software of Imagine Eyes and the proposed image processing framework (Figure 6.2), demonstrated that the proposed framework enhances the retinal image over the larger field of view.

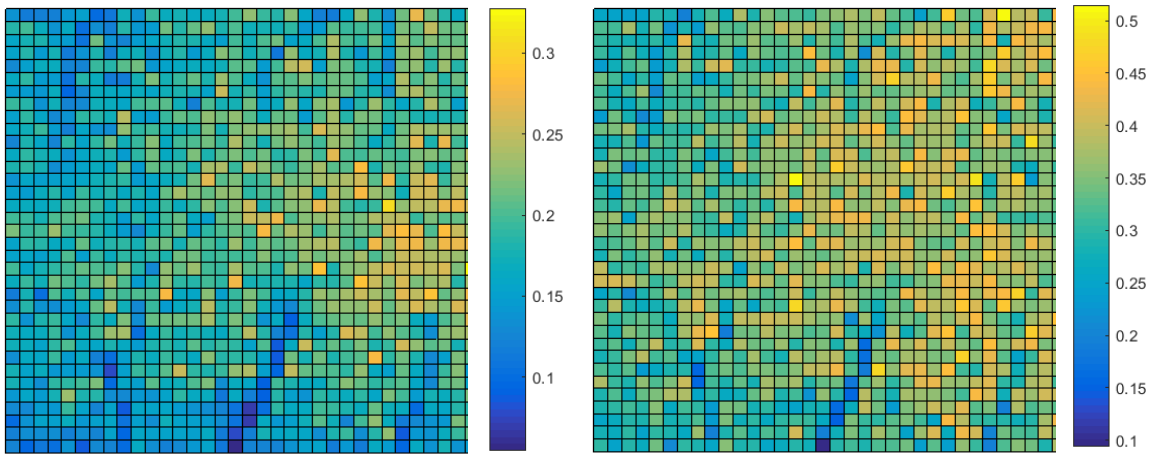
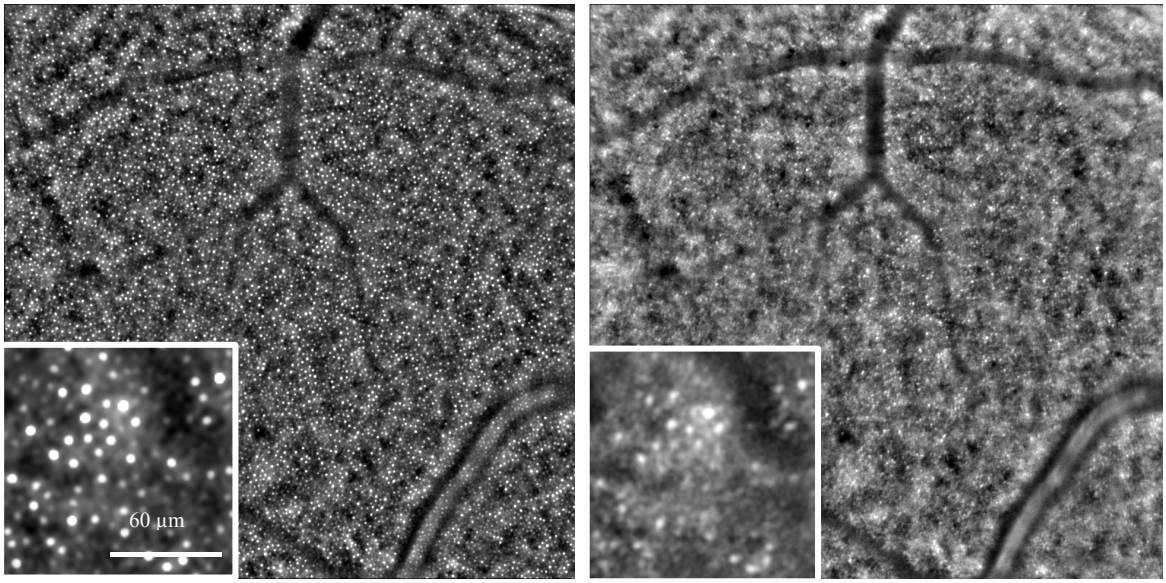


Figure 6.2: Sharpness measure map calculated for retinal images produced by the commercial software of Imagine Eyes (left) and the proposed image processing framework (right).

In this thesis, we only showed retinal images of healthy subjects processed with proposed image processing framework. However, in practice the implemented framework can be adapted for enhancement and detection of photoreceptor cells in pathological retinas. Figure 6.3 shows the retinal image of glaucoma patient obtained with the proposed image processing framework and compared with the image produced by the software of Imagine Eyes. Due to the lack of data on the residual aberrations in pathological eyes after AO correction, the proposed deconvolution method was not able to remove the residual blur completely as well as restore the regularity of cones. Nevertheless, the calculated image quality measure has shown that the resulting image produced with the proposed framework is of higher sharpness than the one produced with the Imagine Eyes software.



$BM_1 = 0.4130$ $BM_1 = 0.2327$

Figure 6.3: Resulting retinal image of the pathological retina obtained with the proposed image processing framework (left) and the software of Imagine Eyes (right).

To conclude, in this thesis we have implemented an image processing framework that allows for gradual improvement of AO high-resolution retinal images and accurate detection of photoreceptor cells. Enhancement of retinal images with the implemented framework will assist eye professionals in visual interpretation of the data. Accurate quantitative assessment of retinal images will allow to examine a large number of images with significant time and cost-savings. This essentially brings benefits to both research and clinical environments, facilitating more clinical research studies devoted to characterisation of the density and spacing distribution of photoreceptor cells in-vivo. Moreover, based on the work presented here, a framework can be developed for characterisation of density and spacing distribution of photoreceptor cells in the diseased eyes. This will help clinicians in examination and tracking of the progression of the eye diseases at cellular level and evaluation of the efficacy of the proposed therapies over time. Eventually, development of such frameworks will promote AO imaging in regular clinical practice, changing the usual treatment process of eye pathologies.

6.2 Contributions

To summarize, the work presented in this PhD thesis resulted in the following contributions:

- A learning-based method was developed for deconvolution of high-resolution retinal images using a multi-variate Random Forest regressor. The proposed method allows for efficient prediction of blur kernels in a large range of high-resolution retinal images. Restoration of the retinal images with the estimated PSFs compensates for the residual optical aberrations thereby facilitating differentiation of photoreceptor cells.
- An automated cone counting algorithm based on the Hessian-LoG filter was proposed. Integration of geometric and intensity image information by the scale-based Hessian-LoG filter proved to provide accurate estimation of cone density. Moreover, the implemented method can be also used for enhancement of AO retinal images. Applying this filter to the retinal images results in significantly improved image sharpness and more circular appearance of photoreceptor cells.
- The implemented image processing system may bring benefits to research and clinical applications by allowing easier visual interpretation of high-resolution retinal images and providing quantitative assessment of cone density distribution.

6.3 Limitations of the Implemented Model

Based on the discussion in Section 6.1, the following limitations of the implemented model were identified:

- The chosen image quality measure can only effectively evaluate the extent of blur present in the retinal images.
- The fine stage of image registration may not perform well in the retinal images with certain pathologies (for example in AMD subjects, where the retina has drusen).
- The proposed deconvolution method is designed to compensate optical aberrations up to the 4^{th} radial order of the Zernike polynomial expansion.
- The accuracy of the PSF estimation depends on the parameters of the eye such as axial length and pupil diameter.
- The proposed image deconvolution model doesn't account for spatially varying blur and 3D nature of the retinal image.
- The intensity threshold in the proposed cone counting methods has to be adjusted for the images of pathological retinas.

6.4 Proposal for Future Work

To date a lot of effort has been applied to optical hardware improvement and development of new technologies in order to provide non-invasive retinal imaging at cellular resolution. Further advances in retinal image processing would maximize the potential of AO imaging in clinical practice. The work presented here has the capacity to be transformed into a highly efficient diagnostic tool; this will assist ophthalmologists in the interpretation of retinal data as well as provision of quantitative statistics. Based on the conclusions and identified limitations of the undertaken research, the following improvements as well as future research studies are suggested for further advancing the proposed image processing framework:

- To develop a generalized measure sensitive to both, noise and blur, which can be used to assess the quality of high-resolution retinal images and therefore to benchmark the performance of image processing techniques performed on retinal images. The difficulty to correctly quantify noise and blur when both are present in the image arises due to their contradicting effects on image properties. In the frequency domain, noise affects the whole frequency band and mainly increases the higher-frequencies, while blur mainly supresses the higher-frequencies. For this reason, in many practical application image quality assessment methods account for only one of these impairments ignoring the other [273].
- Driven by compromise between the complexity of the PSF model and computation time spent for the training of the Random Forest, we have retained the first 15 Zernike terms in the implemented model of PSF. This model can be further refined by including information on positive correlation between certain optical aberrations. This analysis can reveal a joint probability distribution of different types of optical aberrations after AO correction loop. This would allow to reduce the range of values for certain optical aberrations and therefore bring down the number of training samples in the Random Forest, or alternatively allow to include more terms in the model of PSF. While in this study it was assumed that the AO correction is uniform across all aberrations, investigation on the partial compensation for each type of aberrations with AO system can improve the accuracy of PSF estimation as well as limit the number of training data for the Random Forest.

- In a commercial AO instrument, rtx1, the WFS data is not available. However, it would be useful for setting the range of values in the PSF model. As a result, this would allow to significantly reduce the space of valid PSFs, since the "real" PSF does not deviate too far from the values measured by WFS.
- One could notice that at the borders of retinal images, the photoreceptor cells are generally worse resolved than in central parts. Such a difference in image quality is caused by isoplanatic field [274], which defines the area within which the variation of optical aberrations is considered negligible. Thus, the PSF in the central region of the retinal image and at the borders will be different. To account for spatially varying blur, the PSF in the central region and at the borders of retinal images should be calculated separately. In order to segment these two areas, the isoplanatic field of the retina needs to be calculated.
- Based on the proposed model of image deconvolution, it is possible to develop a 3D deconvolution method, which accounts for true nature of the recorded AO high-resolution retinal images. For this, a 3D volume of the retina is required. Up to date, this remains a challenge for the AO flood-illuminated instrument.
- To develop an automated thresholding method for the images processed with the Hessian-LoG filter, robust to the intensity variations present in the images of healthy and pathological retinas.
- The developed image processing framework can be used for further investigation of retinal tissues. Various research studies can be carried out on the images obtained from different regions of the retina in healthy and pathological subjects. A comparison study between image quality analysis of pathological (retinal tissue with lesion, microanerusym, drusen or glaucoma) and healthy eyes can be performed to understand the suitability of methods. The cone counting algorithm based on the Hessian-LoG filter can be used for analysing the integrity of cone photoreceptor mosaic, its density, spacing and reflectance. The performed image analysis can help to reveal cellular changes of retinal pathologies. This will eventually allow clinicians to track the progression of diseases and to evaluate the treatments applied to individual photoreceptor cells for inherited and acquired retinal degenerative diseases.

List of References

[1] D. Pascolini and S. P. Mariotti, "Global data on visual impairments 2010," *Br. J. Ophthalmol.*, vol. 96, no. 5, pp. 614–618, 2012.

[2] S. West and A. Sommer, *Prevention of blindness and priorities for the future*, vol. 79, no. 3. Geneva: Bull WHO, 2001.

[3] *Vision 2020. Global initiative for the elimination of avoidable blindness: action plan 2006-2011*. Geneva: Bull WHO, 2007.

[4] M. Lombardo, S. Serrao, N. Devaney, M. Parravano, and G. Lombardo, "Adaptive optics technology for high-resolution retinal imaging.," *Sensors (Basel).*, vol. 13, no. 1, pp. 334–366, Jan. 2013.

[5] J. Liang, D. R. Williams, and D. T. Miller, "Supernormal vision and high-resolution retinal imaging through adaptive optics.," *J. Opt. Soc. Am. A. Opt. Image Sci. Vis.*, vol. 14, no. 11, pp. 2884–92, Nov. 1997.

[6] H. L. Rao, J. G. Babu, U. K. Addepalli, S. Senthil, and C. S. Garudadri, "Retinal nerve fiber layer and macular inner retina measurements by spectral domain optical coherence tomograph in Indian eyes with early glaucoma.," *Eye (Lond).*, vol. 26, no. 1, pp. 133–9, Jan. 2012.

[7] J. Tam, P. Tiruveedhula, and A. Roorda, "Characterization of single-file flow through human retinal parafoveal capillaries using an adaptive optics scanning laser ophthalmoscope.," *Biomed. Opt. Express*, vol. 2, no. 4, pp. 781–93, Jan. 2011.

[8] O. P. Kocaoglu, B. Cense, R. S. Jonnal, Q. Wang, S. Lee, W. Gao, and D. T. Miller, "Imaging retinal nerve fiber bundles using optical coherence tomography with adaptive optics.," *Vision Res.*, vol. 51, no. 16, pp. 1835–44, Aug. 2011.

[9] K. Takayama, S. Ooto, M. Hangai, N. Arakawa, S. Oshima, N. Shibata, M. Hanebuchi, T. Inoue, and N. Yoshimura, "High-resolution imaging of the retinal nerve fiber layer in normal eyes using adaptive optics scanning laser ophthalmoscopy.," *PLoS One*, vol. 7, no. 3, p. e33158, Jan. 2012.

[10] A. Roorda, Y. Zhang, and J. L. Duncan, "High-resolution in vivo imaging of the RPE mosaic in eyes with retinal disease.," *Invest. Ophthalmol. Vis. Sci.*, vol. 48, no. 5, pp. 2297–303, May 2007.

[11] J. Tam, J. A. Martin, and A. Roorda, "Noninvasive visualization and analysis of parafoveal capillaries in humans.," *Invest. Ophthalmol. Vis. Sci.*, vol. 51, no. 3, pp. 1691–8, Mar. 2010.

[12] "rtx1 Adaptive Optics Retinal Camera. Imagine Eyes," 2012. [Online]. Available: http://www.imagine-eyes.com/product/rtx1/. [Accessed: 08-Jan-2017].

[13] J. Rha, R. S. Jonnal, K. E. Thorn, J. Qu, Y. Zhang, and D. T. Miller, "Adaptive optics flood-illumination camera for high speed retinal imaging.," *Opt. Express*, vol. 14, no. 10, pp. 4552–69, May 2006.

[14] A. Roorda, F. Romero-Borja, W. Donnelly III, H. Queener, T. Hebert, and M. Campbell, "Adaptive optics scanning laser ophthalmoscopy.," *Opt. Express*, vol. 10,

no. 9, pp. 405–12, May 2002.

[15] J. Rha, A. M. Dubis, M. Wagner-Schuman, D. M. Tait, P. Godara, B. Schroeder, K. Stepien, and J. Carroll, "Spectral domain optical coherence tomography and adaptive optics: imaging photoreceptor layer morphology to interpret preclinical phenotypes.," *Adv. Exp. Med. Biol.*, vol. 664, pp. 309–16, Jan. 2010.

[16] O. P. Kocaoglu, S. Lee, R. S. Jonnal, Q. Wang, A. E. Herde, J. C. Derby, W. Gao, and D. T. Miller, "Imaging cone photoreceptors in three dimensions and in time using ultrahigh resolution optical coherence tomography with adaptive optics.," *Biomed. Opt. Express*, vol. 2, no. 4, pp. 748–63, Jan. 2011.

[17] Y. Zhang and A. Roorda, "Evaluating the lateral resolution of the adaptive optics scanning laser ophthalmoscope," *J. Biomed. Opt.*, vol. 11, no. 1, p. 14002, Jan. 2006.

[18] D. T. Miller, O. P. Kocaoglu, Q. Wang, and S. Lee, "Adaptive optics and the eye (super resolution OCT)," *Eye*, vol. 25, no. 3, pp. 321–330, Mar. 2011.

[19] M. B. V. Roberts, *Biology: A Functional Approach*, 4th ed. Nelson Thornes, 1986.

[20] D. A. Atchison and S. George, *Optics of the Human Eye*, vol. 21, no. 5. Butterworth-Heinemann, 2000.

[21] C. Hendry, A. Farley, and E. McLafferty, "Anatomy and physiology of the senses.," *Nurs. Stand.*, vol. 27, no. 5, pp. 35–42, 2012.

[22] Sinauer Associates, "Anatomy of the human eye," 2001. [Online]. Available: https://ic.ucsc.edu/~bruceb/psyc123/Vision123.html.pdf. [Accessed: 22-Dec-2016].

[23] J. C. He, J. Gwiazda, F. Thorn, R. Held, and W. Huang, "Change in corneal shape and corneal wave-front aberrations with accommodation.," *J. Vis.*, vol. 3, no. 7, pp. 456–63, Jan. 2003.

[24] H. Kolb, "How the retina works.," *Am. Sci.*, vol. 91, pp. 28–35, Aug. 2004.

[25] "Physiology. Chapter 10 - Sensory," *Pearson Education, Inc.*, 2011. [Online]. Available: http://droualb.faculty.mjc.edu/Course Materials/Physiology 101/Chapter Notes/Fall 2011/chapter_10 Fall 2011.htm. [Accessed: 08-Jan-2017].

[26] D. Purves, G. J. Augustine, D. Fitzpatrick, L. C. Katz, A.-S. LaMantia, J. O. McNamara, and S. M. Williams, *Neuroscience*, 2nd ed. Sinauer Associates, 2001.

[27] A. V.-D. Fuensanta and D. Nathan, "Topics in Adaptive Optics. The Human Eye and Adaptive Optics," R. K. Tyson, Ed. InTech, 2012, pp. 119–151.

[28] "Vision." [Online]. Available: http://www.skybrary.aero/index.php/Vision_(OGHFA_BN). [Accessed: 23-Dec-2016].

[29] R. Wang, "Cross Section of the Retina," 1999. [Online]. Available: http://fourier.eng.hmc.edu/e180/lectures/retina/node5.html. [Accessed: 26-May-2017].

[30] C. A. Curcio, K. R. Sloan, R. E. Kalina, and A. E. Hendrickson, "Human photoreceptor topography.," *J. Comp. Neurol.*, vol. 292, no. 4, pp. 497–523, Feb. 1990.

[31] S. Richer, J. Cho, W. Stiles, M. Levin, J. Wrobel, M. Sinai, and C. Thomas, "Retinal Spectral Domain Optical Coherence Tomography in Early Atrophic Age-Related Macular Degeneration (AMD) and a New Metric for Objective Evaluation of the

Efficacy of Ocular Nutrition," *Nutrients*, vol. 4, no. 12, pp. 1812–1827, Nov. 2012.

[32] K. Aczel, "Examination of color vision," in *Neuro-ophthalmology*, J. Somlai and T. Kovacs, Eds. Springer, 2016, pp. 90–91.

[33] J. E. Greivenkamp, *Field guide to geometrical optics*. Washington: SPIE Press, 2004.

[34] "Chromatic and Monochromatic Optical Aberrations." [Online]. Available: https://www.edmundoptics.com/resources/application-notes/optics/chromatic-and-monochromatic-optical-aberrations/. [Accessed: 24-Jun-2017].

[35] M. Suheimat, "High Resolution Flood Illumination Retinal Imaging System with Adaptive Optics," Ph.D. dissertation, School of Physics, Science Faculty, National University of Ireland, Galway, Ireland, 2012.

[36] D. H. Marimont and B. A. Wandell, "Matching color images: the effects of axial chromatic aberration," *J. Opt. Soc. Am. A*, vol. 11, no. 12, p. 3113, Dec. 1994.

[37] "What is Chromatic Aberration?" [Online]. Available: http://photographyelement.com/what-is-chromatic-aberration/. [Accessed: 24-Jun-2017].

[38] N. Giordano, "Aberrations of lenses and mirrors," in *College Physics: Reasoning and Relationships*, 1st ed., M. Julet, Ed. Brooks/Cole, Cengage Learning, 2009.

[39] M. Resan, M. Milivojevic, and M. Vukosavljevic, "Wavefront Aberrations," in *Advances in Ophthalmology*, S. Rumelt, Ed. InTech, 2012, pp. 191–205.

[40] "Eye aberrations." [Online]. Available: http://www.telescope-optics.net/eye_aberrations.htm. [Accessed: 23-May-2017].

[41] G. Huang, Z. Zhong, W. Zou, and S. A. Burns, "Lucky averaging: quality improvement of adaptive optics scanning laser ophthalmoscope images," *Opt. Lett.*, vol. 36, no. 19, pp. 3786–8, Oct. 2011.

[42] R. J. Noll, "Zernike polynomials and atmospheric turbulence," *J. Opt. Soc. Am.*, vol. 66, no. 3, p. 207, Mar. 1976.

[43] J. C. Wyant, "Basic Wavefront Aberration Theoryfor Optical Metrology," in *Applied Optics and Optical Engineering, Vol. Xl*, Optical Sciences Center University of Arizona, Tucson, Arizona: Academic Press, Inc., 1992.

[44] C. Perez-Vives, L. B. Salmeron, S. Garcia-Lazaro, D. M. Costa, and T. Ferrer-Blasco, "Adaptive optics, wavefront aberrations and visual simulation," *J. Emmetropia*, vol. 2, no. 2, 2011.

[45] M. Lombardo and G. Lombardo, "Wave aberration of human eyes and new descriptors of image optical quality and visual performance.," *J. Cataract Refract. Surg.*, vol. 36, no. 2, pp. 313–31, Feb. 2010.

[46] D. L. Andrews, "Technology," in *Biomedical Photonics, Spectroscopy, and Microscopy*, 4th ed., Wiley, 2015.

[47] L. N. Thibos, X. Hong, A. Bradley, and X. Cheng, "Statistical variation of aberration structure and image quality in a normal population of healthy eyes.," *J. Opt. Soc. Am. A. Opt. Image Sci. Vis.*, vol. 19, no. 12, pp. 2329–48, Dec. 2002.

[48] H. W. Babcock, "The Possibility of Compensating Astronomical Seeing," *Publ. Astron. Soc. Pacific*, vol. 65, pp. 229–236, Oct. 1953.

[49] D. R. Williams, "Imaging single cells in the living retina.," *Vision Res.*, vol. 51, no.

13, pp. 1379–96, Jul. 2011.

[50] J. W. Hardy, J. Feinleib, and J. C. Wyant, “Real-time Phase Correction of Optical Imaging Systems,” *Proc. OSA Top. Meet. Opt. Propag. through Turbul.*, Mar. 1974.

[51] J. W. Hardy, “Active optics: A new technology for the control of light,” *Proc. IEEE*, vol. 66, no. 6, pp. 651 – 697, 1978.

[52] M. S. Smirnov, “Measurement of the wave aberration of the human eye,” *Biophysics (Oxf).*, vol. 6, pp. 687–703, Jan. 1961.

[53] H. Helmholtz, “Description of an eye mirror for the investigation of the retina of the living eye,” *A Förstner’sche Verlagsbuchhandlung*, 1851.

[54] N. E. Bechrakis and M. H. Foerster, “Ophthalmoscope or Augenspiegel?,” *Arch. Ophthalmol.*, vol. 121, no. 8, Aug. 2003.

[55] J. W. Nordenson, “Augenkamera zum stationaren ophthalmoskop von Gullstrand,” *Ber. Dtsch. Ophth. Ges. 45278*, 1925.

[56] P. J. Same, “Landmarks in the historical development of fluorescein angiography,” *J. Ophthalmic Photogr.*, vol. 15, no. 1, pp. 17–23, Apr. 1993.

[57] D. R. Williams and J. Porter, “Development of Adaptive Optics in Vision Science and Ophthalmology,” in *Adaptive Optics for Vision Science*, J. Porter and H. M. Queener, Eds. John Wiley & Sons, 2006.

[58] W. T. Jackman and J. D. Webster, “On Photographing the Retina of the Living Human Eye,” *Philadelphia Photogr.*, vol. 23, pp. 340–341, 1886.

[59] M. D. Abramoff, M. K. Garvin, and M. Sonka, “Retinal imaging and image analysis.,” *IEEE Rev. Biomed. Eng.*, vol. 3, pp. 169–208, Jan. 2010.

[60] R. H. Webb, G. W. Hughes, and O. Pomerantzeff, “Flying spot TV ophthalmoscope.,” *Appl. Opt.*, vol. 19, no. 17, pp. 2991–7, Sep. 1980.

[61] T. J. Fellers and M. W. Davidson, “Introduction to Confocal Microscopy,” *Olympus Fluoview Resource Center. National High Magnetic Field Laboratory.*, 2007. [Online]. Available: http://www.olympusconfocal.com/theory/confocalintro.html.

[62] J. Schwiegerling and D. R. Neal, “Historical Development of the Shack-Hartmann Wavefront Sensor,” 2005. [Online]. Available: https://www.researchgate.net/publication/241520304_Historical_Development_of_the_Shack-Hartmann_Wavefront_Sensor. [Accessed: 29-May-2017].

[63] B. C. Platt and R. Shack, “History and Principles of Shack-Hartmann Wavefront Sensing,” *J. Refract. Surg.*, vol. 17, 2001.

[64] S. Goelz, J. J. Persoff, G. D. Bittner, J. Liang, C.-F. T. Hsueh, and J. F. Bille, “New wavefront sensor for metrology of spherical surfaces,” in *Proc. SPIE, Active and Adaptive Optical Systems*, 1991, pp. 502–510.

[65] J. Liang, B. Grimm, S. Goelz, and J. F. Bille, “Objective measurement of wave aberrations of the human eye with the use of a Hartmann–Shack wave-front sensor,” *J. Opt. Soc. Am. A*, vol. 11, no. 7, p. 1949, Jul. 1994.

[66] A. W. Dreher, J. F. Bille, and R. N. Weinreb, “Active optical depth resolution improvement of the laser tomographic scanner.,” *Appl. Opt.*, vol. 28, no. 4, pp. 804–8, Feb. 1989.

[67] J. Liang and D. R. Williams, “Aberrations and retinal image quality of the normal

human eye.," *J. Opt. Soc. Am. A. Opt. Image Sci. Vis.*, vol. 14, no. 11, pp. 2873–83, Nov. 1997.

[68] P. Godara, A. M. Dubis, A. Roorda, J. L. Duncan, and J. Carroll, "Adaptive optics retinal imaging: emerging clinical applications.," *Optom. Vis. Sci.*, vol. 87, no. 12, pp. 930–41, Dec. 2010.

[69] H. Hofer, L. Chen, G. Y. Yoon, B. Singer, Y. Yamauchi, and D. R. Williams, "Improvement in retinal image quality with dynamic correction of the eye's aberrations," *Opt. Express*, vol. 8, no. 11, p. 631, May 2001.

[70] "Casao user manual." Imagine Optic, p. 2, 2011.

[71] G. Ramaswamy and N. Devaney, "Pre-processing, registration and selection of adaptive optics corrected retinal images.," *Ophthalmic Physiol. Opt.*, vol. 33, no. 4, pp. 527–39, Jul. 2013.

[72] N. Doble, S. S. Choi, J. L. Codona, J. Christou, J. M. Enoch, and D. R. Williams, "In vivo imaging of the human rod photoreceptor mosaic.," *Opt. Lett.*, vol. 36, no. 1, pp. 31–3, Jan. 2011.

[73] A. Roorda and D. R. Williams, "The arrangement of the three cone classes in the living human eye," *Nature*, vol. 397, no. 6719, pp. 520–2, Feb. 1999.

[74] E. W. Dees, A. Dubra, and R. C. Baraas, "Variability in parafoveal cone mosaic in normal trichromatic individuals.," *Biomed. Opt. Express*, vol. 2, no. 5, pp. 1351–8, Jan. 2011.

[75] D. Merino, J. L. Duncan, P. Tiruveedhula, and A. Roorda, "Observation of cone and rod photoreceptors in normal subjects and patients using a new generation adaptive optics scanning laser ophthalmoscope.," *Biomed. Opt. Express*, vol. 2, no. 8, pp. 2189–201, Aug. 2011.

[76] D. Purves, G. J. Augustine, D. Fitzpatrick, L. C. Katz, A.-S. LaMantia, J. O. McNamara, and S. M. Williams, "Cones and Color Vision," in *Neuroscience*, 2nd ed., J. O. McNamara and S. M. Williams, Eds. Sinauer Associates, 2001.

[77] J. Carroll, M. Neitz, H. Hofer, J. Neitz, and D. R. Williams, "Functional photoreceptor loss revealed with adaptive optics: an alternate cause of color blindness.," *Proc. Natl. Acad. Sci. U. S. A.*, vol. 101, no. 22, pp. 8461–6, Jun. 2004.

[78] R. Garrioch, C. Langlo, A. M. Dubis, R. F. Cooper, A. Dubra, and J. Carroll, "Repeatability of in vivo parafoveal cone density and spacing measurements.," *Optom. Vis. Sci.*, vol. 89, no. 5, pp. 632–43, May 2012.

[79] K. Y. Li and A. Roorda, "Automated identification of cone photoreceptors in adaptive optics retinal images.," *J. Opt. Soc. Am. A. Opt. Image Sci. Vis.*, vol. 24, no. 5, pp. 1358–63, May 2007.

[80] B. Xue, S. S. Choi, N. Doble, and J. S. Werner, "Photoreceptor counting and montaging of en-face retinal images from an adaptive optics fundus camera.," *J. Opt. Soc. Am. A. Opt. Image Sci. Vis.*, vol. 24, no. 5, pp. 1364–72, May 2007.

[81] D. H. Wojtas, B. Wu, P. K. Ahnelt, P. J. Bones, and R. P. Millane, "Automated analysis of differential interference contrast microscopy images of the foveal cone mosaic.," *J. Opt. Soc. Am. A. Opt. Image Sci. Vis.*, vol. 25, no. 5, pp. 1181–9, May 2008.

[82] H. Hofer, L. Chen, G. Y. Yoon, B. Singer, Y. Yamauchi, and D. R. Williams,

"Improvement in retinal image quality with dynamic correction of the eye's aberrations.," *Opt. Express*, vol. 8, no. 11, pp. 631–43, May 2001.

[83] H. Song, T. Y. P. Chui, Z. Zhong, A. E. Elsner, and S. A. Burns, "Variation of cone photoreceptor packing density with retinal eccentricity and age.," *Invest. Ophthalmol. Vis. Sci.*, vol. 52, no. 10, pp. 7376–84, Sep. 2011.

[84] T. Y. Chui, H. Song, and S. A. Burns, "Individual variations in human cone photoreceptor packing density: variations with refractive error.," *Invest. Ophthalmol. Vis. Sci.*, vol. 49, no. 10, pp. 4679–87, Oct. 2008.

[85] M. Lombardo, G. Lombardo, P. Ducoli, and S. Serrao, "Adaptive optics photoreceptor imaging.," *Ophthalmology*, vol. 119, no. 7, p. 1498–1498.e2, Jul. 2012.

[86] K. Y. Li, P. Tiruveedhula, and A. Roorda, "Intersubject variability of foveal cone photoreceptor density in relation to eye length.," *Invest. Ophthalmol. Vis. Sci.*, vol. 51, no. 12, pp. 6858–67, Dec. 2010.

[87] T. Y. Chui, H. Song, and S. A. Burns, "Adaptive-optics imaging of human cone photoreceptor distribution.," *J. Opt. Soc. Am. A. Opt. Image Sci. Vis.*, vol. 25, no. 12, pp. 3021–9, Dec. 2008.

[88] M. Lombardo, S. Serrao, P. Ducoli, and G. Lombardo, "Variations in image optical quality of the eye and the sampling limit of resolution of the cone mosaic with axial length in young adults.," *J. Cataract Refract. Surg.*, vol. 38, no. 7, pp. 1147–55, Jul. 2012.

[89] N. J. Coletta and T. Watson, "Effect of myopia on visual acuity measured with laser interference fringes.," *Vision Res.*, vol. 46, no. 5, pp. 636–51, Mar. 2006.

[90] A. Pallikaris, D. R. Williams, and H. Hofer, "The reflectance of single cones in the living human eye.," *Invest. Ophthalmol. Vis. Sci.*, vol. 44, no. 10, pp. 4580–92, Oct. 2003.

[91] R. S. Jonnal, J. R. Besecker, J. C. Derby, O. P. Kocaoglu, B. Cense, W. Gao, Q. Wang, and D. T. Miller, "Imaging outer segment renewal in living human cone photoreceptors.," *Opt. Express*, vol. 18, no. 5, pp. 5257–70, Mar. 2010.

[92] R. S. Jonnal, J. Rha, Y. Zhang, B. Cense, W. Gao, and D. T. Miller, "In vivo functional imaging of human cone photoreceptors.," *Opt. Express*, vol. 15, no. 24, pp. 16141–60, Nov. 2007.

[93] R. F. Cooper, A. M. Dubis, A. Pavaskar, J. Rha, A. Dubra, and J. Carroll, "Spatial and temporal variation of rod photoreceptor reflectance in the human retina.," *Biomed. Opt. Express*, vol. 2, no. 9, pp. 2577–89, Sep. 2011.

[94] J. Rha, B. Schroeder, P. Godara, and J. Carroll, "Variable optical activation of human cone photoreceptors visualized using a short coherence light source.," *Opt. Lett.*, vol. 34, no. 24, pp. 3782–4, Dec. 2009.

[95] S. S. Choi, N. Doble, J. Lin, J. Christou, and D. R. Williams, "Effect of wavelength on in vivo images of the human cone mosaic.," *J. Opt. Soc. Am. A. Opt. Image Sci. Vis.*, vol. 22, no. 12, pp. 2598–605, Dec. 2005.

[96] M. Pircher, J. S. Kroisamer, F. Felberer, H. Sattmann, E. Götzinger, and C. K. Hitzenberger, "Temporal changes of human cone photoreceptors observed in vivo with SLO/OCT.," *Biomed. Opt. Express*, vol. 2, no. 1, pp. 100–12, Jan. 2010.

[97] A. Roorda and D. R. Williams, "Optical fiber properties of individual human cones.,"

J. Vis., vol. 2, no. 5, pp. 404–12, Jan. 2002.

[98] J. C. He, S. Marcos, and S. A. Burns, "Comparison of cone directionality determined by psychophysical and reflectometric techniques.," *J. Opt. Soc. Am. A. Opt. Image Sci. Vis.*, vol. 16, no. 10, pp. 2363–9, Oct. 1999.

[99] D. Rativa and B. Vohnsen, "Analysis of individual cone-photoreceptor directionality using scanning laser ophthalmoscopy.," *Biomed. Opt. Express*, vol. 2, no. 6, pp. 1423–31, Jun. 2011.

[100] S. Marcos, R. P. Tornow, A. E. Elsner, and R. Navarro, "Foveal cone spacing and cone photopigment density difference: objective measurements in the same subjects.," *Vision Res.*, vol. 37, no. 14, pp. 1909–15, Jul. 1997.

[101] J. A. Martin and A. Roorda, "Direct and noninvasive assessment of parafoveal capillary leukocyte velocity.," *Ophthalmology*, vol. 112, no. 12, pp. 2219–24, Dec. 2005.

[102] R. M. Werkmeister, A. P. Cherecheanu, G. Garhofer, D. Schmidl, and L. Schmetterer, "Imaging of retinal ganglion cells in glaucoma: pitfalls and challenges," *Cell Tissue Res.*, vol. 353, no. 2, pp. 261–8, Aug. 2013.

[103] E. A. Rossi, C. E. Granger, R. Sharma, Q. Yang, K. Saito, C. Schwarz, S. Walters, K. Nozato, J. Zhang, T. Kawakami, W. Fischer, L. R. Latchney, J. J. Hunter, M. M. Chung, and D. R. Williams, "Imaging individual neurons in the retinal ganglion cell layer of the living eye," *Proc. Natl. Acad. Sci. U. S. A.*, vol. 114, no. 3, pp. 586–591, Jan. 2017.

[104] S. I. Balendra, E. M. Normando, P. A. Bloom, and M. F. Cordeiro, "Advances in retinal ganglion cell imaging," *Eye*, vol. 29, no. 10, pp. 1260–1269, Oct. 2015.

[105] A. J. Barber, "A new view of diabetic retinopathy: a neurodegenerative disease of the eye.," *Prog. Neuropsychopharmacol. Biol. Psychiatry*, vol. 27, no. 2, pp. 283–90, Apr. 2003.

[106] J. Tam, K. P. Dhamdhere, P. Tiruveedhula, S. Manzanera, S. Barez, M. A. Bearse, A. J. Adams, and A. Roorda, "Disruption of the retinal parafoveal capillary network in type 2 diabetes before the onset of diabetic retinopathy.," *Invest. Ophthalmol. Vis. Sci.*, vol. 52, no. 12, pp. 9257–66, Nov. 2011.

[107] J. Tam, K. P. Dhamdhere, P. Tiruveedhula, B. J. Lujan, R. N. Johnson, M. A. Bearse, A. J. Adams, and A. Roorda, "Subclinical capillary changes in non-proliferative diabetic retinopathy.," *Optom. Vis. Sci.*, vol. 89, no. 5, pp. E692-703, May 2012.

[108] D. X. Hammer, N. V Iftimia, R. D. Ferguson, C. E. Bigelow, T. E. Ustun, A. M. Barnaby, and A. B. Fulton, "Foveal fine structure in retinopathy of prematurity: an adaptive optics Fourier domain optical coherence tomography study.," *Invest. Ophthalmol. Vis. Sci.*, vol. 49, no. 5, pp. 2061–70, May 2008.

[109] A. Verma, P. K. Rani, R. Raman, S. S. Pal, G. Laxmi, M. Gupta, C. Sahu, K. Vaitheeswaran, and T. Sharma, "Is neuronal dysfunction an early sign of diabetic retinopathy? Microperimetry and spectral domain optical coherence tomography (SD-OCT) study in individuals with diabetes, but no diabetic retinopathy.," *Eye (Lond).*, vol. 23, no. 9, pp. 1824–30, Sep. 2009.

[110] E. L. Fletcher, J. A. Phipps, and J. L. Wilkinson-Berka, "Dysfunction of retinal neurons and glia during diabetes.," *Clin. Exp. Optom.*, vol. 88, no. 3, pp. 132–45, May 2005.

[111] E. Lieth, T. W. Gardner, A. J. Barber, and D. A. Antonetti, "Retinal neurodegeneration: early pathology in diabetes.," *Clin. Experiment. Ophthalmol.*, vol. 28, no. 1, pp. 3–8, Feb. 2000.

[112] M. Parravano, M. Lombardo, G. Lombardo, B. Boccassini, S. Lioi, and M. Varano, "In Vivo Investigation of the Retinal Microscopy in Patients with Type 1 Diabetes Mellitus," *Invest. Ophthalmol. Vis. Sci.*, vol. 53, no. 6, p. 5657, Mar. 2012.

[113] J. L. Duncan, Y. Zhang, J. Gandhi, C. Nakanishi, M. Othman, K. E. H. Branham, A. Swaroop, and A. Roorda, "High-resolution imaging with adaptive optics in patients with inherited retinal degeneration.," *Invest. Ophthalmol. Vis. Sci.*, vol. 48, no. 7, pp. 3283–91, Jul. 2007.

[114] P. Godara, C. Siebe, J. Rha, M. Michaelides, and J. Carroll, "Assessing the photoreceptor mosaic over drusen using adaptive optics and SD-OCT.," *Ophthalmic Surg. Lasers Imaging*, vol. 41 Suppl, pp. S104-8, Jan. .

[115] P. Godara, M. Wagner-Schuman, J. Rha, T. B. Connor, K. E. Stepien, and J. Carroll, "Imaging the photoreceptor mosaic with adaptive optics: beyond counting cones.," *Adv. Exp. Med. Biol.*, vol. 723, pp. 451–8, Jan. 2012.

[116] A. Boretsky, F. Khan, G. Burnett, D. X. Hammer, R. D. Ferguson, F. van Kuijk, and M. Motamedi, "In vivo imaging of photoreceptor disruption associated with age-related macular degeneration: A pilot study.," *Lasers Surg. Med.*, vol. 44, no. 8, pp. 603–10, Oct. 2012.

[117] G. Huang, X. Qi, T. Y. P. Chui, Z. Zhong, and S. A. Burns, "A clinical planning module for adaptive optics SLO imaging.," *Optom. Vis. Sci.*, vol. 89, no. 5, pp. 593–601, May 2012.

[118] A. Sakamoto, M. Hangai, M. Nukada, H. Nakanishi, S. Mori, Y. Kotera, R. Inoue, and N. Yoshimura, "Three-dimensional imaging of the macular retinal nerve fiber layer in glaucoma with spectral-domain optical coherence tomography.," *Invest. Ophthalmol. Vis. Sci.*, vol. 51, no. 10, pp. 5062–70, Oct. 2010.

[119] L. M. Alencar, L. M. Zangwill, R. N. Weinreb, C. Bowd, P. A. Sample, C. A. Girkin, J. M. Liebmann, and F. A. Medeiros, "A comparison of rates of change in neuroretinal rim area and retinal nerve fiber layer thickness in progressive glaucoma.," *Invest. Ophthalmol. Vis. Sci.*, vol. 51, no. 7, pp. 3531–9, Jul. 2010.

[120] A. Kotecha, S. Fernandes, C. Bunce, and W. A. Franks, "Avoidable sight loss from glaucoma: is it unavoidable?," *Br. J. Ophthalmol.*, vol. 96, no. 6, pp. 816–20, Jun. 2012.

[121] H. A. Quigley, "Glaucoma," *Lancet*, vol. 377, no. 9774, pp. 1367–77, Apr. 2011.

[122] R. C. Baraas, J. Carroll, K. L. Gunther, M. Chung, D. R. Williams, D. H. Foster, and M. Neitz, "Adaptive optics retinal imaging reveals S-cone dystrophy in tritan color-vision deficiency.," *J. Opt. Soc. Am. A. Opt. Image Sci. Vis.*, vol. 24, no. 5, pp. 1438–47, May 2007.

[123] M. Michaelides, J. Rha, E. W. Dees, R. C. Baraas, M. L. Wagner-Schuman, J. D. Mollon, A. M. Dubis, M. K. G. Andersen, T. Rosenberg, M. Larsen, A. T. Moore, and J. Carroll, "Integrity of the cone photoreceptor mosaic in oligocone trichromacy.," *Invest. Ophthalmol. Vis. Sci.*, vol. 52, no. 7, pp. 4757–64, Jun. 2011.

[124] Y. Chen, K. Ratnam, S. M. Sundquist, B. Lujan, R. Ayyagari, V. H. Gudiseva, A. Roorda, and J. L. Duncan, "Cone photoreceptor abnormalities correlate with vision

loss in patients with Stargardt disease.," *Invest. Ophthalmol. Vis. Sci.*, vol. 52, no. 6, pp. 3281–92, May 2011.

[125] J. I. Wolfing, M. Chung, J. Carroll, A. Roorda, and D. R. Williams, "High-resolution retinal imaging of cone-rod dystrophy.," *Ophthalmology*, vol. 113, no. 6, p. 1019.e1, Jun. 2006.

[126] K. E. Talcott, K. Ratnam, S. M. Sundquist, A. S. Lucero, B. J. Lujan, W. Tao, T. C. Porco, A. Roorda, and J. L. Duncan, "Longitudinal Study of Cone Photoreceptors during Retinal Degeneration and in Response to Ciliary Neurotrophic Factor Treatment," *Investig. Opthalmology Vis. Sci.*, vol. 52, no. 5, p. 2219, Apr. 2011.

[127] K. R. Alexander and G. A. Fishman, "Prolonged rod dark adaptation in retinitis pigmentosa.," *Br. J. Ophthalmol.*, vol. 68, no. 8, pp. 561–9, Aug. 1984.

[128] C. A. Curcio, N. E. Medeiros, and C. L. Millican, "Photoreceptor loss in age-related macular degeneration.," *Invest. Ophthalmol. Vis. Sci.*, vol. 37, no. 7, pp. 1236–49, Jun. 1996.

[129] N. M. Putnam, H. J. Hofer, N. Doble, L. Chen, J. Carroll, and D. R. Williams, "The locus of fixation and the foveal cone mosaic.," *J. Vis.*, vol. 5, no. 7, pp. 632–9, Jan. 2005.

[130] J. Carroll, S. S. Choi, and D. R. Williams, "In vivo imaging of the photoreceptor mosaic of a rod monochromat.," *Vision Res.*, vol. 48, no. 26, pp. 2564–8, Nov. 2008.

[131] A. Dubra, Y. Sulai, J. L. Norris, R. F. Cooper, A. M. Dubis, D. R. Williams, and J. Carroll, "Noninvasive imaging of the human rod photoreceptor mosaic using a confocal adaptive optics scanning ophthalmoscope.," *Biomed. Opt. Express*, vol. 2, no. 7, pp. 1864–76, Jul. 2011.

[132] A. G. Podoleanu and R. B. Rosen, "Combinations of techniques in imaging the retina with high resolution.," *Prog. Retin. Eye Res.*, vol. 27, no. 4, pp. 464–99, Jul. 2008.

[133] J. C. Christou, A. Roorda, and D. R. Williams, "Deconvolution of adaptive optics retinal images.," *J. Opt. Soc. Am. A. Opt. Image Sci. Vis.*, vol. 21, no. 8, pp. 1393–401, Aug. 2004.

[134] N. Patton, T. M. Aslam, T. MacGillivray, I. J. Deary, B. Dhillon, R. H. Eikelboom, K. Yogesan, and I. J. Constable, "Retinal image analysis: concepts, applications and potential.," *Prog. Retin. Eye Res.*, vol. 25, no. 1, pp. 99–127, Jan. 2006.

[135] M. Lombardo, S. Serrao, P. Ducoli, and G. Lombardo, "Influence of sampling window size and orientation on parafoveal cone packing density.," *Biomed. Opt. Express*, vol. 4, no. 8, pp. 1318–31, Jan. 2013.

[136] N. G. Ghazi and J. W. Much, "The Effect of Lubricating Eye Drops on Optical Coherence Tomography Imaging of the Retina," *Digit. J. Ophthalmol.*, vol. 15, no. 2, 2009.

[137] C. Rao, T. Yu, and B. Hua, "Topics in Adaptive Optics. AO-Based High Resolution Image Post-Processing," in *Topics in Adaptive Optics*, R. K. Tyson, Ed. InTech, 2012, pp. 69–94.

[138] L. Blanco, L. M. Mugniera, and M. Glanc, "Myopic deconvolution of adaptive optics retina images," *Opt. Express*, vol. 19, no. 23, pp. 23227–23239, 2011.

[139] R. V. Canas, "Automated analysis of fluorescein angiography of the human retina," Ph.D. dissertation, School of Engineering and Mathematical Sciences, City

University London, London, UK, 2012.

[140] D. Purves, G. J. Augustine, D. Fitzpatrick, L. C. Katz, A.-S. LaMantia, J. O. McNamara, and S. M. Williams, "Types of Eye Movements and Their Functions," in *Neuroscience*, 2nd ed., J. O. M. and S. M. Williams, Ed. Sinauer Associates, 2001.

[141] S. B. Stevenson and A. Roorda, "Correcting for miniature eye movements in high resolution scanning laser ophthalmoscopy," in *Proc. SPIE 5688, Ophthalmic Technologies XV, 145*, 2005, pp. 145–151.

[142] T. M. Jorgensen, J. Thomadsen, U. Christensen, W. Soliman, and B. Sander, "Enhancing the signal-to-noise ratio in ophthalmic optical coherence tomography by image registration–method and clinical examples," *J. Biomed. Opt.*, vol. 12, no. 4, p. 41208, Jan. 2007.

[143] D. Tomazevic, B. Likar, and F. Pernus, "Comparative evaluation of retrospective shading correction methods.," *J. Microsc.*, vol. 208, no. Pt 3, pp. 212–23, Dec. 2002.

[144] C. Leahy, A. O'Brien, and C. Dainty, "Illumination correction of retinal images using Laplace interpolation.," *Appl. Opt.*, vol. 51, no. 35, pp. 8383–9, Dec. 2012.

[145] D. Paquin, D. Levy, and L. Xing, "Multiscale deformable registration of noisy medical images.," *Math. Biosci. Eng.*, vol. 5, no. 1, pp. 125–44, Jan. 2008.

[146] J. B. Maintz and M. A. Viergever, "A survey of medical image registration.," *Med. Image Anal.*, vol. 2, no. 1, pp. 1–36, Mar. 1998.

[147] B. Fang and Y. Y. Tang, "Elastic Registration for Retinal Images Based on Reconstructed Vascular Trees," *IEEE Trans. Biomed. Eng.*, vol. 53, no. 6, pp. 1183–1187, Jun. 2006.

[148] C. Kulcsár, G. Le Besnerais, E. Ödlund, and X. Lévecq, "Robust Processing of Image Sequences Produced by an Adaptive Optics Retinal Camera," *Opt. Soc. Am.*, p. OW3A.3, 2013.

[149] J. Zheng, J. Tian, K. Deng, X. Dai, X. Zhang, and M. Xu, "Salient feature region: a new method for retinal image registration," *IEEE Trans. Inf. Technol. Biomed.*, vol. 15, no. 2, pp. 221–32, Mar. 2011.

[150] G. Yang, "Towards general-purpose image registration," Rensselaer Polytechnic Institute, Troy, New York, USA, 2007.

[151] A. Perez-Rovira, R. Cabido, E. Trucco, S. J. McKenna, and J. P. Hubschman, "RERBEE: robust efficient registration via bifurcations and elongated elements applied to retinal fluorescein angiogram sequences.," *IEEE Trans. Med. Imaging*, vol. 31, no. 1, pp. 140–150, Jan. 2011.

[152] R. Xia, J. Zhao, and Y. Liu, "A robust feature-based registration method of multimodal image using phase congruency and coherent point drift," in *Proc. SPIE 8919, Pattern Recognition and Computer Vision*, 2013, p. 891903.

[153] F. Laliberte and L. Gagnon, "Registration and fusion of retinal images: a comparative study," *IEEE Trans. Med. Imaging*, vol. 22, no. 5, pp. 715–718, 2002.

[154] F. Laliberté, L. Gagnon, and Y. Sheng, "Registration and fusion of retinal images – an evaluation study," *IEEE Trans. Med. Imaging*, vol. 22, no. 5, pp. 661–73, May 2003.

[155] N. Ryan, C. Heneghan, and P. de Chazal, "Registration of digital retinal images using landmark correspondence by expectation maximization," *Image Vis. Comput.*, vol.

22, no. 11, pp. 883–898, Sep. 2004.

[156] B. Zitova and J. Flusser, “Image registration methods: a survey,” *Image Vis. Comput.*, vol. 21, pp. 977–1000, 2003.

[157] S. Faisan, D. Lara, and C. Paterson, “Scanning ophthalmoscope retinal image registration using one-dimensional deformation fields.,” *Opt. Express*, vol. 19, no. 5, pp. 4157–69, Feb. 2011.

[158] A. Dubra and Z. Harvey, “Registration of 2D images from fast scanning ophthalmic instruments,” in *in Workshop in Biomedical Image Registration*, 2010, pp. 60–71.

[159] C. Viard, K. Nakashima, B. Lamory, M. Paques, X. Levecq, and N. Château, “Imaging microscopic structures in pathological retinas using a flood-illumination adaptive optics retinal camera,” in *Proc. SPIE 7885, Ophthalmic Technologies XXI*, 2011, p. 788509.

[160] S. J. Chiu, Y. Lokhnygina, A. M. Dubis, A. Dubra, J. Carroll, J. A. Izatt, and S. Farsiu, “Automatic cone photoreceptor segmentation using graph theory and dynamic programming.,” *Biomed. Opt. Express*, vol. 4, no. 6, pp. 924–37, Jun. 2013.

[161] R. Matungka, “Studies on Log-Polar Tranform For Image Registration And Improvements Using Adaptive Sampling And Logarithmic Spiral,” The Ohio State University, 2009.

[162] L. Lucchese, G. M. Cortelazzo, and C. Monti, “High resolution estimation of planar rotations based on Fourier transform and radial projections,” in *Proceedings of 1997 IEEE International Symposium on Circuits and Systems*, 2002, vol. 2, pp. 1181–1184.

[163] H. S. Stone, B. Tao, and M. McGuire, “Analysis of image registration noise due to rotationally dependent aliasing,” *J. Vis. Commun. Image Represent.*, vol. 14, no. 2, pp. 114–135, Jun. 2003.

[164] J. Chen, R. Smith, J. Tian, and A. F. Laine, “A novel registration method for retinal images based on local features,” in *Annual International Conference of the IEEE Engineering in Medicine and Biology Society*, 2008, pp. 2242–5.

[165] G. Wolberg and S. Zokai, “Robust image registration using log-polar transform,” in *Proceedings of 2000 International Conference on Image Processing*, 2000, vol. 3, pp. 493–496.

[166] B. S. Reddy and B. N. Chatterji, “An FFT-based technique for translation, rotation, and scale-invariant image registration,” *IEEE Trans. Image Process.*, vol. 5, no. 8, pp. 1266–71, Jan. 1996.

[167] M. Mcguire, “An image registration technique for recovering rotation, scale and translation parameters,” Cambridge MA, 1998.

[168] H. Li, J. Lu, G. Shi, and Y. Zhang, “Tracking features in retinal images of adaptive optics confocal scanning laser ophthalmoscope using KLT-SIFT algorithm.,” *Biomed. Opt. Express*, vol. 1, no. 1, pp. 31–40, Jan. 2010.

[169] C. Harris and M. Stephens, “A combined corner and edge detector,” in *Alvey vision conference*, 1988.

[170] C. Solomon and T. Breckon, *Fundamentals of Digital Image Processing: A Practical Approach with Examples in Matlab*. Wiley-Blackwell, 2011.

[171] A. A. Hefnawy, “Super Resolution Challenges and Rewards,” in *Intelligence for Nonlinear Dynamics and Synchronisation*, A. Bouchachia and K. Kyamakya, Eds.

Atlantis Press/World Scientific, 2010, pp. 163–206.

[172] R. C. Gonzalez and R. E. Woods, *Digital Image Processing*, 2nd ed. NJ: Prentice Hall: Upper Saddle River, 2002.

[173] R. Verma and J. Ali, "A Comparative Study of Various Types of Image Noise and Efficient Noise Removal Techniques," *Int. J. Adv. Res. Comput. Sci. Softw. Eng.*, vol. 3, no. 10, 2013.

[174] R. A. Schowengerdt, "Techniques for Image Processing and Classifications in Remote Sensing." .

[175] M. Sonka, V. Hlavac, and R. Boyle, *Image Processing, Analysis, and Machine Vision*. Cengage Learning, 2014.

[176] G. W. Greenwood and A. M. Tyrrell, *Introduction to Evolvable Hardware: A Practical Guide for Designing Self-Adaptive Systems*. John Wiley & Sons, 2006.

[177] T. R. Singh, S. Roy, and K. M. Singh, "Global DCT Domain Power Law Transformations in Image Enhancement Technique," in *2013 International Symposium on Computational and Business Intelligence (ISCBI)*, 2013, pp. 269–273.

[178] S. G. Rosolen, B. Lamory, F. Harms, J.-A. Sahel, S. Picaud, and J.-F. LeGargasson, "Cellular-resolution in vivo imaging of the feline retina using adaptive optics: preliminary results.," *Vet. Ophthalmol.*, vol. 13, no. 6, pp. 369–76, Nov. 2010.

[179] N. Nassif, B. Cense, B. Park, M. Pierce, S. Yun, B. Bouma, G. Tearney, T. Chen, and J. de Boer, "In vivo high-resolution video-rate spectral-domain optical coherence tomography of the human retina and optic nerve.," *Opt. Express*, vol. 12, no. 3, pp. 367–76, Feb. 2004.

[180] C. Tomasi and R. Manduchi, "Bilateral filtering for gray and color images," in *IEEE Sixth International Conference on Computer Vision*, 1998, pp. 839–846.

[181] J. Arines, "Partially compensated deconvolution from wavefront sensing images of the eye fundus," *Opt. Commun.*, vol. 284, no. 6, pp. 1548–1552, Mar. 2011.

[182] J. Arines and S. Bara, "Hybrid technique for high resolution imaging of the eye fundus," *Opt. Express*, vol. 11, no. 7, p. 761, Apr. 2003.

[183] A. P. Dhawan, R. M. Rangayyan, and R. Gordon, "Image restoration by Wiener deconvolution in limited-view computed tomography," *Appl. Opt.*, vol. 24, no. 23, p. 4013, Dec. 1985.

[184] I. Iglesias and P. Artal, "High-resolution retinal images obtained by deconvolution from wave-front sensing," *Opt. Lett.*, vol. 25, no. 24, p. 1804, Dec. 2000.

[185] D. Catlin and C. Dainty, "High-resolution imaging of the human retina with a Fourier deconvolution technique.," *J. Opt. Soc. Am. A. Opt. Image Sci. Vis.*, vol. 19, no. 8, pp. 1515–23, Aug. 2002.

[186] T. E. Bishop, B. S.D., B. Amizic, A. K. Katsaggelos, T. Chan, and R. Molina, "Blind Image Deconvolution: Problem Formulation and Existing Approaches," in *Blind Image Deconvolution: Theory and Applications*, P. Campisi and K. Egiazarian, Eds. CRC Press, 2007.

[187] J. J. Green and B. R. Hunt, "Improved restoration of space object imagery," *J. Opt. Soc. Am. A*, vol. 16, no. 12, p. 2859, Dec. 1999.

[188] H. Li, J. Lu, G. Shi, and Y. Zhang, "Real-time blind deconvolution of retinal images

in adaptive optics scanning laser ophthalmoscopy," *Opt. Commun.*, vol. 284, no. 13, pp. 3258–3263, Jun. 2011.

[189] R. Unbehauen and M. Zou, "New algorithms of two-dimensional blind deconvolution," *Opt. Eng.*, vol. 34, no. 10, p. 2945, Oct. 1995.

[190] G. Chenegros, L. M. Mugnier, F. Lacombe, and M. Glanc, "3D phase diversity: a myopic deconvolution method for short-exposure images: application to retinal imaging," *J. Opt. Soc. Am. A*, vol. 24, no. 5, p. 1349, May 2007.

[191] S. R. Fanello, C. Keskin, P. Kohli, S. Izadi, J. Shotton, A. Criminisi, U. Pattacini, and T. Paek, "Filter Forests for Learning Data-Dependent Convolutional Kernels," in *IEEE Conference on Computer Vision and Pattern Recognition (CVPR)*, 2014, pp. 1709–1716.

[192] A. Criminisi, J. Shotton, and E. Konukoglu, "Decision Forests: A Unified Framework for Classification, Regression, Density Estimation, Manifold Learning and Semi-Supervised Learning," *Found. Trends® Comput. Graph. Vis. Vol. 7 No 2-3, pp 81-227*, Jan. 2012.

[193] Y. LeCun, Y. Bengio, and G. Hinton, "Deep learning," *Nature*, vol. 521, no. 7553, pp. 436–444, May 2015.

[194] C. J. Schuler, H. C. Burger, S. Harmeling, and B. Scholkopf, "A Machine Learning Approach for Non-blind Image Deconvolution," in *IEEE Conference on Computer Vision and Pattern Recognition (CVPR)*, 2013, pp. 1067–1074.

[195] R. Battu, S. Dabir, A. Khanna, A. K. Kumar, and A. S. Roy, "Adaptive optics imaging of the retina.," *Indian J. Ophthalmol.*, vol. 62, no. 1, pp. 60–5, Jan. 2014.

[196] K. Loquin, I. Bloch, K. Nakashima, F. Rossant, and M. Paques, "Photoreceptor detection in in-vivo adaptive optics images of the retina: Towards a simple interactive tool for the physicians," in *Proceedings of International Symposium on Biomedical Imaging*, 2011, pp. 191–194.

[197] F. Mohammad, R. Ansari, J. Wanek, and M. Shahidi, "Frequency-based local content adaptive filtering algorithm for automated photoreceptor cell density quantification," in *19th IEEE International Conference on Image Processing*, 2012, pp. 2325–2328.

[198] F. Díaz-Doutón, A. Benito, J. Pujol, M. Arjona, J. L. Güell, and P. Artal, "Comparison of the retinal image quality with a Hartmann-Shack wavefront sensor and a double-pass instrument.," *Invest. Ophthalmol. Vis. Sci.*, vol. 47, no. 4, pp. 1710–6, Apr. 2006.

[199] J. M. Wanek, M. Mori, and M. Shahidi, "Effect of aberrations and scatter on image resolution assessed by adaptive optics retinal section imaging," *J. Opt. Soc. Am. A*, vol. 24, no. 5, p. 1296, Apr. 2007.

[200] M. Bidaut Garnier, M. Flores, G. Debellemanière, M. Puyraveau, P. Tumahai, M. Meillat, C. Schwartz, M. Montard, B. Delbosc, and M. Saleh, "Reliability of cone counts using an adaptive optics retinal camera.," *Clin. Experiment. Ophthalmol.*, vol. 42, no. 9, pp. 833–40, Dec. 2014.

[201] R. Obata and Y. Yanagi, "Quantitative analysis of cone photoreceptor distribution and its relationship with axial length, age, and early age-related macular degeneration.," *PLoS One*, vol. 9, no. 3, p. e91873, 2014.

[202] R. B. Fisher, T. P. Breckon, K. Dawson-Howe, A. Fitzgibbon, C. Robertson, E. Trucco, and C. K. I. Williams, *Dictionary of Computer Vision and Image Processing*.

Chichester, UK: John Wiley & Sons, Ltd, 2014.

[203] Z. Wang, A. C. Bovik, H. R. Sheikh, and E. P. Simoncelli, "Image Quality Assessment: From Error Visibility to Structural Similarity," *IEEE Trans. Image Process.*, vol. 13, no. 4, pp. 600–612, Apr. 2004.

[204] D. Kanjar and V. Masilamani, "A New No-Reference Image Quality Measure for Blurred Images in Spatial Domain," *J. Image Graph.*, vol. 1, no. 1, 2013.

[205] M. Hassan and C. Bhagvati, "A Survey On Different Approaches Used In Image Quality Assessment," *Int. J. Appl. Inf. Syst.*, vol. 9, no. 1, 2015.

[206] M. Oszust, L. Chen, B. Jansen, P. Schelkens, M. Carli, and F. Battisti, "Full-Reference Image Quality Assessment with Linear Combination of Genetically Selected Quality Measures," *PLoS One*, vol. 11, no. 6, p. e0158333, Jun. 2016.

[207] D. Marr, S. Ullman, and T. Poggio, *Vision: A Computational Investigation Into the Human Representation and Processing of Visual Information*. New York: Freeman, 1982.

[208] F. Crete, T. Dolmiere, P. Ladret, and M. Nicolas, "The Blur Effect: Perception and Estimation with a New No-Reference Perceptual Blur Metric," in *Proc. SPIE 6492, Human Vision and Electronic Imaging XII, 64920I*, 2007.

[209] E. Peli, "Contrast in complex images," *J. Opt. Soc. Am. A*, vol. 7, no. 10, p. 2032, Oct. 1990.

[210] E. H. Adelson and A. P. Pentland, "The perception of shading and reflectance," in *Perception as Bayesian Inference*, D. C. Knill and W. Richards, Eds. Cambridge University Press, 1996, pp. 409–424.

[211] Y. Z. Goh, A. B. J. Teoh, and M. K. O. Goh, "Wavelet Based Illumination Invariant Preprocessing in Face Recognition," in *2008 Congress on Image and Signal Processing*, 2008, vol. 3, pp. 421–425.

[212] H. K. Chethan and G. H. Kumar, "Illumination Reduction for Camera Captured Documents Using Block Processing and Homomorphic Filtering Technique," in *2011 International Conference on Communication Systems and Network Technologies*, 2011, pp. 350–354.

[213] L. Yongping, W. Chao, and A. Xinyu, "Illumination Processing in Face Recognition," in *Face Recognition*, O. Milos, Ed. InTech, 2010.

[214] G. Ramaswamy, "Pre-processing, Registration and Quality Assessment of Adaptive Optics Assisted Retinal Images," Ph.D. dissertation, School of Physics, National University of Ireland, Galway, 2013.

[215] C.-L. Liu, "A Tutorial of the Wavelet Transform," 2010. [Online]. Available: http://disp.ee.ntu.edu.tw/tutorial/WaveletTutorial.pdf. [Accessed: 27-Oct-2014].

[216] R. Polikar, "The Wavelet Tutorial," 1994. [Online]. Available: http://users.rowan.edu/~polikar/WAVELETS/WTpart1.html.

[217] W. Zhao and C. Zhao, "Facial Illumination Compensation Based on the Wavelet Transform," in *International Conference on Affective Computing and Intelligent Interactio*, 2012, vol. 10, pp. 270–274.

[218] M. Foracchia, E. Grisan, and A. Ruggeri, "Luminosity and contrast normalization in retinal images.," *Med. Image Anal.*, vol. 9, no. 3, pp. 179–90, Jun. 2005.

[219] A. Huertas and R. Gebejes, “Texture Characterization based on Grey-Level Co-occurrence Matrix,” in *Proceedings in Conference of Informatics and Management Sciences*, 2013, no. 1(2).

[220] B. Münch, P. Trtik, F. Marone, and M. Stampanoni, “Stripe and ring artifact removal with combined wavelet—Fourier filtering,” *Opt. Express*, vol. 17, no. 10, p. 8567, May 2009.

[221] N. J. Coletta and D. R. Williams, “Psychophysical estimate of extrafoveal cone spacing.,” *J. Opt. Soc. Am. A.*, vol. 4, no. 8, pp. 1503–13, Aug. 1987.

[222] J. I. Yellott, “Spectral analysis of spatial sampling by photoreceptors: topological disorder prevents aliasing.,” *Vision Res.*, vol. 22, no. 9, pp. 1205–10, Jan. 1982.

[223] R. F. Cooper, C. S. Langlo, A. Dubra, and J. Carroll, “Automatic detection of modal spacing (Yellott’s ring) in adaptive optics scanning light ophthalmoscope images.,” *Ophthalmic Physiol. Opt.*, vol. 33, no. 4, pp. 540–9, Jul. 2013.

[224] S. Anitha and V. Radha, “Enhanced Switching Median Filter for Denoising in 2D Patterned Textile Images,” *Procedia Eng.*, vol. 38, pp. 3362–3372, 2012.

[225] C. D. Kuglin and D. C. Hines, “The Phase Correlation Image Alignment method,” in *Proceedings of IEEE Cybernet Society*, 1975, pp. 163–165.

[226] M. Guizar-Sicairos, S. T. Thurman, and J. R. Fienup, “Efficient subpixel image registration algorithms,” *Opt. Lett.*, vol. 33, no. 2, p. 156, 2008.

[227] S. Umeyama, “Least-squares estimation of transformation parameters between two point patterns,” *IEEE Trans. Pattern Anal. Mach. Intell.*, vol. 13, no. 4, pp. 376–380, Apr. 1991.

[228] V. Esteban and S. Torres, “Subpixel Accuracy Analysis of Phase Correlation Registration Methods Applied to Aliased Imagery,” in *16th European Signal Processing Conference*, 2008.

[229] W. M. K. Khairosfaizal and A. J. Noraini, “Eyes detection in facial images using Circular Hough Transform,” in *5th International Colloquium on Signal Processing & Its Applications*, 2009, pp. 238–242.

[230] S. Schulter, C. Leistner, P. Wohlhart, P. M. Roth, and H. Bischof, “Alternating Regression Forests for Object Detection and Pose Estimation,” in *2013 IEEE International Conference on Computer Vision*, 2013, pp. 417–424.

[231] S. R. Fanello, T. Paek, C. Keskin, S. Izadi, P. Kohli, D. Kim, D. Sweeney, A. Criminisi, J. Shotton, and S. B. Kang, “Learning to be a depth camera for close-range human capture and interaction,” *ACM Trans. Graph.*, vol. 33, no. 4, pp. 1–11, Jul. 2014.

[232] L. Bar, N. Sochen, and N. Kiryati, “Semi-blind image restoration via Mumford-Shah regularization.,” *IEEE Trans. Image Process.*, vol. 15, no. 2, pp. 483–93, Feb. 2006.

[233] A. N. Tikhonov and V. Y. Arsenin, *Numerical Methods for the Solution of Ill-Posed Problems*. Washington D.C: Winston, 1977.

[234] L. I. Rudin, S. Osher, E. Fatemi, L. I. Rudin, S. Osher, and E. Fatemi, “Nonlinear total variation based noise removal algorithms,” *Phys. D*, vol. 60, no. 1–4, pp. 259–268, Nov. 1992.

[235] T. F. Chan and Chiu-Kwong Wong, “Total variation blind deconvolution,” *IEEE Trans. Image Process.*, vol. 7, no. 3, pp. 370–375, Mar. 1998.

[236] Y.-L. You and M. Kaveh, “Anisotropic blind image restoration,” in *Proceedings of 3rd IEEE International Conference on Image Processing*, vol. 1, pp. 461–464.

[237] R. Caruana, N. Karampatziakis, and A. Yessenalina, “An empirical evaluation of supervised learning in high dimensions,” in *Proceedings of the 25th International conference on Machine learning (ICML)*, 2008, pp. 96–103.

[238] P. Cichosz, *Data Mining Algorithms. Explained using R*. Chichester, West Sussex, UK: Wiley, 2015.

[239] N. Dalal, N. Dalal, and B. Triggs, “Histograms of Oriented Gradients for Human Detection,” in *IEEE Conference on Computer Vision and Pattern Recognition (CVPR)*, 2005, vol. 1, pp. 886–893.

[240] A. Criminisi and J. Shotton, Eds., *Decision Forests for Computer Vision and Medical Image Analysis*. London: Springer London, 2013.

[241] J. Shotton, A. Fitzgibbon, A. Blake, A. Kipman, M. Finocchio, R. Moore, and T. Sharp, “Real-Time Human Pose Recognition in Parts from a Single Depth Image,” in *IEEE Conference on Computer Vision and Pattern Recognition (CVPR)*, 2011.

[242] A. Criminisi, J. Shotton, D. Robertson, and E. Konukoglu, “Regression Forests for Efficient Anatomy Detection and Localization in CT Studies,” in *Medical Computer Vision*, Springer Berlin Heidelberg, 2011, pp. 106–117.

[243] G. Biau, “Analysis of a Random Forests Model,” *J. Mach. Learn. Res.*, vol. 13, no. Apr, pp. 1063–1095, 2012.

[244] D. A. Atchison, A. Bradley, L. N. Thibos, and G. Smith, “Useful variations of the Badal Optometer.,” *Optom. Vis. Sci.*, vol. 72, no. 4, pp. 279–84, Apr. 1995.

[245] E. A. Kaye, Y. Hertzberg, M. Marx, B. Werner, G. Navon, M. Levoy, and K. B. Pauly, “Application of Zernike polynomials towards accelerated adaptive focusing of transcranial high intensity focused ultrasound,” *Med. Phys.*, vol. 39, no. 10, 2012.

[246] G. Yang, “Towards general-purpose image registration,” Ph.D. dissertation, Rensselaer Polytechnic Institute, Troy, New York, USA, 2007.

[247] L. N. Thibos, A. Bradley, and X. Hong, “A statistical model of the aberration structure of normal, well-corrected eyes.,” *Ophthalmic Physiol. Opt.*, vol. 22, no. 5, pp. 427–33, Sep. 2002.

[248] A. K. Valeshabad, J. Wanek, P. Grant, J. I. Lim, F. Y. Chau, R. Zelkha, N. Camardo, and M. Shahidi, “Wavefront error correction with adaptive optics in diabetic retinopathy.,” *Optom. Vis. Sci.*, vol. 91, no. 10, pp. 1238–43, Oct. 2014.

[249] J. Rha, R. S. Jonnal, K. E. Thorn, J. Qu, Y. Zhang, and D. T. Miller, “Adaptive optics flood-illumination camera for high speed retinal imaging,” *Opt. Express*, vol. 14, no. 10, p. 4552, May 2006.

[250] L. Mariotti and N. Devaney, “Performance analysis of cone detection algorithms,” *J. Opt. Soc. Am. A*, vol. 32, no. 4, p. 497, Mar. 2015.

[251] L. B. Lucy, “An iterative technique for the rectification of observed distributions,” *Astron. J.*, vol. 79, p. 745, Jun. 1974.

[252] W. H. Richardson, “Bayesian-Based Iterative Method of Image Restoration,” *J. Opt. Soc. Am.*, vol. 62, no. 1, p. 55, Jan. 1972.

[253] Y. Vardi, L. A. Shepp, and L. Kaufman, “A Statistical Model for Positron Emission

Tomography," *J. Am. Stat. Assoc.*, vol. 80, no. 389, p. 8, Mar. 1985.

[254] F. Sroubek and P. Milanfar, "Robust multichannel blind deconvolution via fast alternating minimization.," *IEEE Trans. Image Process.*, vol. 21, no. 4, pp. 1687–700, Apr. 2012.

[255] M. V Afonso, J. M. Bioucas-Dias, and M. A. T. Figueiredo, "Fast Image Recovery Using Variable Splitting and Constrained Optimization," *IEEE Trans. Image Process.*, vol. 19, no. 9, pp. 2345–2356, Sep. 2010.

[256] T. M. Koller, G. Gerig, G. Székely, and D. Dettwiler, "Multiscale Detection of Curvilinear Structures in 2-D and 3-D Image Data," in *IEEE Conference on Computer Vision and Pattern Recognition (CVPR)*, 1995, pp. 864–869.

[257] A. F. Frangi, W. J. Niessen, R. M. Hoogeveen, T. van Walsum, and M. A. Viergever, "Model-based quantitation of 3-D magnetic resonance angiographic images.," *IEEE Trans. Med. Imaging*, vol. 18, no. 10, pp. 946–56, Oct. 1999.

[258] C. Lorenz, I.-C. Carlsen, T. M. Buzug, C. Fassnacht, and J. Weese, "Multi-scale line segmentation with automatic estimation of width, contrast and tangential direction in 2D and 3D medical images," in *Conference on Computer Vision, Virtual Reality and Robotics in Medicine*, 1997, pp. 233–242.

[259] Y. Sato, C. Westin, A. Bhalerao, S. Nakajima, N. Shiraga, S. Tamura, and R. Kikinis, "Tissue classification based on 3D local intensity structures for volume rendering," *IEEE Trans. Vis. Comput. Graph.*, vol. 6, no. 2, pp. 160–180, 2000.

[260] Q. Li, S. Sone, and K. Doi, "Selective enhancement filters for nodules, vessels, and airway walls in two- and three-dimensional CT scans.," *Med. Phys.*, vol. 30, no. 8, pp. 2040–51, Aug. 2003.

[261] S. Zhenghao, M. Zhao, Y. Wang, H. Lifeng, K. Suzuki, M. Zhang, and C. Jin, "Hessian-LoG: a novel dot enhancement filter," *ICIC Express Lett.*, vol. 6, no. 8, pp. 1987–1992, 2012.

[262] J. Liu, J. M. White, and R. M. Summers, "Automated detection of blob structures by Hessian analysis and object scale," in *2010 IEEE International Conference on Image Processing*, 2010, pp. 841–844.

[263] P. K. Saha, J. K. Udupa, and D. Odhner, "Scale-Based Fuzzy Connected Image Segmentation: Theory, Algorithms, and Validation," *Comput. Vis. Image Underst.*, vol. 77, no. 2, pp. 145–174, Feb. 2000.

[264] "Edge Detector." [Online]. Available: http://lab.must.or.kr/(S(2iatfs55hncsa455z1rxqt55))/Print.aspx?Page=Edge-Detector&AspxAutoDetectCookieSupport=1. [Accessed: 22-Dec-2016].

[265] N. Otsu, "A Threshold Selection Method from Gray-Level Histograms," *IEEE Trans. Syst. Man. Cybern.*, vol. 9, no. 1, pp. 62–66, 1979.

[266] L. E. Davis, "A reference guide to the IRAF/DAOPHOT package," *IRAF Programming Group, NOAO, Tucson*. 1994.

[267] J. M. Bland and D. G. Altman, "Statistics notes: Cronbach's alpha," *BMJ*, vol. 314, no. 7080, 1997.

[268] L. I.-K. Lin, "A Concordance Correlation Coefficient to Evaluate Reproducibility," *Biometrics*, vol. 45, no. 1, p. 255, Mar. 1989.

[269] M. Quante, M. Hesse, M. Döhnert, M. Fuchs, C. Hirsch, E. Sergeyev, N. Casprzig,

M. Geserick, S. Naumann, C. Koch, M. A. Sabin, A. Hiemisch, A. Körner, W. Kiess, and LIFE Child Study Investigators, “The LIFE child study: a life course approach to disease and health.,” *BMC Public Health*, vol. 12, p. 1021, Nov. 2012.

[270] M. Lombardo, S. Serrao, and G. Lombardo, “Technical factors influencing cone packing density estimates in adaptive optics flood illuminated retinal images.,” *PLoS One*, vol. 9, no. 9, p. e107402, Jan. 2014.

[271] P. K. Ahnelt, H. Kolb, and R. Pflug, “Identification of a subtype of cone photoreceptor, likely to be blue sensitive, in the human retina.,” *J. Comp. Neurol.*, vol. 255, no. 1, pp. 18–34, Jan. 1987.

[272] H. Ma, C. Jia, and S. Liu, “Multisource Image Fusion Based on Wavelet Transform,” *Int. J. Inf. Technol.*, vol. 11, no. 7, 2005.

[273] E. Cohen and Y. Yitzhaky, “No-reference assessment of blur and noise impacts on image quality,” *Signal, Image Video Process.*, vol. 4, no. 3, pp. 289–302, May 2009.

[274] M. Di Jorio, “The general theory of isoplantatism for finite aperture and field.,” *J. Opt. Soc. Am.*, vol. 39, no. 4, pp. 305–19, Apr. 1949.